Combustor Simulators for Scaled Turbine Experiments



Benjamin F. Hall
University College
University of Oxford

A thesis submitted for the degree of
Doctor of Philosophy

Michaelmas 2015

To Mum and Dad.

Acknowledgements

I enjoyed a serendipitous journey from inquisitive cold-emailer to D.Phil. applicant and this is thanks to the initiative and support of Professor Tom Povey. In the space of a month, Tom had found me a research project, a number of funding routes and a college. Above all else he took a risk in accepting me from the other side of the world, largely unseen, and I am hugely grateful for the opportunity. I hope that your gamble was vindicated by my hard work, my contribution to research, and my not being a goth. As a supervisor Tom has a hands-off approach, that while initially daunting, provides the ultimate learning experience. I appreciate that my D.Phil experience was defined by this approach; that this freedom to learn and to break expensive things is not enjoyed by all students; and that this approach required immense patience on Tom's part – thank you.

Research in the Osney Thermofluids Lab invariably requires extensive technical support. The workshop and maintenance staff were indispensable in bringing experimental plans to reality – thanks for your help! Dominic Harris was the target of my most unreasonable workshop requests and deserves special thanks for his help and patience. Craig Parsons was always at hand and willing to make computer problems go away and you can't put a price on that. Finally, running experiments in close cooperation with Ben Kirollos made this work possible and was a true D.Phil. highlight.

Rolls Royce plc provided financial and technical support to this research, and this is acknowledged with thanks.

Significant parts of this research were performed as part of the EU Low Emissions Core-Engine Technologies research project. The financial and technical support of the Partners is acknowledged.

Finaly I must thank my family for their support. In particular, I thank my mum and dad for their support (both moral and financial) through my many years of education which have extended well in to 'adulthood'. My entire family have been very understanding of my infrequent Skype calls and my even less frequent visits home; for this understanding over 4-plus years, I am indebted.

Abstract

Gas turbine combustors employing a single lean combustion stage represent the next generation of design for reduced NO_X emissions. These lean-burn combustors rely on swirl-stabilised flames resulting in highly non-uniform outflows. Non-uniform conditions adversely affect high-pressure turbine performance. 3D numerical simulations provide a means to understand and optimise engine design, however, the modelling of turbulence means experimental validation is crucial. Turbine test facilities operating at scaled, non-reacting conditions, with simulated combustor flows are an important source of validation data.

This thesis presents advances in combustor simulator design, testing and instrumentation relevant to the challenges of modern, highly-integrated turbine testing. The design of a lean-burn combustor simulator, characterised by swirl and non-uniform temperature, is presented. The design was based on measurements and predictions of engine conditions. Unsteady numerical simulations were employed as a predictive design tool.

An engine-scale combustor simulator was manufactured and characterised experimentally in a bespoke facility. Surveys of flow structure are presented, focusing on experimental turbine inlet data. These data confirmed that the combustor simulator reproduces the important features of a lean-burn combustor; e.g. swirling mainstream flow and high turbulence intensity. The lean-burn combustor simulator will be the first of its kind to be implemented in a rotating turbine test facility, and will provide important validation data.

Measurement techniques were developed alongside the core work. Miniaturised five-hole probe rakes for turbine inlet measurements were developed using additive manufacturing (AM). Building on this work, an open source AM five-hole probe design is presented with experimental validation. The problem of estimating pressure probe bandwidth was also addressed, and a simplified model is presented. These tools have direct applications in turbomachinery research.

Contents

1 Introduction **1**

1.1 Background and motivation 1

1.1.1 Gas turbine emissions and performance 2

1.2 European research 4

1.2.1 Rolls-Royce Programme - SILOET 4

1.2.2 Seventh Framework Programme - LEMCOTEC 5

1.2.3 Seventh Framework Programme - FACTOR 5

1.2.4 Research objectives 6

1.3 Thesis overview 7

1.3.1 Chapter summary 7

2 Review of literature **9**

2.1 Gas turbine combustors 9

2.1.1 Combustor architecture 10

2.1.2 Combustion emissions 12

2.2 Combustor-turbine interactions 14

2.2.1 Combustor simulators in scaled rotating turbine facilities . . . 16

2.2.1.1 EOTDF simulator for the OTRF 17

2.2.1.2 Swirl simulator for the OTRF 20

2.2.1.3 FACTOR Tri-Sector combustor simulator 23

2.2.1.4 Large Scale Turbine Rig at Technische Universität Darmstadt 25

2.2.2 Non-uniform inlet conditions and the high pressure turbine . . 26
2.3 Swirling flows and swirl combustors 29
2.4 Computational methods for swirling flows 32
2.5 Definitions and conventions 35
2.5.1 Spatial averaging of flow properties 35
2.5.2 Temporal averaging of flow parameters 36
2.5.3 Two-dimensional inlet data 36
2.5.4 Swirler quantities 37
2.5.5 Total temperature data 38
2.5.6 Total pressure data 39
2.5.7 Turbine inlet profile definitions 40
2.6 Summary of literature 40

3 Past OTRF combustor simulators - CFD study 42

3.1 Oxford Turbine Research Facility 43
3.1.1 Turbine test facilities 43
3.1.2 Description of the OTRF 45
3.1.3 Context of the current work 45
3.2 EOTDF simulator 49
3.2.1 Numerical setup and modelling 50
3.2.2 Results - Realizable k-ϵ model 52
3.2.3 Results - Reynolds Stress Model 54
3.2.4 Results - k-ω SST model 56
3.2.5 EOTDF study summary 57
3.3 OTRF swirl simulator 60
3.3.1 Numerical setup and modelling 61
3.3.2 Results - Reynolds Stress Model 62
3.3.3 Swirl simulator study summary 63

3.4 Conclusions 65

4 Development of a lean-burn combustor simulator 67

4.1 Combustor simulator concept 67

4.2 Target inlet profiles 70

4.2.1 SILOET Programme 70

4.2.2 LEMCOTEC Programme 73

4.2.3 Swirler aerodynamic design 75

4.2.4 Analysis of temperature profile 77

4.3 Computational design of the combustor simulator 77

4.3.1 Computational method 78

4.3.1.1 Computational method and URANS modelling . . . 79

4.3.1.2 Numerical setup 81

4.3.1.3 Mesh dependency 83

4.3.2 Design challenges 85

4.3.3 Development highlights 87

4.3.4 Computational results 91

4.3.5 Computational design summary 95

4.4 Mechanical design 96

4.4.1 Coolant distribution system 98

4.4.2 Fastener design 99

4.4.2.1 Hub assembly fasteners 102

4.4.2.2 Case assembly fasteners 103

4.5 Swirler mechanical design 104

4.5.1 Mechanical design - fabricated concept 105

4.5.1.1 Stress design and testing 106

4.5.2 Mechanical design - water jet concept 108

4.5.2.1 Stress design and testing 109

4.6 Turbulence generator for a uniform properties case 110
4.6.1 Aerodynamic design of turbulence generator 110
4.6.1.1 Perforate plate concept 111
4.6.1.2 Radial rod concept 112
4.6.2 Mechanical design 113
4.7 Extended computational study of the OLCS 115
4.7.1 Comparison of experimental conditions 117
4.7.1.1 Summary of operating conditions 118
4.7.1.2 Summary of test cases 118
4.7.1.3 Computational method 118
4.7.2 Computational results - SILOET 119
4.7.2.1 Case A - SILOET with axial jet 119
4.7.2.2 Case B - SILOET without axial jet 120
4.8 Computational results - LEMCOTEC 120
4.8.0.1 Case C - LEMCOTEC without axial jet 120
4.8.1 Discussion 124
4.9 Conclusions 125

5 Development of a facility for the experimental characterisation of the OLCS 127

5.1 Overview of facility 128
5.2 OLCS test section 128
5.3 High-pressure feed system design 130
5.3.1 Overpressure protection 132
5.4 Coolant production 133
5.4.1 Vortex tube thermal design 133
5.4.2 Vortex tube mechanical design 136
5.4.3 Vortex tube experimental results 136

5.5 Instrumentation 138
5.5.1 Sensors and data acquisition 138
5.5.1.1 Pressure transducers 139
5.5.1.2 Thermocouples 140
5.5.2 High pressure monitoring and mass flow rate metering 140
5.5.2.1 Condition monitoring 140
5.5.2.2 Mass flow rate metering 141
5.5.3 Test section characterisation 141
5.6 Inlet traverse system 141
5.6.1 Probes for turbine inlet traverse measurements 143
5.6.1.1 Five-hole pressure probe 144
5.6.1.2 Total temperature probes 144
5.6.1.3 High frequency response total pressure (Kulite) probe 145
5.6.1.4 High frequency response hot-wire probe 146
5.6.1.5 Dynamic calibration of the Kulite probe 147
5.6.2 Automated traverse hardware 148
5.6.2.1 Stepper motor setup notes 150
5.6.3 Traverse operation 151
5.6.4 Test procedure 151
5.7 Development of aerodynamic instrumentation 152
5.7.1 Multi-hole probes 152
5.7.2 The Oxford Probe 154
5.7.2.1 Overview of aerodynamic probe design 154
5.7.2.2 Design of the Oxford Probe 155
5.7.2.3 Suggested manufacture process 156
5.7.2.4 Suggested range of use 156
5.7.3 Theory of calibration 157
5.7.3.1 Principle of multi-hole probe calibration 157

5.7.3.2 Calibration coefficients 158
5.7.3.3 Reducing measurement data in an unknown flow - using the Oxford Probe 158
5.7.4 Calibration facility and procedure 159
5.7.4.1 The Oxford Probe Calibration Facility 159
5.7.4.2 Contribution to the OPCF 160
5.7.4.3 Probe traverse system 161
5.7.4.4 Probe roll correction 162
5.7.4.5 Instrumentation and data acquisition 162
5.7.5 Comparison of calibration maps for 16 probes 163
5.7.5.1 Description of the probe tips 163
5.7.5.2 Calibration conditions 165
5.7.5.3 Probe and run-data identification 165
5.7.6 Results 166
5.7.6.1 Typical calibration maps, roll correction and repeatability 166
5.7.6.2 Qualitative comparison of calibration surfaces for different probes 167
5.7.6.3 Quantitative comparison of calibration maps–examples of surface plots 168
5.7.6.4 Quantitative comparison of calibration maps–comparison of all probe types 170
5.7.6.5 Quantitative comparison of calibration mapssummary for all probes 172
5.7.7 Discussion 173
5.8 A frequency response model for pressure probes 173
5.8.1 Background and motivation 174
5.8.1.1 Comparison of existing models 175

5.8.1.2 Basis of comparison 175
5.8.1.3 Distributed-parameter, dissipative-friction models . . 178
5.8.1.4 Low-order models with lumped parameters 180
5.8.1.5 The need for a simplified model 183
5.8.2 Development of a new model 184
5.8.2.1 Tube treatment 185
5.8.2.2 Propagation models 186
5.8.2.3 Proposed model 188
5.8.3 Experimental validation of the new probe model 192
5.8.3.1 Experimental technique 192
5.8.3.2 Experimental results compared to proposed model . 193
5.8.3.3 Discussion 194
5.9 Conclusions 197

6 Experimental results from the OLCS **198**

6.1 Introduction 198
6.2 Summary of cases and measurements 198
6.2.1 Test cases and conditions 198
6.2.2 Measurements 199
6.3 Steady periodicity traverse data 200
6.4 Steady planar traverse data 203
6.4.1 SILOET - cases A and B 203
6.4.2 LEMCOTEC - case C 205
6.4.3 Uniform - case D 206
6.5 Unsteady traverse data 209
6.5.1 SILOET - cases A and B 211
6.5.2 Uniform - case D 213
6.6 Conclusions 213

7 Conclusions **216**

7.1 Numerical methodology 217

7.2 Development of the OLCS 218

7.3 Experimental results 219

7.4 Recommendations for future work 220

References **222**

List of Figures

2.1 An array of discrete can combustors. From Rolls Royce (2015). *The Jet Engine*. John Wiley and Sons, New York, fifth edition. With permission. 11

2.2 An annular combustor with cutaway showing fuel nozzle combustor liner and HP vane. From Rolls Royce (2015). *The Jet Engine*. John Wiley and Sons, New York, fifth edition. With permission. 11

2.3 Emissions characteristics of gas turbine engines. From Lefebvre and Ballal (2010). *Gas Turbine Combustion*. CRC Press, Boca Raton, FL, third edition. With permission. 12

2.4 Schematic sectional comparison of (a) RQL and (b) LPP combustors. From Ford et al. (2012). 13

2.5 Comparison of OTDF and EOTDF generator RTDF profiles. 18

2.6 General arrangement drawing of OTRF EOTDF simulator. From Povey and Qureshi (2008). 19

2.7 The EOTDF system installed in the OTRF. The radial coolant injection system is visible within the annular duct as are the coolant feed hoses. From Povey and Qureshi (2008). 19

2.8 EOTDF generator normalised inlet total temperature ($T/T_{0\,(mass)}$) profile. 20
2.9 General arrangement drawing of the OTRF swirl simulator. 21
2.10 The swirl simulator installed in the OTRF. The array of 16 flat vane swirlers is shown. From Qureshi and Povey (2011). 22
2.11 Laser-sintered four-hole probe rakes. From Qureshi and Povey (2011). 23
2.12 Schematic view of the FACTOR combustor simulator. The coloured surfaces indicate the locations of perforated effusion cooling liners. From Koupper et al. (2014). 24
2.13 Simplified schematic of a combustor and turbine inlet contraction indicating data presentation convention with sample (swirl angle (β)) inlet data and swirl (β) and pitch (α) angle convention. The direction of flow is from left to right. 37
2.14 Swirl and pitch angle definitions. 38

3.1 Schematic illustration of the OTRF. 46
3.2 Photograph of the OTRF showing: (a) The high pressure reservoir bottles; (b) the piston tube; (c) the plug valve assembly; (d) the working section (and containment ring); and (e) coolant reservoir. . 46
3.3 Photograph of the OLCS (highlighted orange) installed in the OTRF upstream of the turbine stage assembly (highlighted green) during LEMCOTEC commissioning, December 2015. 48
3.4 EOTDF generator temperature effectiveness ($T_{0\,eff}$) distribution. . . 50
3.5 (a) EOTDF system CAD geometry and (b) hexahedral computational mesh. 51
3.6 Time-resolved total temperature effectiveness ($T_{0\,eff}$) from URANS solution - Realisable k-ϵ. 53
3.7 Time-averaged total temperature effectiveness ($T_{0\,eff}$) derived from URANS simulation - Realisable k-ϵ. 54

3.8 Time-resolved total temperature effectiveness (T_{0eff}) from URANS solution - RSM. 55
3.9 Time-averaged total temperature effectiveness (T_{0eff}) derived from URANS simulation - RSM. 56
3.10 Time-resolved total temperature effectiveness (T_{0eff}) from URANS solution - k-ω SST. 57
3.11 Time-averaged total temperature effectiveness (T_{0eff}) derived from URANS simulation - k-ω SST. 58
3.12 Circumferentially-averaged temperature (T_{RTDF}) plots for the URANS simulations (time-averaged) and experimental data. 58
3.13 OTRF swirl simulator (L-R) swirl (β) and pitch (α) angle plots. Adapted from Figure 10 of Qureshi and Povey, 2011. 61
3.14 (a) Swirl simulator CAD geometry and (b) hybrid computational mesh. 62
3.15 Time-averaged (L-R) swirl (β) and pitch (α) angle derived from URANS solution - RSM. 63
3.16 Time-resolved flow properties from URANS solution (RSM) showing static pressure on a meridional plane (a,b), the vortex core (a,b), and the swirl angle at the inlet plane (a). 64

4.1 Schematic of the combustor simulator concept showing: (a) the main-stream inlet duct; (b) flat-vane swirlers; (c) swirler diffuser; (d,e) hub and case coolant injection slots; and (f) turbine inlet contraction. . . 69
4.2 SILOET target inlet profiles. Velocity plot shows in-plane vectors and magnitude contours. 72
4.3 SILOET circumferentially-averaged total temperature and total pressure targets. 72
4.4 SILOET circumferentially-averaged flow angle target profiles. 73
4.5 LEMCOTEC target inlet profiles. *Profile shifted to align hot-streak with vortex (swirler) axis. 74

4.6 LEMCOTEC circumferentially-averaged total temperature target (area-weighted). 75
4.7 LEMCOTEC circumferentially-averaged flow angle target profiles. . 75
4.8 Schematic of method to estimate upstream swirl 76
4.9 Example first generation geometry and tetrahedral mesh. 82
4.10 Example second generation geometry and hexahedral mesh on the simplified domain. 83
4.11 The three meshes used in the mesh-dependency study: (a) 2×10^5 cells, (a) 1×10^6 cells, (a) 5×10^6 cells. 84
4.12 Third generation hexahedral mesh on full domain (i.e. including swirler). 85
4.13 Design A1 (tetrahedral mesh including swirler geometry) showing (a) the PVC, (b) the central recirculation zone, (c) the pressure and velocity near the PVC, and (d) the inlet temperature ($T_{0\,eff}$) profile. 88
4.14 Design A2 (hexahedral mesh *excluding* swirler geometry) showing (a) the PVC, (b) the pressure and velocity near the PVC, and (c) the inlet temperature ($T_{0\,eff}$) profile. 89
4.15 Design B (with low momentum jet) showing (a) the steady recirculation bubble, (b) axial velocity on a meridional plane, (c) the inlet temperature ($T_{0\,eff}$) profile, and (d) the inlet swirl angle (β) profile. 90
4.16 Design C1 (adjusted swirler location and coolant baffles) showing (a) the steady recirculation bubble, (b) axial velocity on a meridional plane, (c) the inlet temperature ($T_{0\,eff}$) profile, and (d) the inlet swirl angle (β) profile. 92
4.17 Swirler geometry (and mesh) used in Design C2. 93
4.18 Swirler design detail: case (a) the flat vane extends to the hub tangents; (b) (cf. Figure 4.17) the swirler is 'cut back' in both axial directions. 93

4.19 Design C2 (domain including swirler) showing (a) the steady recirculation bubble, (b) axial velocity on a meridional plane, (c) the inlet temperature ($T_{0\,eff}$) profile, and (d) the inlet swirl angle (β) profile. 94
4.20 Time-resolved URANS results for Design C2. 95
4.21 Circumferentially-averaged temperature (T_{RTDF}) comparison of Designs C1, C2 and B, and the SILOET target. 95
4.22 CAD model of OLCS hardware showing flow paths and; (a) coolant terminal point, (b) common coolant plenum, (c) hub feed rod, (d) hub coolant feed with intermediate plenum, (e) hub injection plenum, (f) case coolant feed, (g) case injection plenum, and (h) mainstream duct swirler assembly. 97
4.23 22.5° sector of the OLCS ($1\frac{1}{4}$ swirler pitches). (a) shows the complete assembly; (b) the fasteners used at the upstream interface, and at the 1-2 (case) and 5-6 (hub) interfaces; (c) the fasteners used at the 2-3 (case) and 6-7 (hub) interfaces; (d) the fasteners used at the downstream interface, and 3-4 (case) and 7-8 (hub) interfaces. . . . 101
4.24 Case component 1 (c.f. Figure 4.23a) showing releiving (venting) cuts on (a) the downstream face and (b) the upstream face. 104
4.25 Mild steel, machined and fabricated swirler (SILOET) consisting of (1) a CNC machined hub, (2) CNC machined case, and (3) 12 laser-cut flat vanes. 106
4.26 (L) Swirler compression load test jig for use in an Instron UTM; the swirler (a) was constrained at the case by (b) which was rigidly attached to the UTM, while the UTM applied a compressive load to the swirler hub using (c). (R) Swirler compression load test jig installed in an Instron UTM. 107
4.27 (L) Load-strain curve for the sample swirlers fabricated from mild steel; 1 welded with fill material and 1 welded without fill material. (R) Deformed fabricated swirlers (sampled with fill material is left). 108

4.28 Single-piece water jet cut aluminium 2014 swirler (LEMCOTEC). . 109
4.29 (L) Load-strain curve for the sample swirlers (two nominally identical water jet cut aluminium 2014 samples). (R) Deformed water jet cut aluminium 2014 swirlers. 110
4.30 Estimate of turbulence quantities for a perforated plate (thickness, $t = 3$ mm) within the OLCS mainstream duct for varying total pressure loss ratio ($\frac{\Delta p_0}{p_0} = 0.01$ to 0.1). d is the perforation (hole) diameter. The dotted curve segments are probably not physically realisable. . 111
4.31 OLCS showing square radial rod turbulence generator concept. Rod count of 40. 113
4.32 Hexahedral wall-resolved mesh used for square rod turbulence generator simulation. 114
4.33 URANS solution of square rod turbulence generator showing turbulence intensity on a surface of constant radius (0.28 m) and at the inlet plane. Turbulence intensity is based on the local velocity. . . . 114
4.34 Turbulence generator FEA results for a 10 bar pressure differential. Yielding occurs only in small compressive regions. (a) downstream side - restrained at hub web; and (b) upstream side - loaded on upstream surfaces. 115
4.35 Turbulence generator manufactured from Aluminium 6082-T6 - water jet cut profile with machined inner diameter for accurate fit. 116
4.36 Case A - atmospheric (AA). Time-resolved URANS results of the OLCS (SILOET config.) at atmospheric experiment conditions with axial jet showing (a) the recirculation zone; (b) the axial velocity on a meridional plane; (c) the inlet total temperature ($T_{0\,eff}$); and (d) the inlet swirl angle (β). 121

4.37 Case A - OTRF (AO). Time-resolved URANS results of the OLCS (SILOET config.) at OTRF conditions with axial jet showing (a) the recirculation zone; (b) the axial velocity on a meridional plane; (c) the inlet total temperature (T_{0eff}); and (d) the inlet swirl angle (β). 121

4.38 Case B - atmospheric (BA). Time-resolved URANS results of the OLCS (SILOET config.) at atmospheric experiment conditions without axial jet showing (a) the recirculation zone; (b) the axial velocity (u_z) on a meridional plane; (c) the inlet total temperature (T_{0eff}); (d) the inlet swirl angle (β); and (e) the PVC as an isosurface of static pressure. 122

4.39 Case B - OTRF (BO). Time-resolved URANS results of the OLCS (SILOET config.) at OTRF conditions without axial jet showing (a) the recirculation zone; (b) the axial velocity (u_z) on a meridional plane; (c) the inlet total temperature (T_{0eff}); (d) the inlet swirl angle (β); and (e) the PVC as an isosurface of static pressure. 122

4.40 Case C - atmospheric (CA). Time-resolved URANS results of the OLCS (LEMCOTEC config.) at atmospheric experiment conditions without axial jet showing (a) the recirculation zone; (b) the axial velocity (u_z) on a meridional plane; (c) the inlet total temperature (T_{0eff}); and (d) the inlet swirl angle (β). 123

4.41 Case C - OTRF (CO). Time-resolved URANS results of the OLCS (LEMCOTEC config.) at OTRF conditions without axial jet showing (a) the recirculation zone; (b) the axial velocity (u_z) on a meridional plane; (c) the inlet total temperature (T_{0eff}); and (d) the inlet swirl angle (β). 123

5.1 Photograph of the complete atmospheric test facility showing; (a) vortex tube; (b) coolant metering system; (c) coolant safety vent line (burst disk removed in image); (d) coolant manifold; (e) mainstream metering system; (f) mainstream safety vent line; (g) mainstream manifold; (h) flexible distribution hoses; (i) OLCS hardware; (j) exit duct; and (k) hub-mounted traverse system. 129
5.2 CAD model sectional view of OLCS (a) with mainstream manifold (b), exit duct (c) and hub-mounted traverse system (d). Dashed lines indicate the extent of the OLCS hardware. 130
5.3 High pressure feed system schematic. 131
5.4 A simple schematic of a counterflow vortex tube. High pressure air is injected tangentially at the inlet to produce highly swirling flow. The separation effect produces cold air at the near orifice, while hot air leaves the opposite end. 134
5.5 Sectional view of the complete vortex tube which utilised the Victaulic pipe fitting system (clamps not shown). Highlighted is (a) the custom-made tangential nozzle and coolant orifice assembly (within a standard 4 inch Victualic tee fitting); (b) the 1 m tube section; and (c) the custom-made needle valve assembly. 136
5.6 The vortex tube inlet nozzle and cold orifice assembly. The tangential inlet nozzle assembly (a) which also integrates the cold orifice (b) is housed within a standard Victaulic 4 inch tee fitting (c). 137
5.7 Experimental data showing the coolant and mainstream temperatures at the respective mass flow metering stations. The mainstream temperature is approximately equal to the VT inlet temperature. From run PG1271. 138
5.8 Sectional schematic of the test section (rotated 90°) showing instrumentation points. The dashed duct wall lines indicate axially spaced pressure tappings (16 each at hub and case). 142

5.9 Photograph of the probes used for traverse measurements of steady properties. (a) Straight and (b) gooseneck thermocouple probes (50 μm butt welded wire K-type); (c) five-hole probe (BH-5HP-001) and (d) holder; machined probe adapters (e) $-10°$ pitch for case access, (f) straight for midspan, and (g) offset and $+14°$ pitch for hub access. . 143

5.10 Photograph of the fast response total pressure probe with embedded Kulite XCQ-062 highlighting: (a) the probe tip and (b) and inset, enlarged view showing the B-screen, and (c) the shielded cable. . . . 146

5.11 Turbulence spectra as power spectral density (PSD) functions as derived from the Kulite and hot-wire probes in a 30 m/s jet. 148

5.12 CAD model of the traverse assembling showing; (a) the mounting frame; (b) stepper motor; (c) 1:100 low backlash epicyclic gear box; (d) drive shaft; (e) bearing housing; (f) traverse arm; (g) radial dovetail slide; (h) probe holder assembly; (i) a five-hole probe; and (j) a thermocouple probe. 149

5.13 Photograph of the traverse system installed in the facility showing; (a) the probe tips at the inlet plane; (b) exit duct hub; (c) traverse arm and dovetail slide; and (d) two-position probe adapter. 149

5.14 Examples of two five-hole probe tip geometries (adapted from Dominy and Hodson (1993)) 155

5.15 (a) Schematic of a pyramid probe tip showing hole numbering and flow angle convention; (b) design of Oxford Probe; and (c) three sizes of Oxford Probe. 156

5.16 (a) Photograph of the working pressure vessel of the Oxford Probe Calibration Facility, showing the transonic nozzle, two (rotational) axis traverse system, and passive ejector pump; (b) Schematic of the traverse system with flow-centred co-ordinate system and probe-centred co-ordinate system 160

5.17 (a) Cross-sectional diagrams of Oxford Probe tips in 3, 4, 6, 8 and 12 mm diameter sizes; (b) Photograph of five DMLS probe tips; (c) Nine of the assembled probes. 164
5.18 Comparison of calibration maps for repeat runs (R3103, R3108 and R3109) for a 12 mm diameter DMLS probe (M-12-02). Run R3019 is shown without (red) and with (black) an applied roll-correction of 5.8° 167
5.19 168
5.20 Error surfaces for probe M-12-01 when using the reference calibration map (obtained from probe M-12-02)an example of low error. 170
5.21 Error surfaces for probe M-12-01 when using the reference calibration map (obtained from probe M-12-02)an example of low error. 171
5.22 Errors as a function of angle with respect to the probe axis—$\epsilon_\alpha(\varphi)$, $\epsilon_\beta(\varphi)$ and $\epsilon_q(\varphi)$—calculated as root-mean-squared error in rolling-average bins of 1 degree width in φ. 171
5.23 RMS errors ϵ_α, ϵ_β and ϵ_q and for all 16 probes tested, across the range $0 < \varphi < 35°$ 172
5.24 Simple probe-transducer system as subcomponents. 174
5.25 Electrical analogy of fluid transmission line model for a simple tube-transducer system. 176
5.26 Differential element representation of a transmission line. Primed values are per unit length. 177
5.27 Magnitude of a simple probe-transducer system using distributed parameter model of tube and the first 3 organ pipe (d, l) harmonic frequencies. 179
5.28 Comparison of the low-order lumped parameters models for a simple probe-transducer system. The distributed parameter, dissipative friction model is included for reference. 181

5.29 Electrical analogy of Xie and Geldart (1997) ($L_t = 0$), Clark and Atkinson (1988) and Van Ommen et al. (1999) models. d$x = l$ in all cases. 183
5.30 Comparison of the modal approximation for N=1 and for dissipative and linear friction, and the lumped parameters model with linear friction. The distributed model with dissipative friction is included for reference. 189
5.31 The natural frequency and damping ratio modification factors (α and β) as defined by Yang and Tobler (1991) for use in the proposed model. 191
5.32 Photograph of complete experimental set up. 193
5.33 Schematic of effective experimental tube set up. 193
5.34 Experimental results for $l = 0.45$ m, $V_T = 200\,\text{mm}^3$ and $\sim 0\,\text{mm}^3$. . 195
5.35 Experimental results for $l = 1.05$ m, $V_T = 200\,\text{mm}^3$ and $\sim 0\,\text{mm}^3$. . 195
5.36 Experimental results for $l = 2.55$ m, $V_T = 200\,\text{mm}^3$ and $\sim 0\,\text{mm}^3$. . 196

6.1 Swirl (β) and pitch (α) angle traverses over 10 swirler pitches for cases A (R1614, R1615), B (R1619, R1616), and C (R1685, R1684). 202
6.2 Case A inlet (P_{IN}) profiles. L-R: Experimental (R1602-13) and URANS (with axial jet), and target profiles. 207
6.3 Case B inlet (P_{IN}) profiles. L-R: Experimental (R1588-94) and URANS (without axial jet), and target profiles. 208
6.4 Circumferentially-averaged profiles for cases A and B. 209
6.6 Circumferentially-averaged profiles for case C. 210
6.7 Case D inlet (P_{IN}) experimental (R1642-44) profiles. 210
6.5 Case C inlet (P_{IN}) profiles. L-R: Experimental (R1671-77) and URANS (without axial jet). 211
6.8 Case A (R1562-63) and B (R1577-78) inlet (P_{IN}) turbulence intensity (%) profiles. 212
6.9 Case D (R1642-44) turbulence intensity on a $z-\theta$ plane at mid-span. z origin is the inlet plane location. 214

Nomenclature

Romans

A	Area (m^2)
A_t	Tensile area (m^2)
$\bar{c}$	Mean speed of sound (m/s)
C	Probe coefficient, Electrical capacitance (Farads)
C_d	Discharge coefficient
d, D	Diameter (m)
D_n	Dissipation number
dB	Decibels: $20\log_{10}(p_1/p_2)$
f	Frequency (Hz)
F	Force (N)
G	Electrical conductance (Siemens)
j	$\sqrt{-1}$
J	Thread engagement ratio
k	Wavenumber (radians/m)
k	Turbulent kinetic energy
l	Length of the tube (m)
L	Length (m), Electrical inductance (Henries)
$L_{e\,min}$	Minimum thread engagement length (m)
$\dot{m}$	Mass flow rate (kg/s)
M	Mach number
n	Polytropic exponent, Component count
N	Number of modes
N	Number of tube (length) lumps
p	Pressure (Pa)
$\bar{p}$	Mean pressure (Pa)
p	Thread pitch (m)
$p_{0\,norm}$	Normalised total pressure
$p_{0\,q}$	Normalised total pressure loss
$p_{0\,rad}$	Normalised radial total pressure
P_{IN}	Inlet plane
P_{TH}	Throat plane
Pr	Prandtl number
PR	Pressure ratio
q	Dynamic pressure (Pa)

r	Radial location
R	Radius (m), Electrical resistance (Ohms)
R_{air}	Gas constant for air
R_x	3D rotation transform about the x-axis
R_y	3D rotation transform about the y-axis
R_z	3D rotation transform about the z-axis
Re	Reynolds number
S	Swirl number
t	Thickness (m), Time (s)
T	Temperature (K)
$T_{0\,eff}$	Temperature effectiveness
T_{RTDF}	Radial temperature distortion factor
Tu	Turbulence
u	Velocity (m/s)
U	Voltage (V)
v	Kinematic fluid viscosity (m^2/s)
V	Volume (m^3)
w	Variable defined by eq. 5.32
x	Coolant mass fraction
y	Variable defined by eq. 5.33
Y	Shunt admittance per unit length
z	Axial location or direction, Variable defined by eq. 5.34
Z	Series impedance per unit length
Z_0	Impedance constant
Z_C	Characteristic impedance

Greeks

α	Pitch angle (°), Natural frequency modification factor
β	Swirl angle (°), Damping ratio modification factor
γ	Ratio of specific heats
Γ	Propagation constant
ϵ	Turbulence dissipation, VT coolant mass fraction
ζ	Damping ratio
θ	Circumferential direction, Roll angle (°)
λ_{c_i}	Root index
μ	Mean fluid dynamic viscosity (Pa s)
ρ	Density (kg/m^3)
$\bar{\rho}$	Mean fluid density (kg/m^3)
σ	Stress (Pa)
τ	Shear wave number
ϕ	Probe cone (included) angle (°)
ψ	Swirler vane angle (°)
ω	Frequency (Rad/s)

ω_d	Damped natural frequency
ω_n	Undamped natural frequency

Subscripts

0	Stagnation (total) property
1-5	Probe hole number
$bolt$	Property of the bolt
c	Coolant stream property
$down$	Property of downstream limiter
err	Error value
h	Main stream property
$hole$	Property of the (threaded) hole
i	Inner (radius or diameter)
Jet	Jet property
$mass$	Mass-weigthed average
$N0$	Stagnation (total) property of jet
$N1$	Upstream property of jet nozzle
$N2$	Downstream property of jet nozzle
nom	Nominal value
o	Outer (radius or diameter)
p	Plastic tube section
P	Property of the probe
ps	Probe quasi-static pressure
r	Radial vector component
reg	Property of pressure regulating valve
rig	Rig property
S	Source (e.g. voltage source U_S)
ss	Stainless steel tube section
Sw	Swirler property
t	Property of the tunnel, Property of the probe tube
T	Property of the traverse, Property of the transducer
$t0$	Quantity at tube open end
tl	Quantity at the tube-transducer interface
Tot	Total, Combined volume of the tube and transducer
up	Property of upstream limiter
UTS	Ultimate tensile strength
$Vane$	Proporty of swirler vane
VT	VT property
$VT\,c$	VT cold end property
$VT\,h$	VT hot end property
$VT\,in$	VT inlet property
z	Axial vector component
θ	Circumferential vector component

$\breve{\theta}$	Circumferentially (area-weighted) average
$\bar{\theta}$	Circumferentially (mass-weighted) average

Abbreviations and acronyms

ANSYS	Software developer (Brand name)
AM	Additive manufacturing
Atm	Atmospheric
BSP	British Standard Pipe
CAD	Computer-aided drafting
CFD	Computational fluid dynamics
CNC	Computer numerical control
CO	Carbon monoxide
CO_2	Carbon dioxide
CRZ	Central recirculation zone
DMLS	Direct Metal Laser Sintering
DLR	German Aerospace Centre
EC	European Commission
EMF	Electromagnetic field
EU	European Union
EOTDF	Enhance Overall Temperature Distortion Factor
FACTOR	Seventh Framework Research Programme
FEA	Finite element analysis
FS	First Sensor (Brand name)
FSO	Full scale output
HP	High pressure
IP	Intermediate pressure
ITD	Inlet temperature distortion
k-ϵ	RANS Turbulence model
k-ω SST	RANS Turbulence model (Shear stress transport)
LDV	Laser Doppler velocimetry
LES	Large eddy simulation
LPP	Lean premixed prevaporised (combustor)
LTI	Linear time-invariant
MIT	Massachusetts Institute of Technology
MS	Mild steel
MT1	OTRF turbine stage
NASA	National Aeronautical and Space Administration
NGV	Nozzle guide vane
NO_X	Nitrogen oxides
OLCS	Oxford Lean burn Combustor Simulator
OPCF	Oxford Probe Calibration Facility
OTDF	Overall temperature distortion factor
OTRF	Oxford Turbine Research Facility

PC	Personal computer
PVC	Precessing vortex core
RANS	Reynolds-averaged Navier-Stokes
RNG	Renormalisation Group
RQL	Rich-Quench-Lean (combustor)
RSM	Reynolds Stress Model
RTDF	Radial temperature distortion factor
SAMULET	Rolls-Royce led British engine research programme
SLA	Selective laser annealing
SLS	Selective laser sintering
SMi	Silicon Microstructures (Brand name)
TC	Thermocouple
UHC	Unburnt hydrocarbon
URANS	Unsteady Reynolds-averaged Navier-Stokes
UTM	Universal testing machine
VB	Vortex breakdown

Chapter 1

Introduction

1.1 Background and motivation

Aviation CO_2 emissions represent a relatively small proportion of global emissions. Total carbon dioxide (CO_2) from aviation accounts for 2% of global greenhouse gas emissions (International Civil Aviation Organization, 2011a). The fact that they are emitted at high altitude makes them unique, however. The emission of particulates, for instance, may increase cirrus cloud formation, contributing to global warming, while condensation trails have a similar effect. While commercial emission-free power options for aviation do not exist in the same way as for land-based power, pressure exists from regulatory bodies to reduce the impact on the environment wherever possible.

For the commercial airliner powered by jet engines, increasing thermal efficiency has the benefit of reducing thrust-specific fuel consumption and CO_2 emissions. In the European Union, where CO_2 from aircraft is levied, reducing fuel consumption and emissions have direct financial benefits. Emissions of unburnt hydrocarbons (carbon monoxide and soot) and oxides of nitrogen (NO_X) are also of concern. NO_X emissions cause photochemical smog in the atmosphere, are a precursor to ozone, and are a respiratory irritant to humans. The reduction of NO_X emissions has therefore been a particular focus of legislators world-wide, and (in response) engine manufacturers. NO_X emissions standards were first introduced in 1981 and subsequently tightened in 1993, 1999 and 2005 (International Civil Aviation Organization, 2011b).

NO_X forms in the combustor stage of the engine, predominately through 'thermal NO_X' production. Thermal NO_X results from the dissociation of atmospheric nitrogen at temperatures above 1850 K, and subsequent oxidation. By limiting peak combustion temperatures, NO_X can be virtually eliminated. Much of the development of combustor technology (in aviation but also land based power systems) has focused on the elimination of thermal NO_X emissions. The focus of this thesis is on improving understanding of how one particular low-emission combustor technology—lean premixed prevaporised (LPP or simply 'lean-burn') combustors—can be integrated most efficiently in to modern jet engines.

This thesis discusses the design of a lean-burn non-reacting combustor simulator for the Oxford Turbine Research Facility (OTRF). The simulator is capable of producing a range of swirl, temperature and total pressure profiles with characterised turbulence characteristics. The resulting combustor simulator, referred to as the Oxford Lean burn Combustor Simulator (OLCS), will assist future experimental work on the OTRF. This work will examine the combined impact of engine-realistic combustor flows on a modern high-pressure stage with film cooling.

1.1.1 Gas turbine emissions and performance

The cycle efficiency of a practical gas turbine engine depends on turbine entry temperature. Higher turbine entry temperatures limit component life, however, creating a ceiling for realisable efficiency gains for a given material technology. The drive towards efficiency improvement in gas turbines has seen turbine entry temperature increase beyond the metal alloy melting point. These operating conditions necessitate active cooling of the high-pressure stage. While film cooling of the high-pressure stage is well developed and widely implemented in commercial engines to deliver increasing entry temperatures, there remains a limited understanding of how secondary turbine inlet characteristics such as non-uniform temperature and residual swirl at the high-pressure turbine inlet affect the aerodynamic and thermal performance of the cooled components.

In the past, the turbine has been optimised for idealised uniform flow conditions. The non-uniformities that exist in reality then typically represent sources of inefficiency. Means to numerically model turbine aerofoil flows are relatively recent innovations, and turbine inlet flows were (and remain) difficult to quantify accurately. In rich-burn low-NO_X combustors (widely used in Rolls-Royce engines up to and including the Trent XWB), high momentum dilution jets are used to dissipate secondary flows (e.g. injector swirl); the outflow can be tailored to the turbine designers specification. As a result non-uniform inlet temperature resulting from discrete fuel injectors has been the focus of related engine research.

The lean-burn combustor is set to supersede the rich-burn combustor as a means to further reductions in NO_X emissions. Lean-burn combustors operate at fuel-lean conditions throughout, minimising peak flame temperatures and reducing NO_X as a result. Swirling primary air flow is used to maintain flame stability, however the system lacks dilution jets (since 70% of the air enters at the primary stage) to remove swirl. These combustors produce inlet conditions that are typically non-uniform across the suite of flow properties. That is, lean-burn combustors are characterised by swirling flow, non-uniform temperature and total pressure, and high and non-uniform turbulence intensity.

Swirl at the turbine inlet can alter vane loading as well as influence secondary flow formation and therefore the migration of temperature distortion through the vane passage. Swirling flows tend to be complex; recirculation, vortex breakdown and the precessing vortex core are common unsteady features that make the design of a lean-burn combustor simulator challenging. Inlet total pressure non-uniformity and inlet turbulence properties are also known to affect high-pressure stage aerodynamic and thermal loading, and therefore require careful consideration in any study of combustor-turbine interactions. Understanding the combined impact of engine-realistic temperature, swirl, total pressure and turbulence properties at the turbine inlet is therefore of significant value to engine designers.

1.2 European research

Europe is home to a number of engine manufacturers, and by extension, significant research and development (R&D). This R&D effort exists both in the industrial and academic settings, with collaboration between the two being commonplace. The central body of research presented in this thesis—that relating to the development of a combustor simulator—was carried out under the objectives of two industrial research programmes; the Rolls-Royce 'SILOET' Programme and the European Union Seventh Framework Programme, 'LEMCOTEC'. The Seventh Framework Programme, 'FACTOR', ran in parallel. These projects shared some important challenges and goals relating to combustor simulator development.

1.2.1 Rolls-Royce Programme - SILOET

The Rolls-Royce Strategic Investment in Low-carbon Engine Technology (SILOET) project was designed to promote the development of low carbon aircraft engine technology. The goal of the programme was to deliver a 2% improvement in engine efficiency. Achieving this goal would be the culmination of seven research areas looking at lightweight structures, high temperature materials, lean-burn combustor design, virtual engineering tools, and advanced components (University of Southampton, 2015).

The SILOET programme includes a turbine research project in the OTRF, which is examining the impact of lean-burn combustor flows on cooled turbine performance. A high-pressure turbine stage of modern design, with cooled vane and rotor has been designed and manufactured for the OTRF. The development of the OLCS was directly in aid of this research programme, providing the ability to simulate lean-burn combustor conditions, and allowing the impact of these conditions on film-cooled vane and rotor performance to be investigated for the first time in the OTRF.

1.2.2 Seventh Framework Programme - LEMCOTEC

The Low Emissions Core-Engine Technologies (LEMCOTEC) programme (part of the European Union Seventh Framework Programme) set out to bring about a 'reduction of emissions directly related to aircraft engines'. The main objective was the improvement of engine efficiency by increasing the engine pressure ratio (LEMCOTEC, 2012).

LEMCOTEC consists of five sub-projects; whole engine assessment, ultra high pressure ratio compressors, lean combustion for ultra-high pressure ratio engines, structures and thermal management, and management and dissemination. The research in the OTRF is part of the structures and thermal management project, focusing on improving the understanding of aerofoil film cooling flows in the presence of non-uniform inlet conditions – non-uniform temperature and swirl being identified as of particular interest. As part of this project, a LEMCOTEC turbine (distinct from the SILOET turbine) of modern design, optimised for lean-burn conditions was designed and manufactured for the OTRF. In this instance, only the vane was film-cooled. The LEMCOTEC OTRF programme will utilise the OLCS to simulate lean-burn inlet conditions, studying in detail, the impact on the aerodynamic and thermal performance of the vane and rotor.

1.2.3 Seventh Framework Programme - FACTOR

The Full Aerothermal Combustor-Turbine Interactions Research (FACTOR) programme (also part of the European Union Seventh Framework Programme) is focused on the study of combustor-turbine interactions, specifically the interaction of cooling flows and secondary flows. The central aim of the programme is to reduce specific fuel consumption by optimising (reducing) cooling flows.

The aim of the FACTOR programme was to provide a comprehensive set of reference data for turbine performance under realistic combustor outflow conditions. This was based around the development of a new turbine test facility at the Institute

of Propulsion Technology at the DLR in Göttingen - the Next Generation Turbine Test Facility (NG-Turb). The facility will include a lean-burn combustor simulator, which has been developed at the University of Florence. The FACTOR combustor simulator was developed in parallel to the OLCS, sharing similar goals (of simulating lean-burn combustor flows), and is discussed in detail in Chapter 2.

The FACTOR programme also includes a (now complete) project which utilised the OTRF to investigate the impact of non-uniform turbine inlet conditions on intermediate pressure (IP) vane performance. Specifically this looked in detail at heat transfer on low-turning IP vanes.

1.2.4 Research objectives

The research described within this thesis set out to further the understanding of high-pressure turbine (vane and rotor) aerodynamic and thermal performance under inlet conditions characteristic of lean-burn combustors. This overarching goal was to be achieved experimentally by the development a lean-burn combustor simulator (the OLCS) and its implementation in a rotating turbine test facility (the OTRF). The thesis also includes two complementary investigations of pressure measurement methods. The research aims were as follows:

- Design and manufacture a combustor simulator (the OLCS) for use in industrial research programmes planned for the OTRF, relating specifically to the performance of the high-pressure turbine under lean-burn combustor conditions.
- Design and construction of an experimental facility for the detailed characterisation of the OLCS prior to its implementation in the OTRF.
- Confirmation of the computational design process, providing confidence in the system prior to OTRF testing, and producing experimental characterisation data to compliment OTRF data.

- Delivery of a system to the OTRF (including turbine inlet instrumentation) capable of producing well-characterised and understood turbine inlet profiles for future industrial research.

The following experimental methods problems were also addressed:

- The feasibility of an open source five-hole probe, using low cost additive manufacturing to widen access to such experimental tools.
- The development of a straightforward and accurate model for calculating the frequency response of pressure probes

1.3 Thesis overview

The central topic of this thesis is the development of a lean-burn combustor simulator (the OLCS) for a rotating turbine test facility at the University of Oxford. The turbine test facility and combustor simulator will contribute directly to industrial research on gas turbines for civil jet engine applications. The structure is focused on the CFD-based design and experimental characterisation of the OLCS. This section serves to outline the main chapters of the thesis.

1.3.1 Chapter summary

The remaining chapters of the thesis are summarised below:

Chapter 2 examines the existing literature relevant to the development of combustor simulators for turbine test facilities, specifically; combustor architecture as a prelude to combustor simulators in the literature; the relevance to the high-pressure turbine; swirling flow and relevant CFD methods; and finally some data processing definitions.

Chapter 3 provides a short introduction to the OTRF in the broader context of turbine test facilities, and describes the role of the OLCS in OTRF research. It then focuses on a CFD investigation of the existing OTRF combustor simulators, which

was carried out as a precursor to the CFD design of the OLCS. The purpose of the study was develop a CFD methodology with understood strengths and weaknesses.

Chapter 4 describes the iterative CFD-based design of the OLCS and the mechanical design of the resulting system. The target inlet profiles are discussed, followed by the computational method and finally results; a number of design highlights are discussed in detail in order to illustrate the evolution of the design. The mechanical design of all key components is described.

Chapter 4.7 presents an extended study of the OLCS, specifically examining the hardware as built. Results at OTRF conditions are presented alongside those of an atmospheric pressure case relevant to the facility discussed in Chapter 5 and the experimental results of Chapter 6.

Chapter 5 describes the development of an experimental facility for the characterisation of the OLCS (outside of the OTRF). The chapter focuses on the integration of a high-pressure air supply system and instrumentation with the OLCS hardware.

Chapter 6 presents a range of experimental characterisation data for the OLCS gathered from the facility described in Chapter 5.

Chapter 2

Review of literature

The focus of this thesis is the development of a combustor simulator for the OTRF capable of producing scaled turbine inlet conditions representative of a lean-burn combustor. The system is known as the Oxford Lean Burn Combustor Simulator (OLCS). To this end, the review of literature included in this chapter is focused on that directly relevant to the development of the OLCS. This includes a discussion of fundamental combustor designs, a review of existing combustor simulators for scaled turbine test facilities, a review of literature related to swirling combustor flows, and finally a review of literature on computational methods for such flows.

There are two notable pieces of supporting work in the chapters addressing the development of instrumentation (Chapter **??**) and pressure probe frequency response (Chapter 5.8). The literature is addressed separately within each of these chapters, rather than in this section.

2.1 Gas turbine combustors

The combustor stage of a gas turbine is responsible for the heat addition to the engine cycle. Achieving a working combustor design was a significant hurdle in early engine development by Frank Whittle in Britain (Lefebvre and Ballal, 2010). The architecture of the combustor stage has evolved significantly and fundamentally since the first gas turbine for aero (jet) engine applications, which is the application of interest

herein (as distinct from industrial engines). Lefebvre and Ballal (2010) provided an excellent historical summary of gas turbine combustor design dating back to the earliest systems developed in the 1940s in the United Kingdom, the United States and Germany. A summary of the main types of combustor architecture is provided below.

2.1.1 Combustor architecture

The first gas turbine engines employed 'tubular' (or 'can') combustors (Figure 2.1) in which each flame tube was housed in a separate air casing (Rolls Royce, 2015). This type of combustor is still frequently employed in land-based industrial gas turbines where compactness is less important than in aero engine applications. The discrete and modular nature of the combustion system makes development (particularly testing) economical; however, the relatively large size of the system is undesirable for aero applications (Lefebvre and Ballal, 2010).

The next generation of combustor architecture consisted once again of discrete flame tubes, but instead housed collectively in an annular air casing (Rolls Royce, 2015), and was known as the 'tubo-annular' (or 'can-annular') combustor. Lefebvre and Ballal (2010) explain that the tubo-annular combustor has the advantage of being more compact than the tubular system while maintaining the mechanical strength and ease of development of a tubular combustor.

The annular air casing concept of the tubo-annular combustor led to the annular combustor (Figure 2.2) which is particularly favourable in terms of compactness. It also provides benefits in terms of reduced combustor pressure loss (Lefebvre and Ballal, 2010) over both tubular systems. Lefebvre and Ballal (2010) point out that the main challenge associated with annular combustor liners is the high buckling load experienced by the outer liner which limited its use in early engines. Annular combustors are now the standard in modern aero engines. This thesis is henceforth focused on modern engines utilising annular combustors.

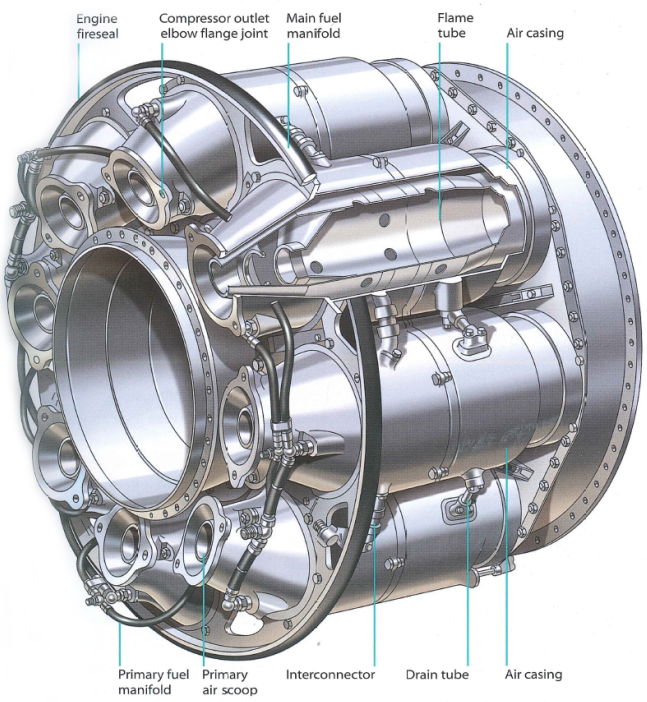


Figure 2.1: An array of discrete can combustors. From Rolls Royce (2015). *The Jet Engine*. John Wiley and Sons, New York, fifth edition. With permission.

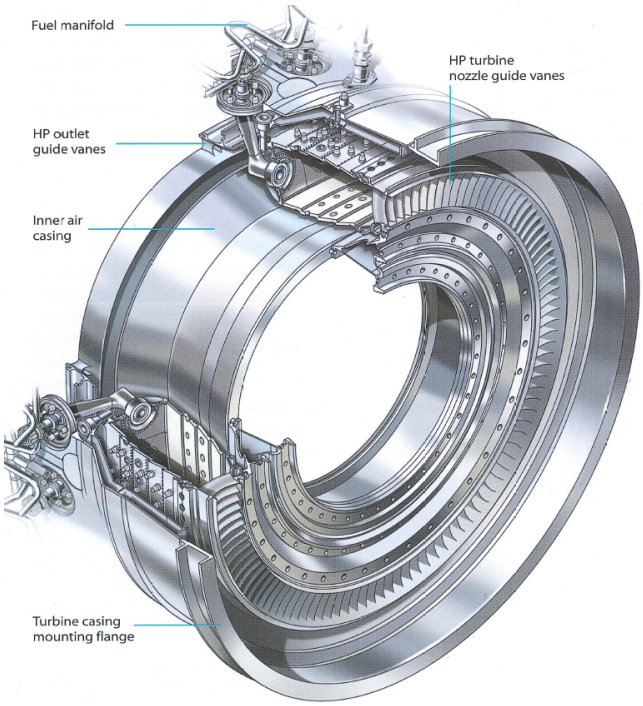


Figure 2.2: An annular combustor with cutaway showing fuel nozzle combustor liner and HP vane. From Rolls Royce (2015). *The Jet Engine*. John Wiley and Sons, New York, fifth edition. With permission.

2.1.2 Combustion emissions

Modern combustors in aero engines must comply with strict regulations on emissions, particularly related to nitrogen oxides (referred to as NO_X) but also unburned hydrocarbons (UHCs) and carbon monoxide (CO). NO_X emissions have faced increasingly strict regulation in recent decades and modern engines for both aero and industrial applications typically employ some kind of 'low-NO_X' combustor design. The formation of nitrogen oxides is directly linked to the peak combustion temperature (since NO_X emissions are mostly due to the endothermic oxidation of atmospheric nitrogen - thermal NO_X) and can be kept to a minimum by keeping this peak below a threshold - approximately 1850 K (Lefebvre and Ballal, 2010). The central challenge in designing combustors for low emissions is that while low combustion temperatures reduce NO_X, they increase UHC and CO emissions, as illustrated in Figure 2.3.

In the case of aero engines which burn liquid fuels, there are two developments in combustor design aimed specifically at reducing NO_X emissions while maintaining

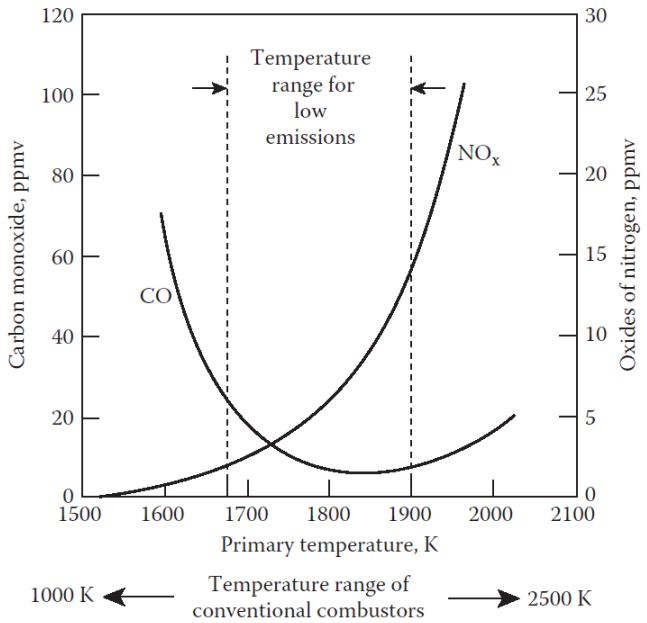


Figure 2.3: Emissions characteristics of gas turbine engines. From Lefebvre and Ballal (2010). *Gas Turbine Combustion*. CRC Press, Boca Raton, FL, third edition. With permission.

low UHC and CO emissions - the Rich-Quench-Lean (RQL) combustor, and the Lean Premix Prevaporise (LPP) combustor.

In RQL combustors, sometimes simply referred to as 'rich-burn' combustors, the combustion process is carried out in 3 distinct zones. The first stage is characterised by a fuel rich primary zone which provides stable combustion at a wide range of operating conditions and limits NO_X formation by limiting excess oxygen. The flow is quenched rapidly—therefore avoiding the time required for appreciable NO_X production—with coolant air in the form of high momentum dilution jets. In the final lean dilution zone, the temperature is high enough to achieve complete combustion of remaining UHC, CO and soot that forms in the primary zone, while remaining below that at which NO_X formation becomes significant. A RQL combustor is illustrated schematically in Figure 2.4a.

LPP combustors, often referred to simply as 'lean-burn' combustors, currently represent the state of the art in emissions reduction for aero engines. LPP combustors

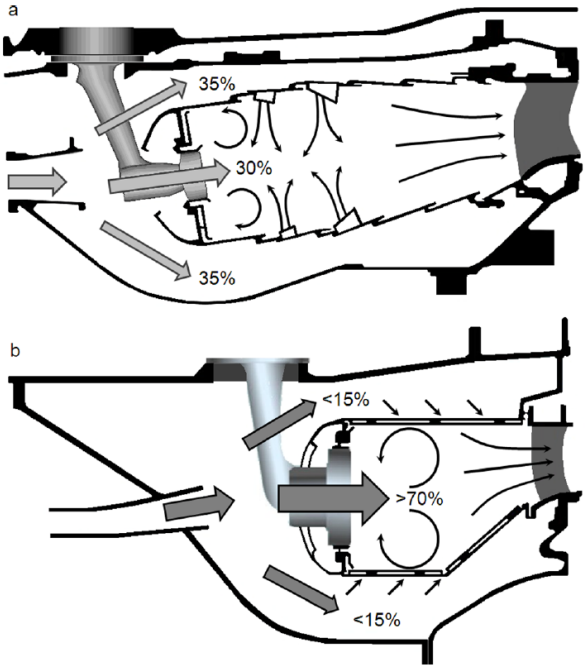


Figure 2.4: Schematic sectional comparison of (a) RQL and (b) LPP combustors. From Ford et al. (2012).

differ from RQL and conventional combustors (Figure 2.4 provides a comparison) in that the majority (70% (Ford et al., 2012)) of the air flow is introduced to the (annular) flame tube through a primary air swirler including a premixed, highly homogeneous fuel-air mixture. In doing so, combustion occurs at an air-fuel ratio that is close to the lean blowout limit (Lefebvre and Ballal, 2010). By combusting a homogeneous fuel-air mixture, relatively uniform temperature is achieved, avoiding stoichiometric regions which produce large quantities of NO_X. The primary air swirler creates a low-velocity central recirculation zone immediately downstream which acts as a flame holder, preventing lean blowout. A lean-burn combustor is illustrated schematically in Figure 2.4b.

The OLCS was designed to simulate the (scaled) conditions produced by a lean-burn (LPP) combustor. These conditions are characterised by high residual swirl (due to the high mass flow rate of gas injected at the primary air swirler and lack of dilution jets), non-uniform inlet temperature and total pressure, and high turbulence. These inlet conditions are discussed in detail in Chapter 4.

2.2 Combustor-turbine interactions

The combustor and first HP stage (particularly the vane) must endure the most extreme conditions within the engine - absolute pressures and temperatures of 50 bar and 1900 K being typical of turbine entry conditions for modern jet engines. Rolls Royce (2015) dramatically stated that "the first task of the turbine system is survival". The pragmatic observer would counter that it is to power the HP compressor. This former sentiment could be read as a relic of the historical approach to engine design, where the combustor design was established and handed over to the turbine designer. In the absence of detailed measurements within engines (which remain challenging) or in scaled turbine facilities, and 3D computational fluid dynamics (CFD), it was difficult to realise a more integrated design process. The proliferation of such research

more recently, and in particular, exponential increases in computing power available for 3D CFD, has seen a concerted shift towards integration of the combustor and turbine design processes and detailed studies of the interaction between the two stages.

Extending component life while increasing turbine entry temperature (and therefore cycle efficiency) relies on a detailed understanding of how flow exiting the combustor interacts with the first HP stage - specifically, how non-uniform flow quantities (e.g. total temperature, total pressure, velocity and turbulence) affect HP stage aerodynamics and heat transfer. As mentioned above, the availability of 3D CFD has been a catalyst for the increased interest in and understanding of combustor-turbine interactions, providing high resolution information throughout the flow field. The necessity to model turbulence in high Reynolds number industrial flows has meant that experimental data for validation of simulations remains crucial. To this end, increasingly engine-realistic experiments in scaled turbine facilities have continued to be of interest to engine designers.

There are two areas of particular interest in the context of this thesis:

1. Previous combustor simulators for scaled turbine facilities - particularly their design and performance
2. The impact on the HP stage as measured experimentally using the above simulators.

Existing combustor simulators in the literature provide a helpful starting point in understanding the possible mechanisms by which engine-realistic conditions can be achieved - for instance, how one might introduce temperature non-uniformity. Additionally, it is helpful to understand whether certain designs were more successful than others such that previously identified pitfalls may be avoided.

The scope of this thesis does not extend to including detailed analysis of HP stage measurements (using the resulting combustor simulator system in the OTRF) due to research programme delays. However, it remains necessary to understand the

existing HP stage measurements in the literature resulting from similar simulators. Doing so provides context and highlights the importance of continuing this line of research towards increasingly engine-realistic (scaled) conditions.

2.2.1 Combustor simulators in scaled rotating turbine facilities

Several combustor simulators for scaled rotating (fully-annular) turbine facilities exist in the literature. These simulators have been designed for a number of different rotating facilities around the world, including the OTRF. The earliest simulators focused on inlet temperature non-uniformity (The Warm Core Turbine Test Facility at the NASA Lewis Research Center (Schwab et al., 1983), The Large Scale Rotating Rig at the United Technologies Research Center (Butler et al., 1989), and The Rotating Blow-Down Facility at the Massachusetts Institute of Technology (MIT) (Haldeman, 1989; Shang and Epstein, 1997)), as did relatively recent simulators of Hurrion (2002) and Povey and Qureshi (2008) for the OTRF and that of Haldeman et al. (2004) for the Turbine Test Facility at the Ohio State University Gas Turbine Laboratory. The combustor simulator of Barringer et al. (2004) was used to examine the effects of non-uniform inlet total pressure in addition to non-uniform temperature. These systems have been reviewed collectively and comprehensively by Povey and Qureshi (2009). Acknowledging this, a detailed description of the aforementioned systems has not been reproduced here.

Recent trends in combustor simulators have been towards simulating modern swirl-stabilised lean-burn combustors. The first of these systems in a rotating facility was that of Qureshi and Povey (2011) which focused on simulating high residual combustor swirl at the vane inlet. The work of Koupper et al. (2014) focused on the development of a 'Tri-Sector' combustor simulator as part of the FACTOR research programme, as a precursor to a fully-annular system for the Next Generation Turbine Test Facility (NG-Turb) (DLR, 2014) operated by the German Aerospace Center (referred to as the DLR). This combustor simulator focused on producing inlet swirl and

non-uniform temperature, and extensive inlet characterisation (including turbulence) was carried out.

A subset of the above-cited research was of particular relevance to the development of the OLCS. Firstly, the Overall Temperature Distortion Factor (OTDF) (Hurrion, 2002) and Enhanced Overall Temperature Distortion Factor (EOTDF) (Povey and Qureshi, 2008) generators for the OTRF provided an obvious starting point for a combustor simulator for the OTRF with non-uniform temperature. The swirl simulator of Qureshi and Povey (2011) provided an important reference as the first swirl simulator implemented in an annular rotating facility—the OTRF—and is therefore particularly relevant to subsequent combustor simulators for the OTRF which consider residual combustor swirl. Finally, the FACTOR combustor simulator (Koupper et al., 2014), while not yet applied to a rotating facility, is the closest analogue to the OLCS.

It is noted that the development of the FACTOR system occurred concurrently with the development of the OLCS. As a result, the development of the OLCS (Hall et al., 2013) pre-dated the open literature relating to the FACTOR system. The FACTOR system is discussed predominantly within this section in the interest of a complete review of literature at the time of publication.

2.2.1.1 EOTDF simulator for the OTRF

The earliest studies (see Hurrion (2002), Povey et al. (2007), Povey and Qureshi (2008), Qureshi et al. (2011b), and Qureshi et al. (2012)) of turbine inlet non-uniformity in the OTRF looked at the isolated effect on non-uniform inlet temperature (leaving total pressure and velocity uniform). The first OTRF combustor simulator was the OTDF generator of Hurrion (2002). This was succeeded by the second generation EOTDF generator of Povey and Qureshi (2008) which was capable of producing a greater level of radial and overall (circumferential) temperature non-uniformity than the OTDF system. This is illustrated in terms of the RTDF profile of Figure 2.5. It

is noted that the OTDF measurements were taken at the NGV leading edge, while the EOTDF measurements were taken 21.0 mm upstream of this, which is likely to account in part for the flatter profile in the former case.

The EOTDF system differed from the OTDF system mainly in terms of the injection slot geometry. In both cases the slots were effectively plain in shape, however their relative axial positions and areas were reviewed carefully for the EOTDF system. The marked difference between profiles illustrated the importance of carefully considering the mixing length and relative stream velocities when designing systems to simulate specific 2D temperature profiles at or near the vane inlet.

The EOTDF simulator was an important point of reference for developing a new system for the OTRF which was to included temperature non-uniformity. The method of coolant injection and overall integration with the existing OTRF hardware was of particular importance. The EOTDF system utilised ambient temperature air as coolant injected through plain slots for simplicity.

The EOTDF simulator is shown schematically in Figure 2.6 and installed in the OTRF in Figure 2.7. The EOTDF simulator utilised circumferential slots at the endwalls and discrete radial injection baffles to generate hot-streaks. The endwall slots were responsible for the generation of radial temperature non-uniformity while

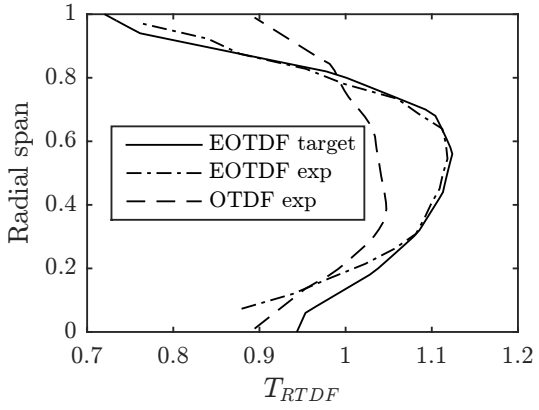


Figure 2.5: Comparison of OTDF and EOTDF generator RTDF profiles.

the radial injection baffles provided circumferential (overall) non-uniformity. The total pressure and velocity of each coolant stream was selected specifically to minimise mixing in the shear layers and to maintain a uniform total pressure at the HP vane inlet. The total pressure was measured to be effectively uniform in the same plane (Povey and Qureshi, 2008). Figure 2.8 illustrates that the EOTDF simulator produced a well-defined hot-streak with a strong radial temperature distortion factor (RTDF).

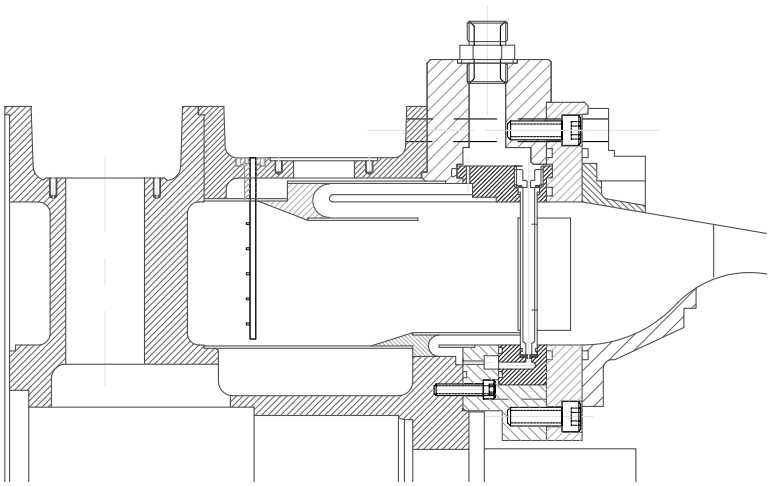


Figure 2.6: General arrangement drawing of OTRF EOTDF simulator. From Povey and Qureshi (2008).

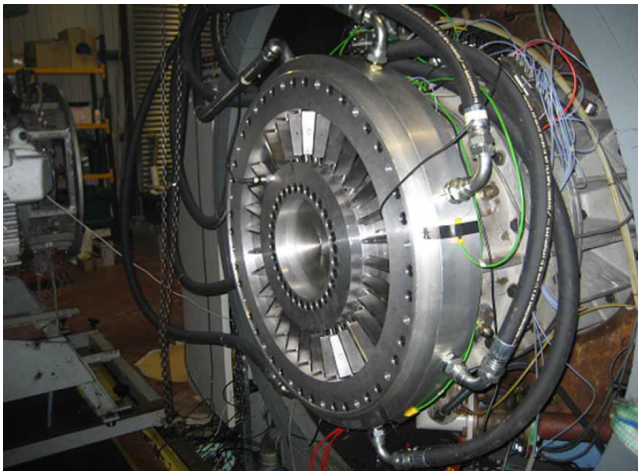


Figure 2.7: The EOTDF system installed in the OTRF. The radial coolant injection system is visible within the annular duct as are the coolant feed hoses. From Povey and Qureshi (2008).

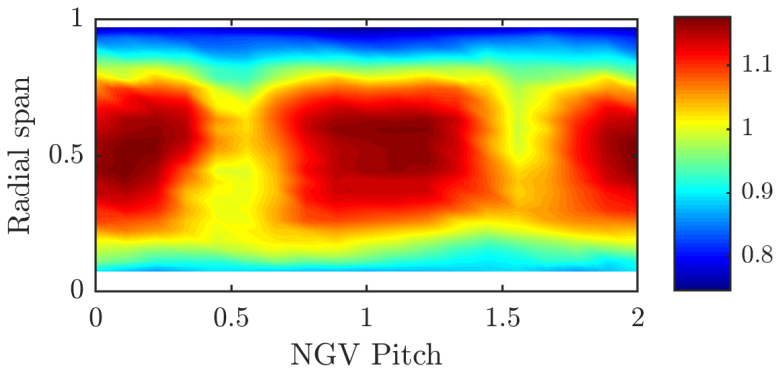


Figure 2.8: EOTDF generator normalised inlet total temperature ($T/T_{0\,(mass)}$) profile.

The OTRF studies of non-uniform inlet temperature were of greatest relevance to annular rich-burn (RQL) combustors—characterised by discrete burners, high momentum dilution jets, and very low residual swirl—however were also of use in understanding how to achieve temperature distortion in a simulator for lean-burn combustors. OTRF experiments with hot-streaks demonstrated that non-uniform inlet temperature altered HP vane heat transfer by altering the local driving gas temperature (Qureshi et al., 2011b) and also affected aerodynamics in the HP rotor (Qureshi et al., 2012). The effect of local driving temperature on HP vane heat transfer confirmed the importance of relative clocking between discrete combustor burners (and therefore hot spot location) and the vane row.

2.2.1.2 Swirl simulator for the OTRF

Swirl-stabilised lean-burn combustors are currently the state of the art in terms of compact, low-emission designs for aero engine applications. Unlike previous low-NO_X combustor designs, such as RQL combustors, lean-burn combustors are characterised by high residual inlet swirl. Acknowledging the need for experimental measurements of HP turbine aerodynamic and thermal performance under swirling inlet flow conditions, Qureshi and Povey (2011) designed an inlet swirl simulator for the OTRF - the first of its kind in a rotating turbine facility.

The OTRF swirl simulator (Qureshi and Povey, 2011) aimed to produce high (at least $\pm 40\,^{\circ}$) swirl at the inlet to the HP vane under isothermal conditions. There was not a specific total pressure target for the simulator, although the swirling flow dictated that the profile would have been non-uniform also.

The design of the system was carried out using a combination of steady RANS CFD simulations and a linearised (from the annular geometry) wind tunnel model (Qureshi and Povey, 2011). The steady RANS simulations of this work predicted the general vortical structure of the flow and some reasonable agreement was observed between simulations and experiments. It is important to note, however, that 3D swirling flows invariably consist of unsteady features and so should be modelled using an unsteady solver. Convergence in a steady solver for such a case implies an excessively diffusive numerical set up, either by way of coarse mesh resolution, insufficient order of spatial discretisation, a diffusive turbulence model or most likely, some combination thereof. An appropriate CFD approach is the focus of Chapter 3.

The final system consisted of 16 flat-vane swirlers of 40° vane angle, patterned around the annular duct, immediately upstream of the vane inlet contraction. The swirl simulator of Qureshi and Povey (2011) is illustrated as a general arrangement drawing in Figure 2.9. The system is shown installed in the OTRF in Figure 2.10.

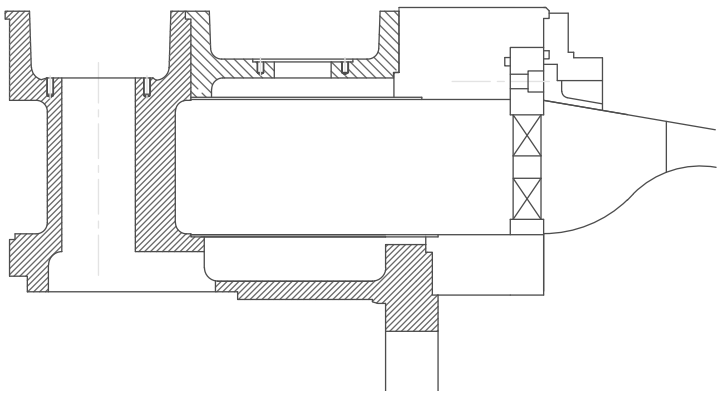


Figure 2.9: General arrangement drawing of the OTRF swirl simulator.

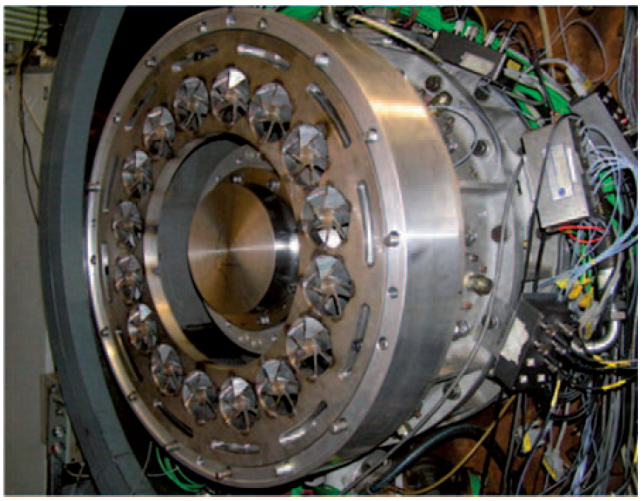


Figure 2.10: The swirl simulator installed in the OTRF. The array of 16 flat vane swirlers is shown. From Qureshi and Povey (2011).

The swirl simulator of Qureshi and Povey (2011) was used in the first experimental investigation of the effects of residual combustor swirl on the HP stage in an engine-scale rotating facility. Based on the pilot study results, the system produced high ($\pm 50\,^{\circ}$) swirl at the inlet to the vane - specifically a plane at the theoretical vane leading edge. Upon close inspection of the published data, it appears that values above this may have been present in the flow, however were either outside the probe calibration range or were clipped during data processing. The data taken in the OTRF (at a plane 29.5 mm upstream of the vane leading edge) for the fully-annular swirl simulator generally supported the pilot study measurements although its relative sparseness and incomplete coverage severely limited its wider usefulness. Aerodynamic measurements on the vane surface showed that the high swirl altered the vane loading significantly (Qureshi et al., 2011a).

A notable innovation in the work of Qureshi and Povey (2011) was the use of four-hole probe rakes produced almost entirely using Additive Manufacturing (AM) - Direct Metal Laser Sintering (DMLS). The facets of the truncated tetrahedral probe tips were formed directly by the DMLS process while the pneumatic tubes were finished by inserting stainless steel tubing. The resulting rakes are shown in Figure

2.11. The probes were found to yield consistent calibration maps of a high quality (Qureshi and Povey, 2011). This initial proof of concept demonstrated the capability of DMLS for probe and complete rake applications, which was developed further in the current work - see Chapter **??**.

2.2.1.3 FACTOR Tri-Sector combustor simulator

The Tri-Sector combustor simulator at the University of Florence (as part of FACTOR) was developed as a full-scale, 3 swirler sector ($\frac{3}{20}$ of the annulus) pilot facility. The pilot facility was in aid of a fully-annular version to be used in the Next Generation Turbine Test Facility (NG-Turb) at the DLR in Göttingen. The pilot study was initiated as a result of uncertainty around the ability of CFD to adequately serve as a predictive design tool for turbulent mixing in swirling flows Koupper et al. (2014).

The FACTOR Tri-Sector rig set out to simulate high inlet swirl ($\pm 40°$ peak) measured half an axial chord length upstream of the vane leading edge. In addition, it set out to simultaneously simulate a highly non-uniform temperature profile at the same location (Koupper et al., 2014). The target temperature profile was comparable to the profile produced by the EOTDF generator of Povey and Qureshi (2008) in terms of both OTDF and RTDF. The work of Koupper et al. (2014) was focused on validating the 'tri-sector' concept, doing so by comparing LES solutions for a

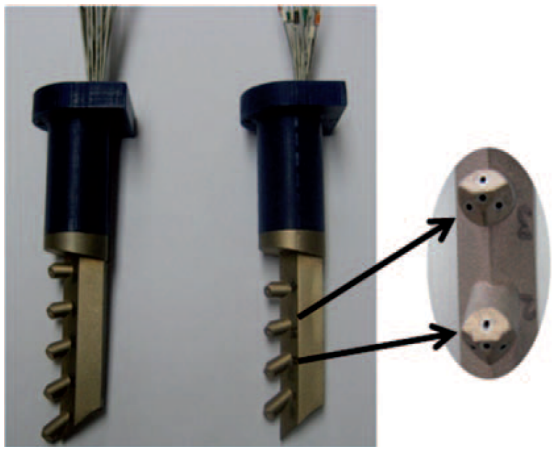


Figure 2.11: Laser-sintered four-hole probe rakes. From Qureshi and Povey (2011).

periodic 'mono-sector' domain against a non-periodic 'tri-sector' domain with walls at the circumferential extents of the domains.

The FACTOR combustor simulator concept is generically illustrated in Figure 2.12. There are a number of notable features of the design. Firstly, it is apparent that the geometry was derived directly from that of an aero LPP combustor (cf. Figure 2.4b), particularly the dump injector arrangement (ignoring the downstream cylindrical duct) and effusion-cooled walls. Maintaining the typical coolant to mainstream mass flow split (two-thirds mainstream), and coolant injected via perforated effusion cooling holes were explicit design specifications (Koupper et al., 2014). The second notable design feature is then one which deviates from a typical LPP combustor - the cylindrical swirler duct. The purpose of this duct was to 'preserve and confine the hot spot' (Koupper et al., 2014).

Bacci et al. (2015a) presented mean flow field measurements from the Tri-Sector rig, using a combination of particle image velocimetry (PIV) and probe (five-hole and thermocouple) traverse measurements. PIV measurements confirmed the ability of the simulator to reproduce key lean-burn combustor features (e.g. a central recirculation zone). A number of configurations with and without the swirler duct

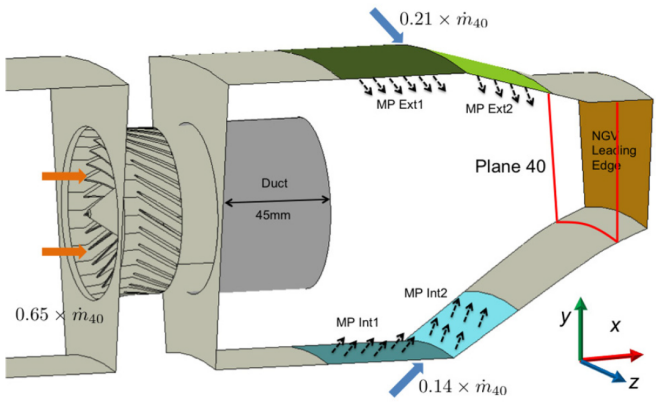


Figure 2.12: Schematic view of the FACTOR combustor simulator. The coloured surfaces indicate the locations of perforated effusion cooling liners. From Koupper et al. (2014).

were investigated. For the combustor-like case without the duct, mixing processes significantly reduced the inlet swirl and produced a vortex that was not well defined. Turbulence measurements using hot-wire anemometry (HWA) (Bacci et al., 2015b) showed circumferentially averaged values of 20% at midspan was typical of the swirling flow field of the simulator. The unsteady measurements were used to identify the presence of a precessing vortex core (PVC) in certain cases.

In parallel, (Andreini et al., 2015) utilised the experimental results of (Bacci et al., 2015a) to carry out a validation study of a hybrid RANS-LES modelling approach (the scale adaptive simulation - SAS). The results demonstrated the strength of this approach in modelling complicated combustor-type flows at a more economical computation cost than LES and DES approaches. This approach should certainly be considered if the work of Chapters 4 and 4.7 is revisited.

2.2.1.4 Large Scale Turbine Rig at Technische Universität Darmstadt

The Large Scale Turbine Rig (LSTR) at Technische Universität Darmstadt is a rotating low speed turbine test facility based around a 3:1 geometric scale, 1.5 stage HP turbine (first stage HP vane (cooled) and rotor, and second stage vane) (Krichbaum et al., 2015). The facility was designed to match engine Reynolds number and included a combustor simulator to produce engine-realistic inlet conditions.

The combustor simulator consisted of an array of primary air swirlers. The swirlers were designed to produce residual swirl at the vane inlet consistent with engine conditions while also producing a realistic central recirculation zone. The facility included vane platform cooling, although no combustor liner cooling. It did not consider non-uniform inlet temperature related to the combustor in the way that the OLCS and the FACTOR combustor simulator did.

2.2.2 Non-uniform inlet conditions and the high pressure turbine

The scaled turbine facilities and combustor simulators discussed above have (or will do so in future) collectively provided great insight in to the effect of non-uniform inlet conditions on aerodynamics and heat transfer in the first HP stage. While this kind of data was not available for presentation in this thesis (due to research programme delays), it is important to understand the significance of the effects and the clear motivation therefore to study them in further detail, particularly for emerging combustor designs.

A range of studies, both numerical and experimental, have been carried out with the aim of improving understanding of the effect of HP turbine inlet non-uniformities on aerodynamic and thermal performance. The earliest work in this area focused on non-uniform inlet temperature in isolation. Povey and Qureshi (2009) provided a comprehensive review of such experimental studies, the most recent of which (i.e. Qureshi et al., 2011b; Barringer et al., 2009b; Mathison et al., 2012) are discussed below. Dorney et al. (1999) provided a review of earlier experimental and numerical work. While this early work was inspired by rich-burn combustors, the focus of recent work has shifted to the effect of inlet swirl—both in isolation and in combination with non-uniform temperature—characteristic of modern lean-burn combustors. Collectively these studies have sought to address the issues of vane and rotor aerodynamic and thermal performance, as well as overall stage efficiency.

The work of Barringer et al. (2009b) on the Turbine Research Facility at the Wright-Patterson Air Force Base considered the combined effects of inlet total temperature and total pressure non-uniformity. The work investigated experimentally the migration of inlet temperature and total pressure non-uniformity through the HP stage using a combustor simulator described by Barringer et al. (2004). It was reported that increased total pressure at the end walls altered stagnation enthalpy

redistribution, increased total pressure loss, and altered vane exit flow angles, effects that require careful consideration when designing vane cooling and rotor blade aerodynamics respectively. It was found that certain total pressure and temperature profiles reduced vane end wall heat transfer by $30 - 40\%$ at the hub and $25 - 35\%$ at the case (Barringer et al., 2009a). Profiles with elevated total pressure at the end walls reduced vane passage secondary flows preventing convection of hot main flow gas to the end walls.

The EOTDF generator of Povey and Qureshi (2008) was able to produce a pronounced radial and circumferential temperature profile clockable with respect to the vane leading edge. This simulator differed from that used by Barringer et al. (2004) and Barringer et al. (2009b) in that the inlet total pressure was intentionally uniform in order to investigate, in isolation, the migration and impact of non-uniform inlet temperature. Qureshi et al. (2011b) utilised this facility and found negligible difference for HP vane aerodynamics for the cases of non-uniform and uniform inlet temperature. The same work reported significant span-wise variation in heat flux arising with non-uniform temperature, due primarily to changes in local driving gas temperature. Similar behaviour was observed for HP rotor heat transfer (Qureshi et al., 2012). In a complimentary study on the same facility, Beard et al. (2011) reported reductions in turbine efficiency of 0.88%, which was attributed off-design relative whirl angle and total pressure at the rotor directly resulting from non-uniform inlet temperature. In the associated numerical study of Simone et al. (2012), significant temperature non-uniformity was shown to persist beyond the first HP stage, suggesting that similar consideration should be given to subsequent stages.

Mathison et al. (2012) presented the design of an inlet temperature profile generator for the shock-tunnel based Turbine Test Facility at the Ohio State University Gas Turbine Laboratory. This short-duration (50 ms run time) facility made use of shockwave compression to heat the flow, while temperature profiles were achieved using a passive heat exchanger upstream of the vane inlet. This facility employed a

cooled HP vane, with investigation of temperature profiles with and without cooling flows presented in (Mathison et al., 2012). Vane cooling flow was found to significantly impact the rotor inlet temperature profile where inlet hot streaks were present, compared to the case with no cooling. Film cooling therefore represents a further consideration necessary to achieve fully integrated design of low-NO_X engines.

Qureshi and Povey (2011) discussed the design of a combustor-representative swirl simulator commissioned on the OTRF. The simulator was capable of producing inlet swirl in the order of ± 50 degrees at the vane inlet. The authors found that inlet swirl of this order resulted in significantly altered vane loading at 10% and 90% span, and significant changes in Nusselt number over the vane surface compared to the case without inlet swirl (uniform inlet conditions). Beard et al. (2013) reported an efficiency penalty of 1.24% (mixed out value), the majority of which was attributed to the resulting off-design vane loading. Schmid et al. (2014) also reported an efficiency drop due to altered vane loading in numerical results, noting a dependence on vortex rotation direction.

While the combined effects of non-uniform inlet temperature and swirl relevant to lean-burn combustors are yet to be reported from rotating experimental facilities (e.g. the forthcoming work in the OTRF and the NG-Turb facilities), a number of numerical studies exist which have offered predictions of their significance when combined. Khanal et al. (2013) highlighted the importance of studies with realistic (i.e. combined) turbine inlet conditions, identifying the non-linearity (invalidity of superposition) of swirl and non-uniform temperature in terms of turbine performance. This study, as well as that of (Rahim and He, 2014), identified vortex direction and vortex-vane clocking as having a marked effect on vane and rotor aerodynamic and thermal loading. Insinna et al. (2014a) additionally looked at the impact on vane cooling, finding that combined hot-streaks and swirl caused span-wise variation in density ratio and blowing ratio linked to the mainstream density and velocity fields.

Griffini et al. (2015) specified that swirl alters the stagnation line on the vane leading edge, altering pressure ratios across the leading edge cooling hole array.

The significance of inlet temperature profiles (with and without total pressure profiles), and inlet swirl profiles on HP stage aerodynamic and thermal performance have—with the exception of some recent numerical investigations—been studied separately. Non-uniform temperature has been shown to influence heat transfer by altering local driving gas temperatures, while total pressure and swirl impact both aerodynamic loading and heat transfer through secondary flow effects. Simulations have predicted combined effects exceeding the sum of the separate effects, placing emphasis on proper understanding. There have to date been no experiments in the open literature which consider combined, engine-realistic inlet temperature, total pressure, swirl, and turbulence profiles in a rotating turbine facility. To improve turbine design for lean-burn combustor inlet conditions, experiments which consider the combined effects of these inlet distortions are vitally important.

2.3 Swirling flows and swirl combustors

With the exception of the swirl simulator of Qureshi and Povey (2011), the Tri-Sector rig of Koupper et al. (2014), and the facility at Darmstadt (Krichbaum et al., 2015), the combustor simulators discussed above are characterised by predominantly axial velocity fields typical of conventional combustors or RQL combustors with low residual swirl. The swirl simulator of Qureshi and Povey (2011) was integral to the only high swirl experiments in a rotating turbine facility to date. In contrast to the majority of existing experimental research, the combustor simulator (OLCS) design discussed herein consists of a flow field dominated by swirling flow. The presence of recirculation in strong swirling flows provides flame stability in a reacting swirl combustor by creating a low velocity region of hot gas. Although it is an accepted feature of such combustors, it must be well understood in order to design a non-reacting combustor simulator.

Swirl strength is typically characterised in terms of the non-dimensional swirl number (S), defined as the ratio of axial flux of the tangential momentum to the axial flux of the axial momentum multiplied by the nozzle radius (R_o) (Chigier and Beer, 1964). In terms of axial (u_z) and tangential (u_θ) velocities this becomes:

$$S = \frac{\int_{R_o}^{R_i} u_z \, u_\theta r^2 \, \mathrm{d}r}{\int_{R_o}^{R_i} u_z^2 \, R_o r \, \mathrm{d}r} \tag{2.1}$$

For flat vane swirlers which are of particular interest to this work due to their simplicity, this can be simplified in terms of outer radius (R_o), hub radius (R_i) and vane angle (ψ) (Lilley, 1977):

$$S = \frac{2}{3}\left(\frac{1-(R_i/R_o)^3}{1-(R_i/R_o)^2}\right)\tan\psi \tag{2.2}$$

It was shown by Harvey (1962) that for flows for which S is above a critical value, vortex breakdown (VB) will occur and a central recirculation zone will form. Strong swirl refers to flow in which a central recirculation zone forms. Huang and Yang (2009) explain VB in terms of the radial equilibrium (Equation 2.3). Radial equilibrium dictates the existence of a radial pressure gradient proportional to the square of tangential velocity. As the tangential velocity decays in the downstream direction (for instance as a result of downstream diffusion or viscous effects at wall boundaries), static pressure is recovered and an adverse pressure gradient forms on the vortex axis, resulting in reversed axial flow (recirculation).

$$\frac{\delta p}{\delta r} \sim \frac{\rho u_\theta^2}{r} \tag{2.3}$$

Faler and Leibovich (1977) identified seven categories of VB, with two forms prevalent in high Reynolds number flows: bubble and spiral breakdown. Generally speaking, however, there are no universal criteria for predicting the onset of type of VB (Kempf et al., 2008). The precessing vortex core (PVC) is a phenomenon which is often discussed in relation to VB. It is an asymmetric, large scale, coherent flow feature,

generally assuming a corkscrew shape. It occurs under certain conditions, generally at high Reynolds and swirl numbers (Wang et al., 2004). Alekseenko et al. (2008) identify PVCs and VB as forms of perturbed elongated vortex filaments, with recirculation a typical feature of both. The occurrence of VB is well understood in terms of onset with respect to S, though the mode is variable and less predictable. The specific conditions which cause the onset of a PVC are also poorly understood. These phenomena have the potential to cause large-scale flow field instability within a swirl combustor simulator, placing emphasis on proper understanding.

The PVC phenomenon has been reported in a number of studies examining gas turbine swirl combustors (Wang et al., 2004; Wang et al., 2007; Roux et al., 2005; Selle et al., 2003; Guo et al., 2001) under reacting flows. Critically, those studies (Roux et al., 2005; Selle et al., 2003) which examined both non-reacting and reacting flows, found the PVC was damped under the latter condition. Roux et al. (2005) investigated non-reacting and reacting flows in a model swirl combustor both experimentally and numerically (using large eddy simulation - LES). A precessing vortex core was present for the non-reacting case but was suppressed in the reacting case. This was also the finding of the LES study of Selle et al. (2003) and the URANS study of Wankhede et al. (2010). Roux et al. (2005) attributed this to dilation due to heat release and the presence of viscous combustion products. O'Connor and Lieuwen (2011) commented on the significance of heat release on flow structure and the resulting lack of analogy between reacting and non-reacting swirl flows.

Only relatively recently has substantial progress been made on describing the parameters affecting PVC excitation and suppression. The effect of combustion—to suppress the PVC—has only relatively recently been understood analytically; Oberleithner et al. (2013) was able to show that the density gradient associated with combustion was responsible for PVC suppression. Terhaar et al. (2015) extended this by identifying the key parameters governing PVC excitation and suppression in

swirling combusting flows, with the steepness of density gradient and intensity of central recirculation being key. Using similar analytical approaches, the same researchers (Terhaar et al., 2013) also described the impact of axial injection on PVC excitation, describing the tendency towards suppression which had been earlier observed anecdotally (both in this work and elsewhere (e.g. Wankhede et al., 2010)).

The sensitivity of swirling flow structure to density gradient represents a clear difficulty for a non-reacting simulator where combustion induced heat release is not present. More generally, Cameron et al. (1989) found that the recirculation zone in the experimental model combustor investigated was smaller in size and weaker in terms of negative axial velocity magnitude in the reacting case than in the non-reacting case. It is also simply the case that in the absence of heat addition and axial acceleration, the relationship between upstream and downstream swirl number cannot be consistent between reacting and non-reacting flows.

2.4 Computational methods for swirling flows

Numerical methods including both unsteady Reynolds-averaged Navier-Stokes and LES have been used in a number of investigations (e.g Wang et al., 2004; Wang et al., 2007; Roux et al., 2005; Selle et al., 2003; Guo et al., 2001; Lu et al., 2005) of turbulent swirling flows directly relevant to swirl combustors. Huang and Yang (2009) provided a comprehensive review of LES studies of gas turbine combustion for 2000-2009. These investigations include simplified (often axisymmetric) domains where swirl was imposed via inlet boundary condition (Wang et al., 2004; Guo et al., 2001; Lu et al., 2005) and more complex domains which included resolved swirler geometry (Wang et al., 2004; Roux et al., 2005; Selle et al., 2003).

The modelling of turbulence is critical to the ability of URANS to accurately predict high Reynolds number flow. Strong streamline curvature and pressure gradients make swirling flows particularly challenging to predict, placing further emphasis

on turbulence modelling. The ability of URANS to predict instability in swirling flows was examined by Wegner et al. (2004). The authors noted the established inadequacy of linear two-equation models for swirling flows and focused on the Reynolds Stress Models (RSM) as the preferred closure method. Grotjans et al. (1998) studied a number of turbulence models, comparing results to laser Doppler anemometry data, finding only the RSM to give accurate prediction of the tangential velocity profile of the hydrocylone test case. The second order closure of the Reynolds Stress tensor in the RSM makes it better suited to the strong streamline curvature and pressure gradients present in swirling flows. The anisotropy of turbulence in swirling flows contradicts the Boussinesq assumption of two-equation models. By comparison of URANS, LES and experimental data, it was concluded (Wegner et al., 2004) that URANS was able to accurately predict the formation of a PVC, the associated precession frequency, mean velocities of the flow and the dimensions of the recirculation region. However, the energy in the unsteady motion was under predicted. Yang et al., 2003 used the Speziale-Sarkar-Gatski RSM and the k-ϵ model to model a lean direct injection combustor under non-reacting conditions. The authors noted the superior performance of the RSM in capturing recirculation regions, producing results that agreed well with experimental data. Turrell et al. (2004) and Schmid et al. (2014) adopted the RSM in their numerical studies of swirling combustor flows. The theoretical advantages of the RSM for engineering flows are often disputed and in some flows simpler two-equation models can outperform it. In the case of swirling flows, the literature generally supports the superiority of the RSM amongst the pure URANS models.

LES represents a more recent development in CFD methods which has shown promising capabilities in predicting swirling flows. Wang et al. (2004) carried out laser Doppler velocimetry (LDV) and LES simulations of a model dump combustor under non-reacting conditions and found that mean and variable velocity, and Reynolds shear stress were accurately predicted, as was the presence of a PVC in one case. Wang

et al. (2007) studied a model turbine swirl injector under non-reacting conditions and also found agreement of mean and variable velocity, turbulence properties and vortex instability between LES and experimental results. Roux et al. (2005) examined a further swirl combustor experimentally (LDV) and with LES under both reacting and non-reacting conditions, reporting that LES was able to predict mean and variable velocity, the presence of a PVC for non-reacting flow, and its suppression for reacting flow. This mirrored the findings of Selle et al. (2003) for different swirl combustor geometry. Roux et al. (2005) noted the necessity of including the swirler geometry in the computational domain where accurate solutions were required. This view was reinforced by the findings of Lu et al. (2005). In this work, deficiencies in LES predictions were attributed to poorly defined upstream boundary conditions, in a domain that did not include the swirler.

The literature supports the conclusion that CFD is capable of accurate predictions of non-reacting, swirling flows as encountered in lean-burn combustor simulators relevant to this research. URANS presents as a capable, relatively low computational cost tool, while the more accurate but more computationally expensive LES approach is able to predict the same flows with greater accuracy.

Since the research presented in this thesis was undertaken, two highly relevant numerical methods studies were published. The recent experimental validation of SAS by Andreini et al. (2015) identified a promising solution for LES-like results at reduced computational cost. This should be considered for future work as a viable alternative to URANS with the RSM. Meanwhile, the work of Insinna et al. (2014b) addressed the incompatible computational requirements of swirling combustor and aerofoil flows, which often means simulations are truncated at this interface or vanes are excluded (e.g. Hall et al., 2014; Koupper et al., 2014). A detailed domain including NGV would naturally be preferred where this kind of solution was readily available.

2.5 Definitions and conventions

A number of definitions and conventions are frequently used within scaled turbine and combustor simulator literature. It is helpful to first understand these before attempting to review the data presented within this thesis. Much of the explanation of fundamental data processing techniques is aggregated within this section, making it a useful reference when interrogating the data presented in subsequent chapters.

2.5.1 Spatial averaging of flow properties

When reducing flow properties sampled over surfaces or planes to a single representative value, it is necessary to carry out weighted averaging. The average is most commonly weighted in one of two ways - mass-weighted or area-weighted. Cumpsty and Horlock (2006) drew attention to the fact that when averaging spatially non-uniform data, some information will be discarded - that is, there does not exist a uniform flow which is equivalent in all quantities to a given non-uniform flow.

In the case of total (stagnation) temperature, Cumpsty and Horlock (2006) demonstrated that the mass-weighted average is appropriate; while temperature is an intensive property, it is linearly related to enthalpy which is extensive. The mass-weighted average of total temperature has been applied unless otherwise stated.

It is commonplace to adopt a mass-weighted average for total (stagnation) pressure. Cumpsty and Horlock (2006) asserted that while this cannot be 'justified rigorously', it converges to more rigorous weightings where the amplitude of the total pressure non-uniformity is small (compared to the absolute pressure). This is the case for total pressure measurements at and near the vane inlet, and so the mass-weighted average has been adopted for total pressure unless otherwise stated. The area-weighted average of static pressure has been used unless otherwise stated.

The final properties which are presented in a reduced format (typically as 1D curves) in this thesis are velocity angles: the swirl angle (β) and pitch angle

(α) (defined below). In this case, area-weighted averages have been employed. It is difficult to argue that flow angles are extensive (and therefore best handled with a mass-weighted average). Additionally, in the case that the local flow angle approaches 90°, assuming finite tangential velocity, by definition the axial velocity approaches zero. In this case the mass-weighting process implies no contribution of this high flow angle region to the overall average, which seems dubious. It can be shown that for low flow angles ($< 45°$), the difference between the mass-weighted and area-weighted average is negligible, but diverges as the flow angles increase.

2.5.2 Temporal averaging of flow parameters

Unsteady CFD simulations have been employed frequently in this work. When presenting results from unsteady simulations it is often necessary to compute the time-average using the solution from many time steps. An argument could be made that (quasi) extensive properties such as total temperature and total pressure should be weighted by mass flow rate when performing temporal averaging as is necessary when computing spatial averages. For the data presented herein, such a weighting has an insignificant effect on the resulting time-averaged data. The arithmetic mean has been used when calculating time averages for all properties. This is the standard approach to processing unsteady statistics in both ANYSY Fluent and CFX.

Time-resolved CFD simulations were run for at least 10 domain flow-through periods and monitored to ensure regular periodic oscillations had developed. This was to ensure unsteady convergence was achieved.

2.5.3 Two-dimensional inlet data

Turbine inlet data are frequently presented as 2D planar surface plots within the annular duct of the turbine - the surface normal is the machine axis (z). Unless otherwise stated, these data are viewed from upstream. The circumferential periodicity of the engine is almost always exploited to reduce instrumentation requirements or

computational demands. Data are typically measured or computed, and presented across a discrete number of vane pitches or swirler pitches. This is illustrated in Figure 2.13, which shows a typical sampling plane located in the vane inlet contraction - the swirler provides an upstream point of reference. Figure 2.13 also shows the swirl (β) and pitch (α) angle convention in the context of the combustor simulator geometry; this convention is discussed in further detail below.

2.5.4 Swirler quantities

Where residual inlet swirl is being considered, data are most often presented in terms of swirl angle (β) plot and a pitch angle (α). β and α are defined in terms of the local velocities u_z, u_r, and u_θ:

$$\alpha = \tan^{-1}\left(\frac{u_r}{u_z}\right) \qquad (2.4) \qquad\qquad \beta = \tan^{-1}\left(\frac{u_\theta}{u_z}\right) \qquad (2.5)$$

Where u is the local velocity and the subscripts z, r, and θ denote the axial, radial and tangential components in polar coordinates about the machine axis respectively. The swirl and pitch angle sign conventions are shown in the context of the vane in

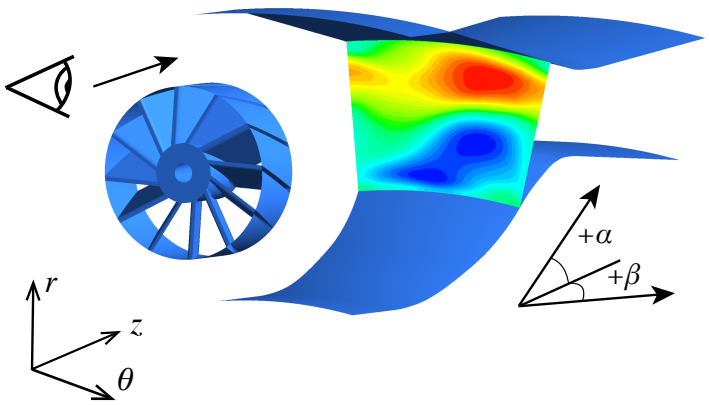


Figure 2.13: Simplified schematic of a combustor and turbine inlet contraction indicating data presentation convention with sample (swirl angle (β)) inlet data and swirl (β) and pitch (α) angle convention. The direction of flow is from left to right.

Figure 2.14 (and in the context of the swirler and turbine inlet contraction - cf. Figure 2.13).

The non-dimensional quantities M_{Sw} and Re_{Sw} required the calculation of a local velocity. This was based on the axial mass flux and the swirler passage area (A_{Sw}) given by:

$$A_{Sw} = \frac{\pi}{4}(D_{Sw,o}^2 - D_{Sw,i}^2) - 0.5 n_{vane} t_{vane}(D_{Sw,o} - D_{Sw,i}) \tag{2.6}$$

Where $D_{Sw,i}$ and $D_{Sw,i}$ are the swirler outer diameter and inner (hub) diameter respectively, and n_{vane} and t_{vane} the swirler vane count and thickness. In the case of Re_{Sw}, the length parameter was taken as OD_{Sw}.

2.5.5 Total temperature data

Temperature data presented in this thesis has been normalised to allow comparison between different facilities and operating conditions. In the case of experiments where stream temperatures were unsteady (and traverse data was not collected simultaneously), it was necessary to present normalised data using the following parameter:

$$T_{0\,eff} = \frac{T_0 - T_{0\,c}}{T_{0\,h} - T_{0\,c}} \tag{2.7}$$

Where T_0 is the local total temperature, $T_{0\,h}$ is the mainstream total temperature, and $T_{0\,c}$ is the coolant total temperature. This parameter has been used extensively as a common base for comparison of temperature profiles.

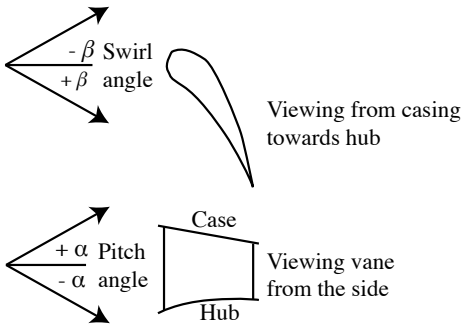


Figure 2.14: Swirl and pitch angle definitions.

When presenting data (particularly previous OTRF data), 1D radial profiles are presented in terms of the Radial Temperature Distortion Factor (RTDF):

$$T_{RTDF} = \frac{T_{0\,\bar{\theta}}}{T_{0\,(mass)}} \tag{2.8}$$

Where $T_{0\,m\bar{\theta}}$ is the mass-weighted average calculated over an annular (circumferential) sub-area, and $T_{0\,(mass)}$ is the mass-weighted average over the entire plane. Experimental results, which were not carried out at matched temperature conditions, are presented in 1D format as the mass-weighted circumferential average of $T_{0\,eff}$, referred to as $T_{0\,eff\,\bar{\theta}}$.

2.5.6 Total pressure data

Total pressure data are presented in terms of one of the following parameters:

$$p_{0\,norm} = \frac{p_0}{p_{0\,(mass)}} \tag{2.9}$$

$$p_{0\,q} = \frac{p_{0\,Sw} - p_0}{q_{Sw}} \tag{2.10}$$

Where p_0 is the local total pressure, $p_{0\,(mass)}$ is the mass-weighted average value on the plane, $p_{0\,sw}$ is the total pressure just upstream of the swirler and q_{sw} is the dynamic pressure through the swirler (based on R_o and u_{axial}).

Circumferentially-averaged profiles of total pressure are also useful for comparing sets of inlet profile data. In the current work, these are calculated with the same mass-weighted approach described above for total temperature. Specifically:

$$p_{0\,rad} = \frac{p_{0\,\bar{\theta}}}{p_{0\,(mass)}} \tag{2.11}$$

Experimental results, which were not carried out at matched temperature conditions, are presented in 1D format as the mass-weighted circumferential average of $p_{0\,q}$, referred to as $p_{0\,q\,\bar{\theta}}$.

2.5.7 Turbine inlet profile definitions

Data from a number of OTRF programmes are presented within this thesis. The plane on which data have been measured to characterise conditions at the inlet to the first HP vane has not remained constant, typically due to physical constraints in installing instrumentation.

'Inlet plane' refers to a plane with surface normal parallel to the machine axis (z) and located at or upstream of the vane leading edge. The location of the inlet plane with respect to the vane leading edge is summarised for the relevant OTRF programmes in Table 2.1.

Table 2.1: The axial location of experimental measurements relative to the first HP vane leading edge. The positive axial direction is downstream.

Combustor simulator	**Relative axial location**	
	T_0, p_0	α, β
EOTDF Simulator (OTRF)	-21.0	None
Swirl Simulator (OTRF)		-29.5
Swirl Simulator (pilot)	None	0
OLCS (OTRF)	-29.5	-29.5
OLCS (Atm test)	-12.5	-12.5

2.6 Summary of literature

Increasingly stringent emissions regulations are placing emphasis on improved turbine efficiency and combustor design. There exists a need to understand the effects of lean-burn combustor designs on high pressure turbine performance if optimal efficiency is to be realised alongside the emissions reductions these combustors promise. Growing interest exists in the literature around this problem; an initial experimental study and a number of numerical studies have predicted significant implications for turbine performance under lean-burn conditions - generally efficiency penalties and off-design thermal performance. The body of experimental work is set to increase rapidly in the coming years.

The development of non-reacting lean-burn combustor simulators is now an area of interest for a number of research groups. Similar challenges relating to replicating swirling flow structures—or simply understanding what they should be—under non-reacting conditions have emerged in a multiple studies. The design of such systems using numerical methods also represents a challenge. Careful use of URANS modelling appears to be a viable way forward, while scale resolving methods represent the best practice where resources allow.

Chapter 3

Past OTRF combustor simulators - CFD study

The OTRF (described below) has undergone continuous development from its conception as a facility designed to match 1D scaled engine conditions (Hilditch et al., 1994) with spatially uniform HP turbine inlet conditions. The first OTRF studies of non-uniform inlet conditions looked at non-uniform temperature only (e.g. Hurrion, 2002; Povey et al., 2003) and subsequently the effect of residual inlet swirl (non-uniform velocity and total pressure) (Qureshi et al., 2011a). These studies reflect the transition of combustor design from rich-burn to swirl-stabilised lean-burn combustors. The Qureshi et al. (2011a) investigation of inlet swirl was the first experimental investigation of the impact of swirl in a rotating turbine facility. The experimental investigations of separate inlet temperature distortion and swirl laid the foundation for OTRF experiments examining the impact of swirl-stabilised lean-burn combustor profiles. Swirl-stabilised combustors are typically characterised by concurrent non-uniform total temperature and total pressure, discrete vortices resulting from high mass flux primary air swirlers, and high turbulence.

The combustor simulator systems used in the previous OTRF studies were developed primarily using a combination of analytical analysis as well as experimental testing (Hurrion, 2002; Povey and Qureshi, 2008), with some limited predictive CFD in the case of the swirl simulator of Qureshi and Povey, 2011. While not providing

an established CFD methodology for the design of such systems, the experimental results of these studies were useful as validation data. This chapter provides an overview of the previous OTRF combustor simulator systems and discusses their use in establishing the CFD methodology used as a predictive design tool for the development of the OLCS (see Chapter 4). A review of combustor simulators in the literature is provided in Chapter 2.

3.1 Oxford Turbine Research Facility

The focus of the research presented herein was the development of a combustor simulator—referred to as the Oxford Lean burn Combustor Simulator (OLCS)—for the Oxford Turbine Research Facility (OTRF). At the outset, the intention was to develop, commission, and operate the OLCS as part of the SILOET turbine programme scheduled originally for 2013-2014 (Chana et al., 2013); detailed discussion of the OLCS performance at engine-matched conditions, and in particular the impact of the simulated combustor non-uniformities on turbine aerodynamic and thermal performance were to be a significant component of the final work. This chapter has been included to provide context for the development of the OLCS, which forms a large part of this thesis, and to outline the future research which it will be utilised in.

3.1.1 Turbine test facilities

Turbine test facilities address the need to gather experimental data to improve the understanding of turbine flows. They achieve this through direct observation and also indirectly by providing validation of numerical studies. This need arises as a result of the extreme conditions encountered in much of the turbine, particularly the first HP stage where gas temperatures exceed the melting point of the advanced metal components. It is the high temperatures that make extensive instrumentation impossible and indeed, any kind of instrumentation extremely challenging. The development of

high temperature sensors remains a very active area of research (e.g. Massini et al., 2011; Hunter et al., 2003).

Turbine test facilities circumvent the issue of inhospitable operating conditions by exploiting fluid and heat transfer similarity which is achieved by matching certain non-dimensional properties (rather than absolute dimensional properties). By operating at so-called 'scaled conditions', turbine test facilities are able to produce meaningful experimental data at conditions which allow extensive instrumentation with conventional sensor technology (e.g. unshielded thermocouples and silicon-based pressure sensors).

The non-dimensional properties which should be matched depend on the measurements of interest. Mach number (the ratio of velocity and the local speed of sound), Reynolds number (which quantifies the relative importance of viscous and inertial forces) and specific speed (for rotating facilities) are critical for the investigation of external aerodynamics of turbine aerofoils. Heat transfer experiments additionally rely on the ratio of free stream gas temperature and component (wall) temperature, as well as turbulence intensity and length scale.

Test facilities for turbine experiments may take a number of different forms—Qureshi (2010) covered them in some detail, citing the comprehensive work of Hirsch (1993)—including stationary linearised aerofoil cascades, partial and completely annular cascades, and annular rotating facilities with at least one vane-rotor stage. Annular rotating facilities have the advantage of being geometrically and functionally most similar to an engine, while partial cascades (whether linear or annular) typically suffer from issues relating to periodicity. Operation of such a facility may be continuous (steady) or short-duration (transient).

In the case of engine-scale rotating facilities—the focus of the current work—transient operation is advantageous in terms of running costs, and also allows meaningful heat transfer measurements of uncooled components (where the system temperatures would otherwise equilibrate in a continuous facility). Continuous facilities, while expensive to operate, hold advantages in terms of gathering high resolution data using laser diagnostic methods such as particle image velocimetry (Qureshi, 2010).

3.1.2 Description of the OTRF

The OTRF is a rotating transient wind tunnel facility used to investigate the aerodynamic and thermal performance of approximately engine-scale high-pressure gas turbine hardware. The facility is capable of operating at engine-matched non-dimensional parameters (Chana et al., 2003), specifically Mach number, Reynolds number, gas-to-wall temperature ratio, turbulence and non-dimensional rotor speed. Early studies (e.g. Hilditch et al., 1994) investigated a single HP turbine stage while the facility was extended later to include an intermediate pressure (IP) vane (Chana et al., 2003). Chana et al. (2013) provided a comprehensive review of the history and development of the OTRF over several decades up to 2013. The most recent turbine programme (see Johansson et al., 2014), employed a 1.5 stage turbine, focusing on performance of the IP vane.

The OTRF is illustrated schematically in Figure 3.1. The operating principle is based around an isentropic light piston tube; high pressure air is introduced behind the piston, driving it down the tube, compressing and heating the gas ahead of it approximately isentropically. The hot, compressed gas is released in to the evacuated working section by the fast-acting plug valve and provides a steady state run time of approximately 500 ms. In advance of firing the piston tube and introducing the working fluid, spin-up (to operating speed) of the HP rotor is achieved using an air motor. During the steady test window, an axial turbobrake (described by Goodisman et al., 1992) matches the power production of the rotor, maintaining constant rotational speed. The OTRF is shown photographically in Figure 3.2

3.1.3 Context of the current work

The OTRF has now provided a significant contribution to the understanding of turbine flows and to the improvement of design methods over 4 decades (Chana et al., 2013). An important aspect of its contribution to understanding has been its use as a test bed for cutting edge and emerging engine technologies. For instance, shroudless

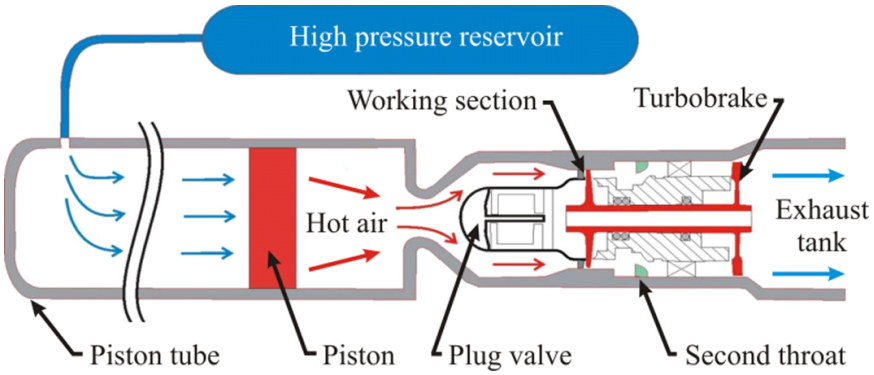


Figure 3.1: Schematic illustration of the OTRF.

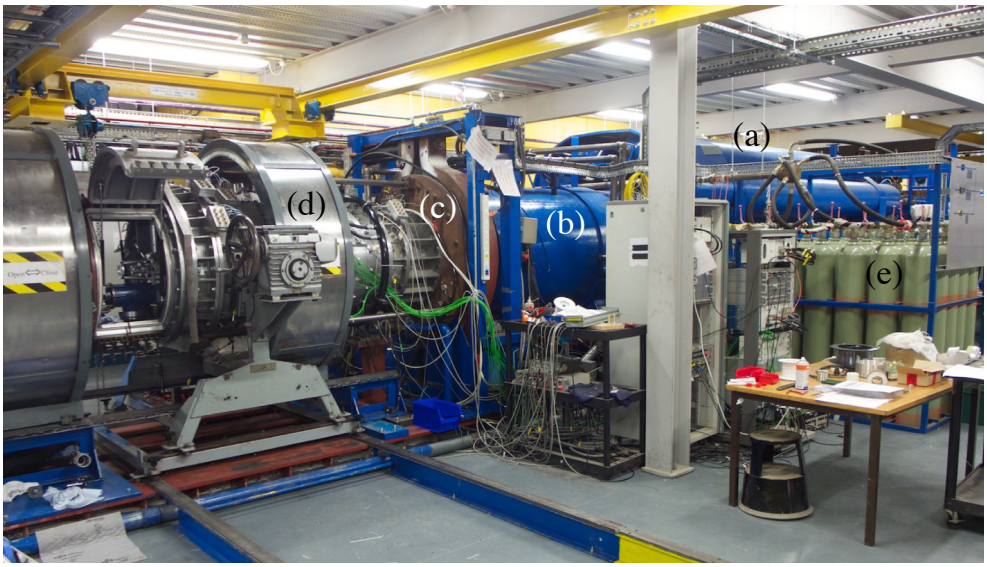


Figure 3.2: Photograph of the OTRF showing: (a) The high pressure reservoir bottles; (b) the piston tube; (c) the plug valve assembly; (d) the working section (and containment ring); and (e) coolant reservoir.

HP turbines, which are now seeing implementation in commercial engines (e.g Rolls Royce XWB-97 (Norris, 2013)), have been employed since the MT1 was installed in 1992 (Hilditch et al., 1994). In a similar vein, the development of the OLCS is intended to promote understanding of turbine performance under conditions representative of those generated by next generation lean premixed prevaporised (LPP) low emissions combustors. The OLCS and the associated turbine programmes represent the progression from the first lean-burn-focused study in the OTRF, which used the swirl simulator of Qureshi and Povey (2011) to investigate the effects of residual inlet swirl—an important feature of lean-burn combustors—on HP stage performance.

The OLCS was designed specifically for the OTRF, in terms of engine design considerations (e.g. swirler to vane count ratio), aerodynamic and thermal specifications (coolant and mainstream states and mass flow rates), and mechanical interfaces. The OLCS is shown installed in the OTRF in Figure 3.3. It remains the case that the OLCS will be used in at least two turbine programmes planned for the OTRF, the first of which (LEMCOTEC) is currently undergoing commissioning (Dec 2015) - the OLCS is shown installed in the OTRF in Figure 3.3. As noted above, the SILOET programme was originally scheduled to precede the LEMCOTEC programme, and was the prime motivation for the development of the OLCS. As a result the development of the OLCS—and indeed the work presented in this thesis—focused on the SILOET programme.

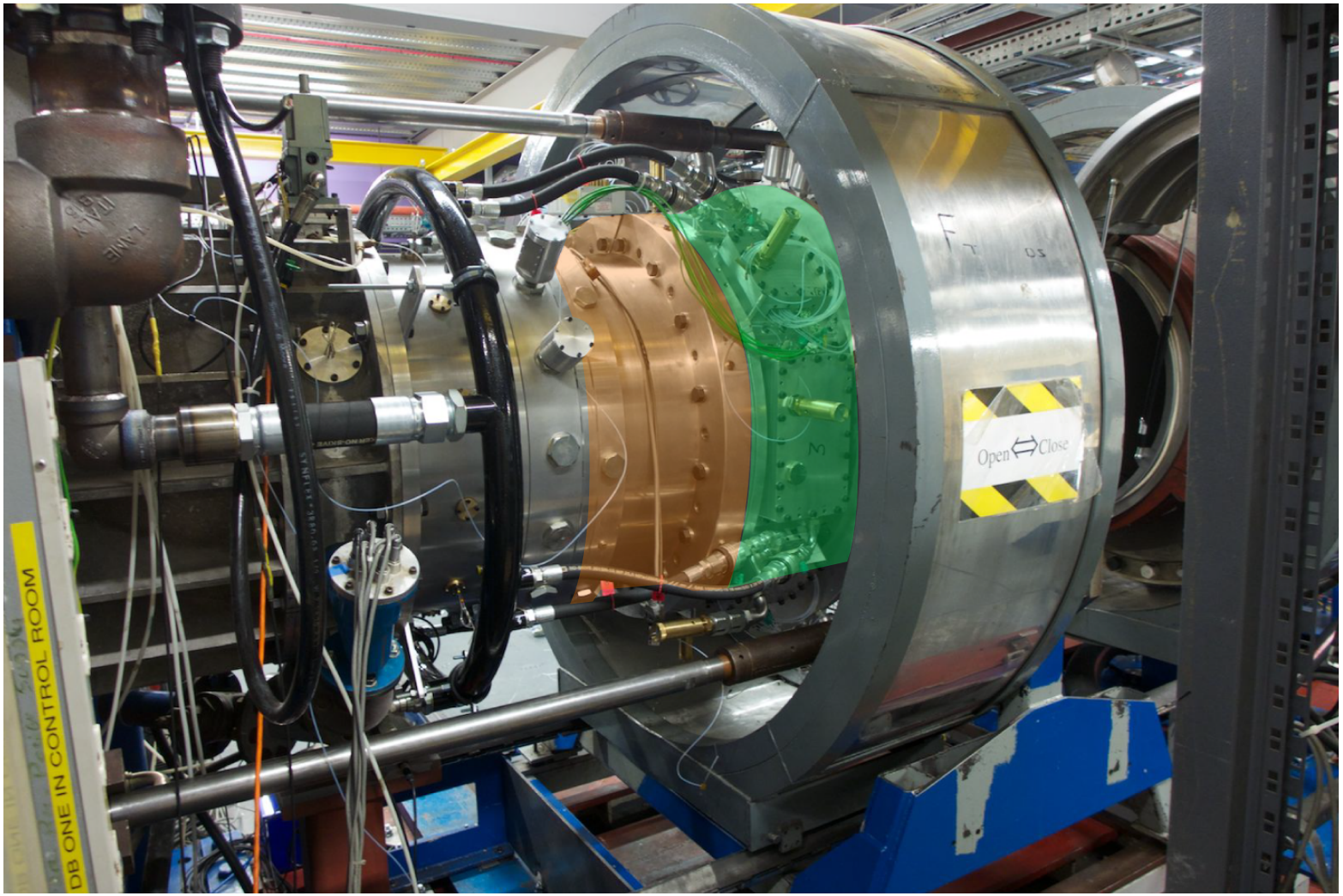


Figure 3.3: Photograph of the OLCS (highlighted orange) installed in the OTRF upstream of the turbine stage assembly (highlighted green) during LEMCOTEC commissioning, December 2015.

The following sections discuss the simulation of previous OTRF combustor simulators. The simulation cases are summarised in Table 3.1.

Table 3.1: Summary of past combustor simulator cases.

Combustor Simulator	**Mesh type**	**Turbulence model**
EOTDF	Hexa	Realisable k-ϵ
EOTDF	Hexa	RSM
EOTDF	Hexa	k-ω SST
Swirl	Hexa-core	RSM

3.2 EOTDF simulator

The EOTDF simulator of Povey and Qureshi (2008) was used to investigate the migration of non-uniform total temperature profiles through the HP stage of a modern turbine (MT1) (see Qureshi et al., 2011b; Qureshi and Povey, 2011). The EOTDF simulator produced well-defined hot-streaks which were measured in high spatial resolution upstream of the vane leading edge.

The central success of the EOTDF generator of Povey and Qureshi (2008) was the generation of a well-defined temperature profile which closely matched the design target. This was also an important aspect of the design of the OLCS. In the case of the EOTDF system, the temperature profile was carefully designed using an analytical approach which considered the turbulent mixing length of two adjacent streams (Povey and Qureshi, 2008). The effectiveness ($T_{0\,eff}$) profile produced by the EOTDF generator is shown in Figure 3.4. The system is discussed in further detail in Chapter 2.

That the OLCS would be characterised (see OLCS target profiles in Chapter 4) by a swirling mainstream flow field meant that 3D CFD was adopted early in the design process, rather than similar analytical methods to those of Povey and Qureshi (2008). The experience, and in particular the experimental data from the EOTDF simulator, provided a useful tool in the development of the OLCS. By simulating

the EOTDF system using CFD and comparing against experimental measurements, it was possible to gain an understanding of the ability of such tools to accurately predict high Reynolds number turbulent mixing processes.

The impact of turbulence modelling was of particular interest; the mixing of the coolant streams with the hot main stream would be driven predominantly by turbulent mixing in the free shear layer at the stream interfaces.

By simulating the EOTDF generator using CFD, it was possible to gain an understanding of the ability of a commercial CFD code (in this case ANSYS Fluent) to accurately capture the mixing of streams of different temperature in an engine-scale, 3D annular geometry at scaled engine (OTRF) conditions. The study examined the ability of various turbulence models to predict shear layer mixing between the coolant and main streams. Numerical setup was also considered with particular interest given to the meshing approach required for accurate predictions as well as the most appropriate discretisation scheme.

3.2.1 Numerical setup and modelling

The geometry of the EOTDF simulator was reproduced to a high level of detail as a CAD model (see Figure 3.5a) using a combination of drawings and direct measurements of the manufactured hardware. The hub coolant baffle was cut back by 4 mm

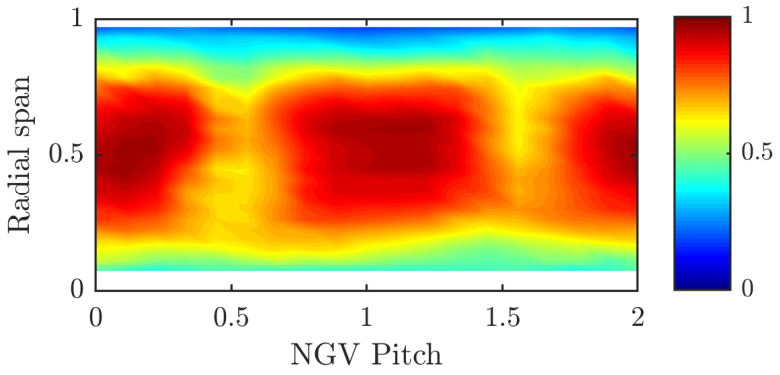
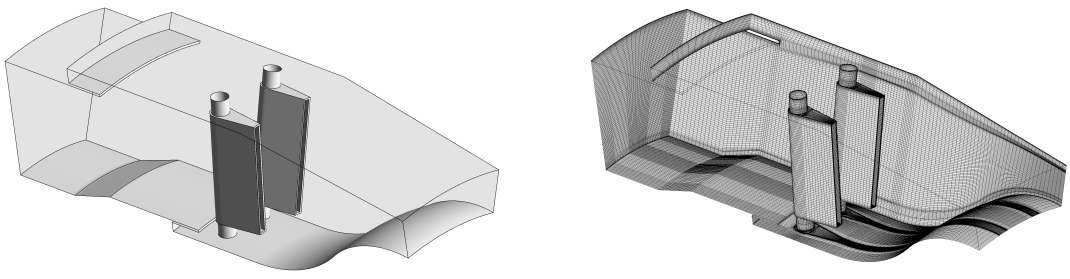


Figure 3.4: EOTDF generator temperature effectiveness (T_{0eff}) distribution.

in the model to avoid geometry which was difficult to mesh (at the radial rods). This small change was not expected to impact the results significantly. Notably, the HP vane geometry was excluded from the domain for simplicity and also to assess (with respect to experimental results taken in the presence of vanes) the impact of their exclusion. This CAD model was used to generate an unstructured hexahedral mesh which could be solved in Fluent.

Two different meshes were used, the first for use with k-ϵ turbulence models did not include fine resolution in the near-wall regions. The second mesh (Figure 3.5b) for use with k-ω turbulence models resolved the near wall region to achieve a y^+ value at wall boundaries of less than 1. The mesh resolution in the free stream (in terms of global maximum cell size) was held constant to the greatest extent possible between the two meshes. In all cases, second order spatial discretisation was utilised for all equations.

The domain was set up with mass flow inlet boundary conditions for the main stream and coolant streams. While this was not strictly representative of OTRF operation in which the main stream was effectively a variable total pressure inlet, it allowed the mass flow rate splits to be precisely and more easily controlled. Since the simulation was intended to reproduce the steady part of the OTRF test (rather than to capture the characteristics of the run startup and shutdown transients) this assumption was acceptable. An average static pressure outlet condition was used.



(a) (b)

Figure 3.5: (a) EOTDF system CAD geometry and (b) hexahedral computational mesh.

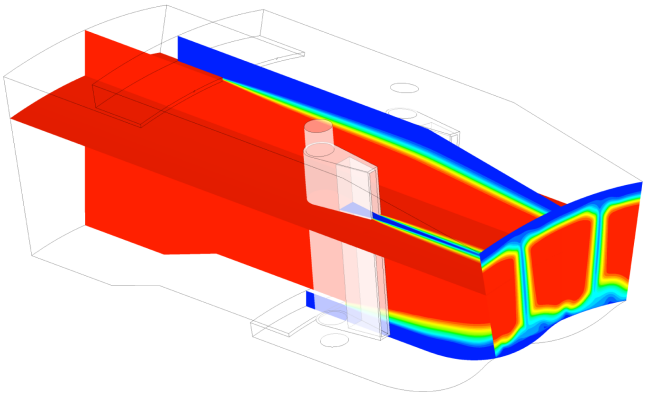
A number of turbulence models were examined and are discussed separately below with respect to results. The turbulence models examined were the Realisable k-ϵ model, the ϵ-based Reynolds Stress Model (RSM) and the k-ω SST model.

The domain was solved using an implicit (iterative) unsteady compressible pressure-based Reynolds-Averaged Navier-Stokes (RANS) solver with SIMPLE pressure-velocity coupling. A compressible ideal gas model of air was used. The time step was set at 10^{-5} s across all cases, which resulted in convergence of each time step in 20-30 iterations. The simulations were run for several through-flow periods until repeating periodic behaviour was observed in the unsteady parts of the solution.

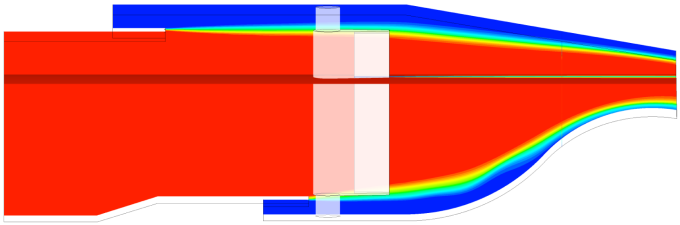
3.2.2 Results - Realizable k-ϵ model

The realizable k-ϵ model is the most recent of the k-ϵ turbulence models. It is regarded as superior to the standard k-ϵ model and has been shown to be superior to the RNG variant for a range of standard validation problems (ANSYS, 2013). The model was developed to overcome the non-physical results produced by the standard and RNG k-ϵ models under conditions of high strain rate (ANSYS, 2013). The realisable k-ϵ model with enhanced wall functions was used to simulate the EOTDF system.

Figure 3.6 shows time-resolved results of the simulation of the EOTDF generator using the realisable k-ϵ model. The figure illustrates the total temperature ($T_{0\,eff}$) over a meridional plane in the centre of the domain and at the inlet plane for a single time step. For the EOTDF system and MT1 turbine, the inlet plane was located 21.0 mm upstream of the vane leading edge. In this time-resolved figure, it is clear that the hot streak is characterised by a relatively large region of uniform temperature. The mixing of the main (hot) and coolant streams appears to be confined to a relatively small region. Some evidence of unsteadiness in the form of the asymmetric, 'wobbly' shape of the hot streak is seen in Figure 3.6a at the inlet plane, and Figure 3.6b on the meridional plane at the hub mixing layer.



(a) Inlet plane, meridional plane, and plane of constant radius.



(b) Meridional plane.

Figure 3.6: Time-resolved total temperature effectiveness ($T_{0\,eff}$) from URANS solution - Realisable k-ϵ.

It was necessary to average a series of URANS simulation time steps in order to make a comparison to the experimental data. This was done by sampling every fifth time step (giving a sample rate of 20 kHz) over a period of 10 ms which captured several periods of oscillatory motion in the flow. The time-averaged URANS results are shown in Figure 3.7. It is clear that the simulation does not predict the same level of mixing between the main and coolant stream as indicated by the experimental data (cf. Figure 3.4). In Figure 3.6 (a-b) a fairly narrow mixing layer is seen in all locations, with no vortical shedding. It is possible that the failure of the realizable k-ϵ model to predict vortical shedding—which would enhance the mixing between streams—is responsible for the poor agreement.

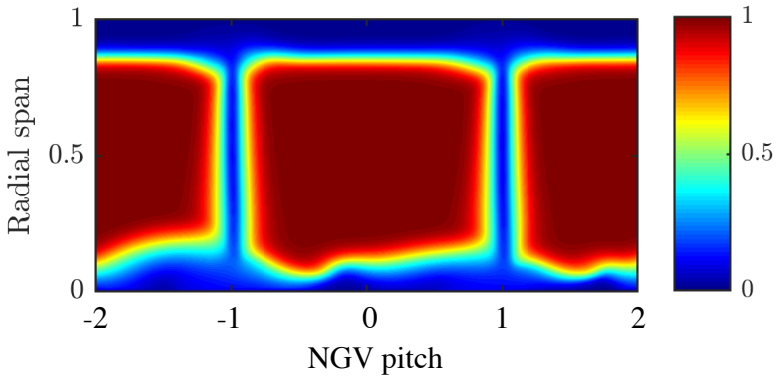


Figure 3.7: Time-averaged total temperature effectiveness ($T_{0\,eff}$) derived from URANS simulation - Realisable k-ϵ.

3.2.3 Results - Reynolds Stress Model

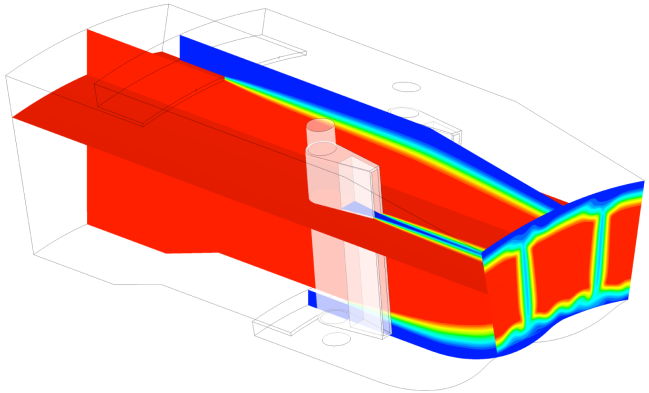
The Reynolds Stress model (RSM) differs from the two-equation eddy viscosity models (e.g. the Realisable k-ϵ and k-ω SST models) in that it solves equations for the six Reynolds Stress terms. The RSM therefore does not assume isotropic diffusion of eddy viscosity, as is the case of two-equation models. By avoiding this assumption, it is more capable in predicting highly 3D flows, particularly swirling flows. The ANSYS FLUENT Theory Guide (ANSYS, 2013) states that while the model may not always be superior to simpler two-equation models, it is the preferred choice (amongst RANS models) for swirling flows in combustors.

The EOTDF case is not dominated by swirling flow, and in fact, the Reynolds Stress Model was not necessarily anticipated to be superior to the realizable k-ϵ model or k-ω SST model. Since it was the preferred choice for swirling flows—which would be the dominant flow feature in the swirl stabilised combustor simulator to be designed subsequently—it was of interest to investigate the capability of the model in predicting the mixing of the main and coolant streams which would also be important in the latter case. The ϵ-based Reynolds Stress model with linear pressure-strain relationship and enhanced wall functions was used.

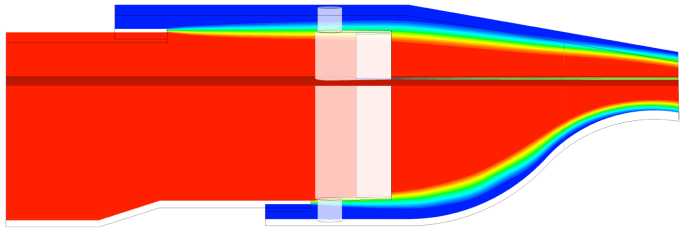
Figures 3.8 shows the results of the simulation of the EOTDF generator using the Reynolds stress model. The figure illustrates the total temperature ($T_{0\,eff}$) over

a meridional plane in the centre of the domain and at the inlet plane for a single time step. In this figure the results are superficially similar to those of the realizable k-ϵ model of the previous section. The shear layer on the meridional plane is typical of a RANS solution and no shedding features are visible. Increased mixing is apparent at the inlet plane (greater extent of green).

As in the previous section, URANS simulation data at the inlet plane was time averaged to aid comparison with the experimental data (Figure 3.4). While the shape of the hot-streak differs to that predicted by the k-ϵ, the extent of mixing is similarly under-predicted.



(a) Inlet plane, meridional plane, and plane of constant radius.



(b) Meridional plane.

Figure 3.8: Time-resolved total temperature effectiveness ($T_{0\,eff}$) from URANS solution - RSM.

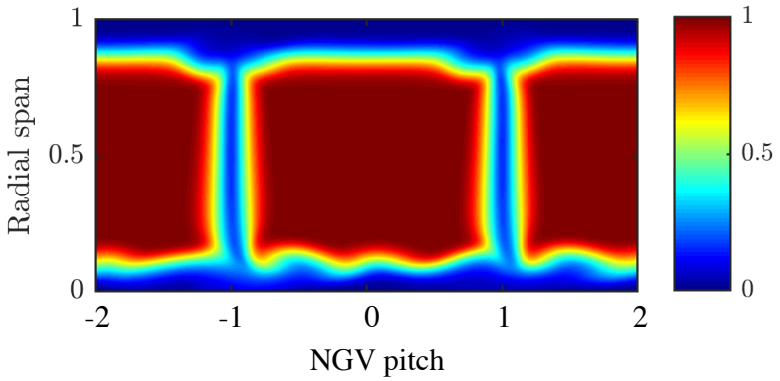


Figure 3.9: Time-averaged total temperature effectiveness ($T_{0\,eff}$) derived from URANS simulation - RSM.

3.2.4 Results - k-ω SST model

The k-ω SST model is widely considered to be the most versatile turbulence model. It combines the standard k-ω in the near-wall region with the k-ϵ model in the free stream. Since the k-ω SST model should provide superior modelling at the near wall regions prior to the mixing of the main and coolant streams, it was of interest to investigate whether the results were appreciably improved, particularly over the ϵ-based Reynolds Stress model which was the preferred option for swirling flows.

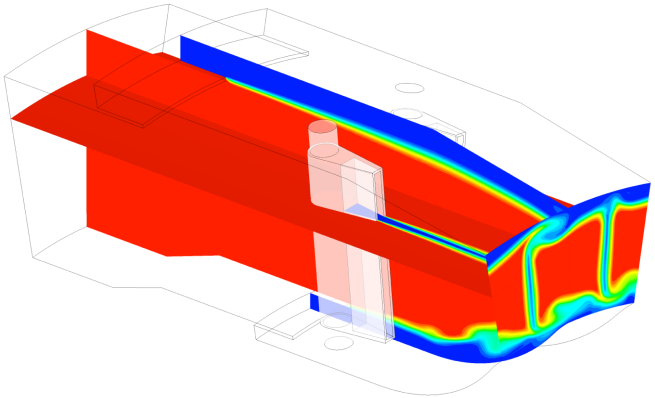
Figure 3.10 shows time-resolved results of the simulation of the EOTDF generator using the k-ω SST turbulence model. The figured illustrates the total temperature ($T_{0\,eff}$) over a meridional plane, a surface of constant radius and the inlet plane. As was the case for the two k-ϵ models, the time-resolved hot-streak is characterised by a region of constant temperature. The results show significantly greater unsteadiness in terms of vortical structures visible in the hub and case shear layers - Figure 3.6b. Contrary to this increased unsteadiness near the hub and case, the shear layers associated with the radial coolant injection did not display any unsteadiness near the mid span - Figure 3.10a.

The (2D) time-averaged inlet total temperature profile was calculated and is presented in Figure 3.11. In the time-averaged sense, significantly greater mixing was

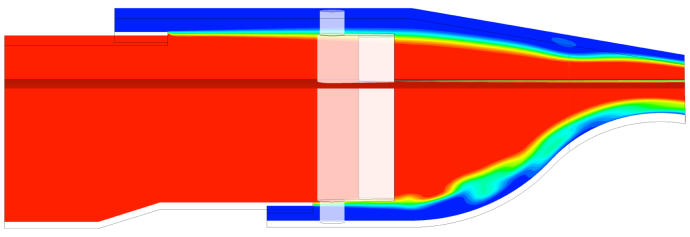
observed for this simulation, particularly in the span-wise direction. It is still the case that the mixing was under-predicted in comparison to the experimental data (cf. Figure 3.4).

3.2.5 EOTDF study summary

The URANS simulations of the EOTDF generator provided results of appreciable variability in terms of the key mechanism of interest, the mixing of the hot mainstream with the injected coolant flows. A direct comparison is provided in Figure 3.12 in terms of RTDF profiles based on time-averaged data for each simulation. This clarifies once again that the Realisable k-ϵ model performed most poorly in predicting mixing,



(a) Inlet plane, meridional plane, and plane of constant radius.



(b) Meridional plane.

Figure 3.10: Time-resolved total temperature effectiveness ($T_{0_{eff}}$) from URANS solution - k-ω SST.

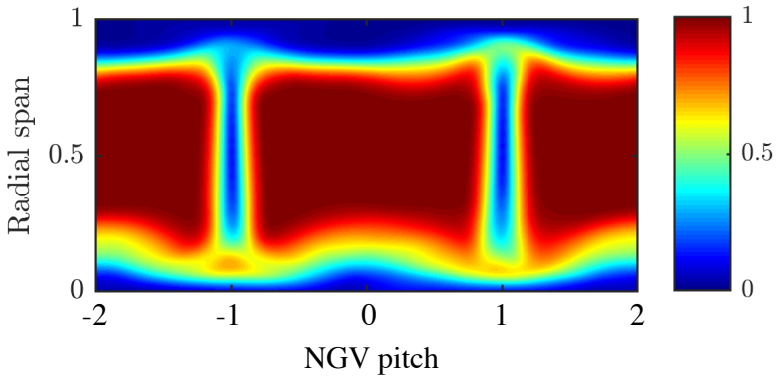


Figure 3.11: Time-averaged total temperature effectiveness ($T_{0\,eff}$) derived from URANS simulation - k-ω SST.

with some improvement gained by implementing the Reynolds Stress Model, and finally the k-ω SST providing the best prediction of mixing.

In assessing the possible causes for the relative performance of each of the applied models, it is helpful to first understand the nature of the problem. In the locally unstable case of mixing in a free shear layer downstream of a separating plate for two streams of unequal velocity (as described by Menter (2012)), the turbulent energy generated in the upstream boundary layer is quickly dwarfed by that generated in the free shear layer. Menter (2012) explains that this makes such a problem insensitive to boundary layer treatment. By contrast, in the case at hand, whereby the streams

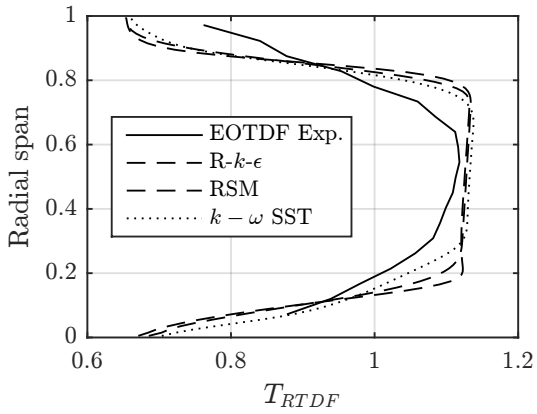


Figure 3.12: Circumferentially-averaged temperature (T_{RTDF}) plots for the URANS simulations (time-averaged) and experimental data.

of the EOTDF system were carefully designed to be of matched velocities, turbulence generation in the shear layer will be low and that generated in the upstream boundary layer will significantly affect the mixing process. This is likely to account for the difference between the wall-resolved k-ω SST case and the wall-modelled Realisable k-ϵ and RSM cases. In the k-ω SST simulation, significantly greater shear layer unsteadiness was observed. The difference between the Realisable k-ϵ and RSM simulations was likely due to the fact that the RSM (due to its higher order of turbulence closure) tends to be less diffusive and therefore the turbulence generated in the (modelled) upstream boundary layers was more accurately transported to the free shear layer.

It is possible that unsteady phenomena were temporally filtered as a result of the chosen time step. The time step of 10^{-5} s could only resolve unsteady features with a frequency of less than 50 kHz, meaning higher frequency features would not be resolved. This may have contributed to the absence of widespread shear layer unsteadiness in the solutions and the under-prediction of mixing.

The aim of the EOTDF CFD study was not to adjust the simulation set up until an exact agreement was reached with experimental results, although agreeable results were naturally preferred. The aim was to establish the basic numerical set up requirements for a flow of this kind, and to understand the relative strengths and weaknesses of various commonly used turbulence models. It is clear from the results presented above that the particular case on free shear layer mixing with near-zero velocity differential is a particularly difficult case for URANS to predict and relies heavily on boundary layer treatment and turbulence modelling. Generally speaking, it appears that the reliance of URANS simulations on modelled turbulence means a tendency to under-predict the kind of mixing of interest in the EOTDF generator. It is likely that a case where the stream velocity differential is greater would be better handled.

A number of possible approaches would be available in the case that improved simulations for the EOTDF generator (or cases with similar flow mechanisms). These

approaches would employ some form of scale resolving simulation, rather than the conventional Reynolds-averaged, turbulence modelling approach. The simplest such approach would be to employ a Scale-Adaptive Simulation. This would produce equivalent turbulence generation in the near wall region to the k-ω SST model, however a more rigorous treatment of turbulence in the shear layer, as in the case described by Menter (2012).

3.3 OTRF swirl simulator

The swirl simulator of Qureshi and Povey, 2011 was used in the first experimental investigation of the effects of residual combustor swirl on the HP stage in an engine-scale rotating facility (the OTRF). The system produced high swirl at the inlet to the vane which allowed the effect of this kind of combustor non-uniformity to be investigated in the MT1 turbine.

The swirl simulator was the first step towards simulating lean-burn combustor conditions in the OTRF. As the first combustor simulator in the OTRF with simulated inlet swirl, the results were obviously of particular interest when developing the OLCS, which would also be characterised by strongly swirling mainstream flow. Prior to the design of the current combustor simulator, CFD simulations of the swirl simulator were carried out. The purpose of this was to establish a validated CFD methodology that was suitable for strong swirling flows in relatively complex 3D geometry, or at least learn of any limitations which should be considered.

Experimental data taken within the OTRF and a low-speed, atmospheric pilot rig were available for comparison with CFD results (see Qureshi and Povey (2011)). Sparse data collection within the OTRF meant the most useful of these data were swirl and pitch angle profiles derived from four-hole pressure probe measurements in the pilot study. These were taken on a plane located at the theoretical vane leading edge. The swirl angle and pitch angle are defined in Figure 2.14. The pilot study swirl

profile of Qureshi and Povey (2011) is shown in Figure 3.13. The probe calibration was limited to a range of $\pm 50\,^{\circ}$, which accounts for missing data as well as the clipping of data to this range. Clipping is clearly visible in Figure 3.13 where a region of constant swirl angle is visible from approximately 0.6 to 0.9 radial span for swirler pitch equal to zero, while missing (likely out of range) data ranges are clearly visible below this.

3.3.1 Numerical setup and modelling

As with the EOTDF system, the swirl simulator geometry was captured in detail as a 3D CAD model (Figure 3.14a), including swirler geometry and turbine inlet contraction. The HP vane geometry was excluded as in the EOTDF case. The exact geometry at the intersection of the flat swirler vanes and swirler hub was difficult to replicate in CAD, since the physical swirlers had fillet welds at the root and tip of the vanes. The swirler vane hub and root intersections were also problematic in terms of mesh generation. It was necessary to apply fillets at the root and leave sharp intersections at the tip to maintain mesh quality. This compromise was not likely to affect the results significantly.

The domain was discretised using a hybrid hexahedral-tetrahedral mesh (3.14b) to achieve a high quality orthogonal mesh in the free stream region. Since the flow field would be expected to be dominated by features in the free stream downstream

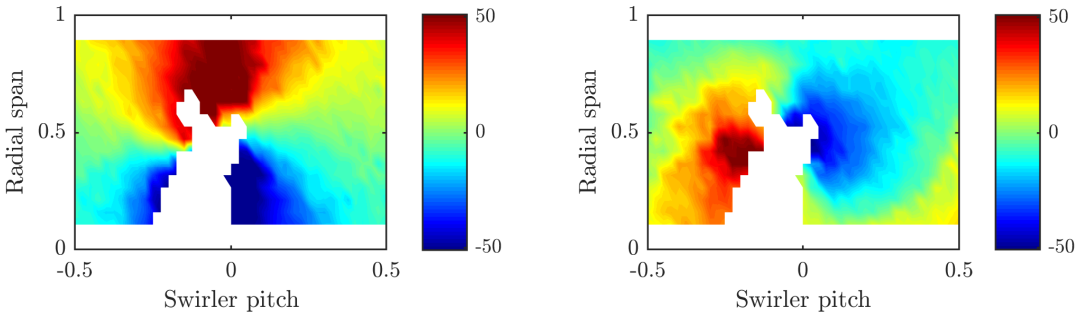
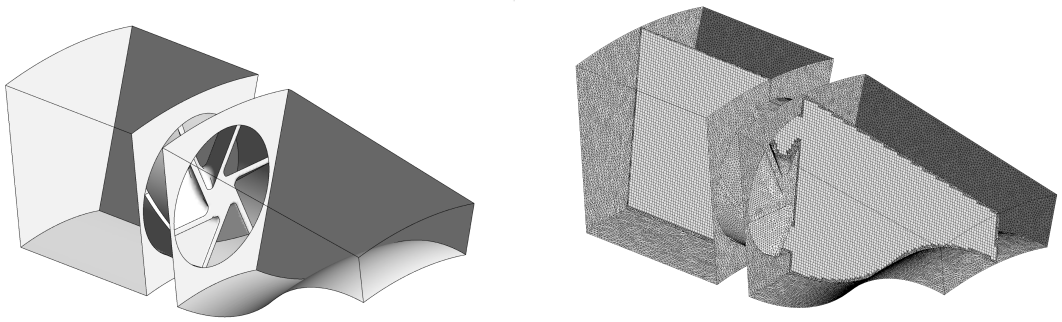


Figure 3.13: OTRF swirl simulator (L-R) swirl (β) and pitch (α) angle plots. Adapted from Figure 10 of Qureshi and Povey, 2011.



(a) (b)

Figure 3.14: (a) Swirl simulator CAD geometry and (b) hybrid computational mesh.

of the swirlers, near wall treatment was less of a priority. A hexahedral-only mesh was made impossible by the given swirler geometry.

Only the ϵ-based Reynolds Stress Model was examined for the Swirl Simulator. The primary reason for this was that the literature (see Chapter 2) indicated strongly that the Reynolds Stress Models—of which there are a number of variants—were the only URANS turbulence models suitable for simulations with swirling flows (characterised by strong streamline curvature and large pressure gradients). Additionally, the swirler geometry—which was predefined in the context of this study—was not conducive to a good (or even fair) quality wall-resolved mesh, meaning that the k-ω SST model would perform poorly or in the best case (using enhanced wall functions) identically to the standard (two-equation) k-ϵ model, which would be expected to perform poorly for swirl-dominated flows.

As in the case of the EOTDF Generator simulations, a mass flow boundary condition was used for simplicity. The domain was solved using an implicit unsteady pressure-based RANS solver with SIMPLE pressure-velocity coupling. A compressible ideal gas model of air was used. The time step was set at 10^{-5} s.

3.3.2 Results - Reynolds Stress Model

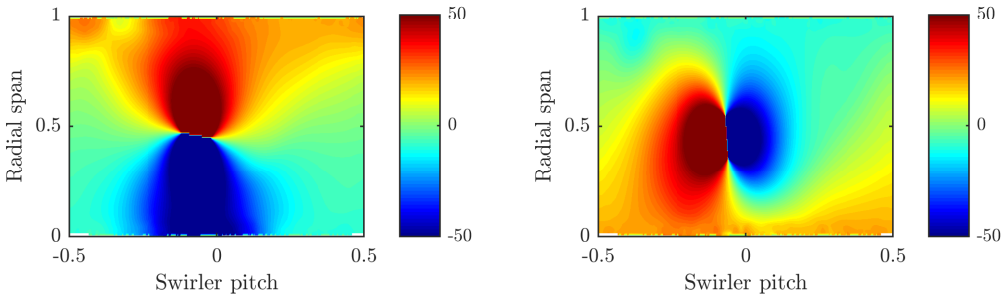
Figure 3.15 shows the URANS swirl (β) and pitch (α) angle profiles, clipped to $\pm 50°$ to aid comparison to the pilot study data (cf. Figure 3.13). The URANS solution

showed good agreement over the majority of the measured plane. Swirl and pitch angles in excess of ±50° were present in the CFD solution towards the vortex core, in regions where the pilot study data was unresolved or out of range. The time resolved results from the simulation (Figure 3.16) shows that recirculation is occurring at the vortex centre, which would be problematic for a four-hole probe like the one used by Qureshi and Povey (2011). Generally the simulation appeared to predict the flow structure and swirl magnitudes well (acknowledging the limitations of the experimental data).

The swirl strength ($S = 0.6$, based on swirler geometry) was such that vortex breakdown would have been expected for a weakly diverging duct. While recirculation was present downstream of the swirler hub, the vortex core remained steady and intact beyond this - critically, the recirculation zone which did form was relatively small in the (vortex-centric) radial direction and it remained stationary along with the vortex core. The axial acceleration and associated favourable axial pressure gradient within the contraction acted to stabilise the vortex, a tendency noted by Mitchell and Délery (2001).

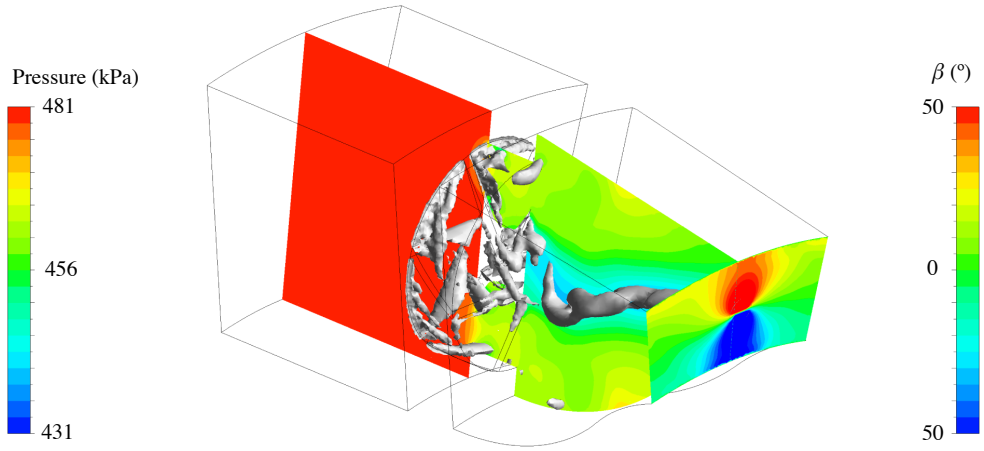
3.3.3 Swirl simulator study summary

The CFD simulation presented herein was in reasonable agreement with the available experimental data. The applied CFD method performed well in terms of predicting

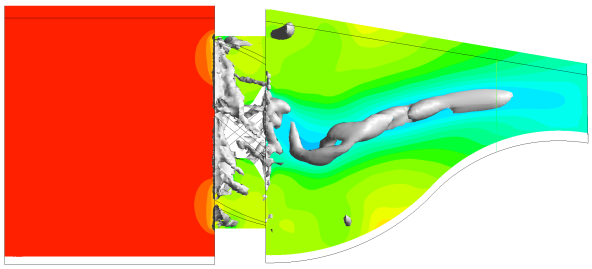


(a) (b)

Figure 3.15: Time-averaged (L-R) swirl (β) and pitch (α) angle derived from URANS solution - RSM.



(a)



(b)

Figure 3.16: Time-resolved flow properties from URANS solution (RSM) showing static pressure on a meridional plane (a,b), the vortex core (a,b), and the swirl angle at the inlet plane (a).

the inlet swirl and pitch profiles, which was of central importance in the subsequent development of the OLCS. It is clear that analysis of greater depth is impeded by a lack of experimental data, particularly in terms of the swirler flow structure in the region between the swirlers and the vane leading edge. The simulation suggests that the peak swirl values exceed the stated ±50° (Qureshi and Povey, 2011) and that recirculation existed across a significant axial extent. Both are implied by the results of Qureshi and Povey (2011) where results are in error or out of range (probe range was ±50°) near the vortex centre - by definition flow angle approaches 90° as axial velocity approaches zero. The general flow structure was not discussed by Qureshi

and Povey (2011) and only limited CFD was presented. The additional insight gained in this small study suggests that a further investigation of how the vortex core and recirculation zone interacted with HP stage may yield interesting results.

As a general note, even in the case that vanes are excluded from the simulation (which is in itself a noteworthy simplification), it is prudent to extend the domain further past the plane of interest in the downstream direction, well beyond the low-pressure, recirculating core of the vortex. This approach was adopted in later simulations presented elsewhere in this thesis.

3.4 Conclusions

The study of the past OTRF combustor simulators set out to help establish a simulation approach that could be used with some confidence in the development of the OLCS. The OLCS was to be developed entirely using CFD as a predictive tool.

In the case of the EOTDF Generator, three turbulence models were compared, since there was not considered to be a clear choice at the outset. It was found that in the specific case of shear layer mixing where stream velocities were matched, all of the examined models had limitations. The wall-resolved simulation employing the k-ω SST model appeared to perform best in terms of predicted stream mixing, suggesting that it was driven by boundary layer turbulence generation (rather than shear layer generation) in this case. It would be expected that for an arbitrary case of unmatched velocities, all turbulence models would perform better.

The swirl simulator was modelled only with the Reynolds Stress Model. This was due to the fact that the important flow mechanisms were free stream mechanisms related to the swirling flow (e.g. recirculation) for which the Reynolds Stress Model was widely established as being superior to the alternatives. Additionally, it could be concluded a priori that where a quality boundary layer mesh was not feasible (as was the case for the particular swirler design), the k-ω SST would perform similarly to

the standard k-ϵ (since the k-ω SST uses the standard k-ϵ model in the free stream). In any case, the simulation was able to predict the inlet profiles with reasonable accuracy, and also provided additional insight in to the flow structure that was not examined by Qureshi and Povey (2011). The swirler geometry for the OLCS was carefully designed to aid mesh generation based on the experience in this study.

Chapter 4

Development of a lean-burn combustor simulator

To facilitate upcoming turbine research programmes in the OTRF focusing on lean burn combustors, a combustor simulator capable of producing scaled (temperature and pressure) HP turbine inlet conditions representative of a lean burn engine was required. Where previous OTRF combustor simulators (discussed in the Chapters 2 and 3) focused on the generation of a single non-uniform flow property (i.e. total temperature or swirl), this system was required to simultaneously generate realistic non-uniform inlet profiles of total temperature, total pressure, swirl and turbulence. The following section discusses the conception of the simulator hardware, the analysis of the target inlet profiles to guide specific design decisions, the iterative CFD design process undertaken to achieve the target inlet profiles and finally the mechanical design of the final system. Included also, is the aerodynamic and mechanical design of a compatible turbulence generation plate for obtaining increased inlet turbulence under otherwise uniform conditions.

4.1 Combustor simulator concept

The central design objective was a non-reacting combustor simulator capable of producing a range of (lean burn) engine-realistic non-uniform inlet profiles. Variable swirl and temperature distortion were desired to allow the simulator to be used in multiple

lean burn combustor-turbine interaction studies planned for the OTRF. Some fundamental design decisions regarding the introduction of swirl to the mainstream and the injection of coolant are discussed in this section.

The conceptual design of the simulator was initiated from a limited number of pre-defined constraints related to the OTRF itself, and existing design decisions related to the engine programmes in which the simulator would be used. The simulator was required to integrate with the OTRF between the upstream plug valve assembly and the turbine inlet contraction, ideally being separate and modular with respect to both interfacing systems. The simulator was designed for a HP vane count of 40, and a swirler count of 20 - these design choices had been made prior to the design of the combustor simulator and were chosen to allow the optimal generation of periodic CFD domains for HP stage simulations.

The initial concept drew on the experience of Povey and Qureshi (2008) and Qureshi and Povey (2011) in designing the OTRF EOTDF Generator and the swirl simulator respectively. The swirl simulator featured a simple swirler with flat-plate vanes (vane count of 6). A swirl profile with peak values of at least $\pm 50\,^{\circ}$ was acheived (Qureshi and Povey, 2011). This result was in line with the findings of Kilik, 1976, who found flat vane swirlers were effective in creating swirl and performed only moderately worse than more complex curved blade swirlers in terms of swirl strength and pressure drop. Based on this previous experience, the initial concept adopted a swirler with flat vanes with blade angle tailored to the required swirl strength.

The design of the EOTDF Generator (Povey and Qureshi, 2008) used annular coolant injection slots at the hub and case to create a radial temperature profile, with radial coolant injection baffles used to create circumferential variation. By design, the inlet total pressure profile for the EOTDF Generator was uniform. Annular slots hold an advantage over alternative options such as dilution holes and perforated plates in terms of manufacture and achieving circumferentially uniform mass flow distribution. Additionally, the axial position of the slot trailing edge would allow control of mixing

and therefore temperature profile. Finally, the slot area directly controls the total pressure of the coolant stream, which was an important consideration where a specific, non-uniform profile was required.

The design study considered the combination of swirling flow and temperature distortion as the central challenges of simulating lean-burn combustor exit flow. Being able to control the interaction between the mainstream and coolant flows, to at least some extent, was therefore of importance. The adopted approach was to exhaust the swirler flow through discrete round to rounded-sector diffusers. This delayed mixing of adjacent vortices and controlled the diffusion of the mainstream flow from the swirler and into the larger annular cross-section. This design avoiding corner recirculation zones, which can become unsteady. The concept is shown in Figure 4.1. The mechanical design (discussed below) allowed for interchangeable swirlers to achieve swirl profiles of different strengths.

Radial temperature variation was simulated with the injection of coolant flow through annular slots at the hub and case. The temperature and mass flow of the hot mainstream and cold injected flow could both be varied. The design allows for adjustment of the axial location of the coolant injection and slot area (and therefore velocity) as a means to control the total pressure and total temperature profiles.

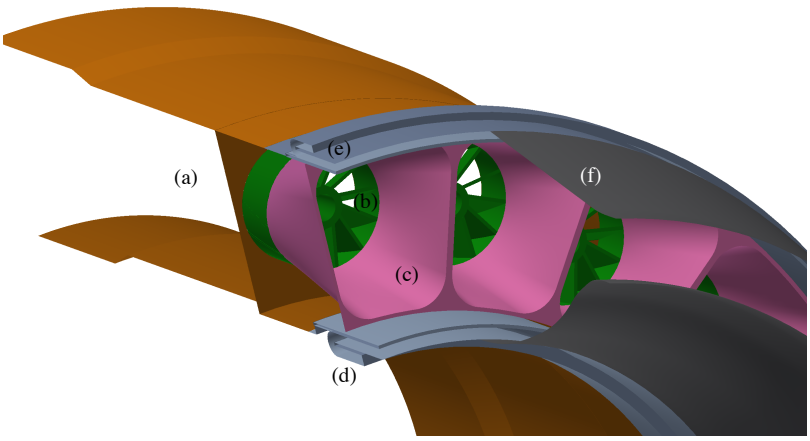


Figure 4.1: Schematic of the combustor simulator concept showing: (a) the mainstream inlet duct; (b) flat-vane swirlers; (c) swirler diffuser; (d,e) hub and case coolant injection slots; and (f) turbine inlet contraction.

4.2 Target inlet profiles

The OLCS was designed to be modular and adjustable (as described above), and therefore capable of achieving a range of target inlet profiles. At the outset of the design process, two separate OTRF lean-burn engine programmes had been planned around the combustor simulator. The first of these was the SILOET turbine, which formed the primary focus of the design process for a number of reasons. SILOET was originally scheduled as the first of the two programmes to run in the OTRF, placing a priority on achieving the respective target profiles first. Secondly, the SILOET profiles (discussed in detail below) consisted of lower peak swirl values which was expected to make the set of target profiles relatively simpler to achieve. From the resulting system, modifications were made as necessary to best match the target profiles of the second programme, LEMCOTEC.

The target profiles are presented below. Further analysis which guided specific design decisions such as coolant distribution and injection, and swirler geometry is then presented.

4.2.1 SILOET Programme

The SILOET lean-burn engine programme consisted of a fully-cooled (vane and rotor) HP turbine stage and uncooled IP vane. The turbine was designed for swirl-stabilised lean-burn inlet conditions. The implementation of this turbine in the OTRF required a new combustor simulator capable of producing engine-realistic inlet profiles characteristic of a lean-burn (LPP) combustor. The basic OTRF flow parameters for this turbine (as relevant to the inlet profiles) are summarised in Table 4.1.

The full set of target profiles is illustrated in Figure 4.2. The total temperature profile was characterised predominantly by variation in the radial direction, indicative of annular combustor endwall cooling flows. The relatively limited overall variation (i.e. circumferential variation) was likely a result of the swirling mainstream flow

Table 4.1: Summary of nominal OTRF scaled turbine conditions

Property	**Unit**	**SILOET**	**LEMCOTEC**
$T_{0\,h}$	K	500	530.6
$T_{0\,c}$	K	290	290
$T_{0\,mass}$	K	475	475
$\dot{m}_{Tot}$	kg/s	14.96	23
$\dot{m}_h$	kg/s	13.18	17.69
$\dot{m}_c$	kg/s	1.78	5.31

structure entraining these endwall cooling flows. The swirl and pitch profiles were indicative of a single vortex per swirler pitch as expected, with peak swirl values of approximately $\pm 25°$. This is illustrated more clearly by the velocity vector plot derived from the swirl and pitch angle data. The turbulence data was taken as is, and was used only for comparison to results, rather than to guide the design. It was assumed that turbulence generation would be controlled predominantly by the mainstream flow structure.

The static pressure profile at the NGV inlet plane was not provided, however it could be assumed to be approximately uniform. Based on this assumption, and using the total pressure profile and flow angles, it was possible to estimate (by iteration) an approximate value of uniform static pressure and therefore also local velocities that satisfied the total pressure profile and total mass flow rate.

The target data were further reduced to guide the design of the simulator. A plot of RTDF is shown in Figure 4.3 along with the radial profile of total pressure.

One-dimensional plots of swirl and pitch profile are presented in Figure 4.4. The figures show the span-wise variation of circumferentially-averaged (area weighted) swirl (β) and pitch (α) angle.

The target plots illustrate that the centre of the vortex is not located at zero swirler pitch. It was not clear whether this was due arbitrary clocking of the profiles (i.e. the theoretical swirler was also offset circumferentially) or whether a circumferential migration of the vortex was implied. For the purpose of designing the simulator and configuring experiments, it was assumed that the centre of the swirler was located at the circumferential origin of the plot.

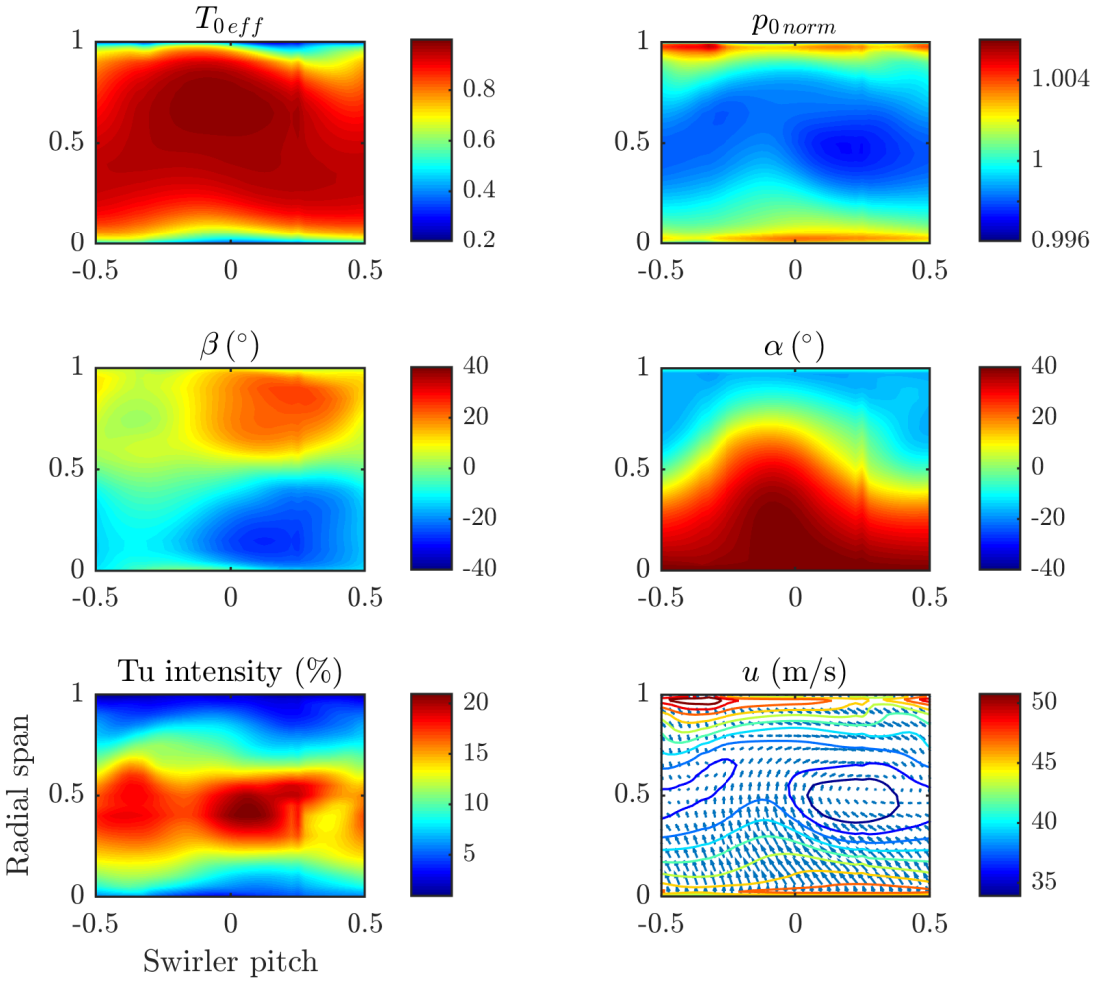


Figure 4.2: SILOET target inlet profiles. Velocity plot shows in-plane vectors and magnitude contours.

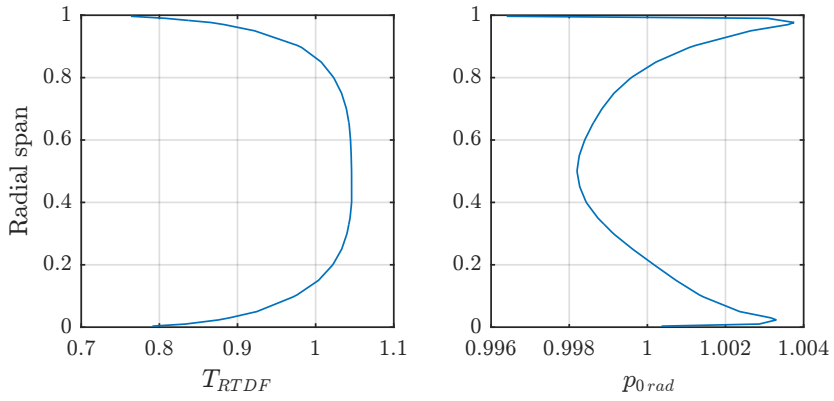


Figure 4.3: SILOET circumferentially-averaged total temperature and total pressure targets.

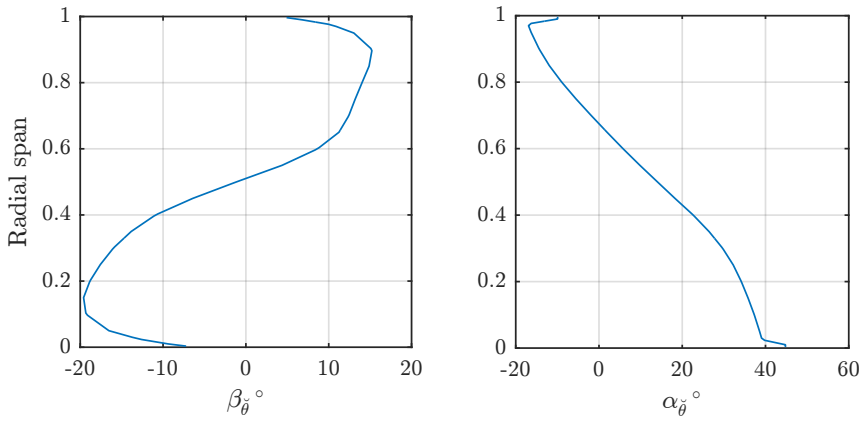


Figure 4.4: SILOET circumferentially-averaged flow angle target profiles.

4.2.2 LEMCOTEC Programme

The LEMCOTEC lean-burn engine programme consisted of a HP turbine stage with cooled vane, and IP vane. As was the case for the SILOET turbine, the LEMCOTEC turbine was designed for swirl-stabilised lean-burn inlet conditions. The basic OTRF flow parameters for this turbine (as relevant to the inlet profiles) are summarised in Table 4.1.

The set of target inlet profiles provided for the LEMCOTEC research programme are illustrated in Figure 4.5. It is noted that for the total temperature profile, as received, the hot-streak did not align with the swirler axis. In fact, on close inspection it can be seen that the temperature profile is scaled directly from EOTDF Generator data (cf. Figure 3.4 - NGV pitch value 1 to 2). The misalignment was remedied initially by shifting the data such that the hot-steak aligned with the swirler axis (see Figure 4.5 - $T_{0\,eff}$ (shifted)) which provided an acceptable result. It is noted however, that since the target data was not internally consistent—the temperature being derived from a known non-swirling flow field—the assumption that they were physically realisable was abandoned during the design stage.

The 1D reduced data derived from the 2D target inlet profiles are presented in Figures 4.6 and 4.7. Since the provided target profiles were questionable in terms of

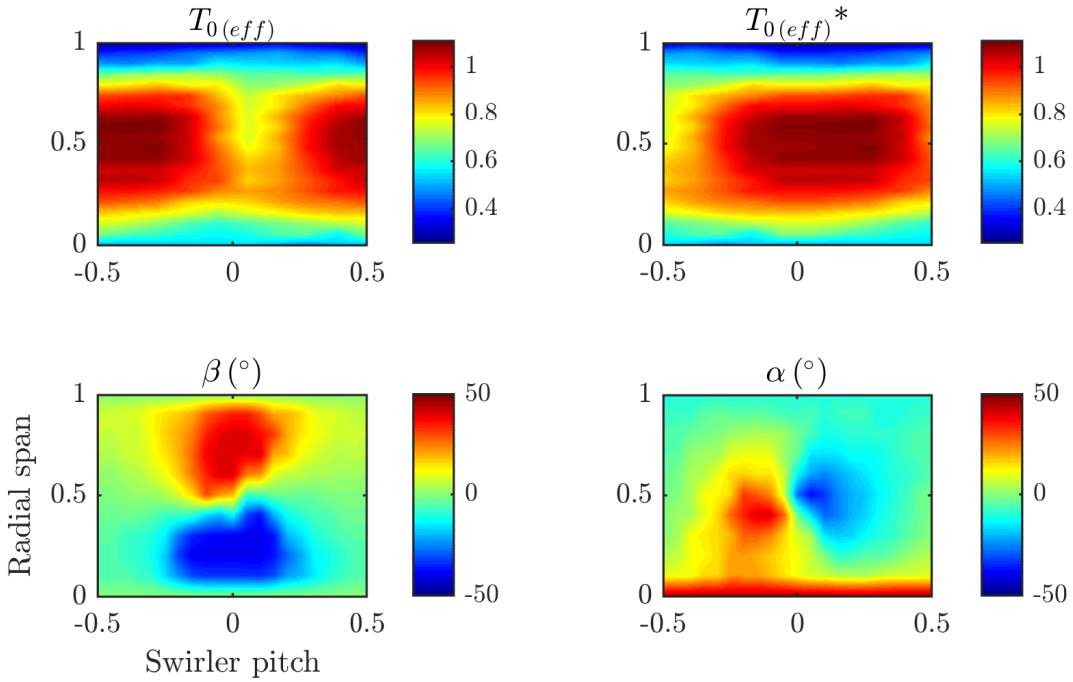


Figure 4.5: LEMCOTEC target inlet profiles. *Profile shifted to align hot-streak with vortex (swirler) axis.

their physical realisability, the 1D profiles were used as a guide by which to establish a new set of inlet profiles. That is, rather than attempt to design the OLCS to be able match the 2D profiles of Figure 4.5, the important features of the 1D profiles would be reproduced as best possible. The nominal target parameters for the LEMCOTEC case then became:

- High (relative to the SILOET profiles) peak swirl angle of $\pm 40°$
- A large degree (relative to the SILOET profiles) of radial temperature non-uniformity (Figure 4.6)
- A radial total pressure profile characteristic of a lean-burn combustor - high total pressure related to combustor liner cooling flows.
- Turbulence would be driven largely by the resulting vortex structure and would be expected therefore to be high, $> 15\%$ turbulence intensity.

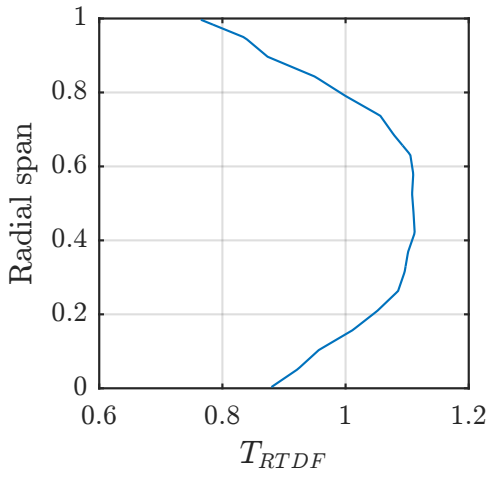


Figure 4.6: LEMCOTEC circumferentially-averaged total temperature target (area-weighted).

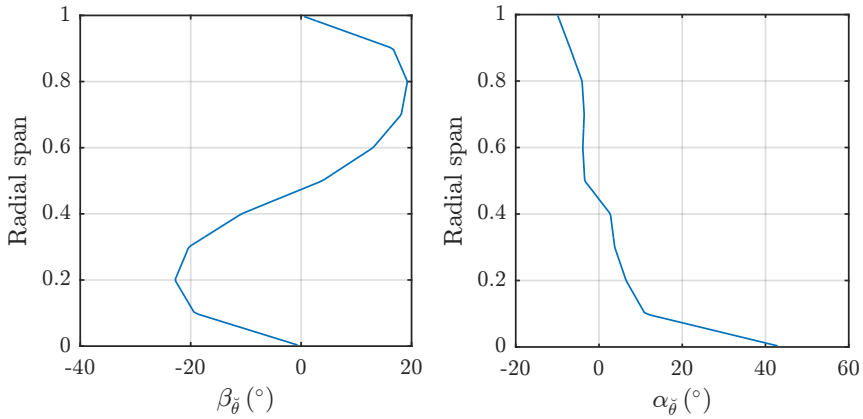


Figure 4.7: LEMCOTEC circumferentially-averaged flow angle target profiles.

It is also noted that the lack of a total pressure profile made mass-weighted averages impossible (acknowledging that for the given level of swirl strength, the spatial non-uniformity of mass flow would be significant). Area-weighting was therefore used in the circumferentially averaged temperature data of Figure 4.6.

4.2.3 Swirler aerodynamic design

The design of the OLCS was principally carried out using an iterative CFD approach. This was necessary due to the complexity of the swirling mainstream flow, which has a highly non-uniform velocity profile. It was still necessary to calculate an initial

estimate of the upstream swirl strength (at the swirler exhaust) and associated swirler geometry. From this, an initial swirler design could be developed for testing within CFD simulations.

The swirler vane angle was estimated initially using a coarse approximation which considered the change in area between the swirler exhaust plane and the vane inlet plane. Due to the complexity of the actual flow structure, analytically estimating the decay of angular momentum, and the true velocity profile would be difficult - impractical for an initial estimate. By assuming conservation of angular momentum, and considering the change in effective flow area of a single vortex, it was possible to calculate an approximation of the required swirler geometry. This simple method treated the swirler exhaust flow as being contained within a frictionless circular duct of varying diameter, and assumed solid-body rotation of the flow (velocity linearly proportional to radial location). Uniform density and axial velocity were assumed. This is illustrated in Figure 4.8.

For the SILOET peak inlet swirl angle of approximately $\pm 25°$, this method suggested a peak swirl angle at the swirler exhaust of 23.5°. This was then taken as a direct estimate of the swirler vane angle. For the LEMCOTEC case with peak inlet swirl angle of $\pm 40°$, the same process implies a swirler vane angle of 35.5°.

The swirler casing and hub diameters were sized primarily to minimise the pressure drop. That is, the casing diameter was increased to the practical maximum

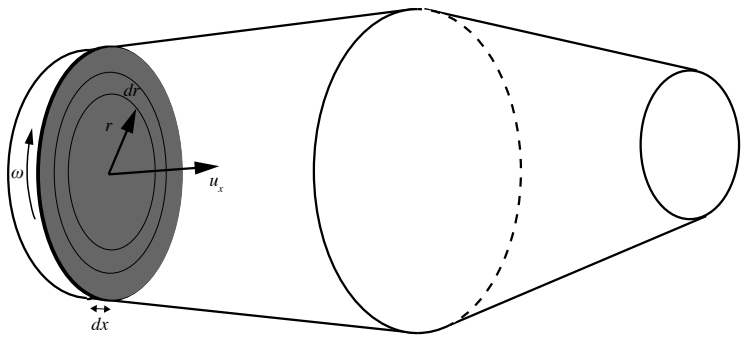


Figure 4.8: Schematic of method to estimate upstream swirl

considering the annular duct diameter while the swirler hub was minimised considering ease of manufacture of the resulting geometry. The casing (inner) diameter was 72.5 mm, while the hub diameter was 25.0 mm.

4.2.4 Analysis of temperature profile

The SILOET 2D total temperature inlet profile was analysed in order to determine the fraction of total coolant mass flow rate injected at the hub and case. The method utilised to achieve this was described by Qureshi (2010) with the exception that a complete mass-weighted approach was used in the current work. Qureshi (2010) assumed uniform velocity when designing the EOTDF Generator, which was reasonable in that instance, but not accurate for highly swirling flow. The method involved discretising the inlet profiles on to a radial-circumferential grid of even spacing. For each grid area, the required ratio of coolant to mainstream (hot) flow to satisfy the local total temperature was calculated. Coolant in the range $0\% < r < 50\%$ (radial span) was assigned to the hub injection, and $50\% < r \leqslant 100\%$ to the case injection. The same hub-coolant mass flow rate split was assumed for the LEMCOTEC profiles.

When this was calculated initially, a coding error lead to an erroneous result which was carried through the design. The correct value could be adopted without modification to the system. The design value and corrected value are noted in Table 4.2.

Table 4.2: OLCS case coolant mass fraction

	Design value	**Corrected**
Case coolant fraction	0.53	0.58

4.3 Computational design of the combustor simulator

The concept for the OLCS described at the outset of this chapter was modelled in CAD and simulated using CFD in order to examine the resulting inlet properties,

specifically the 2D inlet profiles. Where in previous combustor simulator designs for the OTRF, minimal or no CFD had been carried out, the additional complexity inherent in a system combining a swirling mainstream with non-uniform total temperature and total pressure meant that this part of the development process was crucial. In fact, it was found that the mainstream flow structure was highly variable and had a significant impact on all flow parameters at the inlet plane.

The following sections discuss the justification behind the chosen CFD methodology, in addition to that provided by the study of the previous OTRF simulators. The set up of the simulations is discussed in further detail and important results are presented. It is noted that a number of additional concepts were tested in attempts to address short comings of the original concept (presented above) however for brevity only those important to the evolution of the design from the original to final concept are presented.

4.3.1 Computational method

The development of the OLCS was based around an iterative design process which utilised unsteady RANS as a predictive tool. This was necessitated by the overall complexity of a flow field characterised by strong swirl and the mixing of multiple streams, something that was infeasible to calculate using simple analytical methods. This was in contrast to Qureshi and Povey (2011), who used a simple CFD approach (coarse unstructured tetrahedral meshes and steady RANS) supplemented by a experimental pilot study for the design of the swirl simulator. For the swirl simulator, it was shown (in Chapter 3) that the swirling flow was inherently somewhat steady (due to the location of the swirler adjacent to the vane inlet contraction), however this is rarely the case for strong swirling flows found in combustors where large recirculation zones are the norm (by design) and precessing vortex cores (PVCs) may form. As the OLCS required engine-realistic performance, a thorough understanding

of the unsteady flow field was required and an appropriate 3D unsteady CFD method was adopted. The details of this method are discussed in detail below.

Unsteady CFD is often broken in to two families; Unsteady Reynolds-Averaged Navier-Stokes (URANS) in which turbulence is modelled and only relatively large scale unsteady motion is resolved; and scale resolving simulations which attempt to resolve the energy-containing turbulent structures. Of the latter group, the Large Eddy Simulation (LES) and the Detached Eddy Simulation (DES) are widely considered the leading computational approaches for swirling combustor flows. The underlying principle for both LES and DES is to resolve turbulence features down to the scale—typically the Taylor length scale—at which turbulence transport is relatively easily modelled. The computational cost for LES and DES is high—1 to 2 orders or magnitude greater than for URANS—making its use as a predictive tool in an iterative design process impractical. The computational resources available for the development of the OLCS were not suitable for LES or DES. Acknowledging this, the OLCS development was performed using URANS with the Reynolds Stress model (RSM) for turbulence closure. This computational compromise has been shown to be capable of resolving the important flow features (Wegner et al., 2004; Yang et al., 2003). A general discussion of computational methods for swirling flows is provided in Chapter 2, while a preliminary CFD study which investigated URANS performance is included in Chapter 3. Chapter 2 also discusses the Scale Adaptive Simulation (SAS) which is gaining interest (e.g. Andreini et al., 2015) as an approach with 'LES-like' results at significantly reduced computational cost which should be considered for future work.

4.3.1.1 Computational method and URANS modelling

For all URANS simulations carried out in the development of the OLCS, the commercial CFD code Fluent was used. The fundamental aspects of the solver set up were:

- Unsteady pressure-based RANS solver (3D double-precision) in ANSYS Fluent
- SIMPLE pressure-velocity iterative algorithm
- Second order spatial discretisation (computational grids discussed below)
- Second order (backward difference) implicit (iterative) temporal discretisation - time step of 10^{-5} s
- Reynolds Stress Model (RSM) for turbulence closure
- Near wall treatment based on standard wall functions

A segregated solver (e.g. SIMPLE pressure-velocity algorithm) is well suited to the high pressure gradients present in strong swirling flows. Swirling flow causes a high degree of coupling between the momentum equations (Jawarneh and Vatistas, 2006). Additionally the RSM creates a high degree of coupling between the momentum equations and turbulent stresses which can lead to numerical stability issues. Avoiding additionally coupling of the governing equations by using a segregated solver was therefore desirable to aid numerical stability and convergence.

For all URANS cases discussed, turbulence closure was achieved using the RSM with near-wall modelling. The suitability of this model is discussed in Chapter 2 and demonstrated in Chapter 3.

Time step selection must consider the expected frequency of unsteady phenomena in the flow and be sufficiently small to resolve these fluctuations without imposing a temporal filtering effect. In practice this must be balanced against available computing resources and time, both of which were heavily constrained in this design work. The selected time step of 1×10^{-5} ensured an RMS Courant number much lower than unity across the domain, was sufficient to resolve PVC oscillations which were in the order of 250 Hz. This time step was also at the limit of what was practical with the available computational resources.

Individual implicitly calculated time steps were allowed to converge by 4 orders of magnitude in terms of scaled residuals. The solution was calculated for at least 10 flow-through periods of the combustor (i.e. the region downstream of the swirler) and was deemed to have converged once periodic fluctuations had developed.

4.3.1.2 Numerical setup

The domain was configured with mass flow inlet boundary conditions (see table 4.1 for quantities) and an average pressure outlet boundary condition. Inlet turbulence was set at a medium value of $4-5\%$ for the coolant feeds - stream mixing was found to be fairly insensitive to this, however. Mainstream turbulence was set at a low value (2%) for cases which included a swirler, based on experience with background turbulence intensity in the OTRF duct. For cases without a swirler (explained below), the mainstream turbulence was set at 15% based on those simulations with swirler geometry.

The use of URANS and the need for a relatively small time step (10^{-5} s) with respect to flow-through period led to relatively high computational cost (although still much lower than for LES). A number of meshing approaches were explored in the optimisation of this process.

The first generation of meshes were of unstructured tetrahedral elements. This allowed semi-automated mesh generation for complex 3D geometry (e.g. the swirlers). Figure 4.9 illustrates a first generation geometry and mesh. In these early cases the domain spanned upstream of the swirler to the axial location of the trailing edge of the vanes. The vanes were not included in the simulation. It was assumed that the potential field of the vane would have limited impact on inlet profiles. Klapdor (2010) showed that while the potential field of the vane affects the flow field, the effect is most significant in the region immediately (within one quarter of an axial chord length) upstream. Specifically it was shown that between one half and one axial chord length upstream, small differences in flow field magnitudes existed. The

back-pressure of the domain could be set explicitly in the simulation to ensure that the static pressure was correct in the absence of the vanes and that Reynolds number was therefore correct in the upstream region of the domain. Inlet profiles were taken on a plane half an axial chord upstream of the (theoretical) leading edge.

The computation time for this first generation of mesh was significant and minor alterations to the geometry (which were frequent) meant calculating a new mesh. To reduce the domain size and computational demand, and to allow a completely hexahedral mesh to be more easily generated, a second-generation domain was developed which excluded the swirler. A hexahedral mesh derived from a block-structured topology could be modified rapidly to reflect geometry changes. This domain was bounded upstream by the swirler exhaust plane. An inlet boundary condition with constant swirl angle was imposed. Importantly, the inlet swirl could be easily varied without the need to adjust geometry and create a new mesh. The removal of the swirler from the domain also avoided convergence problems with the RSM related to poor quality tetrahedral cells often generated adjacent the complex swirler geometry. It is noted that a major compromise of this approach was that it neglected the wakes of the swirler vanes and introduced a more uniform velocity profile than would be the case in reality. Figure 4.10 shows an example of a second generation mesh. This mesh

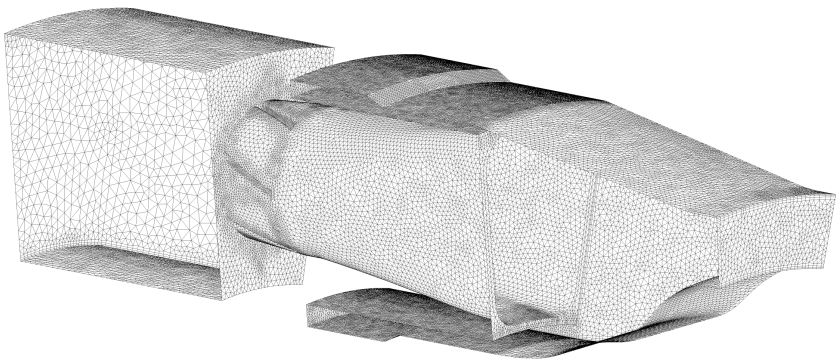


Figure 4.9: Example first generation geometry and tetrahedral mesh.

approach was used for all preliminary design iterations; detailed domains including swirlers were then revisited at the latter stages of the design process (discussed below).

4.3.1.3 Mesh dependency

A mesh dependency study was carried out for the second generation of mesh. The mesh dependency study examined meshes of approximately 0.2, 1, and 5 million cells (see Figure 4.11), in addition to the design case of approximately 0.5 million cells.

For each case flow was investigated in two critical areas; the central recirculation zone and the shear mixing layer at the coolant slots. These two features had a significant impact on the resulting inlet profiles. All mesh resolutions successfully captured the central recirculation zone. There was slight variation in the size of the central recirculation zone between meshes, but the maximum negative axial velocity was in good agreement between cases. Mixing of the coolant with the main stream was also an important aspect of the simulation. This was found to be insensitive to mesh size in the range studied. Some numerical diffusion was evident at the slot trailing edge. This decreased as mesh size increased, and became less significant further downstream where there was good agreement in terms of the inlet temperature

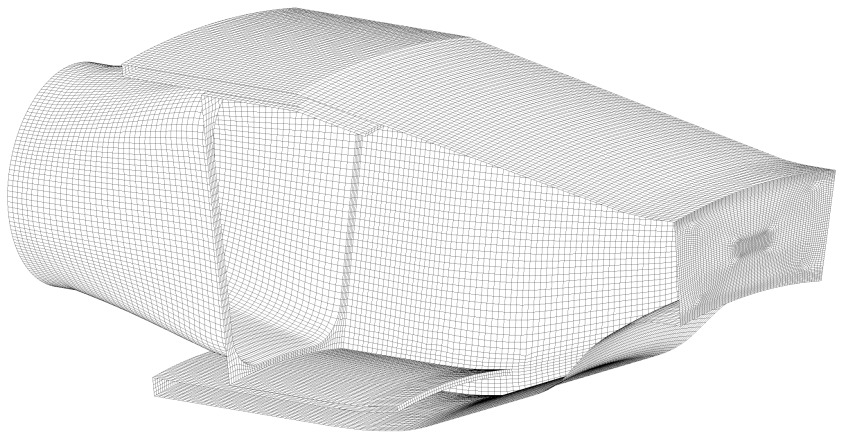
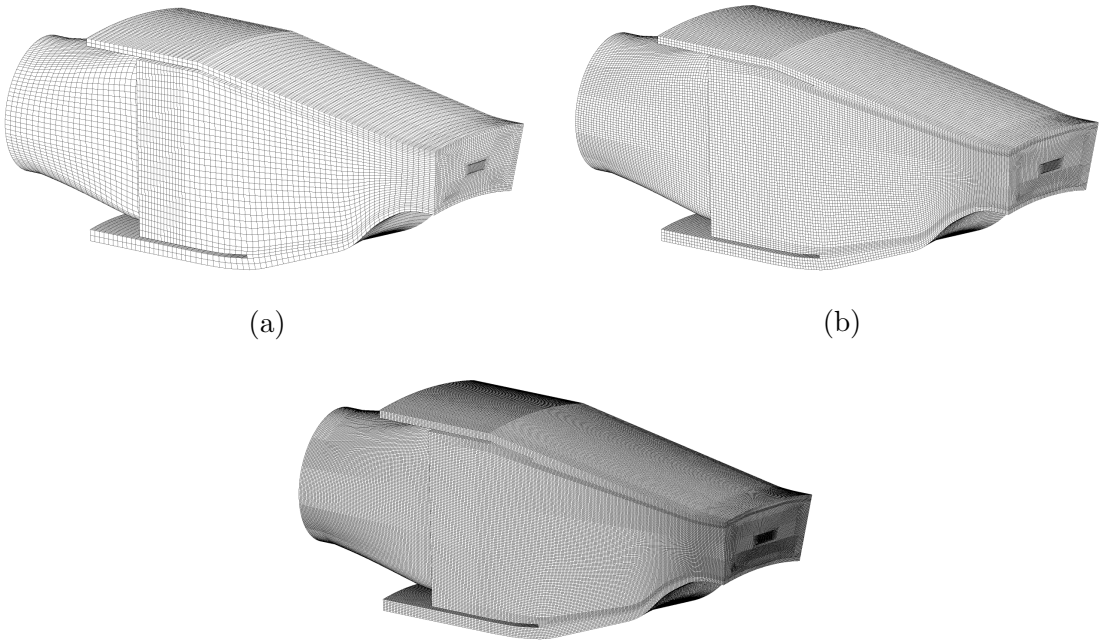


Figure 4.10: Example second generation geometry and hexahedral mesh on the simplified domain.



(a) (b)

(c)

Figure 4.11: The three meshes used in the mesh-dependency study: (a) 2×10^5 cells, (a) 1×10^6 cells, (a) 5×10^6 cells.

profile between the three cases. The inlet profiles were essentially identical across all cases.

The approximate swirl number at the inlet plane (where R_O was based on a circle of area equal to that of 1 inlet plane sector) was used to judge mesh convergence. On this basis, using the method set out by Celik et al. (2008), the grid convergence index was determined to be 10%. While relatively high, this was deemed suitable for the application at hand.

Throughout the design process, consistent mesh resolution was employed to ensure internal consistency of process and subsequent results. This avoided evolution of design based on mesh-dependent solution variation.

The final design was reassessed using a full domain mesh (including full swirler geometry) with URANS. A high quality unstructured hexahedral mesh was derived from a multi-block topology. The cell count was approximately 1.3 million. This placed it at the coarser end of mesh resolution considered in the dependency study.

The inlet profiles were shown to be reasonably insensitive to mesh resolution across the range investigated. The hexahedral mesh used in the URANS simulation is shown in Figure 4.12.

4.3.2 Design challenges

It has been demonstrated that for combustor simulators without swirl (focusing on rich-burn combustor designs), inlet profiles characterised by non-uniform inlet total temperature and total pressure can be achieved by focusing attention on the coolant injection system (e.g Povey and Qureshi, 2008; Barringer et al., 2004). By contrast, non-reacting combustor simulators—such as the OLCS—with swirl must consider the impact of vortex instabilities which affect the overall flow structure (depending on the mode of instability) and ultimately the inlet profiles. Turbulence intensity and length scale, which are a function of flame characteristics, can also be difficult to simulate under non-reacting conditions. Acoustic properties and pressure fluctuations also present a challenge since there is no energy release.

For swirling flows above a critical swirl number, it is well established that vortex breakdown occurs, characterised by the formation of a central (at the vortex core)

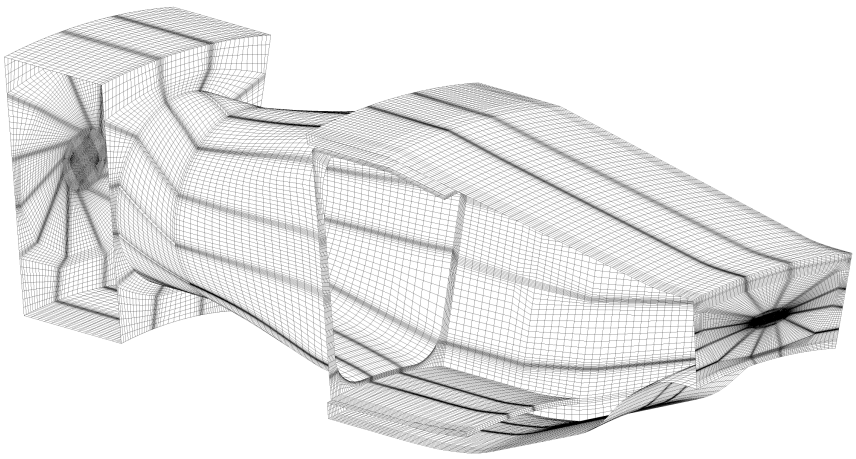


Figure 4.12: Third generation hexahedral mesh on full domain (i.e. including swirler).

recirculation zone. In general, the structure of swirling flow depends on swirl number, Reynolds number, duct geometry (Alekseenko et al., 2008) and density gradient resulting from heat release (Oberleithner et al., 2013). For certain flows—particularly non-reacting flows (Oberleithner et al., 2013)—a coherent flow instability referred to as a Precessing Vortex Core (PVC) (a helical perturbation of the vortex core) can also form, often significantly altering the flow structure in an unsteady sense. The potential for differing flow structures between swirling flow under reacting and non-reacting conditions has been identified previously (Roux et al., 2005; Selle et al., 2003; Cameron et al., 1989). Specifically, the presence of combustion has been shown to damp PVC excitation (Roux et al., 2005; Selle et al., 2003; Wankhede et al., 2010) and reduce the size of the recirculation zone (Cameron et al., 1989); both features that have a significant impact on the overall flow field. Relatively recently (subsequent to the development of the OLCS) in the work of Oberleithner et al. (2013) an understanding has emerged of the mechanisms which cause the self-excited PVC to form frequently in non-reacting flows and only rarely in similar reacting flows.

It is clear that a significant challenge exists in simulating swirl-stabilised combustor flows in a non-reacting environment. The variability of the vortex breakdown flow structure and potential for PVC excitation being central to this, raising the question of whether fundamental flow similarity could be achieved. With only steady inlet profiles as a basis for comparison, a conclusion regarding overall flow similarity would not be possible in any case. Returning to the comparatively simply goal of matching steady (2D) inlet profiles, rather than overall (3D) flow structure, the challenge remained that for a given combustor simulator geometry, the resulting vortex structure may or may not be conducive to achieving the target inlet profiles. For instance, the formation of a PVC significantly alters the 3-dimensional pressure distribution and velocity field. The pressure distribution and velocity fields affect the migration of coolant flow and therefore the inlet total temperature and total pressure profiles. This section examines some of the flow structures which were encountered during the CFD design process.

4.3.3 Development highlights

During the CFD development process numerous iterations of geometry were investigated, many of which were similar to those of Figures 4.9 and 4.10, and some based on quite different swirler exhaust geometries, although all maintained the hub and case coolant slot concept. It is not practical to discuss each of the design ideas in detail; instead a selection of designs that were of a common lineage towards the final design are discussed in detail. As previously mentioned, the development process focused initially on achieving the SILOET targets (discussed above). A summary of the important parameters investigated in the presented cases is given in Table 4.3.

Table 4.3: Summary of key design simulation cases

Case	**Mesh type**	**Swirler** ψ (°)	**Swirler included**	**Diffuser length** (mm)	**Swirler exit to NGV** (mm)	**Axial jet**	**Coolant slot trailing edge offset** (mm)
A1	tetra	21	Yes	140	262	No	-10
A2	hexa	21	No	140	262	No	-10
B	hexa	21	yes	140	302	Yes	-10
C1	hexa	25	yes	80	242	Yes	40
C2	hexa	25	yes	80	242	Yes	40
Mesh study	hexa	25	no	80	242	Yes	40

Figure 4.13 shows URANS results (first generation tetrahedral mesh, cf. Figure 4.9) for a design ('A1') that consisted of an axial swirler, nominally design to produce ±25 degrees of (peak) inlet swirl (as per the SILOET target profiles), positioned upstream of annular slots for coolant injection. The central recirculation zone (light blue) and the PVC (grey) are illustrated. The figure also shows pressure distribution, velocity field and inlet temperature profile. The simulation showed the PVC sweeping a significant part of the flow field in the radial direction, altering pressure and velocity in its vicinity. Coolant was drawn to regions of low static pressure creating an unsteady and non-uniform temperature profile.

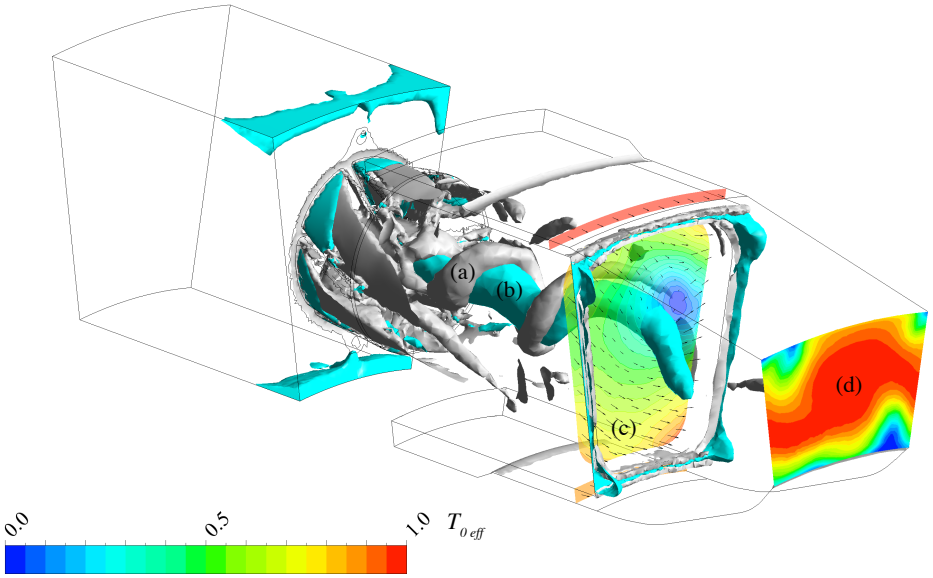


Figure 4.13: Design A1 (tetrahedral mesh including swirler geometry) showing (a) the PVC, (b) the central recirculation zone, (c) the pressure and velocity near the PVC, and (d) the inlet temperature ($T_{0\,eff}$) profile.

The computational cost of running unsteady simulations (even URANS) was high and as a result, the progress of the development was slow in real time. A solution to this was to simplify the domain by excluding the swirler geometry. This helped in two ways. Firstly, it removed a significant fluid domain volume and therefore directly reduced the mesh size. Secondly, it allowed a hexahedral mesh to be generated relatively easily - for a given cell edge length, hexahedral meshes have lower cell counts than tetrahedral meshes. Design 'A2'—a variation on A1—with the swirler excluded, a hexahedral mesh and an artificial swirling inlet boundary condition is illustrated in Figure 4.14. Once again a PVC oscillates through the flow causing significant unsteady mixing and ultimately unsuitable distributions of flow properties at the vane inlet. It is also apparent that the artificial inlet swirling boundary condition affects the flow field and it would be necessary to validate a final design using a fully-detailed domain (i.e. including the swirler).

Based on the results of simulations up to this point, it was concluded that attempting the suppress the excitation of the PVC may offer an improvement to

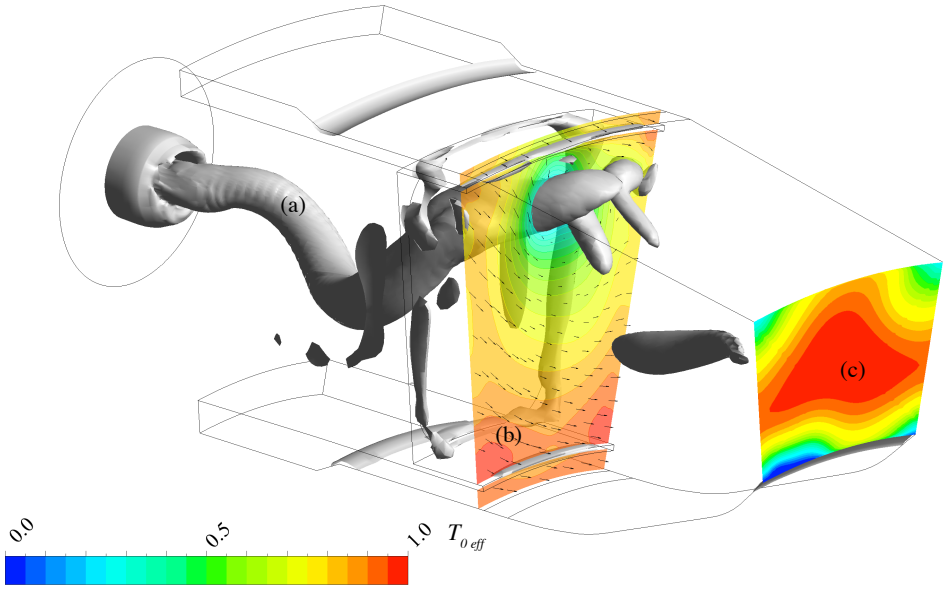


Figure 4.14: Design A2 (hexahedral mesh *excluding* swirler geometry) showing (a) the PVC, (b) the pressure and velocity near the PVC, and (c) the inlet temperature ($T_{0\,eff}$) profile.

the inlet profiles by reducing the mixing significantly. VB suppression is an active area of research with application, for example, to delta wing aircraft. A number of suppression methods have been proposed, including blowing at the vortex centre with corotating cool jets (Herrada and Shtern, 2003), and rotating rods at the vortex centre (Lo Jacono et al., 2008) (although practical applications of this are limited). The former technique can be used to increase the total pressure at the vortex axis to reduce the adverse axial pressure gradients. The use of colder fluid increases the influence on the radial equilibrium due to the increased density. Co-rotating flow increases vorticity magnitude on the axis, partially offsetting the downstream decay of tangential velocity.

Design A2 was modified to include an axial jet at the vortex centre. An axial jet was successfully utilised by Jochmann et al. (2005) to achieve a steady, axisymmetric flow for a model swirl combustor that had previously exhibited a PVC under non-reacting conditions. For simplicity, the effect of a jet with no swirl and temperature

equal to the mainstream was investigated. The results of the URANS simulation with vortex centre jet (design 'B') is illustrated in Figure 4.15.

The vortex instability mode was observed to have changed to one that was quasi-axisymmetric and steady in nature (cf. Design A, Figure 4.14, with PVC)—i.e. the PVC was suppressed—in agreement with the observations of Jochmann et al. (2005). True axisymmetry was precluded by the local geometry. The prevailing vortex flow structure, illustrated in Figure 4.15, was similar to the bubble mode described by Faler and Leibovich (1977). It is noted that contrary to the intention, the axial jet did not suppress VB altogether but instead suppressed the PVC which was responsible for the bulk unsteadiness of the flow field.

The resulting temperature profile (Figure 4.15c) was steady in time but poorly defined in the radial direction. Swirl strength decayed significantly with downstream distance. For the case shown, swirler outlet angle of 35° decayed to a maximum

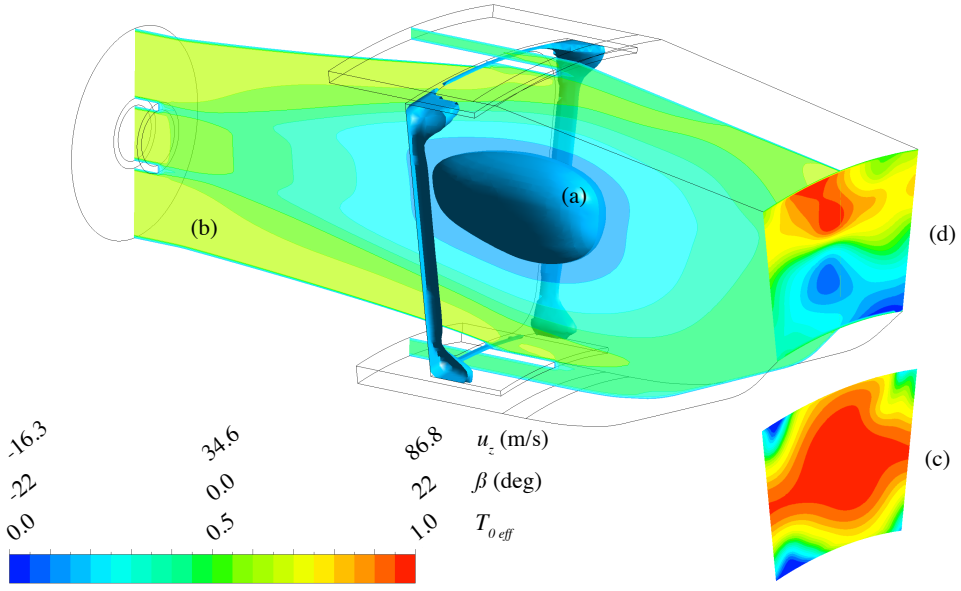


Figure 4.15: Design B (with low momentum jet) showing (a) the steady recirculation bubble, (b) axial velocity on a meridional plane, (c) the inlet temperature ($T_{0\,eff}$) profile, and (d) the inlet swirl angle (β) profile.

of 23° at the inlet plane. Increasing the upstream swirl angle to 40° reduced the inlet maximum swirl angle to 20°, a result associated with an increase in size of the recirculation zone.

Design 'C1' was similar to design B, but with reduced axial distance between the swirler and the inlet plane. The revised circular to rounded-sector transition duct was approximately half the length of designs A and B. The coolant injection point was extended axially in the downstream direction. The temperature profile was improved by moving the coolant slot trailing edge downstream to reduce the mixing length. The simplified domain and URANS results for this geometry are shown in Figure 4.16. This design produced a steady, radially well-defined temperature profile. The decay of swirl strength with axial distance was shown to be significantly reduced. It was observed that the recirculation zone increased in size when compared to design B. This was most likely a result of the more rapid diffusion associated with the shorter duct length.

Both the swirl profile and temperature profile for design C1 were close to the target. Results from a full domain simulation 'C2' (including swirler) of the same basic design are discussed in the following section.

4.3.4 Computational results

Design C2 (Figure 4.12) explicitly included the swirler in the domain, rather than a simplified upstream boundary condition. This was achieved with the hexahedral mesh illustrated in Figure 4.12. The overall mesh for geometry C2 required 1.3 million cells.

The swirler geometry (Figure 4.17) differed in two ways from the first generation design (and that used in the swirl simulator of Qureshi and Povey (2011)). Firstly, a higher vane count was used (12 versus 6) to produce a more homogenous swirler exhaust velocity profile to approach the constant swirl angle imposed in the simplified domain. Secondly the swirler vane-hub intersection was designed to allow

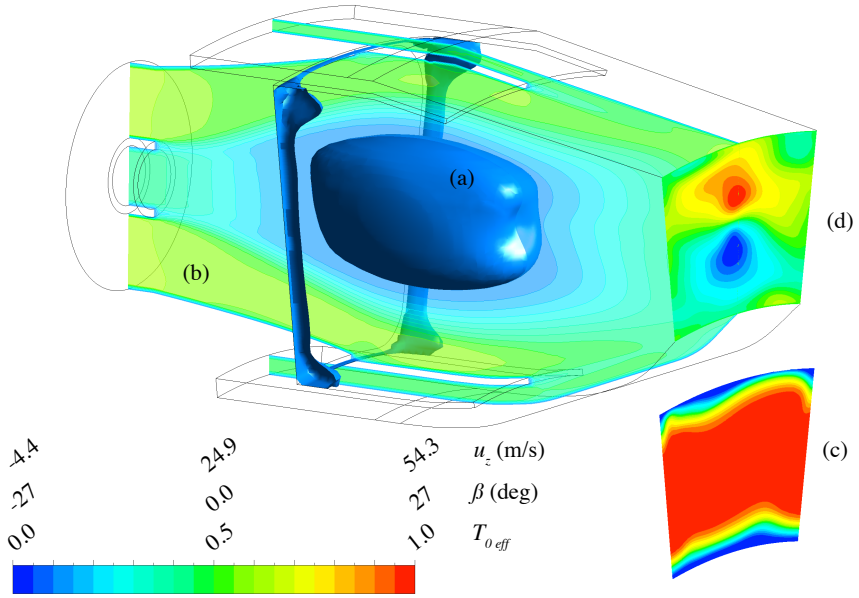


Figure 4.16: Design C1 (adjusted swirler location and coolant baffles) showing (a) the steady recirculation bubble, (b) axial velocity on a meridional plane, (c) the inlet temperature ($T_{0\,eff}$) profile, and (d) the inlet swirl angle (β) profile.

hexahedral mesh generation. As described in Figure 4.18, the axial dimension of the swirler is reduced such that the vanes do no extend all the way to the hub tangent. this results in simpler (more easily meshed) geometry at the vane-hub intersection.

The results for the URANS simulation for geometry C2 are shown in Figure 4.19. The extended (to include the swirler) domain C2 produced similar results to the simplified domain of Design C1, with some exceptions. The peak swirl angle at the swirler exit plane for geometry C2 exceeded the intended design value by approximately 7 degrees. This resulted in the larger recirculation bubble and stronger recirculation (in terms of peak negative axial velocity) shown in Figure 4.19. The form of the recirculation bubble was similar and the PVC suppressed in both cases (C1 and C2).

Although the recirculation bubble for geometry C2 is somewhat larger than for C1, the decay of the swirl in the axial direction was minimal for both geometries (compared to earlier iterations above). The stable recirculation bubble in both cases

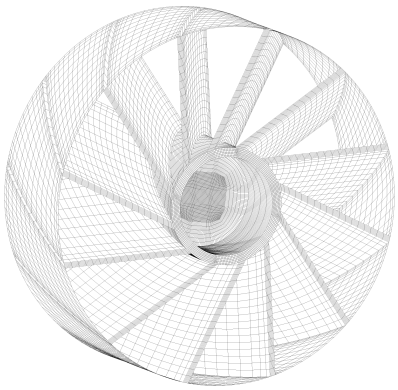


Figure 4.17: Swirler geometry (and mesh) used in Design C2.

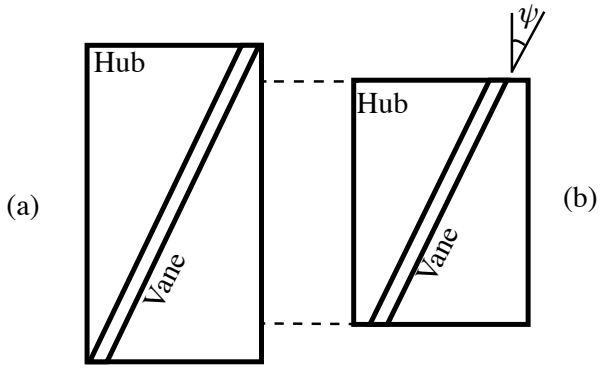


Figure 4.18: Swirler design detail: case (a) the flat vane extends to the hub tangents; (b) (cf. Figure 4.17) the swirler is 'cut back' in both axial directions.

resulted in steady inlet swirl and temperature profiles. It is expected that reducing the swirler vane angle in C2 would lead to a close match to the C1 results.

Figure 4.20 illustrates the inlet total temperature ($T_{0\,eff}$), total pressure, and swirl and pitch angles. The inlet temperature profile for geometry C2 showed slightly more overall temperature distortion than geometry C1. This is likely to be an effect of the higher swirl strength. It can be inferred directly from the 2D temperature plot that an excessive amount of unmixed coolant ($T_{0\,eff} = 0$) exists at the hub and case, compared to the SILOET target profiles (4.2). Additionally, the total pressure profile illustrates a lack of high moment fluid at the hub and case compared to the respective SILOET target. Both the total temperature and total pressure profiles could be

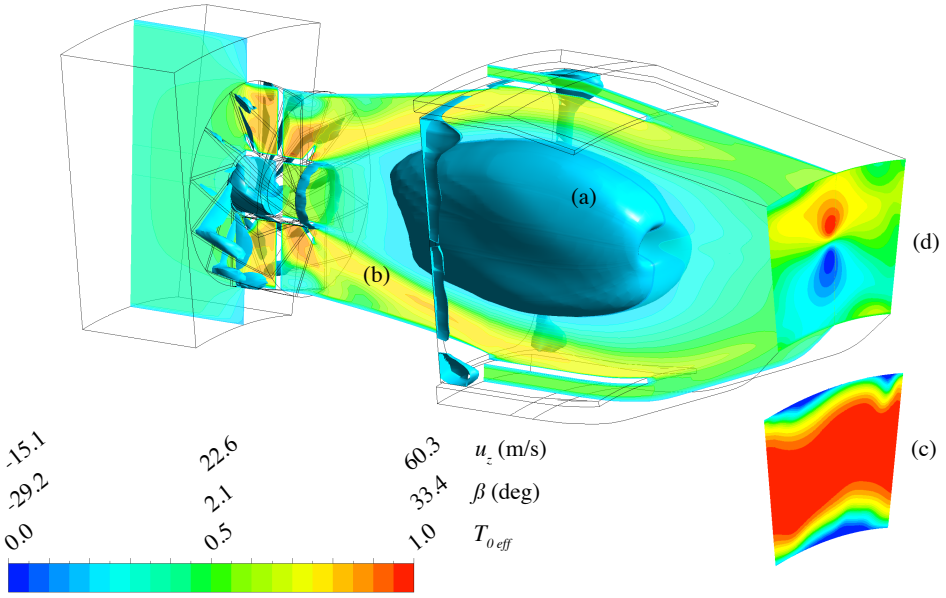


Figure 4.19: Design C2 (domain including swirler) showing (a) the steady recirculation bubble, (b) axial velocity on a meridional plane, (c) the inlet temperature ($T_{0\,eff}$) profile, and (d) the inlet swirl angle (β) profile.

improved by increasing the coolant stream momentum flux, promoting greater mixing and higher total pressure at the hub and case.

The results presented in Figure 4.20 illustrated well-defined swirl and pitch profiles at the inlet plane. These 2D profiles represent a single vortex with a core that is offset slightly in the pitch-wise direction.

Figure 4.21 shows the RTDF profile for designs B, C1 and C2. The RTDF profiles for designs C1 and C2 are characteristic of a lean-burn combustor, with strong temperature gradients at the hub and case. Design B has a more rounded RTDF profile due to greater circumferential non-uniformity. As discussed above, design C2 (and C1) would be improved (with respect to the SILOET targets) by increasing the coolant momentum flux to promote greater mixing between the coolant streams and mainstream.

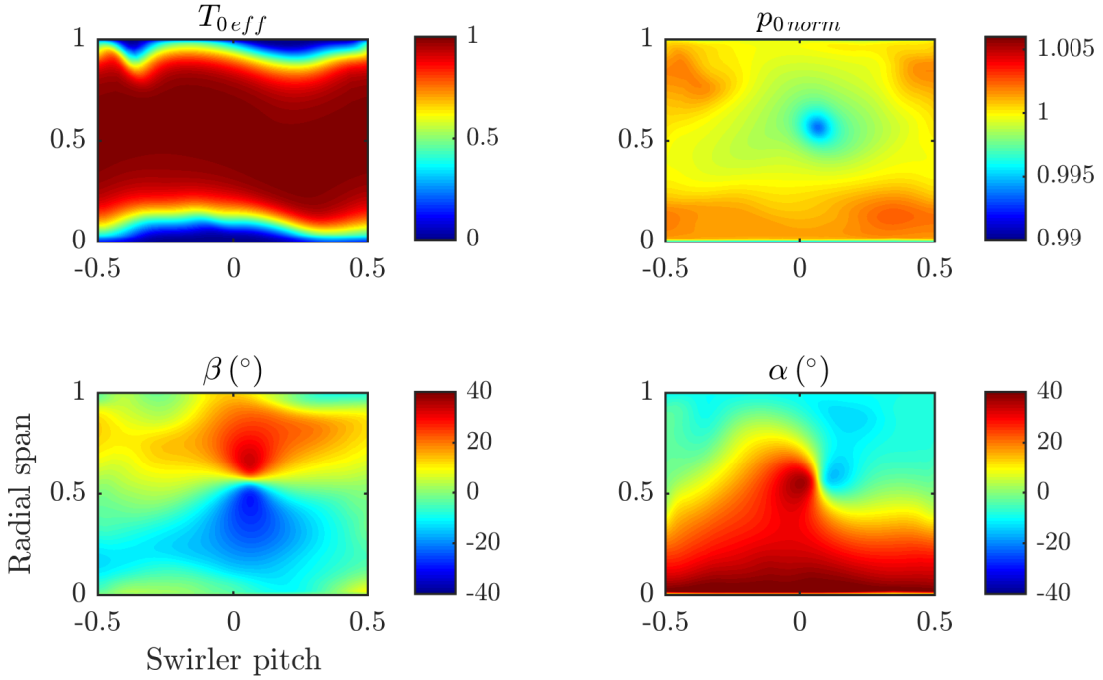


Figure 4.20: Time-resolved URANS results for Design C2.

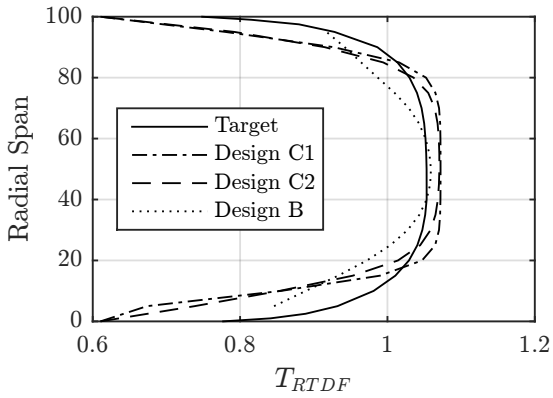


Figure 4.21: Circumferentially-averaged temperature (T_{RTDF}) comparison of Designs C1, C2 and B, and the SILOET target.

4.3.5 Computational design summary

The previous section presented the most relevant cross-section of CFD-based design work that contributed to the development of the OLCS. The design process highlighted the significant complexity involved in designing a combustor simulator to produce a suite of matched inlet profiles, rather than a single matched profile as in

previous work in the OTRF (e.g Hurrion, 2002; Povey and Qureshi, 2008; Qureshi and Povey, 2011). It was observed that the prevailing mainstream flow structure, which was sensitive to a range of factors, had the potential to significantly impact the inlet profiles. In particular, the excitation of a PVC was shown to have the potential to produce excessively unsteady and mixed-out profiles which bore no resemblance to the prescribed target profiles. It was found that methods exist to suppress the PVC excitation to the benefit of the resulting inlet conditions.

Design C2 was considered to be sufficiently capable of achieving the SILOET target profiles, with a clear pathway to refining the hardware to achieve an even closer match. As described above, this would be achieved via the adjustment of the coolant injection slots to increase the coolant momentum flux. Overall, the CFD design process (see also Hall et al., 2013) provided a great deal of insight in to the issues which arise when attempting to simulate swirl stabilised (LPP) combustors in non-reacting turbine facilities.

The mechanical design was based on the concept developed at this point (C2). The combustor simulator was designed and manufactured in a modular system which would allow refinement towards the target profiles based on a combination of further CFD and experimental data from the manufactured hardware. It was necessary to commence the mechanical design at this stage due to research programme scheduling requirements. The mechanical design is discussed in detail in the following section. Additional CFD which encompasses further refinement of the design is presented in Chapter 4.7, which was related to the development of an atmospheric condition test facility for the manufactured hardware (Chapter 5).

4.4 Mechanical design

The OLCS concept developed in the previous section was to be designed and manufactured for use in the engine-scale OTRF (described in Chapter 3.1). The OTRF

is a high pressure, high temperature facility with a design rating of 10 bar (abs) internal pressure and is operated at temperatures above 500 K. The OLCS would need to be designed to comply with these existing operating limits. In addition to the aforementioned operating requirements, the OLCS was intended to be of a modular design which would allow it to be adjusted for use across a range of turbine research programmes with a variety of inlet profiles.

The mechanical design was carried out collaboratively with the assistance of David O'Dell (Mechanical Drafter) and Dr Paul Beard (Postdoctoral Research Assistant), based on the concept described above, and further specifications discussed within this section. Figure 4.22 illustrates the final OLCS as a 3D CAD model which has been assembled to highlight the internal coolant distribution network (note that when correctly assembled, the hub and case networks do not align as shown). The coolant distribution network design is discussed below.

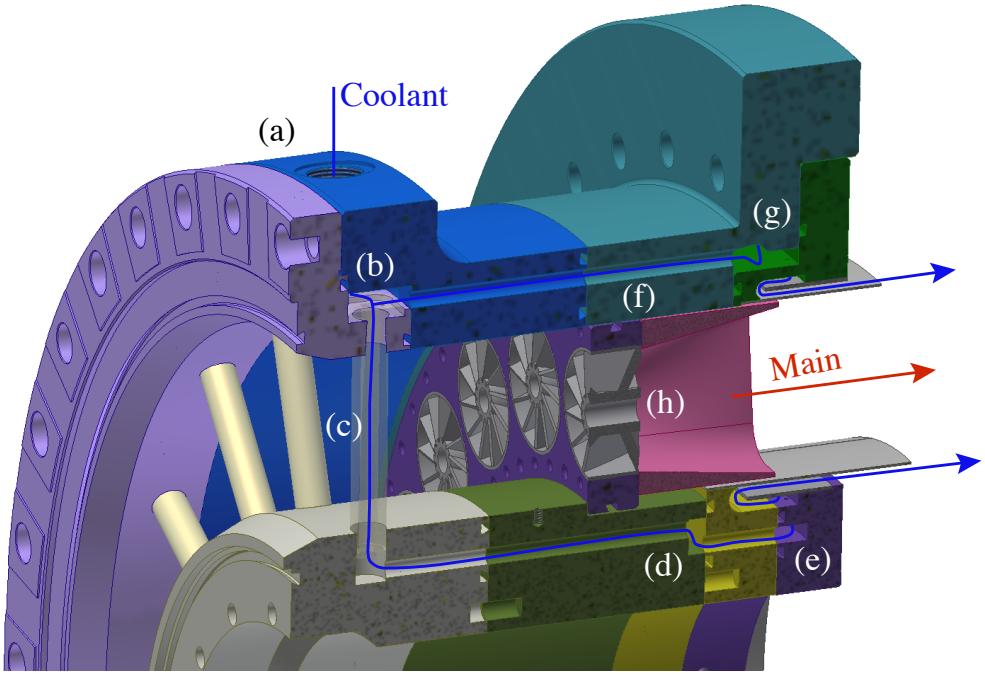


Figure 4.22: CAD model of OLCS hardware showing flow paths and; (a) coolant terminal point, (b) common coolant plenum, (c) hub feed rod, (d) hub coolant feed with intermediate plenum, (e) hub injection plenum, (f) case coolant feed, (g) case injection plenum, and (h) mainstream duct swirler assembly.

Figure 4.22 illustrates the structural ring components which form the annular pressure vessel of the OLCS. Four precision-machined 2014 aluminium alloy (Duralumin) ring components make up each of the hub and case sections of the OLCS. Sealing was achieved using nitrile o-rings, the grooves for which are visible at the component interfaces in Figure 4.22. The critical design detail for the hub and case ring assembly was the fastener design. Providing physical space within the components to accommodate the necessary fasteners (to resist the longitudinal internal pressure load) in addition to the internal coolant distribution network was the driving factor for the component radial wall thickness in all cases. As a result,the components were vastly over-built when considering radial pressure loads (e.g. hoop stress). The task of integrating the fastener and coolant systems in 3D across several components was not trivial and David O'Dell's contribution in this aspect was invaluable. The resulting fastener design is documented below primarily as a record, and secondly to draw attention to the easily overlooked 'worst case' loadings and the resulting design solutions which may be of use to designers of similar systems.

Much of the mechanical CAD modelling and drafting presented in this section was produced by David O'Dell, whose time and assistance were greatly appreciated. Dr Paul Beard's contribution to developing and drafting the final structural components is also acknowledged with thanks.

4.4.1 Coolant distribution system

The OLCS concept required the injection of coolant at the hub and case in order to satisfy the prescribed total temperature and total pressure target profiles. The coolant distribution system was designed to consist of an array of internal passages and plenums to carry the coolant from a common (or set of common) terminal point. The coolant distribution system needed to provide an even distribution in the circumferential sense, while minimising the pressure drop within the internal passages.

The system would also require a mechanism by which the mass flow split between the hub and case could be specified.

The resulting design is shown in 4.22. The coolant distribution design philosophy can be summarised as follows:

- Coolant injected to mainstream duct via an array of sonic holes. This pressure loss dominated the overall total pressure loss. Hub and case hole array flow areas set to achieve desired mass split.
- Annular redistribution plenums (Figure 4.22 (b,e,g)) sized to minimise plenum dynamic head (i.e. maximumise plenum size) relative to plenum exit dynamic head.
- Circular feed passages (Figure 4.22 (c,d,f) shows 1 of 16) sized to keep flow subsonic (Mach < 0.3) and keep internal pressure drop (e.g. (a) to (e)) to less than 10% of total pressure.
- Coolant terminal point (Figure 4.22 (a) shows 1 of 8) sized to keep flow subsonic (Mach < 0.1) in supply pipework.

Dimensions of the resulting system are summarised in Table 4.4

Table 4.4: Summary of OLCS coolant distribution system (c.f Figure 4.22)

Distribution component	**Unit**	**Dimension**
Coolant supply line diameter (a)	mm	25.4
Common plenum sectional area (b)	mm^2	506
Circular passage diameter (c,d,f)	mm	10
Case plenum sectional area (g)	mm^2	~ 400
Hub plenum sectional area (e)	mm^2	180

4.4.2 Fastener design

The OLCS structural components were required to assemble in to a self-contained system and interface with the OTRF at each of the axial extents. The assembly

of the OLCS components was based on internal (fully captive) fasteners which are highlighted across the sub-figures of Figure 4.23. At the upstream and downstream case interfaces, flange connections were used to allow access for assembly. The design process for the hub and case fasteners is discussed below. The design pressure values were:

- Mainstream annulus maximum working pressure of **10 bar absolute**
- Coolant distribution maximum working pressure of **25 bar absolute**

The design of the hub and case assembly fasteners was based on the following assumptions:

- A minimum **Safety Factor (SF) of 5** was required based on a ultimate tensile strength criterion for the fasteners.
- Grade 8.8 metric fasteners (bolts) with a minimum tensile strength (σ_{UTS}) of 800 MPa and minimum yield strength (σ_y) of 640 MPa would be used in all cases.
- The fastener holes in all cases were tapped directly in to the parent hub material— 2014 aluminium— with a tensile strength (σ_{UTS}) of 475 MPa.
- To simplify the analysis, the compressive components were assumed to have zero stiffness - regardless of fastener preload, the entire tensile load was born by the tensile fastener (the bolt).
- The coolant pressure load acted on the entire interface area between each of the adjacent rings (not just the area between the o-ring seals).
- The self weight load of the assembly was insignificant compared to the coolant pressure load.
- The high-pressure (up to 25 bar absolute) coolant was mass flow rate limited and could not pressurise the entire rig to 25 bar in the event of a seal failure.

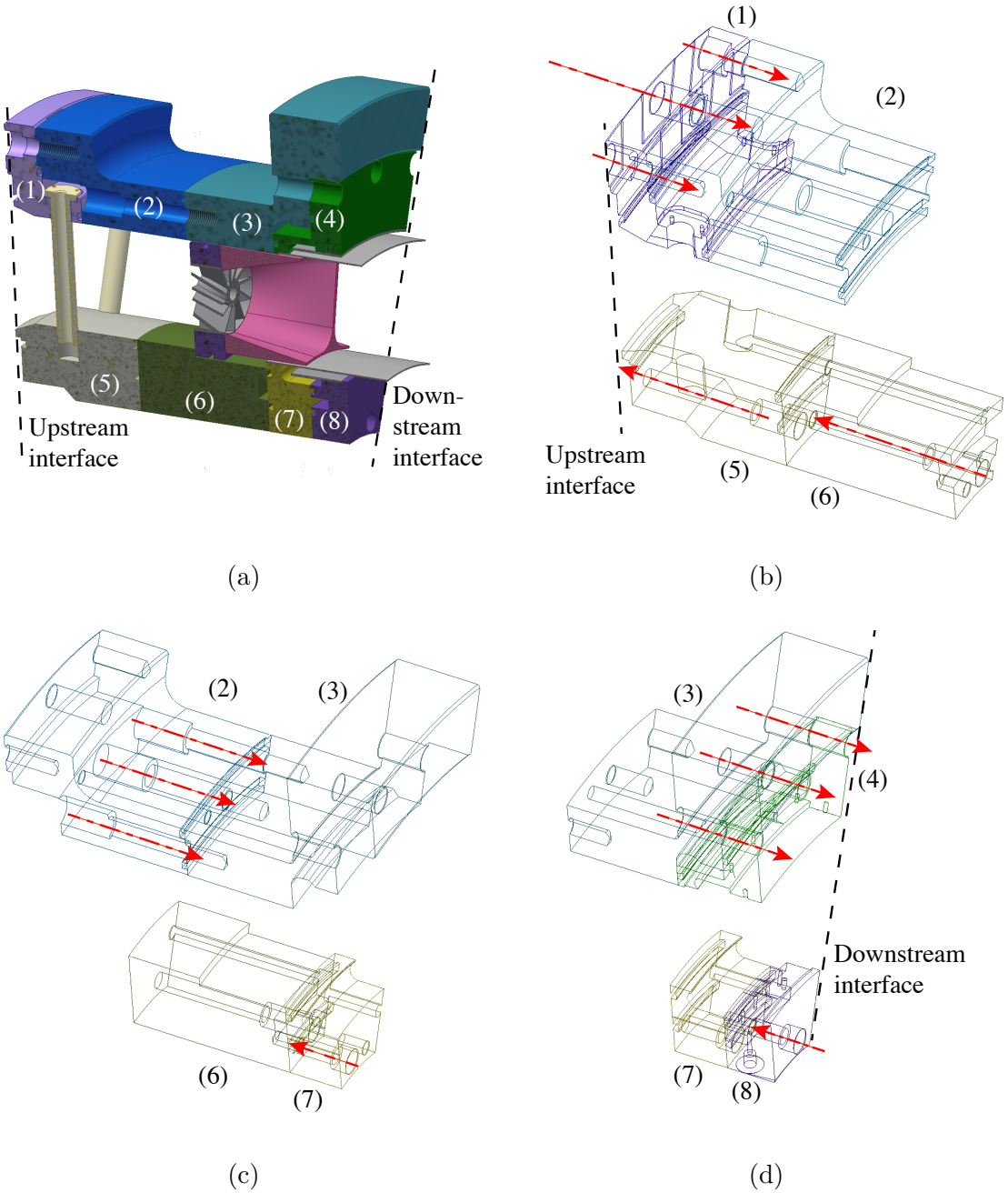


Figure 4.23: 22.5° sector of the OLCS ($1\frac{1}{4}$ swirler pitches). (a) shows the complete assembly; (b) the fasteners used at the upstream interface, and at the 1-2 (case) and 5-6 (hub) interfaces; (c) the fasteners used at the 2-3 (case) and 6-7 (hub) interfaces; (d) the fasteners used at the downstream interface, and 3-4 (case) and 7-8 (hub) interfaces.

- In the event of a seal failure, the mainstream gas (up to 10 bar absolute) could pressurise the entire rig cross section (not just the annular duct) to 10 bar absolute.

Given the nominal metric bolt diameter (D_{nom}) and thread pitch (p), the effective tensile area (A_t) of a bolt is:

$$A_t = \frac{\pi}{4}(D_{nom} - 0.938194\text{p})^2 \tag{4.1}$$

Additionally, the minimum thread engagement length ($L_{e\,min}$) which ensures tensile failure of the bolt (rather than thread) is defined (for differing bolt/hole materials):

$$L_{e\,min} = J\frac{2A_t}{0.5\pi(D_{nom} - 0.64952\text{p})} \tag{4.2}$$

Where the thread engagement ratio (J), which accounts for the difference in material strength between the bolt and hole, is:

$$J = \frac{\sigma_{UTS\,bolt}}{\sigma_{UTS\,hole}} \tag{4.3}$$

4.4.2.1 Hub assembly fasteners

The hub fastener design had two critical functions; firstly to suspend the weight of the hub assembly beginning at the upstream interface; and secondly to resist the pressure load (25 bar absolute) due to the internal coolant distribution network (see Figure 4.22). It is noted that no tensile mechanical connection existed at the downstream hub interface (Figure 4.23d) and as a result there was no tensile load resulting from the pressurised annulus under operating conditions. The entire hub assembly (excluding fasteners and coolant baffles) was manufactured from lightweight 2014 aluminium, meaning that the internal coolant pressure loading was the determining case. The fastener design for the hub components is summarised in Table 4.5.

Table 4.5: Summary of OLCS hub fastener design (cf. Figure 4.23)

Interface	**Fig. ref.**	**Load area** (m^2)	**Load (kN)**	D_{nom}	**No.**	**SF**
Upstream -5	(b)	0.054	135.1	M12	16	8.0
5-6	(b)	0.075	188.1	M12	16	5.7
6-7	(c)	0.065	163.4	M12	16	6.6
7-8	(d)	0.053	133.5	M12	16	8.1

4.4.2.2 Case assembly fasteners

The case structural components (Figure 4.23a (1-4)), as in the case of the hub components were required to resist the self weight loading (insignificant as for the hub) and the pressure load due to the internal coolant network. Additionally, the case structural components formed part of the OTRF pressure vessel which had to resist loading due to an internal pressure of 10 bar absolute. In the event of a seal failure—particularly a leak in to the hub cavity—the entire rig circular cross section could be pressurised to 10 bar absolute; all longitudinal loads were calculated on this basis.

The hub assembly was rigidly connected at the upstream end only, making contact to the downstream components via a seal of effectively zero stiffness. It was assumed therefore that the longitudinal load (due to the internal coolant network) in the hub assembly could not be transmitted to the casing components. The case assembly fastener design is summarised in Table 4.6.

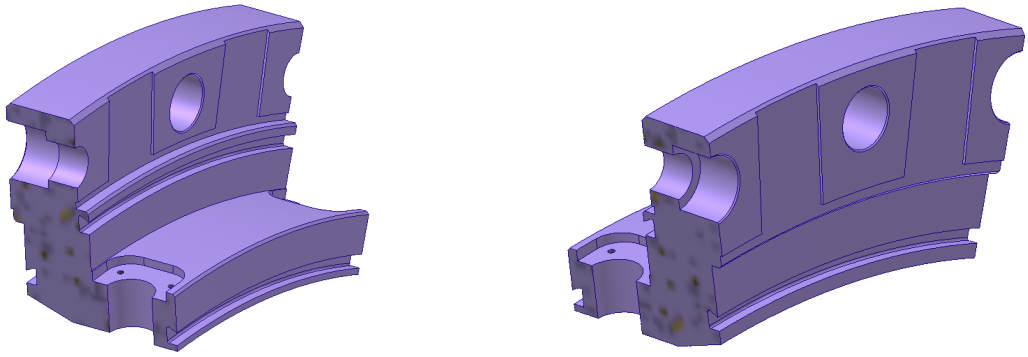
Due to the safety factor in load cases 1 and 3 being close to the design limit specified above, additional measures were taken to mitigate possible over-pressure failure. The contribution of the internal coolant load to the longitudinal load in the casing fasteners was significant. To reduce the loaded area in the event of a seal failure and also to provide venting (therefore reducing the local pressure), case component 1 (see Figure 4.23a) was designed with relief cuts on the mating surfaces. This concept is illustrated in Figure 4.24.

Table 4.6: Summary of OLCS case fastener design (cf. Figure 4.23)

Interface	**Load case**	**Load description (bar abs)**	**Fig. ref.**	**Load area** (m^2)	**Load (kN)**	D_{nom}	**No.**	**SF**
Upstream - 1	1	Mainstream*, 10	(b)	0.50	502.7	M18	16	4.9
1-2	2	Coolant (bench), 2.5	(b)	0.194	48.5	M16	16	41.4
	3	Coolant, 25 Mainstream*, 10	(b)	0.194 0.309	793.5	M16 M18	16 16	5.6
2-3	4	Coolant (bench), 2.5	(c)	0.098	24.6	M16	32	163.1
	5	Coolant, 25 Mainstream*, 10	(c)	0.098 0.309	554.7	M16	32	7.2
3-4-downs.	6	Coolant (bench), 2.5	(d)	0.181	45.3	M18	32	54.3
	7	Coolant, 25 Mainstream*, 10	(d)	0.181 0.309	762.3	M18	32	6.5

4.5 Swirler mechanical design

The OLCS, in contrast the swirl simulator of Qureshi and Povey (2011), was of modular design to allow it to be used for a range of target profiles, and in particular a range of swirl strengths. This was achieved by a system of interchangeable axial swirlers. It was necessary to design a self-contained swirler for each of the two research programmes (SILOET and LEMCOTEC discussed above) considered in this thesis. The aerodynamic design of the swirlers is discussed in Section 4.2.3. The mechanical



(a) (b)

Figure 4.24: Case component 1 (c.f. Figure 4.23a) showing releiving (venting) cuts on (a) the downstream face and (b) the upstream face.

design of the swirlers were driven by two main factors; ease and cost of manufacture, and mechanical strength.

Ease of manufacture was important, since for a high vane count swirler design of which at least 20 units were needed, an excessively complicated design would be proportionately expensive overall. The swirlers were to be designed with a large safety factor on mechanical strength due to their location upstream of relatively delicate aluminium turbine components. Two developments in swirler manufacture for the OLCS are discussed in detail below.

Both variants of swirler discussed below had a hollow hub to allow the introduction of an axial jet. Plugs of 12 mm internal diameter, covered with fine wire mesh were used to control the jet momentum.

The assistance of Dr Igor Dyson in carrying out the destructive testing described below was greatly appreciated.

4.5.1 Mechanical design - fabricated concept

The first iteration of swirler (for the SILOET programme) were of a two-step machined then fabricated (welded) design. This was a direct extension of the design concept used previously in the swirl simulator of Qureshi and Povey (2011). In contrast to the swirlers of Qureshi and Povey (2011), the swirlers for the OLCS were to be modular and interchangeable, being held captive within the simulator by the casing of the swirler (see Figures 4.22 and 4.23a). Additionally, the swirlers were to be of a comparatively high (12 versus 6) vane count, making manufacture more difficult and labour intensive.

In order to minimise cost and simplify the fabrication step, the swirler was designed to consist of 3 components which could all be produced by computer numerical control (CNC) machining and cutting. The swirler was semi-rigid when assembled dry, removing the need for a complicated welding jig. Critically, the swirler was designed such that all welds were applied to exterior points, simplifying the fabrication

considerably. Each swirler consisted of a CNC machined mild steel hub and case, and 12 CNC laser-cut mild steel vanes. The assembly is shown as a 3D CAD model in Figure 4.25.

4.5.1.1 Stress design and testing

The final assembly was inherently stiff due to its interlocking design (see Figure 4.25a). The partial welds at the hub-vane-case intersections served to lock the assembly together and increase the overall stiffness. This fabrication approach and the complex structure that resulted made FEA analysis impractical. To provide certainty around the strength of the design, destructive testing was employed.

A sample of 2 swirlers was produced initially and tested to destruction using an Instron Universal Testing Machine (UTM). One was fabricated by fusing the parent materials (no filler material) and the other was fabricated using filler (which is conventional). The use of filler material meant the swirler casing would require an additional machining step to remove excess weld bead, hence it was of interest to see if any significant difference in strength existed between the two approaches.

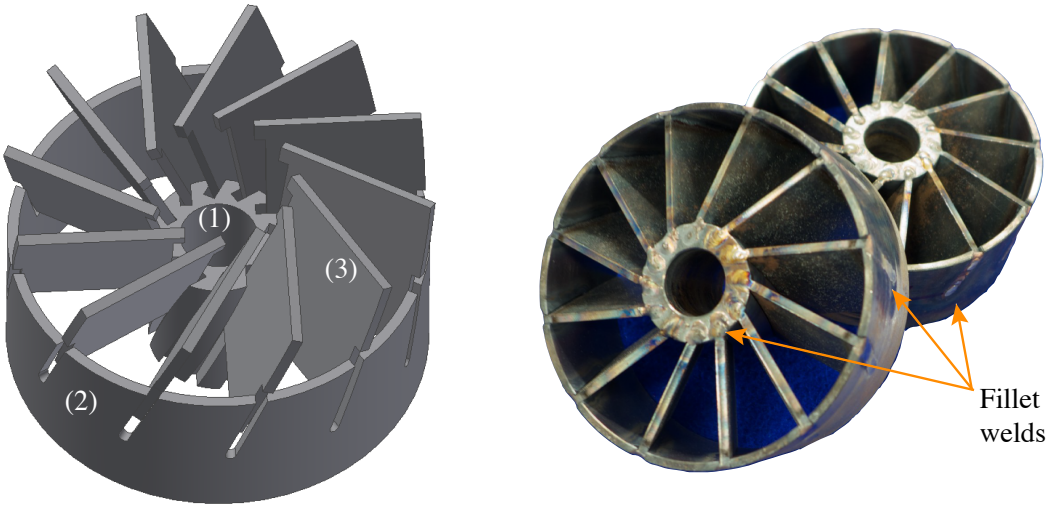


Figure 4.25: Mild steel, machined and fabricated swirler (SILOET) consisting of (1) a CNC machined hub, (2) CNC machined case, and (3) 12 laser-cut flat vanes.

A compression test jig which supported the swirler by the case—as it was to be supported in the OLCS—and allowed loading locally at the swirler hub was manufactured from mild steel (MS). The compression test jig is shown in Figure 4.26. Each specimen was strained (by applying a load at the hub) at a rate of 0.01 mm per second up to a total of 5 mm deflection (which was approximately the limit of the jig). The jig is shown installed in an Instron UTM in Figure 4.26. The resulting load-strain curves and deformed swirlers are shown in Figure 4.27.

It is noted from Figure 4.27 that a significant amount of plastic deformation occurred during the test, however neither sample failed catastrophically in a way which would have endangered the downstream turbine stage. The 'fused' specimen yielded definitively at a load of 20 kN while the 'filled' specimen yielded at around 25 kN. After this yield at 20-25 kN, both specimens returned to a linear load-strain behaviour up until 5 mm of strain. This first yield was likely at the stiff joints around the weld. After this initial yielding it is likely that the relatively flexible vanes were able to deform elastically.

For the extreme case of a 10 bar differential pressure (based on the maximum OTRF working section pressure) across the swirler, the total force would be approximately 4200 N. It is noted that this represents the absolute maximum driving pressure

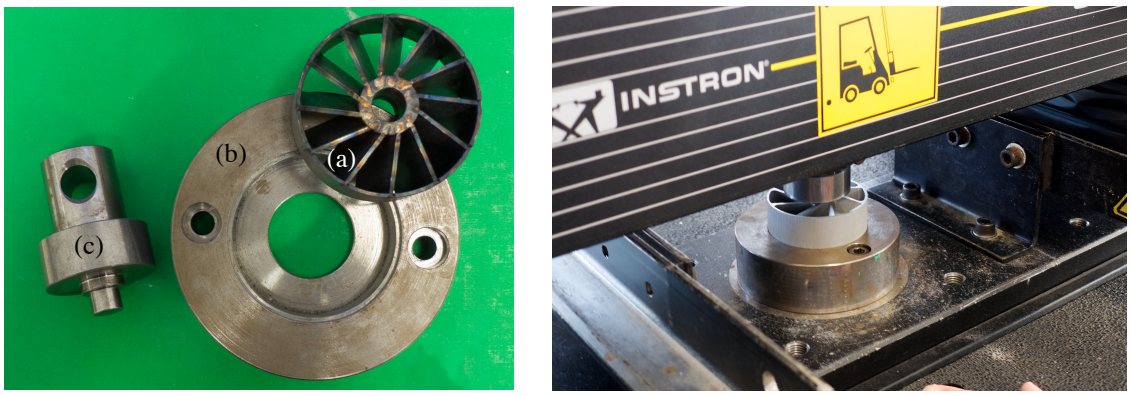


Figure 4.26: (L) Swirler compression load test jig for use in an Instron UTM; the swirler (a) was constrained at the case by (b) which was rigidly attached to the UTM, while the UTM applied a compressive load to the swirler hub using (c). (R) Swirler compression load test jig installed in an Instron UTM.

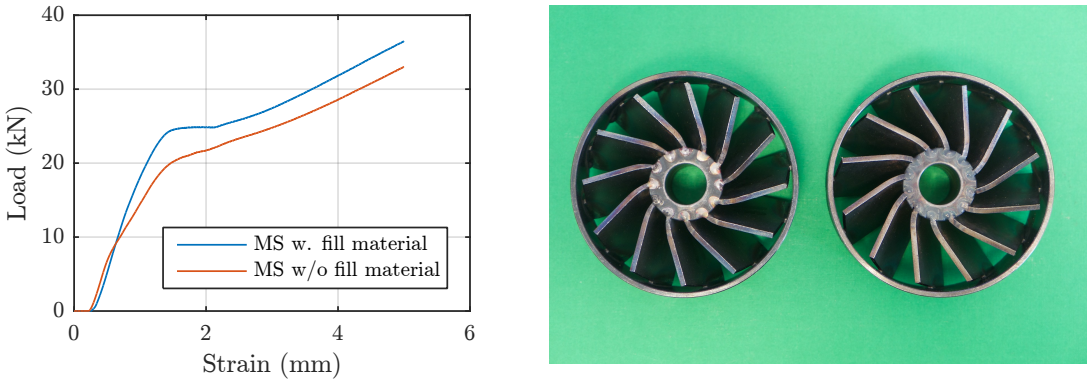


Figure 4.27: (L) Load-strain curve for the sample swirlers fabricated from mild steel; 1 welded with fill material and 1 welded without fill material. (R) Deformed fabricated swirlers (sampled with fill material is left).

difference possible, although a circumstance under which such a load could be born by the swirlers is difficult to conceive in practice. Furthermore, the aerodynamic load on the swirlers under normal operation is insignificant by comparison to this extreme case. On the 4200 N load basis, both specimens exhibited a safety factor of at least 7.8.

4.5.2 Mechanical design - water jet concept

The manufacture of the LEMCOTEC swirlers saw a further iteration of design and manufacturing process. While the swirlers described above were simple to assembly, they required 3 separately precision machined or cut components and finally individual fabrication involving some 36 welds per swirler. Water jet cutting was identified as an ideal process for producing flat vane swirlers in a single step, from a single piece of material. This would also be possible with conventional machining, however it would be prohibitively expensive.

The water jet cutting process is capable only of straight cuts (although these can be in any direction) through the depth of the material. This meant that the swirler passages had to be of lofted profile. The resulting geometry is slightly different to that produced by flat vanes intersecting a cylindrical hub and case, however the

aerodynamic impact would be insignificant. Aluminium 2014 was selected to minimise cutting time compared to mild steel - mild steel being roughly double the cost due to increased machine time. The resulting swirlers are shown in Figure 4.28.

4.5.2.1 Stress design and testing

As in the case of the fabricated swirlers described above, two test specimens were manufactured for destructive testing. In this case the two samples were nominally identical. The test jig was that described in Figure 4.26 (above) and the same Instron UTM was used in the tests. The resulting load-strain curves and deformed swirlers are shown in Figure 4.29.

The specimens performed consistently with both yielding initially at around 18 kN as illustrated in Figure 4.29. The swirlers showed a linear load-strain relationship after the initial yield—as with the fabricated swirlers, likely due to bending of the relatively flexible flat vanes—before finally yielding again at around 31 kN and failing in a brittle mode. The samples agreed very closely through the initial elastic, plastic, and secondary elastic phases.

Based on the same extreme load case described above (with respect to the fabricated swirlers), the swirlers were demonstrated to have a safety factor of at least 7.2. Once again it is noted that the aerodynamic loading under normal operation would be insignificant in comparison to this extreme load case.

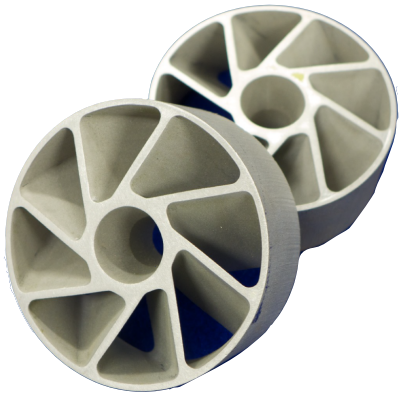


Figure 4.28: Single-piece water jet cut aluminium 2014 swirler (LEMCOTEC).

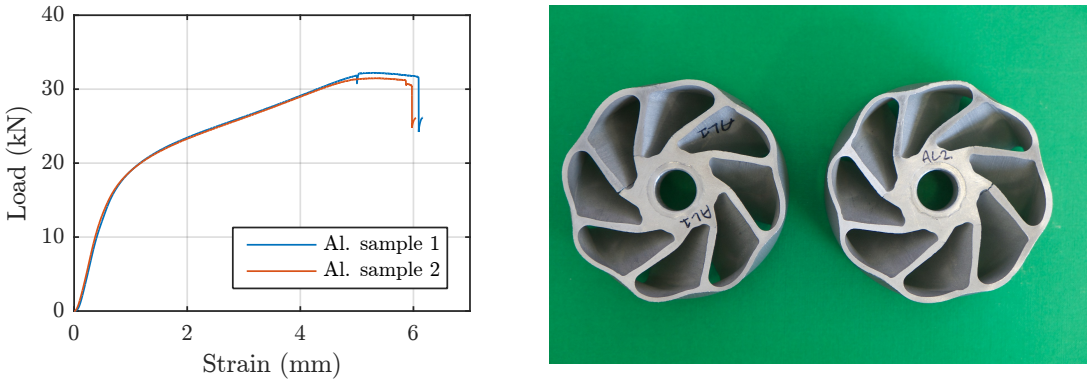


Figure 4.29: (L) Load-strain curve for the sample swirlers (two nominally identical water jet cut aluminium 2014 samples). (R) Deformed water jet cut aluminium 2014 swirlers.

4.6 Turbulence generator for a uniform properties case

OTRF turbine test programmes typically consider a case of 'uniform' inlet conditions in addition to specific combustor profiles. That is, uniform total temperature, total pressure and without residual swirl. To produce meaningful heat transfer results under this uniform test condition, realistic turbulence levels are required. When operated as a plain annular duct (no combustor simulator), the OTRF produces very low turbulence. This led to the installation of circular radial rods upstream of the turbine inlet contraction in early research in the OTRF (Chana et al., 2013). To the same end, it was necessary to design a uniform flow, high turbulence configuration for the OLCS. This configuration for the OLCS was based on replacing the swirler assembly (see Figure 4.22h) with an annular plate designed to generate turbulence. Roach (1987) provided an excellent reference paper on the use of various types of grids for the generation of 'nearly isotropic' turbulence.

4.6.1 Aerodynamic design of turbulence generator

The aerodynamic design process for the turbulence generator initially investigated the use of a perforated plate. Due to difficulty in predicting the resulting turbulence

with the available analytical methods, the perforated plate concept was replaced by a system of square radial rods. These two concepts are described below.

4.6.1.1 Perforate plate concept

Utilising the empirical relationships published by Roach (1987), an initial perforated plate concept was investigated. An example case of a 3 mm thick perforated plate situated in the OLCS mainstream duct (although ignoring the downstream contraction) is described for a range of relative total pressure drops (across the plate) in Figure 4.30 (left plot) - the results are given downstream at the vane inlet (ignoring the contraction). Roach (1987) stipulated that the ratio of effective mesh length (which is proportional to hole diameter and spacing) must be small compared to the minimum duct dimension (<< 10%) - the radial height for an annular duct. Where this is not the case, the duct walls do not allow the growth of turbulent length scales otherwise implied by the mesh length, and the empirical models are not valid.

The dotted curve segments in Figure 4.30 indicate that the mesh length to duct height ratio is greater than 10% and therefore the results were likely not physically realisable. The figure illustrates that for a modest pressure loss (e.g. 3.25%), it was

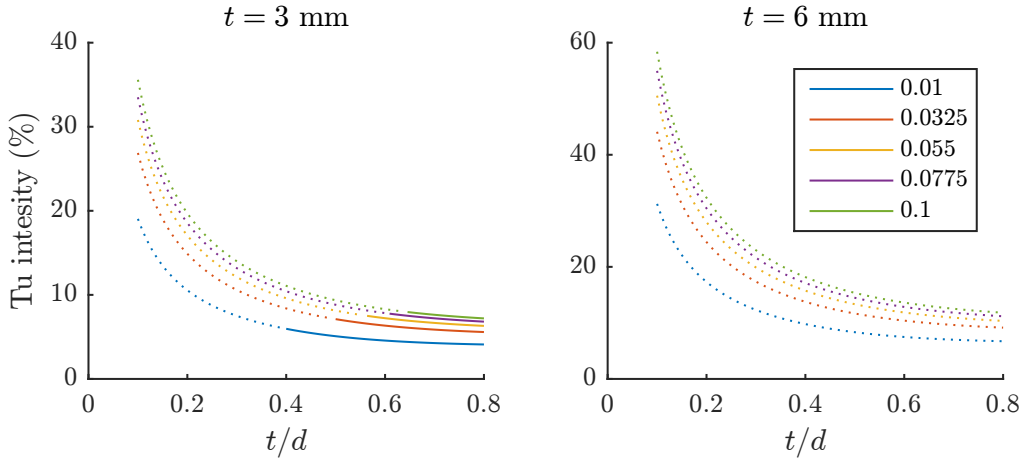


Figure 4.30: Estimate of turbulence quantities for a perforated plate (thickness, $t = 3$ mm) within the OLCS mainstream duct for varying total pressure loss ratio ($\frac{\Delta p_0}{p_0} =$ 0.01 to 0.1). d is the perforation (hole) diameter. The dotted curve segments are probably not physically realisable.

not possible to confidently design a plate to produce isotropic turbulence exceeding 7% intensity (for $t/d = 0.5$) and the gains for increasing the pressure loss were marginal (8% intensity for 10% pressure loss and $t/d = 0.65$). To compound the uncertainty, Figure 4.30 does not consider the effect of the 2:1 inlet contraction, which would be expected to reduce the turbulence intensity by at least a factor of 2 (based on the increase in axial velocity alone). Finally, considering the ultra-conservative structural requirements for components upstream of the turbine (recalling the swirler design above), a plate much thicker than 3 mm would be required. For a 6 mm plate and appropriately scaled perforations, no realisable results exist (see Figure 4.30 (right plot)).

4.6.1.2 Radial rod concept

Based on the above analysis, it was decided that a perforated plate could not be designed with adequate certainty to produce medium to high turbulence when considering the OTRF duct geometry, and in particular the turbine inlet contraction. In light of this, an alternative based on the circular radial rods for which there was relevant experience in the OTRF (and critically, experimental data) was examined. The radial rods previously implemented in the OTRF were measured to produce approximately 6% turbulence intensity near the vane inlet. In addition to the advantage of existing experimental data as a reliable point of reference, a system of radial rods or bars could be relatively easily modelled using CFD—radial rods being very easily meshed compared to a perforated plate—which could be used to provide additional confidence in the design.

A design based on square bars was modelled using CFD (URANS). Square rods were selected primarily for ease of manufacture (easily laser or water jet cut from plate stock), and would also provide performance relatively insensitive to Reynolds number compared to circular rods. A rod count of 40 was chosen based on the vane count of 40. The concept is illustrated as a 3D CAD model in Figure 4.31. The URANS

simulation was carried out at OTRF conditions (described earlier in this section) using the same methodology described in Section 4.3.1.2 with the exception of the turbulence model, with the k-ω SST model being used in this case. Additionally, a periodic sector of 45° was necessary given the upstream coolant rod count of 16 and the square rod count of 40. The computational mesh is shown in Figure 4.32. In addition to the square rods for turbulence generation, the domain also included upstream radial coolant distribution rods which were part of the OTRF and OLCS systems.

A time-resolve solution is illustrated in Figure 4.33. Regions of high turbulence intensity are visible in the rod wakes, with relatively uniform intensity prevailing at the inlet plane with a mass-weighted average of approximately 9%.

4.6.2 Mechanical design

A mechanical design of the square rod turbulence generator was developed, consisting of 40 12 mm (wide) x 20 mm (axial depth) rods joined by a common web at the

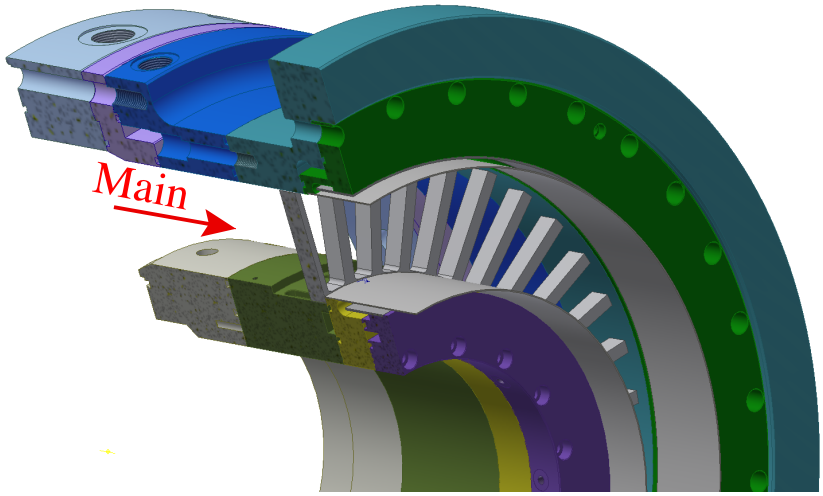


Figure 4.31: OLCS showing square radial rod turbulence generator concept. Rod count of 40.

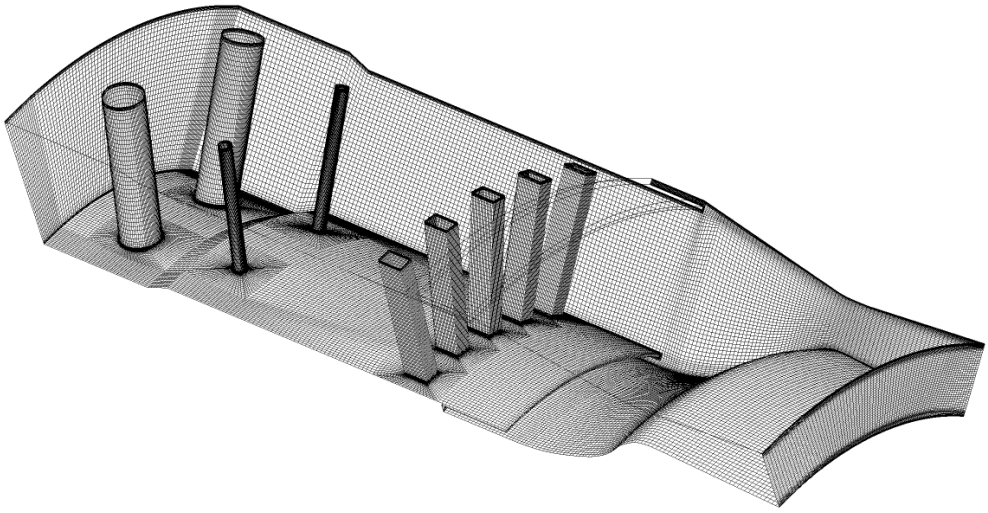


Figure 4.32: Hexahedral wall-resolved mesh used for square rod turbulence generator simulation.

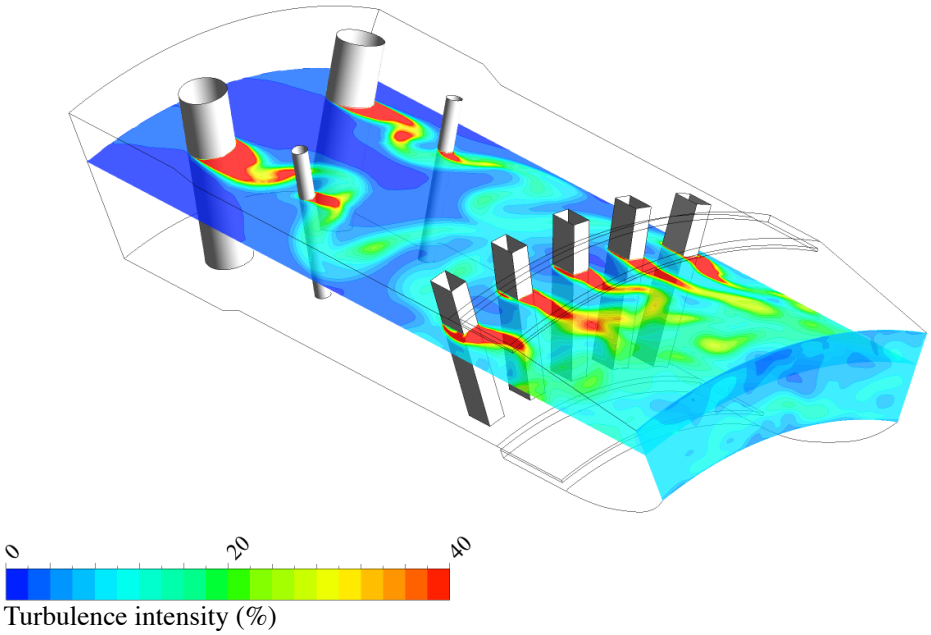


Figure 4.33: URANS solution of square rod turbulence generator showing turbulence intensity on a surface of constant radius (0.28 m) and at the inlet plane. Turbulence intensity is based on the local velocity.

hub. This was to be manufactured by water jet cutting from Aluminium 6082-T6 plate (yield stress of 240 MPa). Finite element analysis was carried out on a periodic sector (which included a key-way) of the turbulence generator using Autodesk Simulation. An extremely conservative loading case of 10 bar differential pressure across the plate was examined, with the plate constrained on the downstream side, at the hub web. The results are shown in Figure 4.34. Critically, for this extremely conservative (high) loading case, yielding occurs only in limited regions under compression. The aerodynamic load under steady conditions would be significantly lower (approximately 2 orders of magnitude) than this extreme case. The manufactured turbulence generator, which could be installed in the OLCS, is shown photographically in Figure 4.28.

4.7 Extended computational study of the OLCS

The previous chapter focused on the development of a combustor simulator (the OLCS) for recreating swirl-stabilised lean-burn combustor flows in the OTRF. Significant progress (from the first similar concept of Qureshi and Povey (2011)) in terms

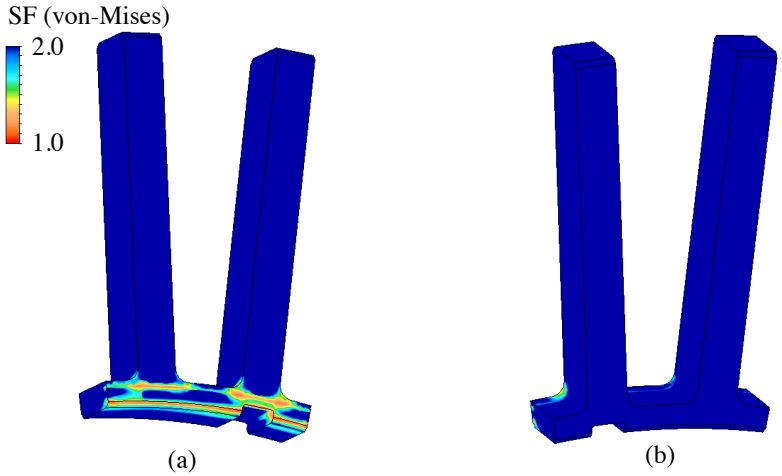


Figure 4.34: Turbulence generator FEA results for a 10 bar pressure differential. Yielding occurs only in small compressive regions. (a) downstream side - restrained at hub web; and (b) upstream side - loaded on upstream surfaces.

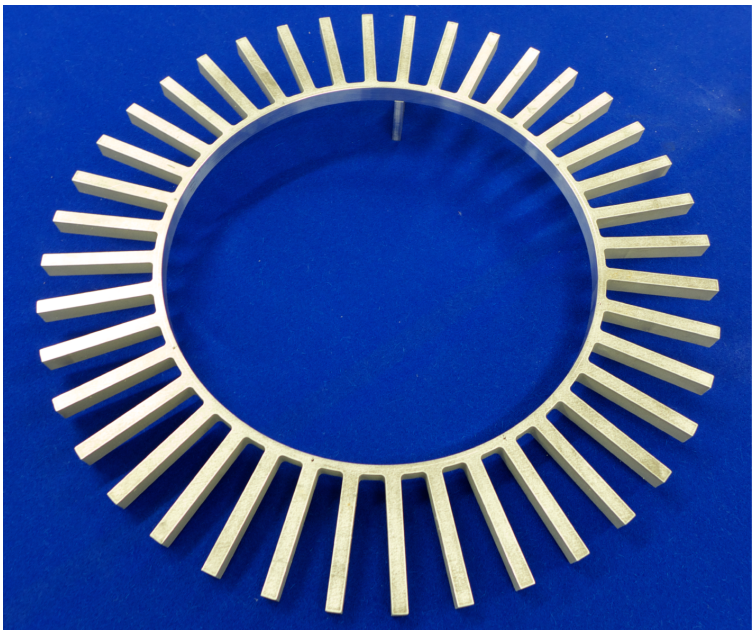


Figure 4.35: Turbulence generator manufactured from Aluminium 6082-T6 - water jet cut profile with machined inner diameter for accurate fit.

of understanding the unsteady 3D flow field was made, and significant challenges relating to flow structure were addressed. It was necessary to progress the manufacture of the OLCS at the conclusion of the initial CFD study (December 2012) due to schedule requirements.

One purpose of the work presented in this chapter was to extend the body of CFD simulations to the 'as built' hardware on a comprehensive computational domain. This included an additional modification to the coolant injection slots to increase the stream mixing and endwall total pressure - a deficiency identified in the previous chapter. The second purpose of this work was to examine the sensitivity of the OLCS performance—particularly the mainstream flow structure—to operating conditions. This was of critical interest as the experimental characterisation of the OLCS (described in Chapter 5 with results in Chapter 6) was—by necessity—carried out at reduced temperature and pressure with respect to the OTRF. Finally, the side-by-side simulations at atmospheric and OTRF conditions provided a link by which to understand and compare the two operating conditions, as well as high resolution 3D data to compliment the experimental data.

It is noted that while such analysis was carried out in advance of the atmospheric experiments, time constraints meant that this was limited to the simplified domain case described in the previous chapter (see Figure 4.10). This was carried out at the nominal configuration with axial jet, the significance of which becomes clear below. The more rigorous cases presented herein were run in parallel to the experimental campaign.

4.7.1 Comparison of experimental conditions

The experimental characterisation of the OLCS presented in this thesis was conducted at atmospheric conditions - approximately ambient operating pressure and near-ambient stream temperatures. This experimental characterisation was carried out as a means to ensure suitable profiles were produced prior to installation in the OTRF, where operating costs and scheduling become critical. Operating the OLCS outside of the OTRF also allowed longer run time (albeit at altered conditions) and ease of access for measurements and inlet plane traverse measurements. The associated experimental set up is described in detail in Chapter 5.

The reduction in operating pressure meant that it was not possible to simultaneously match Reynolds number and Mach number to that of the OTRF tests. Additionally, at reduced back-pressure, a significant mass flow rate of air would be required to match Reynolds number alone, which would have significantly limited run time based on available compressed air. A mass flow rate which allowed suitable continuous run time (approximately 10 minutes) was selected. It was the case that Mach number was approximately matched for the selected mass flow rate, and was subsonic upstream of the vanes in both cases. While Reynolds number was not matched to the OTRF, it was possible to achieve a similar order of magnitude. Additionally, the temperature difference achievable in the atmospheric test was limited to approximately 10-15 K.

Table 4.7: Summary of operating conditions

Property	Units	SILOET		LEMCOTEC	
		OTRF	**ATM**	**OTRF**	**ATM**
p_{rig}	Bar abs	5.54	1.0	8.50	1.0
$\dot{m}_{Tot}$	kg/s	15.0	2.0	23.0	3.0
x		0.12	0.10	0.23	0.18
$T_{0\,h}$	K	500	285	530.6	285
$T_{0\,c}$	K	290	275	290	275
$\mathrm{Re_{Sw}}$	($\times 10^5$)	5.6	1.5	7.3	1.1
$\mathrm{M_{Sw}}$		0.12	0.07	0.11	0.06

4.7.1.1 Summary of operating conditions

The operating conditions are summarised in Table 4.7.

4.7.1.2 Summary of test cases

The examined cases are summarised in Table 4.8. Each case was simulated at both OTRF and atmospheric conditions (see Table 4.7). The two SILOET cases with and without swirler axial jets were investigated in an attempt to measure whether such jets altered the flow structure, particularly the formation or suppression of a PVC. A single LEMCOTEC case was examined. For both the SILOET and LEMCOTEC families of tests, the target profiles are presented and discussed in Chapter 4.

Table 4.8: Summary of CFD comparison cases for atmospheric and OTRF conditions

Case		**Swirler ψ** (°)	**Swirler included**	**Swirler diffuser length** (mm)	**Swirler exit to NGV** (mm)	**Axial jet**	**Coolant slot trailing edge offset** (case, hub, mm)
A	SIL.	20	Yes	80	232	Yes	20, 40
B	SIL.	20	Yes	80	232	No	20, 41
C	LEM.	35	Yes	80	217	No	0

4.7.1.3 Computational method

The computational method was based on that described in Chapter 4; URANS with the Reynolds Stress model was implemented on hexahedral meshes in the ANSYS

Fluent solver. The pressure based solver with SIMPLE pressure-velocity coupling was used. Discretisation was of second order in time and space.

The computational domain was extended downstream to include an exit diffuser. This same diffuser geometry was used in the atmospheric experiment set up (see Chapter 5), although differed from the OTRF geometry, and as before the vanes were excluded. In both cases, however, it extended the outlet boundary condition far beyond the region of interest. A non-reflecting outlet boundary was also used. The extension of the downstream domain and non-reflecting boundary condition are both good practice, however didn't appear to affect the solutions. The domain was extended to include features of the upstream duct, although it is noted that the additional computational expense was probably not warranted - the downstream flow field is dominated by the acceleration, turning and turbulence generation of the swirler.

The domain was discretised in three separate zones with a non-conformal interface upstream and downstream of the swirler. Splitting the domain in this way allowed the best possible mesh quality in each zone at the expense of interpolation error at the interfaces. This compromise was preferred to reduced mesh quality throughout (and extreme difficulty in terms of blocking topology creation) resulting from the relatively complex swirler geometry.

4.7.2 Computational results - SILOET

4.7.2.1 Case A - SILOET with axial jet

Case A considered the configuration to achieve the SILOET targets, *with* the axial jet at the swirler hub. The time-resolved solution at atmospheric conditions ('AA') is presented in Figure 4.36 while the counterpart case at OTRF conditions ('AO') is shown in Figure 4.37. As demonstrated in the previous chapter, the introduction of a low-momentum axial jet at the swirler hub was predicted by the simulation to suppress the formation of a PVC, leaving a quasi-steady, bubble-shaped central recirculation zone (CRZ). In case A, agreement between the atmospheric and OTRF conditions

was profound. A similar set of simulations on a simpler domain (see Figure 4.10) which showed the same similarity (between conditions in the presence of an axial jet) was a key justification for the development of the atmospheric experiment.

4.7.2.2 Case B - SILOET without axial jet

Case B considered the configuration to achieve the SILOET targets, *without* the axial jet at the swirler hub. The time-resolved solution at atmospheric conditions ('BA') is presented in Figure 4.38 while the counterpart case at OTRF conditions ('BO') is shown in Figure 4.39. As predicted by earlier simulations, the flow field was characterised by a PVC, circumscribing a CRZ. While the flow field was superficially similar between BA and BO, it was not completely independent of operating conditions. The form of both the PVC and CRZ differed, both having a larger volume at OTRF conditions. This change in flow structure had the effect of reducing the peak inlet swirl and altering the 2D temperature profile slightly.

4.8 Computational results - LEMCOTEC

4.8.0.1 Case C - LEMCOTEC without axial jet

Case C considered the configuration to achieve the LEMCOTEC targets, *without* the axial jet at the swirler hub. The time-resolved solution at atmospheric conditions ('CA') is presented in Figure 4.40 while the counterpart case at OTRF conditions ('CO') is shown in Figure 4.41. The two simulations show very similar flow structures, particularly in terms of the mainstream CRZ and meridional plane axial velocity distribution. This similarity of mainstream flow structure results in a close similarity of the inlet profiles (Figures 4.40, 4.41 c and d). The URANS flow field was relatively steady in both cases, as indicated by the similarity of the two time-resolved solutions which were taken at arbitrary points in flow time. No PVC was present in the case C simulations, with the main difference from case B simulations being higher swirler vane angle (ψ) and therefore upstream swirl number (S).

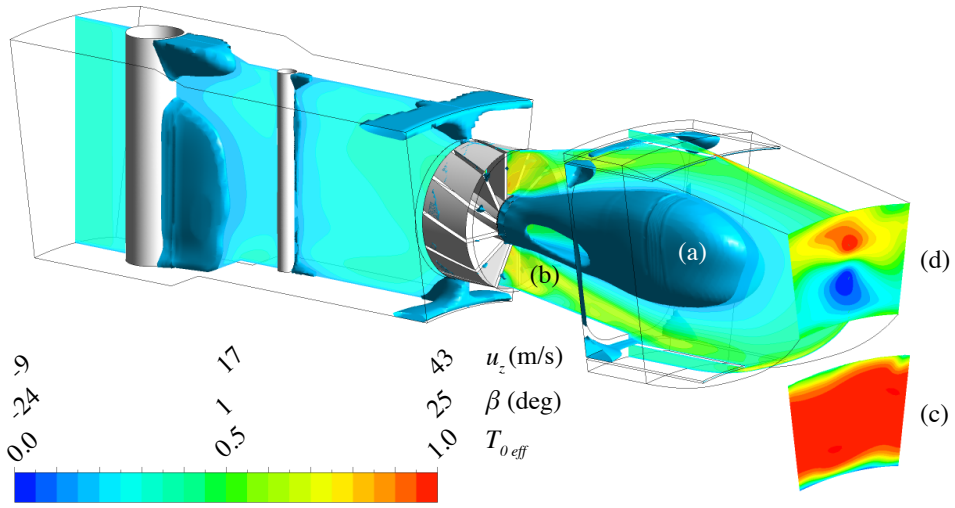


Figure 4.36: Case A - atmospheric (AA). Time-resolved URANS results of the OLCS (SILOET config.) at atmospheric experiment conditions with axial jet showing (a) the recirculation zone; (b) the axial velocity on a meridional plane; (c) the inlet total temperature ($T_{0\,eff}$); and (d) the inlet swirl angle (β).

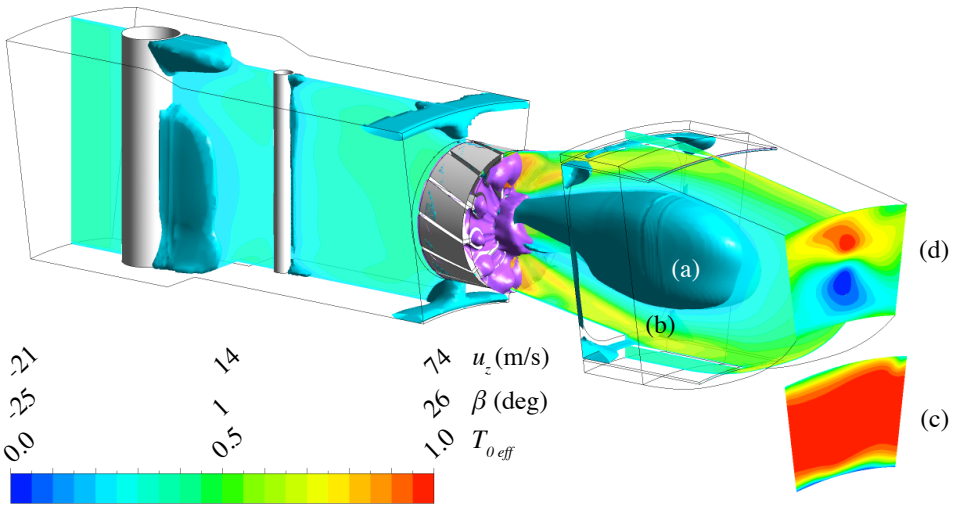


Figure 4.37: Case A - OTRF (AO). Time-resolved URANS results of the OLCS (SILOET config.) at OTRF conditions with axial jet showing (a) the recirculation zone; (b) the axial velocity on a meridional plane; (c) the inlet total temperature ($T_{0\,eff}$); and (d) the inlet swirl angle (β).

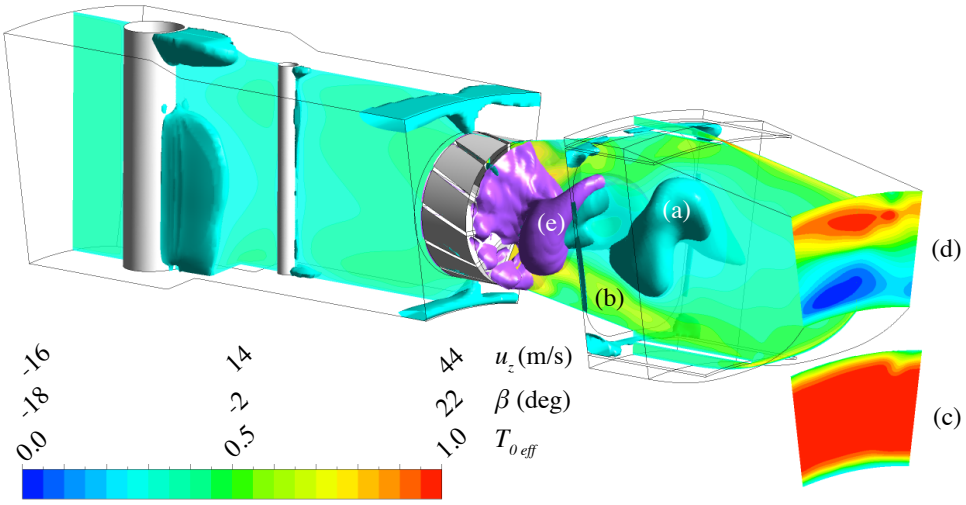


Figure 4.38: Case B - atmospheric (BA). Time-resolved URANS results of the OLCS (SILOET config.) at atmospheric experiment conditions without axial jet showing (a) the recirculation zone; (b) the axial velocity (u_z) on a meridional plane; (c) the inlet total temperature ($T_{0\,eff}$); (d) the inlet swirl angle (β); and (e) the PVC as an isosurface of static pressure.

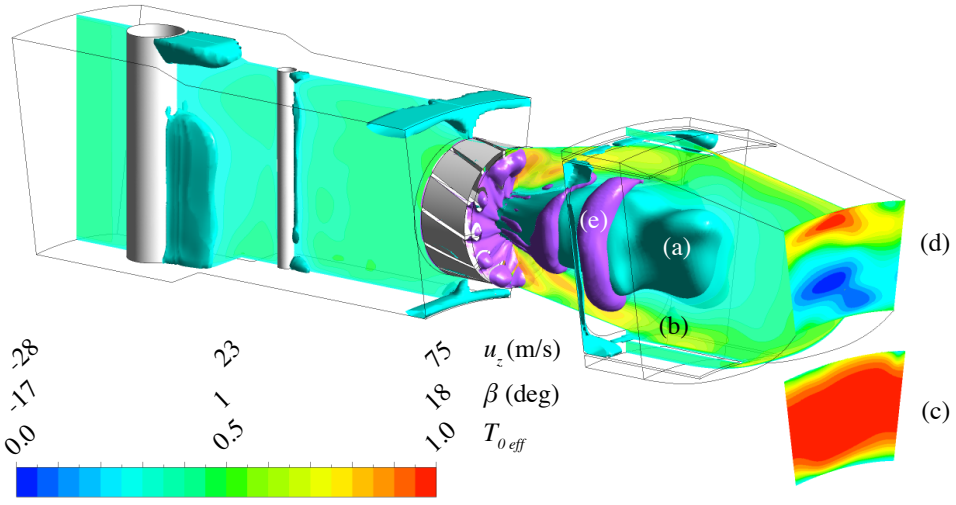


Figure 4.39: Case B - OTRF (BO). Time-resolved URANS results of the OLCS (SILOET config.) at OTRF conditions without axial jet showing (a) the recirculation zone; (b) the axial velocity (u_z) on a meridional plane; (c) the inlet total temperature ($T_{0\,eff}$); (d) the inlet swirl angle (β); and (e) the PVC as an isosurface of static pressure.

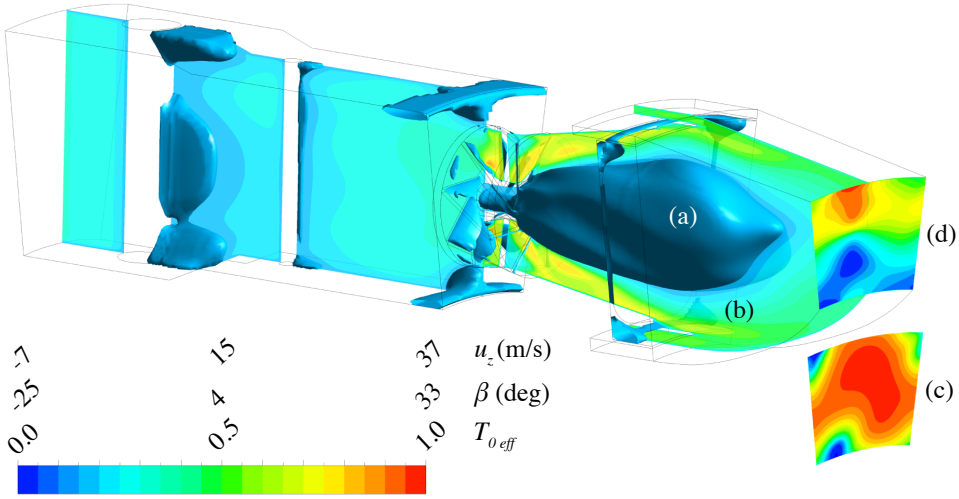


Figure 4.40: Case C - atmospheric (CA). Time-resolved URANS results of the OLCS (LEMCOTEC config.) at atmospheric experiment conditions without axial jet showing (a) the recirculation zone; (b) the axial velocity (u_z) on a meridional plane; (c) the inlet total temperature ($T_{0\,eff}$); and (d) the inlet swirl angle (β).

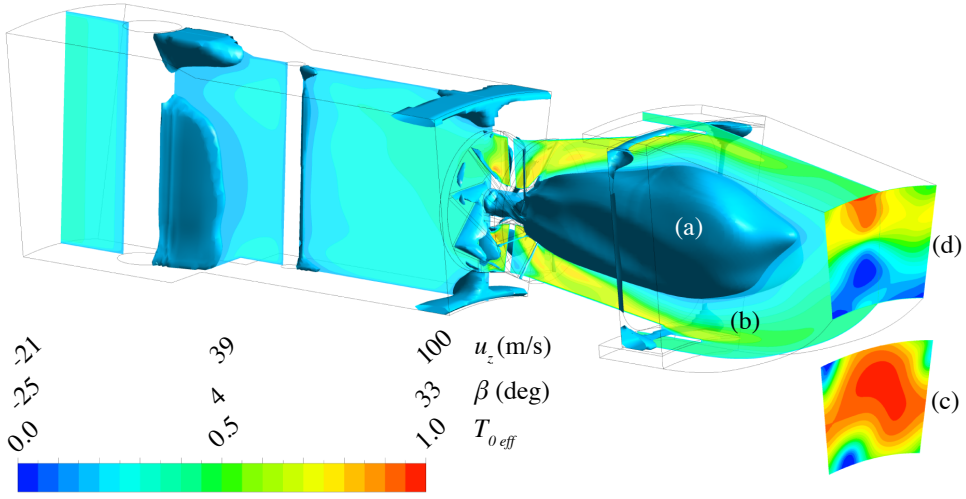


Figure 4.41: Case C - OTRF (CO). Time-resolved URANS results of the OLCS (LEMCOTEC config.) at OTRF conditions without axial jet showing (a) the recirculation zone; (b) the axial velocity (u_z) on a meridional plane; (c) the inlet total temperature ($T_{0\,eff}$); and (d) the inlet swirl angle (β).

4.8.1 Discussion

The results for the SILOET cases (A and B) highlighted a number of important issues. Firstly, as had been predicted prior to the development of the atmospheric experiment, the stabilised case with the axial jet (case A) was predicted to be insensitive to operating conditions (specifically, the mainstream Reynolds number). The simulations for case B predicted that this was not also the case for a mainstream flow structure characterised by the presence of a PVC - that is, the PVC and CRZ were sensitive to Reynolds number.

The results for simulations BA and BO are of obvious importance, since they undermine the incumbent assumption that the experimental characterisation at atmospheric conditions would be universally similar. Reynolds number appears to have a profound effect on the structure of the PVC (where present) and the associated flow features (i.e. the CRZ). The AA and AO cases, while agreeing with each other across the flow field, were also in reasonable agreement with BA at the inlet plane. Agreement with and without the axial jet was also observed in the experimental tests (at atmospheric conditions), which are discussed in detail in Chapter 6.

The result for the LEMCOTEC case (C) demonstrated agreement between the two sets of operating conditions. This was consistent with results of case A in that for a flow field without a PVC, the structure was insensitive to operating conditions (in particular Reynolds number). It is noted that case C did not require any active measures to avoid PVC formation - the simulations predicted the absence of PVCs in both cases without an axial jet.

The CFD study presented in this chapter highlights the variability of flow structure for swirling flows and the role of common features (CRZ and PVC) in this. Since, as noted by Kempf et al. (2008), there is no general criteria for predicting the form of such features, detailed CFD is an important tool in understanding and predicting the performance of systems like the OLCS. While this study did not cover

sufficient operating points to provide generalised guidance, it highlights that care must be taken when attempting to design (by way of pilot experiments) or validate combustor simulators at off-design conditions, and that scaling results from one system to another (without case-specific simulations) would carry significant uncertainty.

4.9 Conclusions

The development of the lean-burn combustor simulator—the OLCS—for the OTRF focused on a CFD-based design study. The study examined a range of designs, with the current chapter presenting a selection of simulations which demonstrated the key design issues. The study highlighted that for high Reynolds number, non-reacting swirling flows, a PVC may form, causing excessive mixing and poorly-match (with respect to targets) inlet profiles. The literature suggested the PVC phenomenon was often suppressed by combustion. A method (a low-momentum axial jet) was developed to suppress the PVC, facilitating good agreement with target profiles.

Generally, it was found that the sensitivity of swirling flow structure (to swirl number, Reynolds number, combustion and geometry) when considering vortex breakdown and PVCs represents the central challenge in the design of lean-burn combustor simulators. For the same geometry combustion has been shown (Oberleithner et al., 2013) to alter swirling flow structure by suppressing PVC formation; it also releases heat, axially accelerating the flow and reducing the downstream swirl number. This axial acceleration means that both upstream and downstream swirl number cannot be simultaneously matched between engine and simulator. Flow similarity between reacting and non-reacting flows is therefore precluded in a number of ways. Understanding the target combustor flow in three dimensions would certainly aid simulator design.

A system capable of achieving a good match to the (SILOET) target inlet profiles was then developed in to a mechanical system for the OTRF. The system

was modularised to allow adjustment in aid of achieving the current target profiles (in the case that experimental data proved to be poorly matched) and also further profiles for future research programmes.

Chapter 5

Development of a facility for the experimental characterisation of the OLCS

An experiment for the characterisation of the OLCS at atmospheric test conditions was designed. This was to allow detailed characterisation of the system and inlet profiles, and if necessary, adjustment of the design prior to use in OTRF experiments. Specifically, it also meant that high resolution measurements of inlet profiles were possible – these are presented in Chapter 6. Due to the inherently complex nature of a high pressure, rotating facility like the OTRF, access for high resolution probe traverses is both difficult and restricted. Previous experimental campaigns in the facility have measured turbine inlet profiles using separate rakes for total temperature, total pressure and flow angles, achieving relatively sparse resolution.

In past OTRF programmes only relatively sparse profiles were available from rig measurements. In the work of Qureshi and Povey (2011) in particular, these were suitable for validation of a more complete data set (e.g. from CFD or a pilot experiment), but provided poor characterisation of the turbine inlet conditions by themselves. While improvement of measurements in the OTRF would be sought, the collection of an additional set of data outside of the OTRF was carried out as a contingency.

This chapter discusses the design and construction of an experimental characterisation facility which operated outside of the OTRF, at atmospheric pressure. The

flow parameters of the test are presented and compared to OTRF conditions in Chapter 4.7 where the impact of the unmatched conditions was examined using unsteady CFD simulations. The supporting hardware is described in this chapter, including instrumentation, while the OLCS is described in detail in Chapter 4. Experimental results are presented in Chapter 6.

5.1 Overview of facility

The experimental facility shown in Figure 5.1 consisted of the full-scale annular OLCS hardware mounted upright (machine (z) axis vertical) on a test stand which doubled as a feed plenum. The OLCS was supplied with air by a high pressure air metering and feed system which was capable of producing two streams of different temperatures. An exit duct was appended to the downstream end of the OLCS to reproduce the turbine inlet contraction profile and an exit diffuser. This collective system was instrumented extensively for steady pressure and temperature measurements, including a two-axis inlet traverse system. This supporting infrastructure is described in detail in the following sections.

5.2 OLCS test section

The OLCS hardware was used directly in the experimental characterisation experiment. Utilising the complete annular hardware removed any uncertainty over periodicity which would have been present in a simpler sector-based pilot experiment. It was necessary to manufacture a manifold system for the mainstream duct and also hardware to reproduce the turbine inlet duct - these are shown in Figure 5.2 (b) and (c). A two-axis traverse system (Figure 5.2d) was also designed and manufactured for semi-automated measurements of properties on 2D planes at the inlet plane and at the geometric throat of the exit duct.

A precision-ground steel base plate (20 mm thickness) served both as the main structural component of the test stand, providing the necessary stiffness for

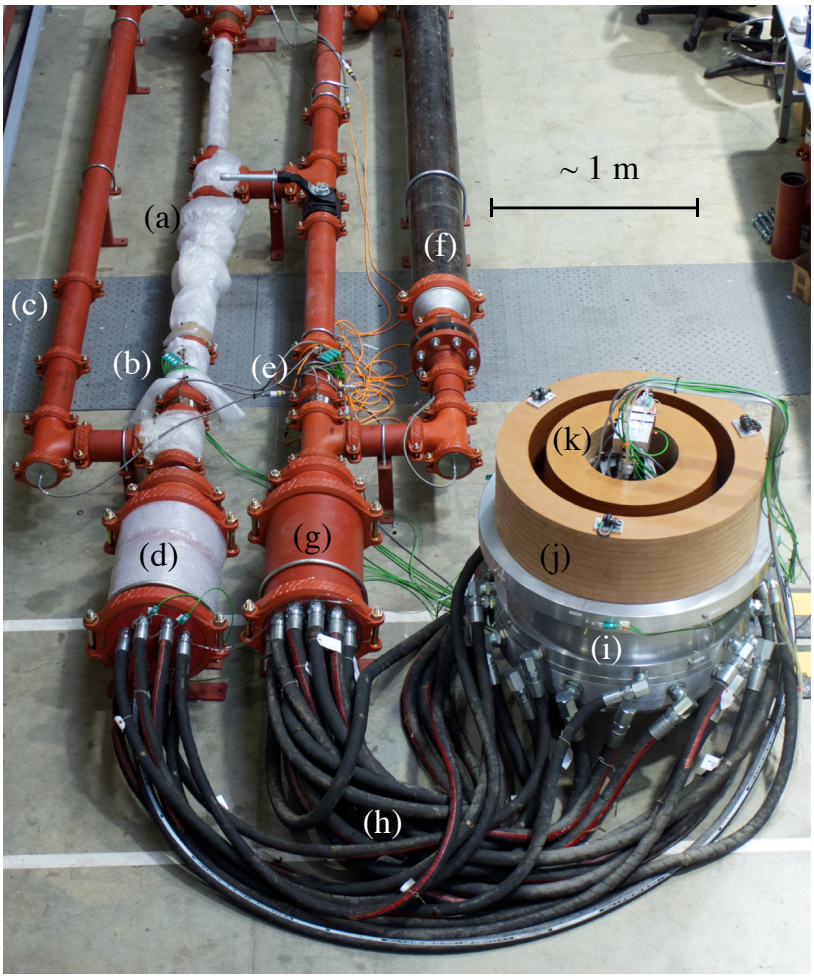


Figure 5.1: Photograph of the complete atmospheric test facility showing; (a) vortex tube; (b) coolant metering system; (c) coolant safety vent line (burst disk removed in image); (d) coolant manifold; (e) mainstream metering system; (f) mainstream safety vent line; (g) mainstream manifold; (h) flexible distribution hoses; (i) OLCS hardware; (j) exit duct; and (k) hub-mounted traverse system.

component alignment, and as part of the mainstream plenum. The base plate included a custom low pressure burst protection system - a 180 mm diameter disk of engineering grade closed-cell foam (Rohacell) designed to fail at 10 kPa. The plenum pressure vessel was completed by a machined aluminium ring (part of an existing upstream OTRF feed system) which consisted of 16 1.5 inch BSP ports for air supply. Finally, a perforated plate (5 mm holes in a honeycomb pattern of 10 mm pitch) separated the plenum from the mainstream duct to ensure even distribution of flow. This hardware is illustrated in Figure 5.2b.

The exit duct (Figure 5.2c) consisted of the turbine inlet profile of the SILOET turbine blended to a 4° diffuser (to minimise exit velocity and noise). As this component was to be used only in the atmospheric pressure experiment, it was machined from low-cost medium density fibreboard (MDF). 10 25 mm thick MDF sheets were saw cut, bonded, then turned and lacquered. A laser cut template was used as a tool guide meaning a duct profile of high accuracy was achieved.

The two-axis traverse system (Figure 5.2d) is discussed in detail in Section 5.6. Instrumentation is described in Section 5.5.

5.3 High-pressure feed system design

An air supply system was designed to integrate the OLCS with existing high pressure air supply infrastructure within the Osney Laboratory. The high pressure infrastruc-

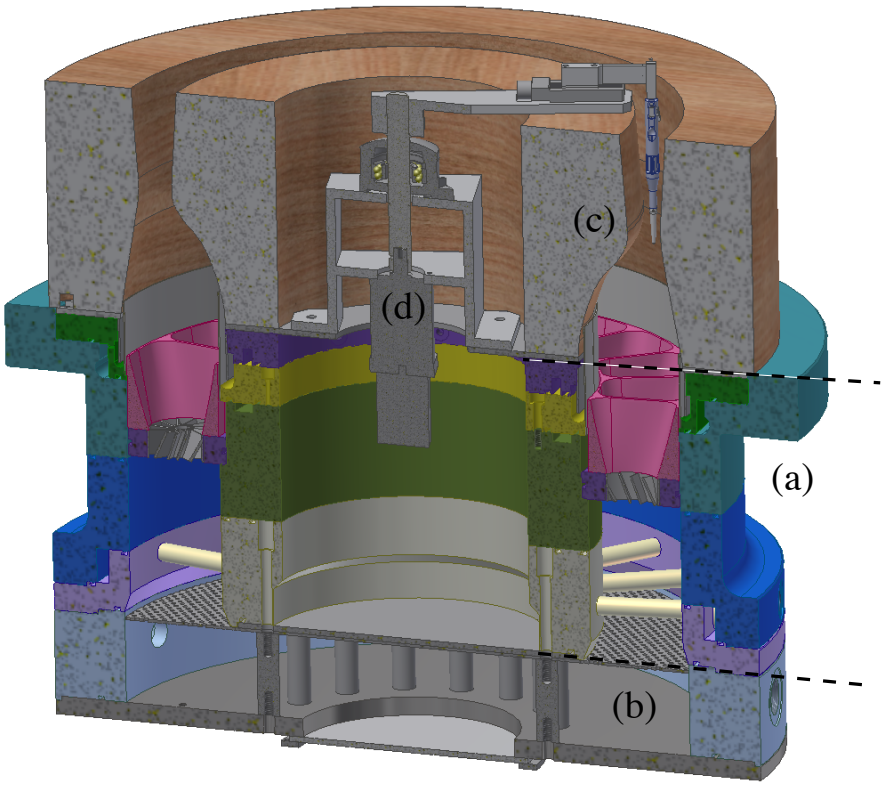


Figure 5.2: CAD model sectional view of OLCS (a) with mainstream manifold (b), exit duct (c) and hub-mounted traverse system (d). Dashed lines indicate the extent of the OLCS hardware.

ture consisted of a compressor, storage and distribution system; 60m^3 of nominally dry air at 28.6 bar absolute and ambient temperature was available when the storage was at capacity. From this central system, an air feed and metering system designed to supply the OLCS was constructed.

The feed system consisted of a mainstream metering and manifold system designed to supply 2.7 kg/s of air at ambient temperature (typically 290 K) in blowdown operation. The mainstream mass flow was set using a sonic nozzle, allowing for high accuracy metering and repeatability. A schematic of the feed system is presented in Figure 5.3.

The coolant system consisted of a large counterflow Ranque-Hilsch Vortex Tube (VT) designed and constructed in-house for this experiment. The design of the VT is discussed in detail below. The VT was capable of producing 0.3 kg/s of cold air at 60 K below the inlet (ambient) air temperature at the coolant metering nozzle. As with the main stream feed, the coolant mass flow was set and metered by a sonic nozzle with appropriate upstream flow conditioning to remove residual swirl from the VT exhaust. The VT hot flow was not used.

In sum, the system was designed to supply a peak mass flow of 3 kg/s to the test section in blowdown mode. Initial experiments were carried out in blowdown

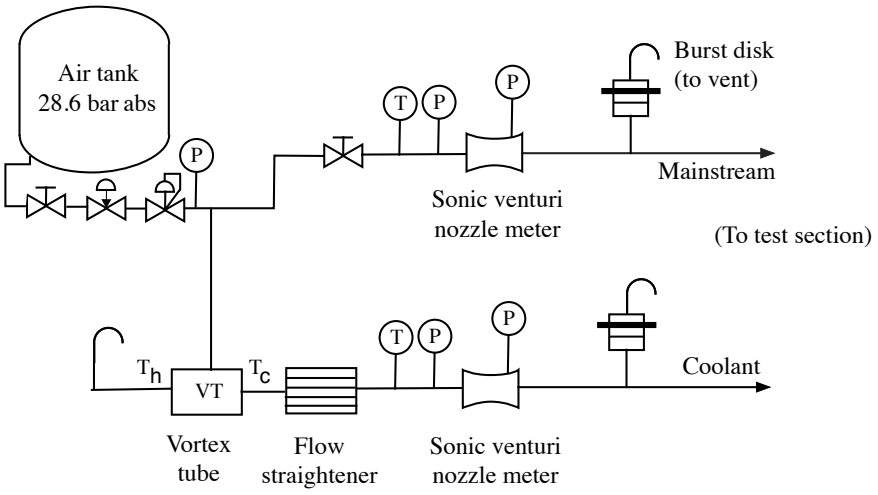


Figure 5.3: High pressure feed system schematic.

mode. The system was modified with the addition of a pressure regulating valve to provide constant mass flow rate and test section pressures to both streams during a single run and run-to-run.

5.3.1 Overpressure protection

Burst disks are a standard overpressure safety component in high pressure fluid systems and do not warrant discussion on their own. This section has been included to document user experience specific to the Osney Laboratory vent system which should be noted by future users.

The test section and low pressure flexible hoses (10 bar gauge operating limit) were protected from overpressure failure by commercial engineered burst disks. These were installed within the high pressure pipework system. It was found that metallic foil type burst disks (even with reverse pressure or vacuum ratings) were not suitable for the vent system installed in the laboratory–which services many high flow rate facilities–due to transient 'reverse' pressure loads which occurred during the operation of other facilities. After a series of unexplained disk failures, the metallic burst disks (which were nominally rated for 1 bar reverse pressure) were replaced with monolithic graphite disks, which performed flawlessly for several hundred runs without a single failure. The graphite disks (Zook 4 inch 'Inverted' Graphite Discs - 6 bar gauge $\pm 5\%$ burst pressure) were not adversely affected by the operation of other experimental facilities which shared the vent system.

In short, it is recommended that experiments using the shared vent line within the Osney Laboratory utilise graphite burst disks in all cases. The installation of pressure transducers directly upstream and downstream of each burst disk can be helpful in diagnosing disk failures.

5.4 Coolant production

Cold air for the coolant stream was produced using a large counterflow Ranque-Hilsch vortex tube (VT) designed and constructed in-house. Typical off-the-shelf VTs are approximately an order of magnitude too small while commercial custom-built large VTs were found to be prohibitive in terms of cost (approximately 30,000 US dollars quoted by one manufacturer), motivating the design and construction of a suitably sized device.

This section examines the design of the VT in terms of its thermal (cooling) capacity and maximum temperature differential, its mechanical design, and finally in terms of experimental validation of the design.

5.4.1 Vortex tube thermal design

The VT has been studied extensively since the concept was first developed by French physicist, Ranque (1934). The VT is a device with no moving parts that generates two streams–one hot, one cold–from a high pressure feed stream. The key feature common to VTs is the highly swirling inlet flow, usually achieved with tangential inlet ports or vanes. A simple schematic of a counterflow VT is shown in Figure 5.4. While the performance of these devices is relatively well understood thanks to a plethora of experimental studies (Yilmaz et al. (2009) provide a review of important contributions up to 2009 while Liu and Liu (2014) provides further coverage up to 2013), a clear understanding of the underlying mechanisms that provide the temperature separation effect has remained elusive (Liu and Liu, 2014).

The purpose of this section is to provide a practical recount of the design of the VT. While experiments where carried out to understand the performance of the resulting device, fundamental research in to the underlying mechanisms was not of interest to the present thesis. However, it is the case that an example of a device significantly larger than those that are readily available commercially may be of use for practical laboratory applications that require large volumes of cold air.

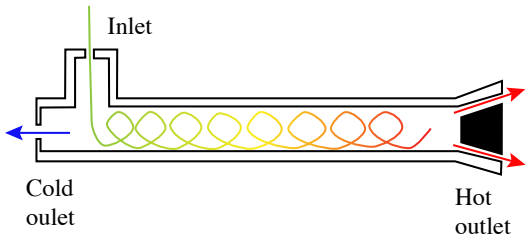


Figure 5.4: A simple schematic of a counterflow vortex tube. High pressure air is injected tangentially at the inlet to produce highly swirling flow. The separation effect produces cold air at the near orifice, while hot air leaves the opposite end.

Yilmaz et al., 2009 provided a comprehensive review of literature relating to common design parameters of vortex tubes. The review provided typical ranges for design parameters–for example the ratio of vortex tube length to diameter–as well as providing quantitative discussion regarding the influence of each parameter on VT performance. By making some basic design decisions relating to the required coolant mass flow and temperature produced by the VT, it was possible to utilise the aforementioned review alongside the comprehensive data set of Westley (1957) to a guide the majority of design decisions.

The available air supply system nominally provided air at $p_0 = 28.6$ bar absolute and $T_0 = 290$ K. The VT cold outlet back-pressure would be set at 5 bar absolute (by the sonic metering system). The overall VT pressure ratio (PR_{VT}) was given by:

$$PR_{VT} = \frac{p_{0\,VT\,in}}{p_{0\,VT\,c}} = \frac{28.6}{5.0} = 5.7 \tag{5.1}$$

Yilmaz et al., 2009 stated generally that the maximum coolant to inlet temperature differential is achieved when the mass fraction of coolant (ϵ) is equal to 0.3. Westley, 1957 presented a series of data sheets which showed that minimum coolant temperature was also a function of PR_{VT} (among other parameters). For $PR_{VT} = 6$ the minimum temperature occurs for values of ϵ from approximately 0.2 to 0.3. Therefore $\epsilon = 0.2$ was selected as the design point to provide the required mass flow for this condition, tending to oversize the system for $\epsilon = 0.3$. Coolant mass fraction is given by the equation:

$$\epsilon = \frac{\dot{m}_{VT\,c}}{\dot{m}_{VT\,in}} \tag{5.2}$$

For $\epsilon = 0.2$ and $\dot{m}_{VT\,c} = 0.3$ kg/s, as required for the coolant stream, it follows that $\dot{m}_{VT\,in} = 1.5$ kg/s. It is then possible to estimate the required area ($A_{VT\,in}$) of the tangential inlet nozzle system from the choked isentropic mass flow equation (solving for $A_{VT\,in}$). It is noted that since the inlet nozzle back-pressure is not known, this serves only as a coarse estimate to initiate the design process:

$$\dot{m}_{VT\,c} = C_d A_{VT\,in} p_{0\,VT\,in} \sqrt{\frac{\gamma}{R_{air} T_{0\,VT\,in}}} (\frac{\gamma+1}{2})^{-\frac{\gamma+1}{2(\gamma-1)}} \tag{5.3}$$

For $p_{0\,VT\,in} = 28.6$ bara, $T_{0\,VT\,in} = 290$ K, $\gamma = 1.4$, and $C_d = 0.8$:

$$A_{VT\,in} = 276\,\text{mm}^2 \tag{5.4}$$

The equivalent nozzle diameter ($d_{VT\,in}$) is given by:

$$d_{VT\,in} = \sqrt{\frac{4A_{VT\,in}}{\pi}} = 19\,\text{mm} \tag{5.5}$$

The data of Westley (1957) showed that for $PR_{VT} = 6$ to 7, the minimum coolant temperature was achieved for $\frac{d_{VT\,in}}{D_{VT}} \approx 0.42$. The variation was relatively small for $\frac{d_{VT\,in}}{D_{VT}} = 0.34\ to\ 0.5$. A value of 0.5 was taken, giving $D_{VT} = 38$ mm.

The length of the VT (L_{VT} - the distance from the inlet nozzles to the hot end valve) was chosen to be at least $20D_{VT}$. $L_{VT} = 1000$ mm was chosen.

The normalised cold orifice diameter $\frac{d_{VT\,cold}}{D_{VT}}$ affects both the VT back-pressure and the minimum coolant temperature. In combination with the hot end valve, it also sets the cold mass fraction (ϵ). Rather than attempt to explicitly define the cold orifice diameter, a range of orifice plates of varying diameter were made. Similarly, an adjustable hot end valve was designed to decouple the cold orifice diameter and cold mass fraction.

5.4.2 Vortex tube mechanical design

The VT mechanical design was based on the estimated parameters of the previous section. As the assembly required a long (1000 mm) tubular section, it was necessary to design the system around a standard nominal pipe and fitting size. Using the estimated $D_{VT} = 38$ mm, 2 inch nominal pipe and Victaulic fittings were chosen for the 1000 mm tubular section of the vortex tube. The complete assembly, based on the Victaulic fitting system (including standard Victaulic fittings and custom made components) is shown in Figure 5.5.

The inlet nozzle and cold orifice assembly of the VT (Figure 5.6) was housed inside a 4 inch (nominal) Victaulic tee fitting using machined mild steel adapters. The maximum D_{VT} possible within this assembly was 44 mm. This was driven by the dimensions of the standard 2 inch victaulic clamp and groove system. Given $D_{VT} = 44$ mm and $\frac{d_{VT\,in}}{D_{VT}} = 0.5$, $d_{VT\,in}$ was taken as 22 mm, giving $A_{VT\,in} = 380$ mm. This was larger than the original estimate of nozzle area–a result of discrete nominal pipe sizes–however excess capacity was preferable.

5.4.3 Vortex tube experimental results

An extensive experimental characterisation of the VT described above was carried out separately and is not presented as part of this thesis. Instead, data from combustor

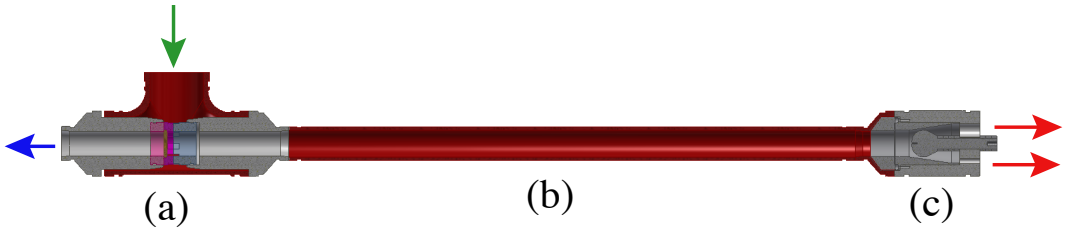


Figure 5.5: Sectional view of the complete vortex tube which utilised the Victaulic pipe fitting system (clamps not shown). Highlighted is (a) the custom-made tangential nozzle and coolant orifice assembly (within a standard 4 inch Victualic tee fitting); (b) the 1 m tube section; and (c) the custom-made needle valve assembly.

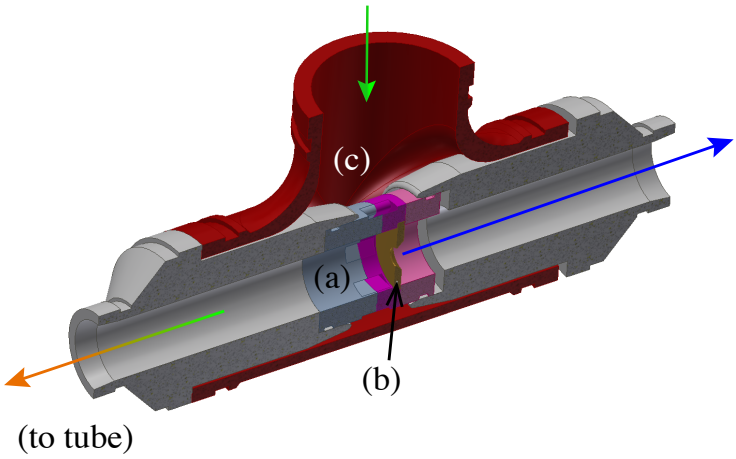


Figure 5.6: The vortex tube inlet nozzle and cold orifice assembly. The tangential inlet nozzle assembly (a) which also integrates the cold orifice (b) is housed within a standard Victaulic 4 inch tee fitting (c).

simulator tests are presented to highlight the minimum temperature achieved and also the coolant mass flow rate.

When configured for SILOET, the VT produced 0.3 kg/s of air at 55-65 K below the inlet temperature ($T_{0\,VT\,in}$) after a short start up transient. In practice, -65 K was achieved only after 10 minutes of continuous running. Figure 5.7 illustrates the typical operation of the VT in terms of inlet temperature ($T_{0\,VT\,in}$) and cold outlet temperature ($T_{0\,VT\,c}$). This was in agreement with the largest stated coolant temperature differences for commercial devices. Westley, 1957 used the following equation to describe non-dimensional temperature difference:

$$T_{ND\,VT\,c} = \frac{T_{0\,VT\,in} - T_{0\,VT\,c}}{T_{0\,VT\,in}} \tag{5.6}$$

For a similar pressure ratio ($PR_{VT} = 6$), and the optimum cold orifice size and hot end valve setting, Westley (1957) achieved $T_{ND\,VT\,cold} = 0.203$. In the configuration described above, the VT of this study achieved $T_{ND\,VT\,cold} = \frac{60\ K}{290\ K} = 0.21$. It is also noted that this temperature was measured approximately 1 m from the VT cold orifice allowing some heat gain.

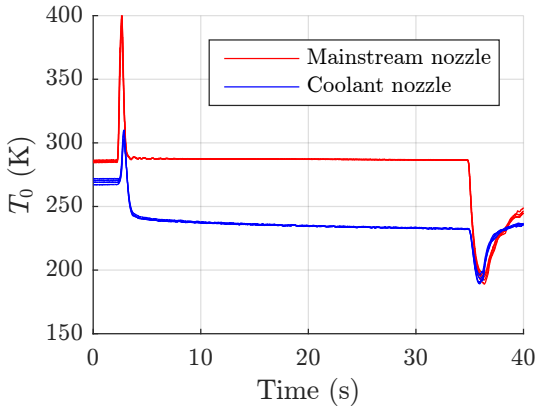


Figure 5.7: Experimental data showing the coolant and mainstream temperatures at the respective mass flow metering stations. The mainstream temperature is approximately equal to the VT inlet temperature. From run PG1271.

5.5 Instrumentation

The combustor simulator atmospheric experiment was extensively instrumented - 85 pressure measurement points and 48 temperature measurements in total. The instrumentation served three main purposes:

1. HP feed system mass flow metering and condition monitoring
2. Combustor simulator LP feed system
3. Combustor simulator inlet plane characterisation

These specific applications are discussed separately in the following sections, along with an overview of the sensor and data acquisition hardware.

5.5.1 Sensors and data acquisition

The approach to steady flow measurement was generally consistent across the experiment. These common details relating to the steady measurement of temperature and pressure–the sensors, data acquisition and basic processing–are summarised in this section and apply unless specifically stated elsewhere. The main exception was for probes used as part of the inlet traverse system which are discussed separately in Section 5.6.

5.5.1.1 Pressure transducers

All pressure measurements (unless specifically stated) utilised remote pressure transducers connected to the test section using 1 mm (internal diameter) tubing - typically a combination of flexible plastic tubing and stainless steel tubing. These measurements were therefore regarded as low-speed (bandwidth < 100 Hz). A single high-speed Kulite pressure transducer was used as part of a traverse probe and is discussed in Section 5.6 below. Low-speed pressure measurements used amplified pressure transducers of two kinds:

- First Sensor (FS) (formerly Sensor Technics) CTE-8000 amplified absolute pressure transducers - 0-10 V output with typical combined (uncalibrated) accuracy of 0.1% of full scale output (FSO)
- Silicon Microstructures (SMi) SM5852 amplified differential pressure transducers - 0.5-4.5 V output with maximum combined (uncalibrated) accuracy of 1.6% of FSO

All sensor were individually calibrated using a Ruska 7250xi Digital Pressure Controller. It is noted that while the combined accuracy of the SM5852 transducers was relatively poor, the calibration process showed the typically uncertainty associated with linearity to be less than 0.2%. Offset errors (for all transducers) were dealt with during data processing using run-by-run zero-offset measurements referenced to a laboratory mercury barometer.

The amplified voltage output signals of all pressure transducers were recording using National Instruments 9205 16-bit analogue to digital converters. Unless otherwise stated, the experimental data presented from the atmospheric experiment was sampled at 2000 Hz.

5.5.1.2 Thermocouples

Temperature measurements used K-type thermocouples (TCs) in all cases. The TCs were of bare wire bead (welded) type, from wire of 0.1 mm diameter. The typical time constant for a TC of this kind is approximately 0.05 s (Omega, 2015) meaning a bandwidth of approximately 2 Hz. The exception to this were TC probes used as part of the inlet traverse system, which are discussed in Section 5.6 below.

TC voltage signals were recorded and converted using National Instruments 9213 or 9214 24-bit analogue to digital thermocouple modules with cold junction compensation. The typical uncertainty for measurements of K-type thermocouples with this system was 0.86 K when used in 'high-speed' mode. This mode allowed a sample rate of 68 Hz.

5.5.2 High pressure monitoring and mass flow rate metering

The high pressure feed system consisted primarily of instrumentation for the metering of mainstream and coolant mass flows - total temperature and total pressure. The section of feed hardware immediately downstream of the metering nozzles, while operating at low pressure, was considered to be part of the high pressure system. In this section, engineered burst disks were installed to protect low pressure hardware from overpressure events. Figure 5.3 illustrates the high pressure feed system, including the instrumentation associated with mass flow metering, the location of burst disks and the boundary with the low pressure test section.

5.5.2.1 Condition monitoring

Pressure measurements were taken upstream of the vortex tube and mainstream branch to provide a tank or regulator output (when installed) reference pressure. Additionally, after ongoing issues with unexplained failures of metallic burst disks, pressure measurements were also taken immediately upstream of each of the mainstream and coolant burst disk as well as in the shared vent line. In the former case, this was to ensure that the recovery of dynamic pressure was not contributing to burst disk failures unbeknown to the operator.

5.5.2.2 Mass flow rate metering

Main stream and coolant stream mass flows were set and metered using sonic nozzles (see Figures 5.1 and 5.3) in accordance with ISO 9300:2005. Nozzles designed in accordance with the standard were precision machined in-house. A length of 10 pipe diameters of straight pipe was present upstream of the nozzle inlet planes. Additionally, a flow straightener was installed immediately downstream of the VT exhaust to remove swirl.

In each case, the nozzle inlet total temperature was measured with a four-probe K-type thermocouple rake, while inlet total pressure was estimated with a wall mounted pressure taping. The Mach number was sufficiently low that $p_0 = p$ to within the measurement uncertainty ($< 0.1\%$). Finally, the nozzle throat static pressure was estimated using a wall pressure tapping downstream of the nozzle exhaust. First Sensor CTE-8000 35 bar absolute transducers were used for all mass flow metering purposes (inlet and exhaust conditions).

5.5.3 Test section characterisation

In addition to the characterisation of the inlet conditions–discussed separately below– it was necessary to carry out extensive measurements of the flow elsewhere in the combustor simulator. Instrumentation was installed in the test section in order to ensure uniform distribution of flow around the test section, characterise the mainstream flow, monitor and characterise the internal coolant network, and characterise the coolant temperature prior to injection.

The test section instrumentation points are described in detail in Table 5.1 and illustrated schematically in Figure 5.8.

5.6 Inlet traverse system

A two-axis traverse system was designed to mount in test section (the OLCS) hub and allow the collection of data on 2D planes within the exit duct section. The

Table 5.1: Summary of test section instrumentation.

Location	**Type**	**Sensor**	**Description**
Main plenum	p_0	SMi ±10 mbar	4 at 90° spaces
Main duct rakes	p_0	SMi ±2 mbar	3 rakes (4 probes each)
	T_0	K-type TC	at 60° spaces
Common coolant plenum	p_0	FS 5 bar abs.	4 at 90° spaces
Case coolant plenum	p_0	FS 5 bar abs.	4 at 90° spaces
	T_0	K-type TC	
Hub coolant plenum	p_0	FS 5 bar abs.	4 at 90° spaces
	T_0	K-type TC	
Case coolant slot	T_0	K-type TC	8 at 45° spaces
Hub coolant slot	T_0	K-type TC	8 at 45° spaces
Case duct tappings	p	SMi ±2 mbar	16 at even axial spacings (at 0°)
Hub duct tappings	p	SMi ±2 mbar	16 at even axial spacings (at 0°)

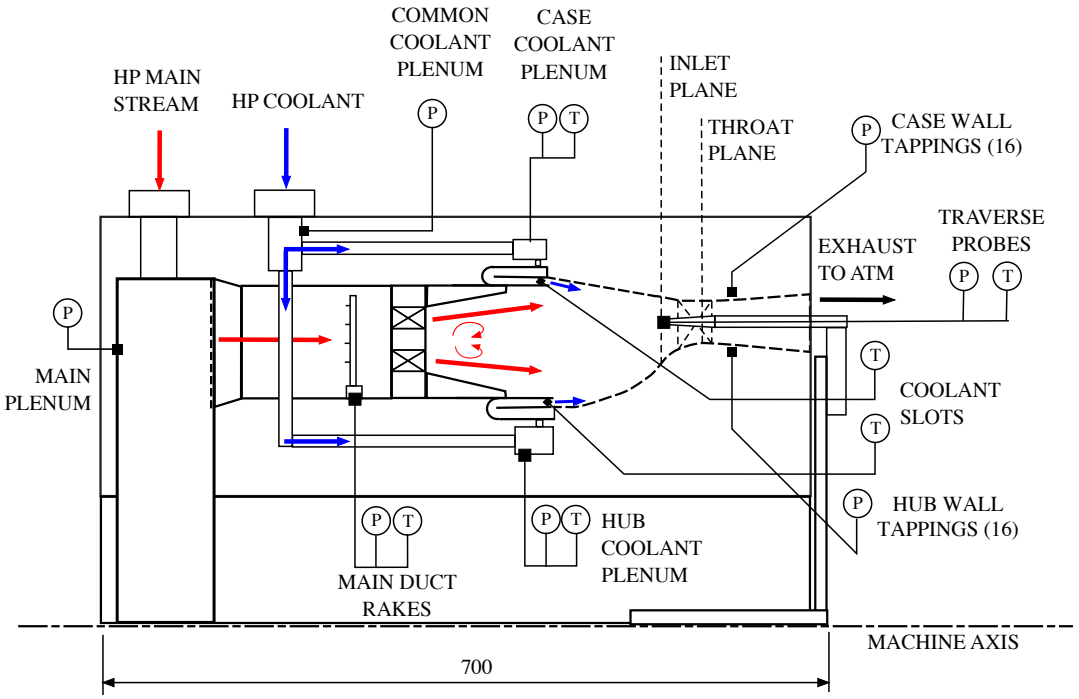


Figure 5.8: Sectional schematic of the test section (rotated 90°) showing instrumentation points. The dashed duct wall lines indicate axially spaced pressure tappings (16 each at hub and case).

traverse assembly was designed to move probes precisely and repeatably within the test section exit duct in the radial-circumferential plane. Probes could be positioned at the inlet plane and also the geometric throat of the exit duct - that is, the system was discretely adjustable in the third axis also. The traverse system is illustrated schematically within the test section in Figure 5.8 and in Figure 5.2 above.

5.6.1 Probes for turbine inlet traverse measurements

Probes were used to measure flow properties within the exit duct. The key properties of interest were steady (time-averaged) values of total and static pressure, pitch (α) and swirl (β) angle, and total temperature. The probes used for the measurement of these properties are described in the following sections and are illustrated in Figure 5.9. Additionally, it was of interest to attempt to measure turbulence intensity and length scale, and also the presence of a precessing vortex core (PVC), which required high frequency response sensors, which are also discussed below.

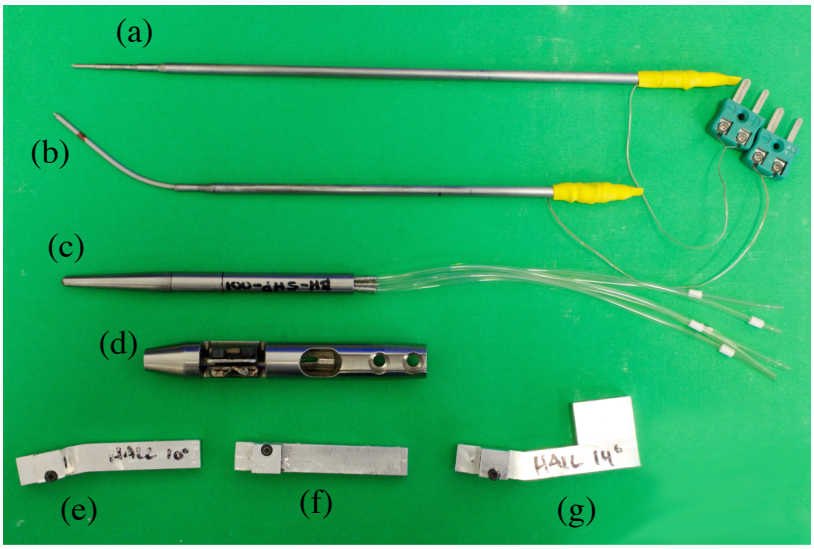


Figure 5.9: Photograph of the probes used for traverse measurements of steady properties. (a) Straight and (b) gooseneck thermocouple probes (50 μm butt welded wire K-type); (c) five-hole probe (BH-5HP-001) and (d) holder; machined probe adapters (e) $-10°$ pitch for case access, (f) straight for midspan, and (g) offset and $+14°$ pitch for hub access.

5.6.1.1 Five-hole pressure probe

A calibrated five-hole probe was used for the measurement of total (p_0) and static pressure (p), and pitch (α) and swirl (β) angles. The probe tip was constructed using Direct Metal Laser Sintering (DMLS) from maraging steel and was finished by hand to produce a clean, truncated pyramidal tip geometry. The finished probe was calibrated in the Oxford Probe Calibration Facility (OPCF). The construction and calibration of such a probe is discussed in detail in section **??**. The probe used in this experimental facility (serial number: BH-5HP-001) is shown in Figure 5.9c.

Pressures from the probe were recorded using SMi SM5852 0.02 bar differential transducers connected by 1 mm (internal diameter) tubing. The transducers were located directly on the traverse system (described below) to minimise the length of interconnecting tubing required and therefore to maximise the probe frequency response. The length of tube from probe tip to transducer was approximately 410 mm. The probe -3 dB cutoff frequency was estimated experimentally (in a process described in Chapter 5.8) to be at least 90 hz.

5.6.1.2 Total temperature probes

Two probes were used to measure total temperature. Both were of the same specification, with one employing a bent (gooseneck) probe shaft to allow greater radial coverage at the inlet plane, towards the hub. Both probes utilise K-type butt welded bare wire (50 μm diameter) thermocouples.

In designing thermocouple probes, the steady state error and frequency response must be considered. The steady state error is due to conduction of heat between the junction and wire support, radiation of heat from the exposed wire and junction, and the imperfect recovery of kinetic energy. For the current work, where the maximum total temperature to be measured was 290 K and the wall temperature was no lower than the coolant temperature of 275 K, the error due to radiation (using the method of Paniagua et al. (2002)) was 0.03 K. At Mach number equal

to 0.1 (the maximum expected in the flow) and total temperature of 290 K, static temperature differs by only 0.6 K - the maximum error due to recovery of kinetic energy. The combination of these errors was small and did not warrant the use of a shielded probe. The conduction error is reduced by increasing the ratio of wire length to diameter. For the probes in question, a ratio of approximately 40 was achieved, which is approaching the practical limit for durability.

The estimated frequency response of this type of thermocouple was 10 Hz. This assumes a time constant of 0.016 s (estimated from Omega, 2015) and that response of a thermocouple is predominately first order (Thirumaleshwar, 2009).

The measurements were recorded with a National Instruments 9214 24-bit analogue to digital thermocouple module (described above).

5.6.1.3 High frequency response total pressure (Kulite) probe

High-speed total pressure measurements were attempted with a probe consisting of a flush, tip mounted Kulite XCQ-062 (B-screen) 100 PSI (6.9 bar) absolute miniature pressure transducer. The probe is shown in Figure 5.10. A Fylde FE-H379-TA high-speed transducer amplifier with anti-aliasing low-pass filter was used to provide excitation and signal amplification. The amplified and low-pass filtered (at 30 kHz) signal was recorded using a dedicated (i.e. only one channel used concurrently) National Instruments 9205 16-bit analogue to digital converter with a sample rate of 70 kHz.

A low-range static calibration of the Kulite transducer was carried out using 2 calibrated SMi SM5852 0.02 bar transducers (described above) to record the reference pressure. The 3 transducers and a 5 mL syringe were interconnected using plastic tubing - the syringe was used to vary the internal pressure while the three transducers were sampled.

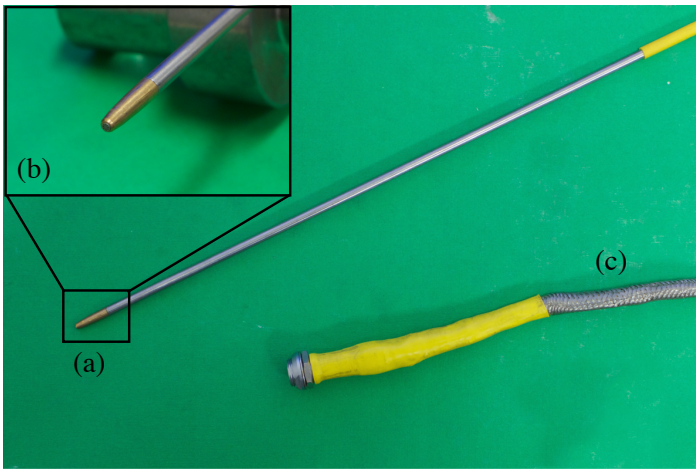


Figure 5.10: Photograph of the fast response total pressure probe with embedded Kulite XCQ-062 highlighting: (a) the probe tip and (b) and inset, enlarged view showing the B-screen, and (c) the shielded cable.

5.6.1.4 High frequency response hot-wire probe

High speed velocity measurements were taken with a Constant Temperature Anemometer (CTA) probe - also referred to as a hot-wire anemometer (HWA) or simply hot-wire. A Dantec Dynamics Streamline Pro CTA system was used with a straight miniature (single) wire probe (Dantec model 55P11). A single wire probe is best suited to 1D flow in which the velocity vectors are parallel to the probe (not wire) axis. Conversely, single wire probes are generally unsuitable for highly 3D flows since they have no response to the velocity component parallel to the wire.

A single wire probe was used as an alternative to the Kulite probe described above (which produced erroneous results), despite the limitations relating to 3D swirling flows. This was simply due to the fact that only single wire probes were available in the time frame required. The reliability of the resulting measurements is discussed on a case-by-case basis alongside the data presented in Chapter 6. The signal was low-pass filtered at 30 kHz within the CTA system and sampled as per the Kulite probe described above.

A steady calibration of the Dantec Dynamics 55P11 hot-wire probe was carried out in a free (circular) jet at atmospheric pressure with respect to a single total

pressure probe (using a calibrated SMi SM5852 0.02 bar transducer). The hot-wire and total pressure probe were positioned side-by-side in the jet with adequate spacing to avoid interference.

5.6.1.5 Dynamic calibration of the Kulite probe

Measurements with the Kulite probe produced clearly erroneous values of turbulence intensity - at times values far in excess of 100%. Initially this was attributed to high frequency noise from the traverse stepper motor (described below), however after reducing signal noise to an insignificant level, erroneous results persisted. The issue was investigated by dynamically calibrating the Kulite probe with respect to the hot-wire probe described above, in a free jet at atmospheric pressure, similar to the work of Moss and Oldfield (1991).

Figure 5.11 compares the turbulence spectra of the jet as measured by the Kulite and hot-wire probes. It was apparent that at velocities as encountered in the OLCS experiment (30 m/s and below), the spectra measured by the Kulite probe had significant erroneous power at high frequencies, which explains the overestimate of turbulence intensity. The disparity between the Kulite and hot-wire spectra were much greater and less systematic than that which Moss and Oldfield (1991) corrected for by calibration. It was decided that a meaningful dynamic calibration was not possible for the probe at this velocity and it was not used any further.

It is possible that a faulty transducer (e.g. a contaminated screen or cavity) was the cause, although it is noted that at higher velocities (50 m/s) the agreement between Kulite and hot-wire spectra was much better. The experience–which cost significant time and effort–highlighted the importance of carrying out dynamic calibration of fast response pressure probes for turbulence measurements.

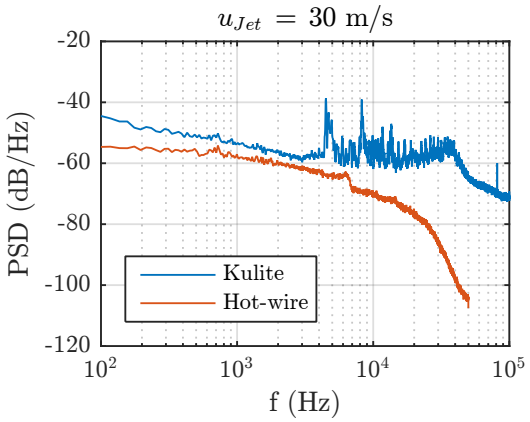


Figure 5.11: Turbulence spectra as power spectral density (PSD) functions as derived from the Kulite and hot-wire probes in a 30 m/s jet.

5.6.2 Automated traverse hardware

The traverse system was semi-automated in that the circumferential axis was controlled by a stepper motor which was in turn controllable via a personal computer (PC). The radial axis was manually adjusted by means of a screw-driven dovetail slide. The manual radial axis was chosen for simplicity and to remove altogether the risk of 'crashing' a probe in to the duct walls (e.g. as a result of a code malfunction). Probes were fixed to the dovetail slide using precision machined adapters. The traverse assembly is illustrated in terms of a 3D CAD model in Figure 5.12 and photographically in Figure 5.13.

A set of precision machined adapters were produced which collectively allowed probe access to the exit duct throat plane, and the greatest possible radial extent of the inlet plane. The inlet plane, being upstream of the exit duct throat, made access difficult (see Figure 5.8) and pre-pitched probe adapters were required to improve probe access. The system provided access from 19% to 91% radial span for straight probes (e.g. the five-hole probe, as in Figure 5.12). Since the region of greatest interest in terms of temperature was near the hub and case, a gooseneck thermocouple probe was required to extend access to the hub. Temperature measurements were then possible over 2% to 99% of radial span.

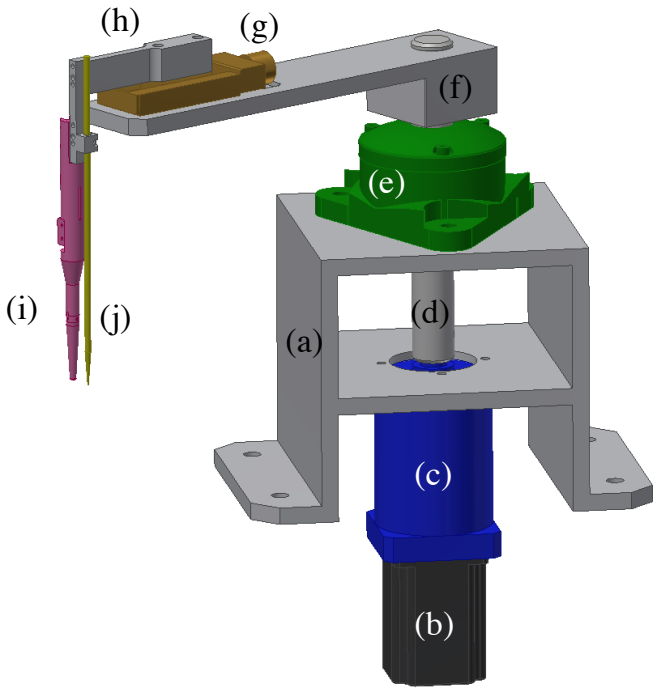


Figure 5.12: CAD model of the traverse assembling showing; (a) the mounting frame; (b) stepper motor; (c) 1:100 low backlash epicyclic gear box; (d) drive shaft; (e) bearing housing; (f) traverse arm; (g) radial dovetail slide; (h) probe holder assembly; (i) a five-hole probe; and (j) a thermocouple probe.

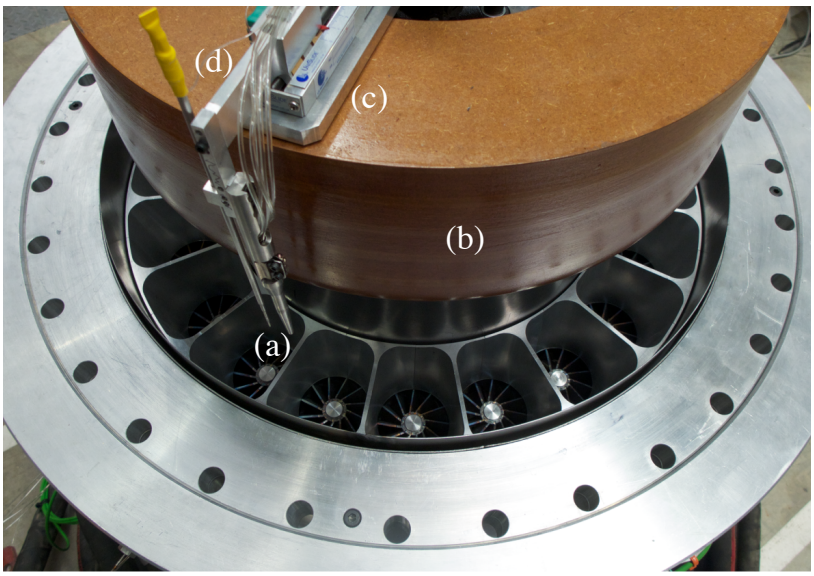


Figure 5.13: Photograph of the traverse system installed in the facility showing; (a) the probe tips at the inlet plane; (b) exit duct hub; (c) traverse arm and dovetail slide; and (d) two-position probe adapter.

5.6.2.1 Stepper motor setup notes

The circumferential axis was driven by a stepper motor (McLennan 23HSX-306) via a 1:100 low backlash (< 10 arcmin) gearbox (Alpha LP070). The stepper motor was controlled by an Applied Motion Products ST5-Q-NN Stepper Drive/Controller which could be programmed–though not natively–using National Instruments LabVIEW software.

Stepper motor drivers consist of high-current DC-DC switch mode power supplies. Additionally, it is usually necessary to utilise a further switch mode AC-DC power supply. This combination of hardware can be a significant source of signal noise - conducted and radiated. There is not a single universal solution to dealing with signal noise, and often noise-generating ground loops are not completely avoidable. However, through significant trial and error, a number of beneficial measures were identified. Since a useful reference guide of this problem does not exist, the following recommendations have been collated:

- Use shielded multi-conductor cable for the stepper motor power cable. The shield should be earthed at the power supply end.
- Ground the stepper motor casing - via a dedicated conductor within the power cable or via the power cable shielding.
- Care must be taken to avoid ground loops when implementing the above points.
- Utilise a power line filter with any AC to DC power supplies to limit noise on the AC (lab) ground which can affect data acquisition systems.
- Consider installing common-mode chokes (on each motor phase) between the driver and motor to reduce noise radiated by the power cable.
- Consider optical isolators for data connections between stepper drivers/controllers and PCs to avoid ground loops.

5.6.3 Traverse operation

The traverse was operated such that a single (automatic and continuous) sweep in the circumferential direction would be carried out during steady flow conditions, the flow would be stopped and the radial position manually adjusted. The circumferential sweep speed was an important consideration. The traverse speed was selected to conserve air (by minimising sweep time) while ensuring that the probes–which had finite bandwidth–were able to accurately resolve the gradients present in the flow. The traverse was operated at 0.02 revs/s (7.2°/s) which meant a probe speed of approximately 0.035 m/s in the mid span region. The suitability of this was confirmed experimentally - for example, the 2D experimental data presented in Chapter 6 show well-resolved details.

5.6.4 Test procedure

The test procedure involved two phases. In the first phase, the coolant stream was run in isolation (mainstream closed) in order to pre-cool the feed and OLCS hardware. Typically 2 to 3 runs of at least 5 minutes each were required. The upstream regulator was wide open during the cooling phase (blowdown mode). The second phase consisted of a series of runs, approximately 30 seconds in length, with both mainstream and coolant flows (specified above). The second phase runs were regulated (typical upstream set point of 21 bar absolute) to provide constant mass flow rate. For each run, a single circumferential traverse sweep was completed and then the radial position adjusted (and recorded manually) at a set increment before repeating. This process was repeated for the required set of traverse probe positions (and various probe combinations).

The inlet plane and geometric throat of the exit duct were traversed across a circumferential range of ±30° (3.3 swirler pitches), where the origin was aligned with a swirler axis. The traverse swept continuously in the circumferential direction and was adjusted in increments of less than 3 mm in the radial directions - measurement

locations are shown on all 2D traverse plots. Traverses were also carried out on both planes across a circumferential range of $\pm 90^{\circ}$ at 3 radial heights to verify periodicity of the OLCS.

During the first (cooling) phase, data was acquired at 100 Hz for the purposes of monitoring the state of the facility and injection coolant temperature. Second phase runs were sampled at 2000 Hz for steady measurements while unsteady measurements (Kulite or hot-wire probes) were sampled at 70 kHz.

5.7 Development of aerodynamic instrumentation

Inlet traverse measurements of aerodynamic properties were carried out using a five-hole pressure probe designed and developed specifically for this experiment. The probe tip was manufactured using additive manufacturing (AM), specifically direct metal laser sintering (DMLS). The probe used in the OLCS characterisation represented an early iteration in the development of an open-source aerodynamic probe – the Oxford Probe. This section describes the design, manufacture and calibration relevant to both the probe used in this research and as an extension, that of the Oxford Probe.

5.7.1 Multi-hole probes

Multi-hole (pressure) probes are used to perform aerodynamic measurements of total and static pressure, and flow angles (therefore velocity and dynamic pressure), in three-dimensional fluid flows. Of the numerous designs in common use, perhaps the most common is the five-hole probe. This is often optimum for characterizing turbomachinery flows, free-jet flows, combustor flows, and for wind tunnel surveys (for example behind aircraft or road vehicle models, or in more fundamental studies).

Probe tip size is normally determined by a combination of: the smallest flow feature to be resolved; the mechanical requirements of the probe; the required frequency response ; andin hot flows, for examplecooling requirements. Overall tip di-

ameters of 2 mm or smaller are not uncommon, but for most tube-transducer systems such miniaturization would result in low bandwidth.

Traditionally, five-hole probes are manufactured by fabrication (soldered tubes, with a machined tip) or by conventional machining (cylindrical bar stock, with drilled holes and machined tip). As probes manufactured by these methods normally deviate substantially from the nominal design (due to the small scale of the probe), individual calibration is necessary, which is a specialist activity which can be expensive.

Additive manufacturing has matured sufficiently to provide a realistic alternative for the manufacture of five-hole probes. Specifically, direct metal laser sintering (DMLS) and selective laser annealing (SLA) processes can be used to produce probes with internal tubes of 1 mm diameter with 1 mm wall thickness between holes, with relatively smooth tube internal walls and with no risk or break-through between individual tubes. The authors have extensive experience to support this, using processes from a number of manufacturers.

The purpose of this paper is to present the probe geometry and calibration maps for an open source probe that can be printed by the end user, and used without the requirement for calibration. The aim is to widen access to probe measurements techniques in educational and research environments, particularly those institutions without specialist calibration facilities. In certain very common operating regimes (including the majority of wind tunnel applications) the open source probe can be used with equivalent accuracy to an individually calibrated bespoke probe. The accuracy and limitations of the open source probe are evaluated and discussed in the context of data from 16 probes that were manufactured (in different materials and at different scales) for comparison. The probe drawings, calibration maps, and processing routine are available to download under a free license.

5.7.2 The Oxford Probe

In this section the general aspects of aerodynamic probe design are reviewed, with an emphasis on five-hole probes. The sensitivity to Reynolds number (Re) and cone angle, are discussed and the design of the Oxford Probe is presented. The suggested end-user manufacture process, and the suggested range of use without calibration is then discussed.

5.7.2.1 Overview of aerodynamic probe design

There are numerous types of multi-hole probe in common use, with different tip designs optimized for different functions. Two (of many) examples of specialist probes include: flattened three-hole probes (Povey et al., 2008) (used for wake traversing, where resolution in one direction is paramount, and where flow angle variation is primarily in the yaw rather than the pitch direction); and omni-directional probes (Rediniotis and Kinser, 1998; Ramakrishnan, 2004) with spherical heads with 12 or more static pressure tappings distributed across the sphere (used when the probe cannot easily be aligned to the flow, or where very large angle variation is expected). For routine wind tunnel measurements, however, probes most commonly have four, five, or seven holes. Of these, the five-hole probe is the most common.

Five-hole probes with spherical, and truncated conical and pyramidal tip designs have been used. Broadly speaking these have similar behavior, but probes with sharp face edges (truncated cone and pyramid) tend to be less sensitive to Reynolds number than hemispherical probes due to more well-defined separation points. Conical and pyramidal probes also have the advantage of being easier to manufacture and allow closer grouping of holes than hemispherical probes. Thus, they have become a more common choice (Centolanzi J, 1957). Included angle is typically in the range 60° (e.g. Yasa and Paniagua, 2012) to 90° (e.g. Krause and Dudzinsky, 1969; Reichert and Wendt, 1994) (marked in Figure 5.14). Two typical designs are shown in Figure 1. Choice of included angle represents a compromise between maximizing useful flow

angle range (smaller angle) and increasing sensitivity (larger angle). Flow disturbance is also minimized with smaller cone angle.

The effect of Reynolds number on the calibration of probes of various geometries similar to those in Figure 1, was investigated (Dominy and Hodson, 1993) to determine which designs exhibited greatest sensitivity. Two effects were observed. Yaw coefficient showed Re sensitivity due to separations on the probe tip. This effect was found to be small above Re = $15x10^3$, with the least Re sensitivity for an included angle of 90° for both conical and pyramidal probes the latter having the lowest Re sensitivity. This is in agreement with the earlier recommendation of Bryer and Pankhurst (1971). Sensitivity of dynamic pressure coefficient to the precise hole geometry (forward facing versus perpendicularly drilled holes) was also observed, but the effect proved more difficult to understand and quantify.

5.7.2.2 Design of the Oxford Probe

The Oxford Probe is a five-hole pyramid probe of the design shown in Figure 5.15a. Details of the design are given in Figure 5.15b. The included angle of the tip is $\psi = 60°$, the tip-to-hole diameter ratio is $Dd = 5$, the ratio of the tip diameter to length of the side of the frontal square is $Dw = 3.75$. The tip is integrated into an extended cone of shallow included angle $phi = 14.2°$, which extends at distance $L > 2.5D$ beyond the tip in the downstream direction. Quantitative analysis below demonstrates that the probe calibration is very insensitive to the extended cone length. Three typical Oxford Probe designs are shown in Figure 5.15c.

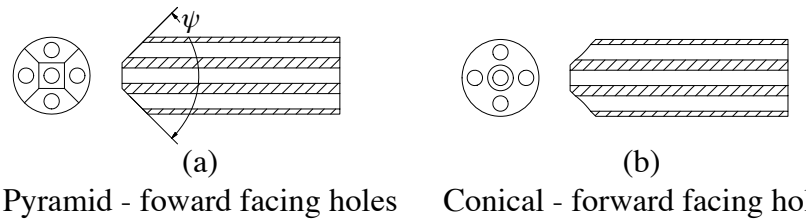


Figure 5.14: Examples of two five-hole probe tip geometries (adapted from Dominy and Hodson (1993))

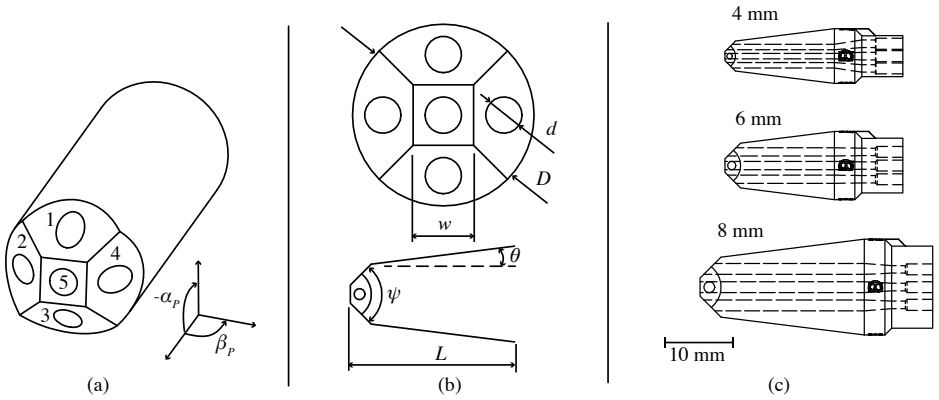


Figure 5.15: (a) Schematic of a pyramid probe tip showing hole numbering and flow angle convention; (b) design of Oxford Probe; and (c) three sizes of Oxford Probe.

5.7.2.3 Suggested manufacture process

It was demonstrated (by comparison of calibration maps for 16 probes) that the probes can be manufactured by additive manufacturing using DMLS or SLA processes. It is recommended that for a DMLS process with a layer height of 0.04 mm, tips should be manufactured no smaller than $D = 4$ mm. For an SLA process with a layer height of 0.1 mm, the minimum recommended size is also $D = 4$ mm. Probes with tips near the bottom end of the suggested size range should be inspected to ensure that internal passages are properly formed, and that there is no leakage between holes.

5.7.2.4 Suggested range of use

The probes can be used with the supplied calibration map with good accuracy in the incompressible range M < 0.3, and in the Re range based on tip size $\mathrm{Re}_{D,critial} > 15 \times 10^3$. Inverting this condition to establish the minimum velocity for a given diameter yields $u_{min} = (\mu \mathrm{Re}_{D,critial})/(\rho D)$. For air at ambient conditions this corresponds to minimum velocities 53,35,26,18 and 9 ms^{-1} for D=4,6,8,12 and 24 mm . For the same range of diameters, the minimum velocities in water at approximately room temperature are 6.7,4.5,3.3,2.3 and 1.1 ms^{-1}. This range of conditions covers a majority of wind tunnel and flume applications found in laboratory and education

environments, including many specialist environments including the inlet flow field in fully scaled (to engine conditions) turbine test facilities, or the inter-stage in turbine test facilities (between rotor and downstream vane, provided the Mach number is low enough). Indeed the probe was originally developed for, and used in, a fully scaled turbine test facility.

The suggested range of use is perhaps conservative, and where indicative measurements are required the Oxford Probe could be used outside the suggested Re range with some degree of confidence. The Oxford Probe would not perform well in compressible conditions without specialist calibration.

5.7.3 Theory of calibration

In this section a brief review of the theory of multi-hole probe calibration is presented. The purpose is to give full understanding of the processing files, which are available under a free license.

5.7.3.1 Principle of multi-hole probe calibration

A five-hole probe can be operated in either nulling mode (the probe is rotated until its axis is aligned to the local flow direction, and the peripheral hole pressure are equal) or calibrated mode, where the unique relationship between probe hole pressures and flow variables (pitch, yaw, total pressure) has been obtained by calibration. This work is concerned with the calibrated mode, which is described in Krause and Dudzinsky, 1969; Bryer and Pankhurst, 1971; Treaster and Yocum, 1978; Main et al., 1996. Calibration is usually performed in a uniform free jet of well-defined properties (velocity and density). The probe tip is typically positioned at the center of the jet, and the probe rotated to every combination of pitch and yaw angle for which a calibration is required. The properties of the jet and the corresponding probe hole pressures are measured. The resulting unique relationship between probe hole pressures and flow angles defines the calibration maps for the probe. This is described in more detail in later sections.

5.7.3.2 Calibration coefficients

During a calibration, for each combination of probe yaw angle (β) and pitch angle (α)with respect to the flowthe jet total pressure, p_0, and static pressure, p, and the five hole pressures (p_1 to p_5, as shown in 5.15) are measured . The dynamic pressure and Re of the jet can therefore also be calculated. Coefficients are defined as follows (see, for example Bryer and Pankhurst, 1971):

$$C_\alpha = \frac{p_1 - p_3}{p_5 - p_{avg}}, \quad C_\beta = \frac{p_2 - p_4}{p_5 - p_{avg}}, \quad C_p = \frac{p_{avg} - p}{p_5 - p_{avg}}, \quad C_{p_0} = \frac{p_5 - p_0}{p_5 - p_{avg}} \tag{5.7}$$

where $p_{avg,1} = 1/2(\min(p_1, p_3) + \min(p_2, p_4)$.

For completeness, it is noted that there is some arbitrariness in the definition of p_avg. Common definitions in the literature include $p_{avg,2} = 1/4(p_1 + p_2 + p_3 + p_4)$ (Krause and Dudzinsky, 1969) and $p_{avg,3} = \min(p_1, p_2, p_3, p_4)$ (Qureshi and Povey, 2011). The first of these alternatives causes the denominator of equations (1) to pass through zero at relatively low angles of incidence: this leads to regions of extremely high sensitivity in which the calibration map is unusable. The second alternative definition does not suffer from the same sensitivity at high angle, but leads to maps that are more sensitive to face geometry (for pyramidal probes) than the definition used in this paper. Our definition represents a compromise that achieves good sensitivity and wide useable angle range.

During the calibration process α, β, p, p_0, and p_1 to p_5 are all known, allowing C_α, C_β, C_p and C_{p_0} to be determined. Calibration maps in the following form are produced: $\alpha(C_\alpha, C_\beta)$; $\beta(C_\alpha, C_\beta)$; $C_p(C_\alpha, C_\beta)$; and $C_{p_0}(C_\alpha, C_\beta)$.

5.7.3.3 Reducing measurement data in an unknown flow - using the Oxford Probe

When the probe is used to perform a measurement in an unknown flow, the only available information is p_1 to p_5, the measured hole pressures. Of the four non-dimensional groups (the coefficients) only C_α and C_β can be directly deduced from

the flow variables. Using the calibration maps $\alpha(C_\alpha, C_\beta)$, $\beta(C_\alpha, C_\beta)$, $C_p(C_\alpha, C_\beta)$ and $C_{p_0}(C_\alpha, C_\beta)$, and knowledge of C_α and C_β (from p_1 to p_5) it is possible to determine α, β, C_p and C_{p_0}) at every point in an unknown flow. Once C_p and C_{p_0}) are determined, expressions (1) can be rearranged to determine the remaining unknowns p and p_0 (from C_p, C_{p_0}, p_{avg}, and p_5).

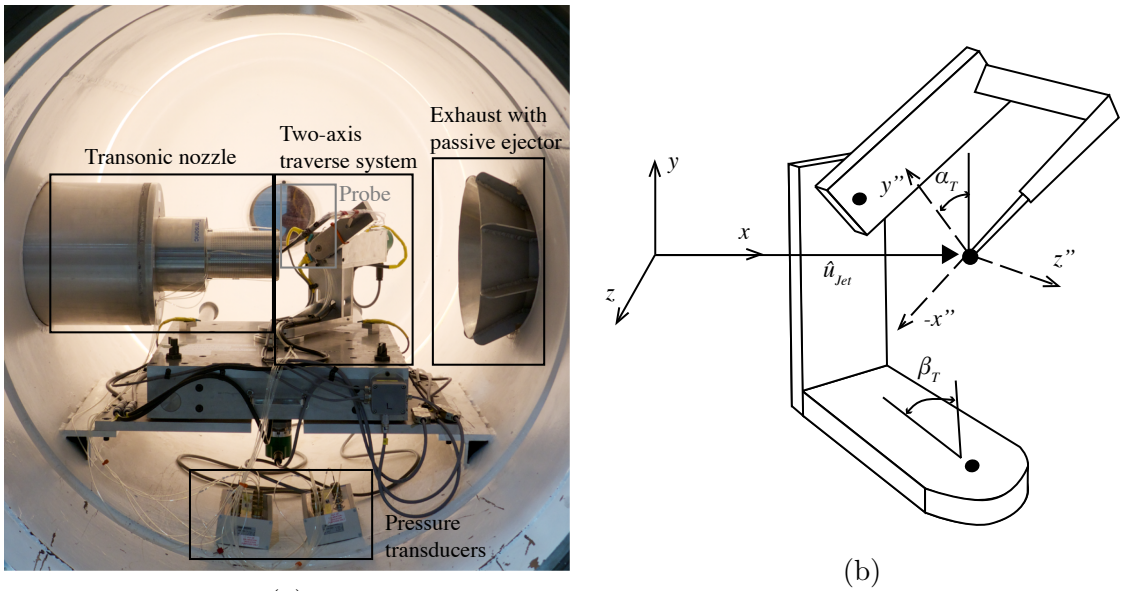
5.7.4 Calibration facility and procedure

In this section an overview of the Oxford Probe Calibration Facility, and discussion of the calibration procedure are presented. Subsequently the methods described in this section are applied to the calibration of a large number of probes, to demonstrate that the Oxford Probe can be used in a wide range of applications without individual calibration.

5.7.4.1 The Oxford Probe Calibration Facility

The Oxford Probe Calibration Facility (OPCF) is a 4-inch (100 mm) free-jet calibration tunnel with robotic two (rotational) axis traverse capability. A wide range of Mach numbers ($0 < M < 1.9$) is achieved using a combination of de Laval nozzles (1.3, 1.5, 1.7, 1.9) and a perforated nozzle ($0 < M < 1.2$). The tunnel can operate with inlet total pressures in the range 0 to 27.5 bar, and with jet static pressures in the range 0.3 to 10 bar, allowing a wide range of Re to be achieved, with independent control of Re and M. The facility has been extensively surveyed to demonstrate almost perfectly uniform jet flow at all Mach numbers. A schlieren system allows shock structure to be visualized in the transonic and supersonic regime. For the calibrations reported in this paper, a perforated transonic nozzle was used at subsonic conditions.

A photograph of the calibration tunnel and a schematic of the two (rotational) axis traverse system are shown in Figure 5.16a and Figure 5.16b respectively.



(a) (b)

Figure 5.16: (a) Photograph of the working pressure vessel of the Oxford Probe Calibration Facility, showing the transonic nozzle, two (rotational) axis traverse system, and passive ejector pump; (b) Schematic of the traverse system with flow-centred co-ordinate system and probe-centred co-ordinate system .

5.7.4.2 Contribution to the OPCF

The OPCF has been design and developed at the University of Oxford, under the direction of Dr. Thomas Povey (Henderson, 2009; Gowland, 2010; Nocera, 2011). At the outset of this research, the facility had been commissioned, including detailed 2D (planar) surveys of the jet profiles , and operated to calibrate a limited selection of probes (Sperrin, 2012; Woodward, 2013) - the two-axis (rotating) traverse (described below) for probe calibration had been installed as part of undergraduate project research. A number of improvements were made such that the facility is now truly capable of automated probe calibration at independently variable Mach and Reynolds numbers. These were:

- The partial redesign of the traverse electronics system to include; fail-safe mechanical limit sensors on both axes; a watchdog timer which disables the motor drive system in the event of a PC failure; and segregation of signal and motor driver (high EMF) systems, inc. shielded signal cables.

- The installation of multi-turn rotary encoders for position measurement and control feedback.
- The development of an automated LabVIEW graphical user interface for remotely controlling the traverse (via PC).
- Design, procurement and commissioning of an orifice plate system for the control of the tunnel static pressure.

5.7.4.3 Probe traverse system

The Oxford Probe Calibration Facility traverse system has two independent rotational axes, controlled by stepper motors and high-ratio (100:1) low-backlash gearboxes. Output shaft backlash is lower than 0.17. Traverse arm angles α_T and β_T (see Figure 5.16b) are measured using absolute-datum multi-turn optical encoders mounted to the motor shaft. The error in α_T and β_T was of order the output backlash (0.17) and can be ignored.

To transform the jet velocity vector in the flow-centered co-ordinate system (x, y, z), u_{jet}, to the jet velocity vector in the probe-centered co-ordinate system (x'', y'', z''), u''_{jet}, two transformations are required. First, a rotation about the flow-centered y-axis (y, see Figure 3b) by the traverse system pitch angle, β_T. Second, a rotation about the probe-centred z-axis ($z' = z''$, see Figure 5.16b) by the traverse system yaw angle, α_T. These rotations are denoted $R_y(\beta_T)$ and $R_{z'}(\alpha_T)$ respectively. The order of the rotations must be correct, because the traverse system pitch is with respect to an intermediate system (x', y', z')—not marked in Figure 5.16b—which has already been subject to the rotation $R_y(\beta_T)$ with respect to the flow-centered co-ordinate system. Thus $\hat{u}''_{jet} = R_{z'}(\alpha_T) \times R_y(\beta_T) \times \hat{u}_{jet}$. These operations result is the following relationship between the yaw and pitch angles of the traverse-system arms, α_T and β_T, and the yaw and pitch angles of the flow in the probe co-ordinate system, α and β:

$$\beta = \tan^{-1} \frac{-\sin \beta_T}{\cos \alpha_T \cdot \cos \beta_T}, \quad \alpha = \tan^{-1} \frac{-\sin \alpha_T \cdot \cos \beta_T}{\cos \alpha_T \cdot \cos \beta_T} = \alpha_T \tag{5.8}$$

It is noted that $\alpha = \alpha_T$ but that, other than for very small pitch angles α_T, $\beta \neq \beta_T$.

5.7.4.4 Probe roll correction

Precise roll-alignment (rotation around the x'' axis) can be difficult to achieve in practice. Probe shaft diameters as small at 5 mm are not uncommon. As an example, a 5 mm diameter shaft has 2.3° roll-offset for every 0.1 mm misalignment from nominal at the shaft diameter (normally via the alignment of scribed marks). Compound errors may result if the calibration holder is different from the holder used in the unknown flow to be surveyed. To estimate the error resulting from roll misalignment, or to correct for misalignment if the roll-offset can be quantified, a roll transformation, $R_{x''}(\theta_T)$, can be employed to move from the nominal probe-centred co-ordinate system (x'', y'', z''), to the true probe-centred co-ordinate system (x''', y''', z'''), Here, θ_T is the estimated or quantified roll angle offset from the nominal position. Thus, $\hat{u}''_{jet} = R_{x''}(\theta_T) \times R_(z')(\alpha_T) \times R_y(\beta_T) \times u_{jet}$ and:

$$\beta_P = \tan^{-1} \left(\frac{\cos \theta_T \sin \beta_T - \cos \beta_T \sin \alpha_T \sin \theta_T}{\cos \alpha_T \cos \beta_T} \right) \tag{5.9}$$

$$\alpha_P = \tan^{-1} \left(\frac{\sin \theta_T \sin \beta_T + \cos \beta_T \sin \alpha_T \cos \theta_T}{\cos \alpha_T \cos \beta_T} \right) \tag{5.10}$$

This correction is used to correct for small roll misalignments in the present comparison by inferring the misalignment from the calibration contours.

5.7.4.5 Instrumentation and data acquisition

Probe pressure measurements, and nozzle upstream total and downstream static pressure, were conducted with 350 mbar differential pressure transducers (Sensor Technics BTE5000) connected via flexible tubing. Measurements were taken differential

to a reference pressure in the calibration plenum. The sensors had a typical combined error related to non-linearity, hysteresis and repeatability of ±0.2% of full scale output. Thermal compensation errors and long-term drift were accounted for on a run-by-run basis by zeroing against a laboratory barometer. The calibration plenum pressure was measured using 5 bar absolute transducers (Sensor Technics CTE8000) with combined uncertainty of ±0.1% of full scale output. The positions of the traverse axes (α_T and β_T) were measured at the motor shaft using absolute multi-turn encoders (Lika ROTACOD EMC58 26-bit) with analogue output. The resolution of the encoder measurements was $1.83° \times 10^{-3}$ at the gearbox output (based on 16-bit acquisition), two orders smaller than the backlash uncertainty. 16-bit analogue-to-digital converters (National Instruments 9205) were used to acquire all voltage signals at 2 kHz to avoid aliasing.

5.7.5 Comparison of calibration maps for 16 probes

To demonstrate that probes manufactured using additive manufacturing according to the Oxford Probe design exhibit excellent repeatability between their calibration maps once above a certain physical size, a large number of probes were manufactured and calibrated. In all 20 probe tips were manufactured using different manufacturing processes and in a variety of sizes, of which 16 were calibrated. Calibrations are compared in this section.

5.7.5.1 Description of the probe tips

The general design of the probes tips has been described above. In all, 20 probe tips were manufactured covering five sizes (D = 3, 4, 6, 8, and 12 mm), two materials (DMLS-steel and SLA-resin), and with two repeats per probe. Diagrammatic drawings of the probe tips are shown in Figure 5.17a. A close-up photograph of five sizes of DMLS probe tip is shown in Figure 5.17b, and nine completed probes manufactured in both DMLS and SLA are shown in Figure 5.17c. The leading truncated

pyramid of all tips were scaled versions of each other. The trailing cones had shallow included angles of 14.2° that extended a distance distance $L > 2.5D$ beyond the tip in the downstream direction. The probes are shown to be insensitive to the extended cone length. The reason for different cone length was to allow standard sized (1.6 mm outer diameter) tubing to be connected on the trailing end. The probe tips had keyways for roll alignment (visible in Figure 5.17a).

Manufacturing resolutions for four additive manufacturing methods (based on vendor enquires) are shown in Table 5.2. Of these four processes the two with the highest build accuracy were chosen to manufacture probe tips for this study: DMLS-steel with a layer height of 0.04 mm and SLA-resin with a layer height of 0.1 mm. Of the 20 manufactured probe tips the only ones that were poorly formed were the 3 mm SLA probe tips, which was unusable due to incomplete formation of the internal passages. For the DMLS process, visual inspection confirmed that the largest four sizes were well formed (4, 6, 8 and 12 mm) with only small defects in comparison to

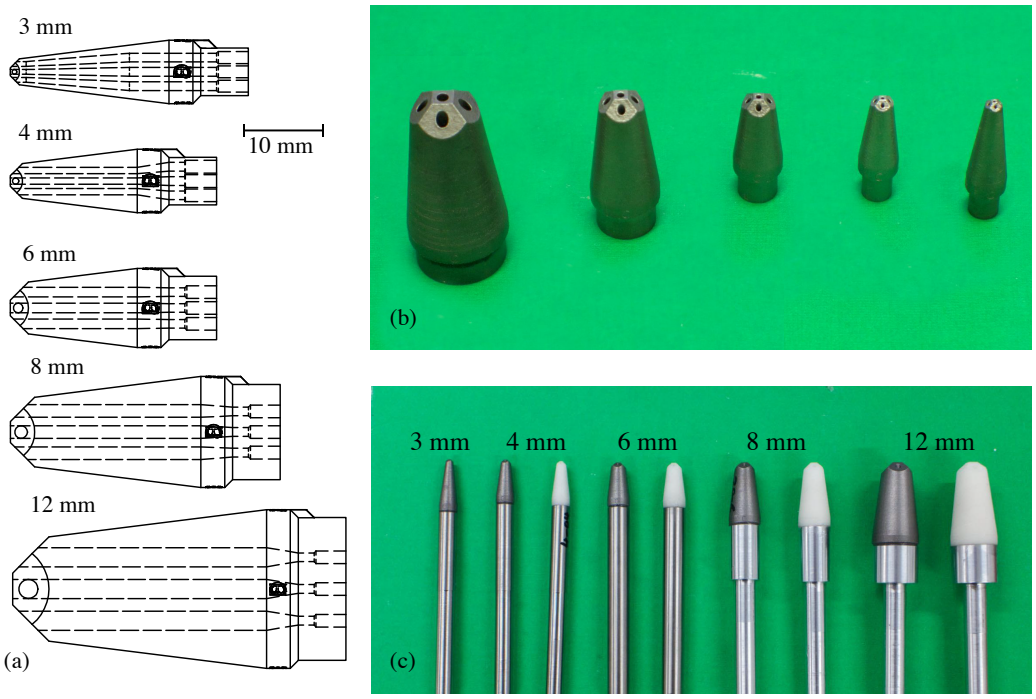


Figure 5.17: (a) Cross-sectional diagrams of Oxford Probe tips in 3, 4, 6, 8 and 12 mm diameter sizes; (b) Photograph of five DMLS probe tips; (c) Nine of the assembled probes.

Table 5.2: Summary of important manufacturing properties for AM processes (CRDM, 2013).

AM process	Material	Typical tolerance (± mm)	Minimum feature (mm)	Layer height (mm)
DMLS	metal	0.05	0.3	0.04
SLA	plastic	0.15	0.5	0.1
SLS	plastic	0.2	0.6	0.1
3D printing	plastic	0.25	0.9	0.25

the scale of the significant tip features. For the SLA probes this was true for tips in the largest three sizes (6, 8 and 12 mm). These numbers represent conservative practical limits for using the Oxford Probe without bespoke calibration. 16 of the 20 manufactured probe tips were calibrated: the DMLS and SLA probe tips in 4, 6, 8 and 12 mm sizes, with two repeats per tip.

The probe tips had keyways for roll alignment, and were mounted in machined metallic shafts. Deviation of the probe tip axis from the shaft axis was measured on a surface table using a digital height gaugemean misalignment was estimated to be 0.6°.

5.7.5.2 Calibration conditions

All 16 assembled probes were calibrated at a single Mach number, M = 0.3 (chosen to be in the subsonic range but with significant dynamic pressure to reduce measurement error), and at a single Reynolds number based on tip diameter, $\mathrm{Re}_D = 8 \times 10^4$. To achieve constant Reynolds number based on tip diameter, the tunnel jet Reynolds number had to be varied by a factor of three. This was achieved by changing the tunnel inlet total pressure and plenum static pressure–the tunnel is equipped with restrictors to facilitate this.

5.7.5.3 Probe and run-data identification

Probes and run-data are identified using the following conventions: metal or plastic (M or P); tip diameter in mm (04, 06, 06, 12); probe sample number (either 01, or

02 for the nominally identical partner); run number (R3001, R3002 etc.). Thus, a probe/run combination is specified with a code in the following form: M-04-01-R3001.

5.7.6 Results

Each of the 16 probes was calibrated according to the procedures described, in the range $-40° < \alpha_T < 40°$ and $-40° < \beta_T < 40°$. The four 8 mm probe and four 12 mm diameter probes were calibrated twice each to demonstrate repeatability. For all calibrations the jet Mach number and Reynolds number (based on probe tip diameter) were within ±10% of the nominal value.

5.7.6.1 Typical calibration maps, roll correction and repeatability

As an example of typical calibration data, the calibration maps—$\alpha(C_\alpha, C_\beta)$; $\beta(C_{/alpha}, C_\beta)$; $C_p(C_\alpha, C_\beta)$; and $C_{p_0}(C_\alpha, C_\beta)$—for one of the 12 mm diameter DMLS probes (M-12-02) are shown in Figure 5.18 for three nominally identical repeat runs (R3103, R3108 and R3109). Lines represent equal-increment iso-values of α, β, C_p and C_{p_0}.

A deliberate additional roll error was introduced for run R3109, the uncorrected data for which is plotted in red. The deviation from the nominal maps is clear. When a roll correction of 5.8° is applied to run R3109 data (see section 5.7.4.4), (and respective corrections to R3101 and R3108) data for the three repeat runs collapse almost perfectly, indicating exceptional repeatability of the calibration process. Negligible variation in the calibration surface occurs with repeat calibration – this is defined quantitatively below.

To eliminate the impact of roll-error on the data presented in this paper (likely roll-alignment error must be estimated in any probe calibration and measurement system, and should be accounted for if the roll-angle offset—between calibration and measurement—can be determined) roll-corrections were applied to all data. The average absolute roll-correction for the calibration runs reported in this work was 2.5°.

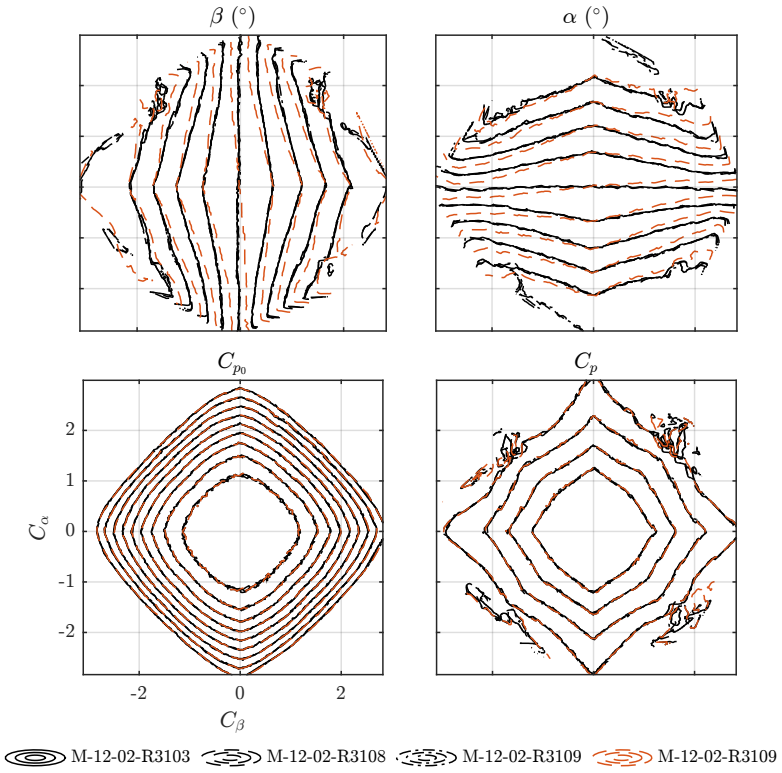


Figure 5.18: Comparison of calibration maps for repeat runs (R3103, R3108 and R3109) for a 12 mm diameter DMLS probe (M-12-02). Run R3019 is shown without (red) and with (black) an applied roll-correction of 5.8°

5.7.6.2 Qualitative comparison of calibration surfaces for different probes

As an example of the comparison of calibration maps for different probes, the maps—$\alpha(C_\alpha, C_\beta)$; $\beta(C_{/alpha}, C_\beta)$; $C_p(C_\alpha, C_\beta)$; and $C_{p_0}(C_\alpha, C_\beta)$—for four different 12 mm diameter probes are compared in Figure 5.19. The data are for two nominally identical DMLS probes (M-12-01 and M-12-02) and two nominally identical SLA probes (P-12-01 and P-12-02).

The qualitative agreement between the four calibration maps is excellent. The maps show good symmetry in all four quadrants (defined by the pyramidal sides of the probes), with only small differences between the maps.

The disagreement in the maps by processing the probe data for all probes using the calibration map for one of the largest DMLS probes (M-12-02) is presented below.

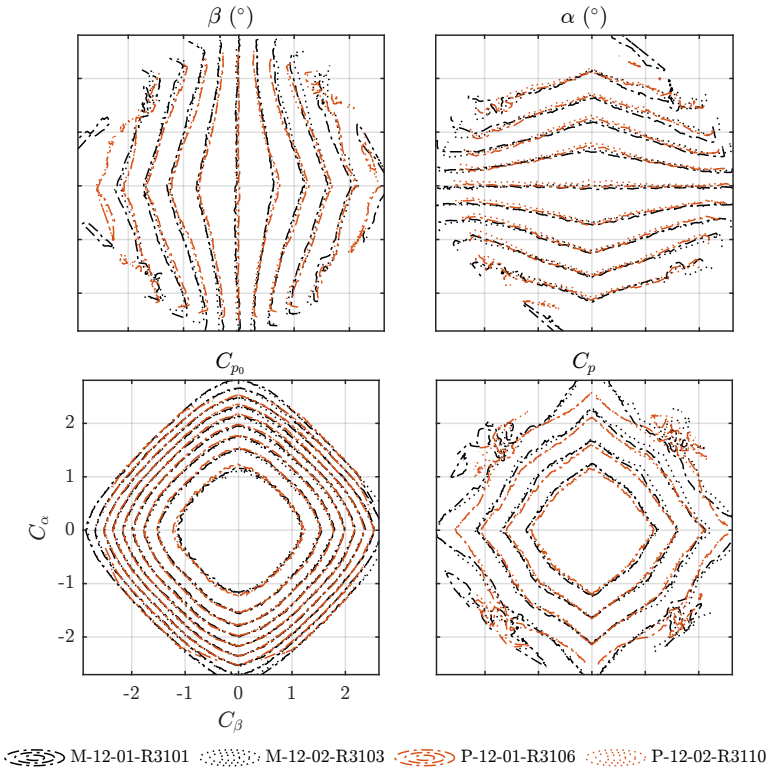


Figure 5.19

The disagreement between the returned (output from calibration map) flow variables and the known tunnel flow variables was used as a measure of the disagreement between maps. The calibration map for probe M-12-02 was used as the reference case, because the largest DMLS probes conform most accurately to the ideal geometry.

When comparing probes of different sizes, the qualitative agreement between individual calibration maps and the reference calibration map deteriorated probes of smaller size, as expected, but not to an extent that made the reference calibration map unusable, even for probes as small as 4 mm in diameter. This is quantified below.

5.7.6.3 Quantitative comparison of calibration maps–examples of surface plots

The error introduced by using a single reference calibration map is now quantifiedin place of a particular calibration map for a given probeto process data for each of

the probes tested. This was achieved by comparing flow properties (α_{ref}, β_{ref}, $p_{0,ref}$ and p_{ref}) derived using the reference calibration map for a given probe probe and comparing to the values measured independently by the tunnel instrumentation. The difference between these two sets of flow variables is the error introduced by using the reference calibration in place of a particular calibration (error due to the look-up method etc. is extremely small in comparison and can be neglected). Probes are compared using the following three metrics:

$$\epsilon_\alpha = \alpha_{ref} - \alpha, \quad \epsilon_\beta = \beta_{ref} - \beta, \quad \epsilon_q = 100\frac{|q_{ref} - q|}{q} \tag{5.11}$$

where dynamic pressures are defined by $q_{ref} = p_{0,ref} - p_{ref}$ and $q = p_0 - p$. Errors $epsilon_\alpha$ and ϵ_β are measured in degrees; error ϵ_q is as a percentage of the true dynamic pressure. This section presents plots of errors arising from the use of the reference calibration as a function of α and β—i.e. $\epsilon_\alpha(\alpha, \beta)$, $\epsilon_\beta(\alpha, \beta)$, and $\epsilon_q(\alpha, \beta)$—for a typical example of a probe with low error (probe M-12-01) and a typical example of a probe with high error (probe M-04-01). The error for all probes as a function of a single angle, the absolute angle of the flow to the probe axis, ϕ, is quantified below.

Figure 5.20 shows the errors $\epsilon_\alpha(\alpha, \beta)$, $\epsilon_\beta(\alpha, \beta)$ and $\epsilon_q(\alpha, \beta)$ for probe M-12-01 when processed using the reference calibration map (derived from probe M-12-02), plotted over the range of α and β corresponding to $\phi < 40°$. The error in α and β was generally lower than 0.5° confirming that probes in this size range can be used very accurately without individual calibration. The error in dynamic pressure was lower than 3% across the majority of the surface, with small localized regions above 10% at the outer limits of the calibration map (for $\phi > 30°$). The resulting error in velocity (not shown) is of order 1.5% across most of the map, with localised regions up to approximately 5% towards the outer edge (for $\phi > 30°$). The sensitivity for $\phi > 30°$ is due to strong gradients in the denominator of equations (5.7) in this region. These errors are quantified as a function of ϕ below.

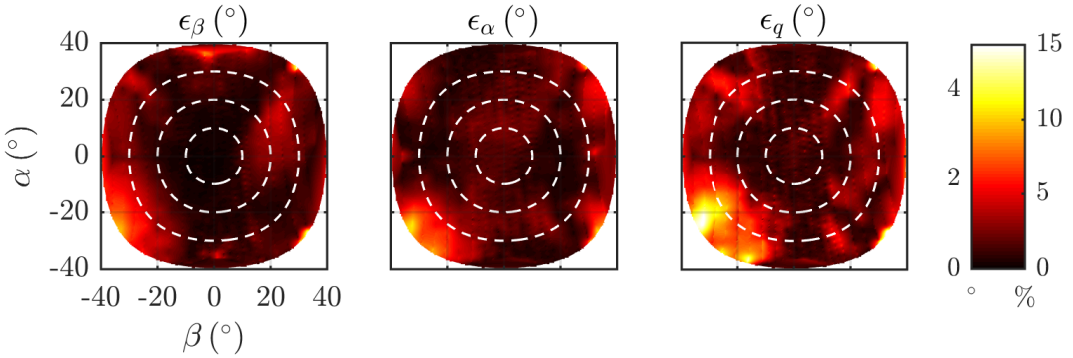


Figure 5.20: Error surfaces for probe M-12-01 when using the reference calibration map (obtained from probe M-12-02)an example of low error.

Figure 5.21 shows the errors $\epsilon_\alpha(\alpha, \beta)$, $\epsilon_\beta(\alpha, \beta)$ and $\epsilon_q(\alpha, \beta)$ for probe M-04-01 when processed using the reference calibration map (derived from probe M-12-02), plotted over the range of α and β corresponding to $\phi < 40°$. In this case data are presented for the smallest probe tip (4 mm) using the reference calibration map. Thus, errors are expected to be larger. The error in α and β was generally lower than 2° confirming that that even the smallest (4 mm) probes tested have reasonable accuracy without individual calibration. Towards the outer edges of the calibration map (for $\phi > 30°$) errors locally increase to 4° to 5° in the most sensitive regions. The error in dynamic pressure was lower than 5% across the majority of the surface, with small localized regions above 15% at the outer limits of the calibration map (for $\phi > 30°$). The resulting error in velocity (not shown) is of order 2.5% across most of the map, with localized regions up to approximately 7% towards the outer edge (for $\phi > 30°$). The four very localised spikes in dynamic pressure error beyond $\phi > 30°$ are thought to be due to slightly modified separation characteristics at high incidence angles, due to shape differences (ratio of build layer height to diameter).

5.7.6.4 Quantitative comparison of calibration maps–comparison of all probe types

The error introduced for all probe types is now quantified—when processing their data using the reference calibration map—as a function of the absolute angle of the

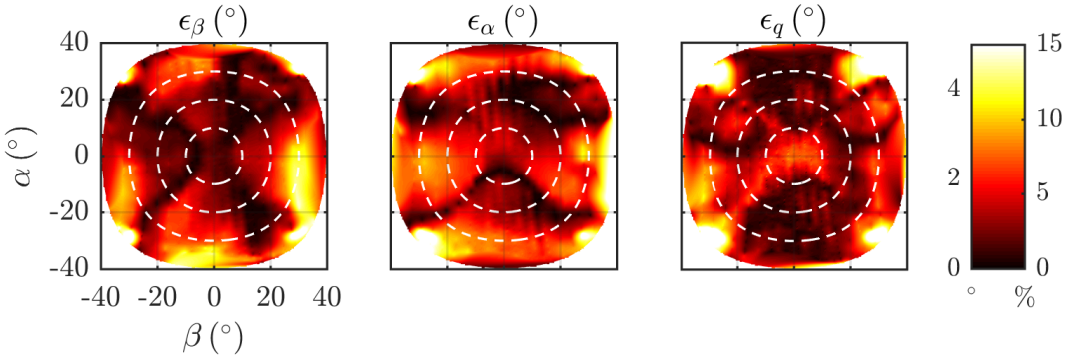


Figure 5.21: Error surfaces for probe M-12-01 when using the reference calibration map (obtained from probe M-12-02)an example of low error.

flow to the probe axis, ϕ. That is, $\epsilon_\alpha(\varphi)$, $\epsilon_\beta(\varphi)$ and $\epsilon_q(\varphi)$ are presented as line plots in Figure 5.22. Here the errors are calculated as root-mean-squared (RMS) error in rolling-average bins of 1° width in φ.

For all eight probe types, the RMS error in α and β is everywhere lower than 2.5° in the range $\varphi < 35°$. This confirms that for both metal and plastic probes, in a size range 4mm $< D <$ 12mm , probes according to the Oxford Probe design can be used with good accuracy without recourse to individual calibration. Indeed, alignment errors and other errors (sensitivity to turbulence, flow property gradients etc.) not normally accounted for in less demanding experiments may be expected to give rise to larger errors than the error resulting from the use of a reference calibration as a proxy for an individual calibration. The error in dynamic pressure is larger, but other than

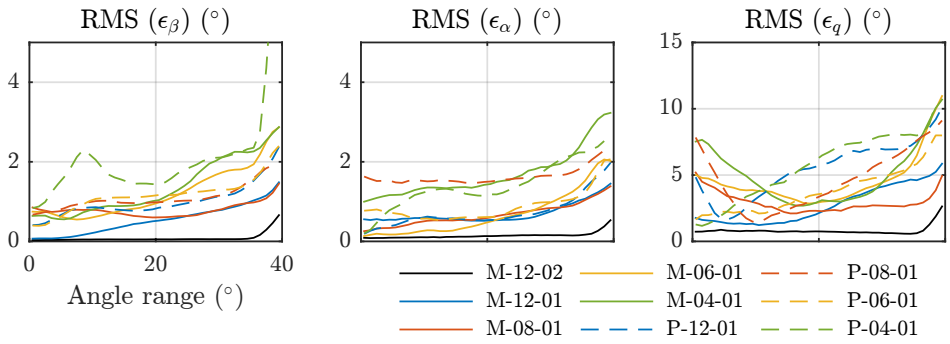


Figure 5.22: Errors as a function of angle with respect to the probe axis—$\epsilon_\alpha(\varphi)$, $\epsilon_\beta(\varphi)$ and $\epsilon_q(\varphi)$—calculated as root-mean-squared error in rolling-average bins of 1 degree width in φ.

for the smallest metal probe (4 mm) and the smallest two plastic probes (4 mm and 6 mm), this error was generally less than 5% in the range $\varphi < 35°$ resulting in errors of less than 2.5% in the value of inferred velocity. Taking all probes into account, including the smallest metal and plastic probes, the error in dynamic pressure in the range $\varphi < 35°$ was everywhere less than 8% leading to errors in velocity less than 4%. Even for the smallest probe tested, the Oxford Probe can be used with reasonable accuracy without individual calibration.

5.7.6.5 Quantitative comparison of calibration mapssummary for all probes

Figure 5.23 quantifies the RMS errors—ϵ_α, ϵ_β and ϵ_q—for all 16 probes tested, across the range $0 < \varphi < 35°$.

For both DMLS-metal and SLA-resin probes in sizes 12, 8, 6 and 4 mm (i.e. all probes tested), the Oxford Probe can be used with an average error in α, β lower than 2°, and an average error in dynamic pressure lower than approximately 7%, equivalent to a velocity error of no more than 3.5%. The equivalent numbers for the smallest (4 mm) plastic probe, which is at the limit of the manufacturing process, were average errors in α and β of 3.5^{circ} and an error in dynamic pressure of 8%, resulting in a velocity error of approximately 4%.

These errors are comparable in magnitude to errors due to installation effects neglected by many users, and show that the Oxford Probe can be used in many

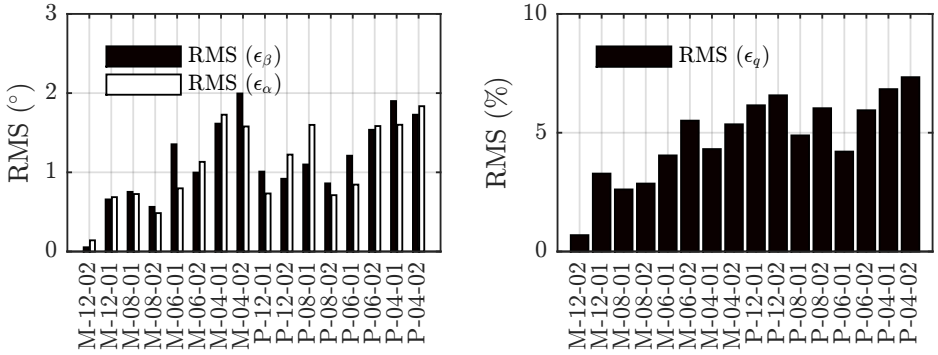


Figure 5.23: RMS errors ϵ_α, ϵ_β and ϵ_q and for all 16 probes tested, across the range $0 < \varphi < 35°$

environments with equivalent accuracy to an individually calibrated probe. On this same basis, the RMS error across the range $0 < \varphi < 35°$ associated with calibration repeatability (discussed first in section 8.1.) was found to be of the same order as that related to data interpolation (i.e. M-12-02 in Figure 10).

5.7.7 Discussion

By detailed analysis of the calibration maps of 16 probes manufactured using additive manufacturing according to the Oxford Probe design, but in different materials and at different scales, it was demonstrated that the open source probe can be used in many environments without individual calibration. The intent is to widen access to multi-hole probe measurement techniques in educational and research environments, by allowing end-users to self-manufacture probes according to the Oxford Probe design, and reduce measurements with the reference calibration and software pack which is available at no fee from the corresponding author. Probes with tip sizes 4 mm and up, and manufactured using DMLS of good build quality can be used with typical error in α, β lower than 2°, and an average error in dynamic pressure lower than approximately 7%, equivalent to a velocity error of no more than 3.5%. This is comparable to bespoke calibrated probes in many situations.

5.8 A frequency response model for pressure probes

The use of remote pressure transducers connected to physical hardware by circular tubing is commonplace in aerodynamic experiments, and were used widely in the characterisation of the OLCS. In the design of experiments, the estimation of measurement bandwidth is critical to ensure meaningful results. This section addressed a need that was identified for a simple and accurate model for the common tube-transducer pressure probe system. This section discusses example cases and makes comparisons to existing models and experimental results, while Section 5.5.1.1 presented estimates relevant to the OLCS experiment derived from the proposed new model.

5.8.1 Background and motivation

Pressure probe systems (probe, line and transducer volume) are used in many research fields for experimental characterization of fluid flows, as well as for routine monitoring in many process industries, in power generation machines and on airplanes, for example. Probe systems may be wall mounted (static pressure tappings) or fully immersed (probes for measurement of total pressure, flow direction etc.).

In general, it is desirable to place pressure transducers as close to the measurement point as possible to maximize measurement bandwidth. In some applications it is possible to install very small transducers (which tend to be expensive and are limited on operating temperature) directly at the point of interest. It is more conventional to have a pressure sensing hole located at the point of interest, connected via circular tubing (the line) of finite length (typically anywhere from a few cm to a few m) to a remote pressure transducer. In the simplest system (where the probe and line have the same internal diameter) the probe-system reduces to a circular tube of constant diameter open at one end and connected to a pressure transducer at the other, as in Figure 5.24. XX More complex systems are discussed.

In the conventional tube-transducer probe-system, the pressure transducer does not indicate the change in pressure at the point where the tube is inserted in the flow (), rather it indicates the response of the entire probe system in terms of

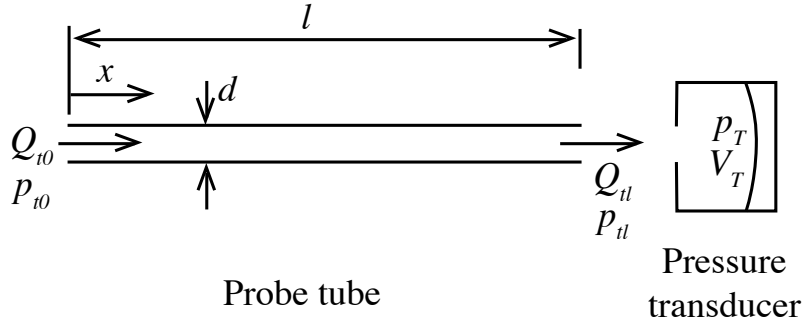


Figure 5.24: Simple probe-transducer system as subcomponents.

the pressure adjacent the transducer diaphragm (). The system acts as an analogue filter, distorting with respect to in both magnitude and phase. The frequency band for which the magnitude and phase remain undistorted (although group and phase delay are always non-zero), defining the bandwidth, is therefore of interest. In practice, the bandwidth is usually defined as the band from 0 Hz (DC) to the -3 dB cutoff frequency or to +3 dB at the first resonance peak, depending on whether the system is under-damped or over-damped.

At the probe-system design stage, a relatively simple method to predict probe-system response would inform decisions regarding transducer choice (in terms of transducer volume V_T), tube length (l) and diameter (d). It is widely understood that minimizing the values of V_T and l/d^2 maximizes bandwidth (Xie and Geldart, 1997), however accurate quantitative prediction remains non-trivial, and is important in preliminary design and for setting, for example, traverse speeds etc.

5.8.1.1 Comparison of existing models

To date, a number of models have been presented for either specific pressure probe configurations (Xie and Geldart, 1997; Van Ommen et al., 1999; Clark and Atkinson, 1988; Caldwell et al., 1959) or generalized formulations Bergh and Tijdeman, 1965; Richards, 1986 that can be built in to models of more complex fluidic systems. The models in the literature are analyzed below using an analogy to electrical circuits. This is a convenient means to understand the assumptions inherent in each model.

5.8.1.2 Basis of comparison

Fluid transmission lines have previously been analyzed by analogy to early work on electrical transmission lines in communication (Kirshner (1975) provides a good summary). Fluid transmission lines are now a standalone subject (e.g. Yang and Tobler, 1991; Almondo and Sorli, 2006; Ayalew and Kulakowski, 2005). Each continuous circular tube section is treated as a lossy transmission line, while connected volumes are

treated as capacitive components. Voltage (U_S, U_T) is analogous to pressure difference and current (I_S, I_T) to volume flow. At the most general level, this is described in Figure 5.25 for the simplest probe-transducer system shown in Figure 5.24.

To gain further understanding of this analogy, a differential element of the transmission line is illustrated in Figure 5.26. A transmission line element consists of distributed series resistance (R' dx) and distributed series inductance (L' dx) per unit length of the conductor collectively the series impedance per unit length (Z' dx). The fluidic analogies are viscous pressure loss and fluid inertance respectively. Additionally, the transmission line consists of distributed shunt admittance (G' dx) and distributed shunt capacitance (C dx) per unit length between the conductor pair collectively the shunt admittance per unit length (Y' dx). The shunt admittance (G') is related to the heat transfer at the tube wall and would be zero for an adiabatic tube. The shunt capacitance is analogous to the storage of compressible fluid within the tube.

The distributed-parameter model (Goodson and Leonard, 1972) of a transmission line is produced by considering the system as dx approaches zero this yields wave equations. These equations are typically manipulated to yield the transfer matrix representation of a transmission line in terms of hyperbolic expressions:

$$\begin{bmatrix} U_S \\ I_S \end{bmatrix} = \begin{bmatrix} \cosh \Gamma l & -Z_C \sinh \Gamma l \\ (-1/Z_C) \sinh \Gamma l & \cosh \Gamma l \end{bmatrix} \begin{bmatrix} U_T \\ I_T \end{bmatrix} \tag{5.12}$$

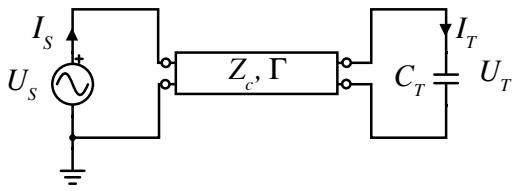


Figure 5.25: Electrical analogy of fluid transmission line model for a simple tube-transducer system.

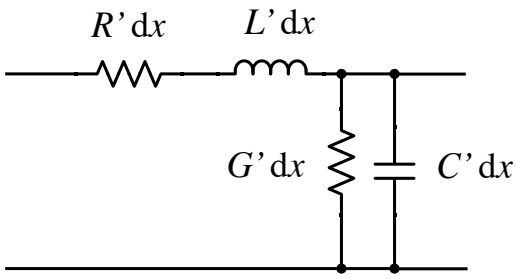


Figure 5.26: Differential element representation of a transmission line. Primed values are per unit length.

The models of Bergh and Tijdeman (1965) and Richards (1986) both use this distributed-parameter treatment for the tube section (or sections). A number of simplified methods exist for approximating the transmission line. The models of Xie and Geldart (1997), Van Ommen et al. (1999) and Clark and Atkinson (1988) Xie and Geldart, 1997; Van Ommen et al., 1999; Clark and Atkinson, 1988 effectively use a lumped-parameter approach, in which the tube is divided in to a finite number of elements (as in Figure 3) of finite length (i.e. dx >> 0). These are discussed in section below. It is also possible to consider only a finite number of harmonic modes Goodson, 1970.

The propagation constant (Γ) and characteristic impedance (Z_C) of equation 5.12 are defined in the most general case:

$$\Gamma = \sqrt{ZY} \qquad (5.13) \qquad\qquad Z_C = \sqrt{Z/Y} \qquad (5.14)$$

It is evident from equations 5.12 to 5.14 that Z and Y completely describe the transmission line system. In the case of ideal electrical components (e.g. linearly resistive elements), the above system of equations can be solved directly in terms of the variables in Figure 5.26. Clearly for the fluidic case, relationships for viscous loss, fluid impedance and fluid capacitance in terms of pressure and volume flow (or velocity) must be derived. The accurate formulation of these terms for the fluidic case is non-trivial, however. The assumptions made in deriving these terms delineate the existing models and are considered in further detail in the following sections.

5.8.1.3 Distributed-parameter, dissipative-friction models

The model of Bergh and Tijdeman (1965) (and equivalent models) have been shown experimentally to describe the physical probe-transducer system with good accuracy (Van Ommen et al., 1999; Bergh and Tijdeman, 1965; Richards, 1986). Both models utilise the distributed parameter treatment of the tube (or tubes), and it is this that allows them to describe the harmonic response, which is dominant in many configurations. Such models use the so-called 'dissipative friction' model (Goodson and Leonard, 1972) based on the work of Iberall (1950) which considers the frequency dependence of the viscous effects and heat transfer in the tube.

The response for a simple system (i.e. Figure 5.24) was modelled using a distributed parameters approach with the dissipative friction model. The magnitude response is shown in Figure 5.27 along with the first 3 resonant frequencies for an open tube of the same dimensions. In this case the transducer volume (V_T - that of a First Sensor CTE-8000) was significant in comparison to the tube volume. The figure illustrates that the system consists of a harmonic response similar to that of an open organ pipe, and an additional resonant peak at lower frequency (which would define the useful bandwidth), which results from the low-order impedance-capacitance system of the tube and transducer. As V_T tends to zero, this latter system disappears and the tube harmonic response dominates, as in Figure 5.27.

The model of Bergh and Tijdeman (1965) and the equivalent model of Richards (1986) have been shown experimentally to describe the physical probe-transducer system with good accuracy (Van Ommen et al., 1999; Bergh and Tijdeman, 1965; Richards, 1986). Both models utilize the distributed-parameter treatment of the tube (or tubes), and it is this that allows them to describe the harmonic response, which is dominant in many configurations. Additionally, both models use the so-called dissipative-friction model Goodson and Leonard, 1972 based on the work of Iberall (1950) and Nichols (1962) which considers the frequency dependence of the viscous effects and heat transfer in the tube.

The response for a simple system (Figure 5.24) has been modeled using a distributed-parameter approach with the dissipative friction model and the magnitude response is shown in Figure 5.27a along with the first 3 resonant frequencies for an open tube of the same dimensions. In this case the transducer volume (200 mm^3 that of a First Sensor CTE-8000) is significant in comparison to the tube volume (1548 mm^3). The figure illustrates that the system consists of a harmonic response similar to that of an open organ pipe, and an additional resonant peak at lower frequency (which would define the useful bandwidth in this case), which results from the low-order impedance-capacitance system of the tube and volume. As the transducer volume tends to zero, this latter system disappears and the harmonic response dominates, as shown in Figure 5.27a.

The distributed-parameter treatment is capable of describing both the low-order and harmonic response. While this enables the models to produce the correct characteristic curves, it is also important that the tube series impedance (Z) and shunt admittance (Y) are well described for the fluidic problem. If Y and Z are poorly described, the characteristic curve may be similar, however the damping and frequency of each resonance mode will be incorrect. The dotted lines of Figure 5.27a and Figure 5.27b illustrate the effect of replacing the dissipative friction model with a simplified

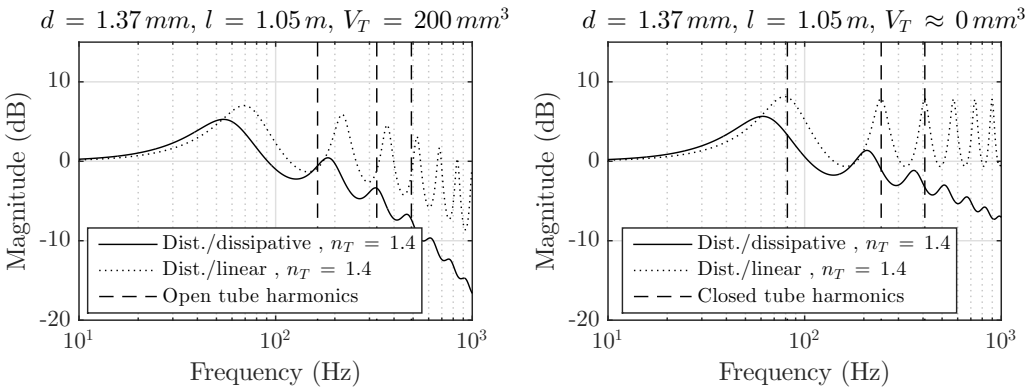


Figure 5.27: Magnitude of a simple probe-transducer system using distributed parameter model of tube and the first 3 organ pipe (d, l) harmonic frequencies.

friction model the linear-friction described in Goodson and Leonard, 1972. The characteristic shape of the curve remains the same, however the magnitude and frequency of the peaks is affected.

Γ and Z_C for the dissipative friction model, along with τ, n and Y on which they depend are defined:

$$\Gamma = \frac{\omega}{\bar{c}}\sqrt{\frac{J_0(\tau\sqrt{\mathrm{Pr}})\gamma}{J_2(\tau\sqrt{\mathrm{Pr}})n}} \qquad (5.15)$$

$$Z_C = \frac{\Gamma}{Y} \qquad (5.16)$$

$$\tau = j\left(\frac{d}{2}\right)\sqrt{\frac{\bar{\rho}j\omega}{\mu}} \qquad (5.17)$$

$$Y = \frac{j\omega}{\bar{c}}\frac{\pi d^2}{4}\frac{\gamma}{\bar{\rho}\bar{c}n} \qquad (5.19)$$

$$n = \left(1 + \frac{\gamma - 1}{\gamma}\frac{J_2(\tau\sqrt{\mathrm{Pr}})}{J_0(\tau\sqrt{\mathrm{Pr}})}\right)^{-1} \qquad (5.18)$$

A number of approximations can be made for equations 5.12 to 5.19 in order to yield a simplified solution. For example, one could replace the Bessel function with an approximation which utilised algebraic terms. Removal of the Bessel function altogether could be achieved with an alternative friction model. The hyperbolic trigonometric terms of equation 5.12 could be approximated by an infinite product as described in Goodson and Leonard (1972).

5.8.1.4 Low-order models with lumped parameters

A number of low-order models exist in the literature. These considered a simple momentum balance across the tube and transducer volume to yield first and second order ODE-based models. The second order model of Clark and Atkinson (1988), the proposed variation of Van Ommen et al. (1999) and the first order model of Xie and Geldart (1997) are all such models. The model of Edelman (Caldwell et al., 1959), while producing reasonable results, is not discussed at length since its derivation was not published.

The magnitude response predicted by the above low-order models (excluding the model of Xie and Geldart (1997)) is shown in Figure 5.28. The figure illustrates that compared to the prediction of a distributed parameter, dissipative friction model, the models of Clark and Atkinson (1988) and Van Ommen et al., 1999 do not predict the first resonance peak accurately and do not predict harmonic resonance (as expected for a second order model). The model of Edelman (Caldwell et al., 1959)) predicts the first resonance and first harmonic frequency with some accuracy for this configuration. The predicted bandwidth (±3 dB frequency) varies widely. The disagreement can be understood through further analysis of the formulation of these models.

The low-order models are relatively easily compared amongst each other on the basis of their common momentum balance formulation. It is not immediately clear how these formulations compare to the distributed parameter models in terms of simplifying assumptions. Simply comparing results from each model for particular cases does not necessarily provide insight in to the shortcomings of the individual models or any means by which to improve them. Nevertheless, as a starting point, the momentum balance (as presented in Van Ommen et al. (1999), although in terms of volume flow rate (Q) for consistency herein) is first considered:

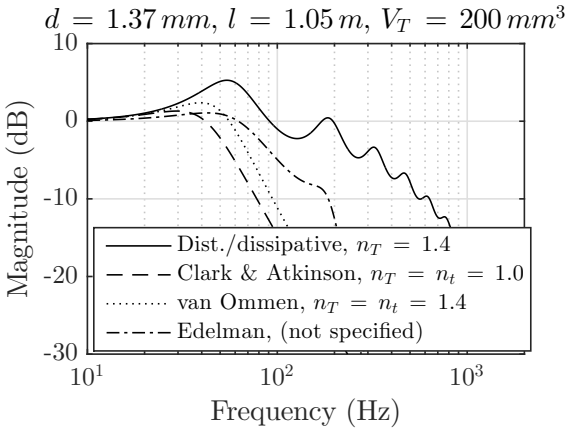


Figure 5.28: Comparison of the low-order lumped parameters models for a simple probe-transducer system. The distributed parameter, dissipative friction model is included for reference.

$$p_T(t) = p_{t0}(t) - \frac{32\mu l}{d^2}\frac{4Q(t)}{\pi d^2} - \bar{\rho}\frac{\mathrm{d}Q}{\mathrm{d}t}\frac{4}{\pi d^2} \tag{5.20}$$

The first right hand side term is the driving pressure at the open end of the tube, the second is the viscous pressure loss (based on the Hagan-Poiseuille equation - referred to as the linear friction model (Goodson and Leonard, 1972)), the third term is the inertia of the fluid in the tube (which is ignored in the model of Xie and Geldart (1997)). The fluid volume flow rate (Q) was then derived from the ideal gas equation (Van Ommen et al., 1999):

$$Q(t) = \frac{V_{Tot}}{n\bar{p}_{x0}}\frac{\mathrm{d}p_T}{\mathrm{d}t} \tag{5.21}$$

Equation 5.21 and its time-derivative can be substituted in to equation 5.20 to yield a second order ODE relating the pressure of interest (p_{t0}) to the transducer-measured pressure (p_T).

It is apparent from equation 5.20 that the pressure is explicitly considered at only two locations—each end of the tube—and that the flow rate is assumed to be constant along the tube. The tube is therefore quasi-zero-dimensional. This precludes the prediction of any harmonic modes by these models. Furthermore, equation 5.21 implies that the expansion of the fluid in the tube and the transducer is treated as a lumped system, which is likely to be an additional source of error.

These models can be more easily understood by considering an electrical circuit analogy - Figure 5.29. This also allows for convenient comparison to the transmission line models of the previous section (cf. Figure 5.25). This circuit (in which $\mathrm{d}x = l$) implies that I_S is constant across the series resistive and inductive components, which collectively represent a zero-dimensional (in space) system, confirming the previous conclusion regarding the treatment of the tube. As per the previous conclusions, the system describes a single capacitive component (noting the parallel connection of C_t and C_T).

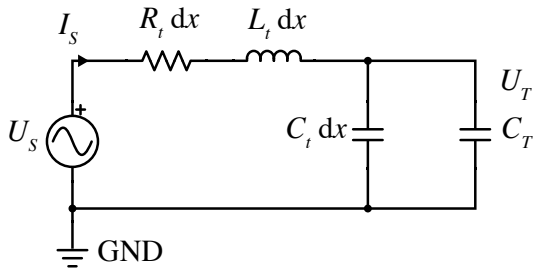


Figure 5.29: Electrical analogy of Xie and Geldart (1997) ($L_t = 0$), Clark and Atkinson (1988) and Van Ommen et al. (1999) models. $\mathrm{d}x = l$ in all cases.

It is apparent that the formulation of these models include some significant simplifications of the physical probe-transducer system. Considering only the momentum balance (equations 5.20 and 5.21), it is not necessarily clear whether the models describes the tube in a meaningful way - the quasi-zero-dimensionality, and lumping of tube and transducer volumes being particularly counter-intuitive. By considering the circuit analogy (Figure 5.29), however, it becomes clear that the components representing the tube (R_t, L_t and C_t) relate to a coarse approximation of a transmission line (cf. Figure 5.26) specifically an approximation where $\mathrm{d}x$ is finite (in this case $\mathrm{d}x = l$) rather than infinitesimal as in the distributed parameters method. These models are therefore a lumped (by length) parameters approximation with the number of lumps (N) equal to 1. By reducing $\mathrm{d}x$ the solution would approach that of a distributed parameter solution (as in the previous section) as N approached infinity. It is likely that the model of Edelman (in Caldwell et al., 1959) was based on a lumped parameters formulation with $N = 2$, possibly with a correction for the damped natural frequency.

5.8.1.5 The need for a simplified model

The general tube-transducer response problem was rigorously described by the Bergh and Tijdeman (1965) model and again by Richards (1986) in an analogous method, both of which are suited to systems of greater complexity than the simplest system of common interest. Nachtigal (1990) presented a simple method for systems that

were approximately lossless (i.e. low l/d^2). Furthermore, the various approaches to the problem of fluidic components such as tubes and volumes were generalised in the 1975 reference text of Kirshner (1975). Despite these resources, attempts to simplify the probe-system response problem for simple systems (the commonly-cited models for probe system response) are often either unwieldy to implement or inaccurate. A simple but accurate method to estimate probe-system response is seen to be helpful.

Fluid transmission in tubes is a wave propagation problem dealt with analytically using mathematical models (e.g. Iberall, 1950) that include transcendental terms not amenable to hand calculations. It is possible to derive general rules of thumb from the full equations (Van Ommen et al., 1999) for the case of simple pressure probes. Alternatively, employing methods to remove (by approximation) the transcendental terms (e.g. Yang and Tobler, 1991; Goodson, 1970) yields a generalized analytical tool and is discussed below.

The aim of this paper is to present a simple but accurate low-order model for probe-system bandwidth estimation using hand calculations (no scripting), that is able to additionally provide a meaningful Bode plot with limited computational effort.

5.8.2 Development of a new model

Of the existing models discussed in the previous section, none could be considered as being both accurate and easy to use. The distributed parameter models (with dissipative friction), while flexible and accurate, are relatively time consuming to implement (requiring numerical methods), while the simpler low-order models were demonstrated to lack accuracy and to overlook harmonics and frequency dependent loss mechanisms entirely. It is clear that a model for the widely considered tube-transducer configuration of Figure 5.24 which achieves a balance between accuracy and ease of implementation would be particularly useful. While the model of Edelman (in Caldwell et al., 1959) is in this category, its lack of published derivation means it

has not been widely adopted. It also predicts the magnitude of the resonance peaks poorly.

This section presents the development of a new model which has the simplicity and ease of use of a low-order model but with improved accuracy - a low-order s-domain polynomial transfer function formulation. The advantage of low-order transfer function models is that expressions for resonant frequency and cut-off frequency can be derived from the system poles. This means that an estimate of the probe bandwidth could be made with the use of simple equations with rational terms.

In discussing the existing models in the previous section, two fundamental aspects of model formulation emerged. The first was the treatment of the tube - either continuous as in the distributed parameter method, or discrete as in the lumped parameters method. The second aspect was the propagation (or friction) model - specifically the treatment of friction, inertance and heat transfer in the tube. These two aspects are discussed separately below.

5.8.2.1 Tube treatment

The mathematical treatment of the tube provides the framework for a model of a tube-transducer system, the treatment of the volume being comparatively simple. In the previous sections, two approaches have been identified in existing probe models - the distributed parameters approach and the lumped parameters approach. The latter approach, when coupled with simple fluidic expressions for R, L and C (e.g. the linear friction model), yields relatively simple equations which can be reduced to an s-domain polynomial transfer function, although the system order increases with N, and the polynomial coefficients become unmanageably large in their exact form. On the other hand, the distributed parameters model, as represented by equation 5.12, does not reduce to an easily used form due to its transcendental terms.

It is possible to simplify equation 5.12 by employing Taylor series approximations of each (tube) matrix element (Kirshner, 1975) or by approximation of the

hyperbolic functions with infinite product expressions, which are referred to as modal approximations (Goodson and Leonard, 1972). The approximation of the hyperbolic trigonometric terms by infinite products has the advantage of preserving the roots of the equations, which is not the case for the Taylor series expansion method (Kirshner, 1975) nor if the tube is approximated using the lumped parameters method. The infinite products method, consisting of N products will resolve the N^{th} harmonic. Hence for bandwidth estimation alone, $N = 1$ might be sufficient.

The seminal modal approximation of Goodson (1970) can be easily used to demonstrate the usefulness of this approach, but does not yield a transfer function which is easily separable in terms of s, making further analysis cumbersome. Addressing a similar set of problems (transcendental, irreducible expressions) for the purpose of creating control models, Yang and Tobler (1991) developed a modal formulation based on second order $\bar{s}$-domain (defined below) polynomial expressions, which lends itself well to the problem at hand.

5.8.2.2 Propagation models

A number of fluid propagation models applicable to the circular tube of a probe-transducer system were summarised by Goodson and Leonard (1972). The most basic model is the lossless model which does not account for the effect of viscosity or heat transfer, instead considering only fluid inertance and tube capacitance. The second commonly considered model is the linear friction model, in which viscous effects proportional to mean (cross sectional) velocity are considered, although heat transfer is not, as in the model of Van Ommen et al. (1999). Finally, the most accurate is the dissipative model developed by Iberall (1950) and Nichols (1962) which accounts for the frequency dependence of viscous effects and heat transfer.

Each of these 3 models can be applied to a particular type of tube configuration with accuracy. Goodson and Leonard (1972) used the dissipation number (D_n) to delineate the types of system which were suited to each model:

$$D_n = \frac{4vl}{\bar{c}d^2} \tag{5.22}$$

Intuitively, where dissipation along the tube is small (Goodson and Leonard (1972) suggest $D_n < 0.0001$) the lossless model gives reasonable results, while the dissipative model provided the best accuracy where D_n is relatively large. A dependence on the line termination—a function V_T—also exists. For pressure probes measuring air at atmospheric conditions (1 bar, 273 K), and considering a criteria of $D_n < 0.01$, the maximum length of a 1 mm tube for lossless treatment is approximately 50 mm, limiting the usefulness significantly.

In general, the dissipative model is accurate across all cases with no mean flow (subsonic, acoustic propagation) although it also holds for small mean flow (Kirshner, 1975), while the lossless case is a useful simplification for tubes of small l/d^2 and V_T. The average friction model should offer some improvement as viscous effects in the tube increase from near-zero, however for air (and other gasses with $\gamma \neq 1.0$) the frequency dependence of the polytropic exponent (n_t) and therefore viscous effects and heat transfer make its region of applicability poorly defined. Goodson and Leonard (1972) suggested that in the case of gasses with $\gamma \neq 1.0$, the dissipative model is the only suitable choice.

Recognising the need for an algebraically simplified way of describing a tube with the accuracy of the dissipative friction model and distributed parameter tube treatment, Yang and Tobler (1991) developed a modal approximation of the distributed parameter treatment. The approximation used second order polynomial terms to represent each harmonic mode, and was based on the linear friction model, but with a correction for frequency dependent effects. This method provided an ideal means to develop a simple and accurate model for a simple probe-transducer system.

5.8.2.3 Proposed model

In the development of a new, simplified model, the first consideration was the simplification of the tube treatment either lumped (by length) parameters or by modal approximation. As mentioned above and illustrated by Kirshner (1975), the infinite product method of Goodson (1970) preserves the roots of the hyperbolic terms, while lumped parameter approximations and Taylor series expansions of the hyperbolic terms do not.

The transducer volume affects the tube harmonic frequencies such that the preservation of the hyperbolic roots does not necessarily mean a preservation of harmonic frequencies. This is demonstrated in Figure 5.30, which compares a modal approximation (N = 1) to the distributed parameters model (both using dissipative friction) - the first harmonics (second peak) do not agree. It is the case that agreement for the Nth mode improves as the N+1 mode is included. The use of linear friction in the modal approximation introduces further error, as expected. Figure 5.30 also includes a lumped parameter approximation (with $N = 2$), which shows surprisingly good agreement given its linear friction assumptions. The latter model deteriorates in extreme cases, such as when the tube-transducer geometry approaches that of a closed-end organ pipe.

Both the standard infinite products method (Goodson and Leonard, 1972) where N = 1 and the lumped parameter approach where N = 2 (which both resolve the first tube harmonic only) result in relatively high order transfer functions with cumbersome coefficients. This makes calculations for estimating bandwidth algebraically awkward. The corrected modal approximation of Yang and Tobler (1991) provides a useful method which deals with the error associated with the linear friction model and results in a low (second) order transfer function.

The corrected modal approximation of Yang and Tobler (1991) is based around the following equation (a modal approximation of the hybrid arrangement of equation 5.12):

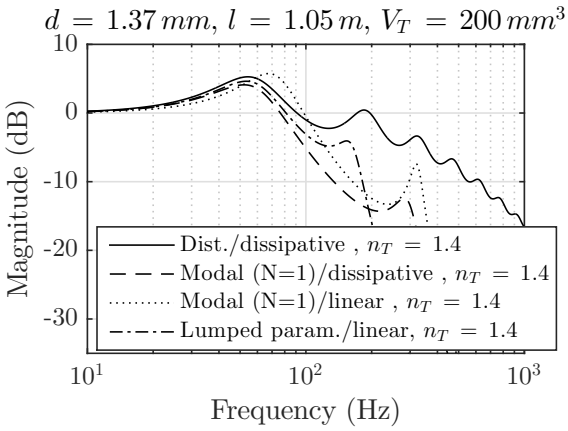


Figure 5.30: Comparison of the modal approximation for N=1 and for dissipative and linear friction, and the lumped parameters model with linear friction. The distributed model with dissipative friction is included for reference.

$$\begin{bmatrix} p_{tl} \\ \\ Q_{t0} \end{bmatrix} = \sum_{i=1}^{\mathrm{N}} \begin{bmatrix} \frac{\frac{2(-1)^{i+1}\lambda_{c_i}}{D_n\alpha^2}}{\bar{s}^2+8\frac{\beta}{\alpha}+\frac{\lambda_{c_i}^2}{\alpha^2}} & -\left(\frac{2Z_0}{D_n z}\right)\frac{(y\bar{s}+8v\frac{\beta}{\alpha}+(\alpha-\gamma)\frac{b\lambda_{c_i}^2}{\alpha^2})}{\bar{s}^2+8\frac{\beta}{\alpha}+\frac{\lambda_{c_i}^2}{\alpha^2}} \\ \\ -\left(\frac{2}{Z_0 D_n\alpha^2 w}\right)\frac{y\bar{s}-(a-\gamma)\frac{b\lambda_{c_i}^2}{\alpha^2}}{\bar{s}^2+8\frac{\beta}{\alpha}+\frac{\lambda_{c_i}^2}{\alpha^2}} & \frac{\frac{2(-1)^{i+1}\lambda_{c_i}}{D_n\alpha^2}}{\bar{s}^2+8\frac{\beta}{\alpha}+\frac{\lambda_{c_i}^2}{\alpha^2}} \end{bmatrix} \begin{bmatrix} p_{t0} \\ \\ Q_{tl} \end{bmatrix} \tag{5.23}$$

Where p_{t0} and Q_{t0} are the pressure and volume flow rate at the open end of the tube (probe tip) and p_{t1} and Q_{t1} are values at the transducer interface. The normalised Laplace frequency $\bar{s}$ is defined:

$$\bar{s} = \frac{d^2 s}{4v} \tag{5.24}$$

Where a finite number of modes are used in the summation, a DC offset error occurs. This is discussed in (Yang and Tobler, 1991). Where N = 1, this offset is given by the infinite sum:

$$\sum_{i=1}^{\infty} \frac{(-1)^i}{2i+1} = \frac{\pi}{4} \tag{5.25}$$

The relationship for the pressure in the transducer (p_T, which is equal to p_{t1} at the transducer interface) and the volume flow rate in to the transducer (Q_{t1}) in terms of $\bar{s}$ can be approximated by (assuming no diaphragm deflection):

$$Q_{ti} = \bar{s} p_T \frac{4 v V_T}{d^2 n_T \bar{p}} \tag{5.26}$$

Using the first row of equation 5.23 for N equal to 1, equation 5.26 and considering the DC offset (which must be applied to the system gain and damping ratio), the following ratio of input pressure (p_{t0}) to transducer pressure (p_T) can be defined in terms of the standard s-domain variable (by ultimately substituting equation 5.24 for $\bar{s}$):

$$\frac{p_T}{p_{t0}} = \frac{\frac{\pi}{4}}{\frac{a^2 d^2}{32 \lambda_{c_i} z}\left(\frac{D_n z d^2}{v^2} + 8\frac{V_T Z_0 y}{n_T \bar{p} v}\right)s^2 + \frac{\pi V_T Z_0}{4 \lambda_{c_i} z}\left(\frac{1}{n_T \bar{p}}\left(8\alpha\beta y + \alpha b \lambda_{c_i}^2 - b\lambda_{c_i}^2 y\right) + D_n \alpha \beta d^2 z\right)s + \frac{D_n \lambda_{c_i}}{2}} \tag{5.27}$$

The natural frequency and damping ratio correction terms α and β can be determined from Figure 5.31. The remaining terms are defined as defined by Yang and Tobler (1991) are also included in equations 5.28 to 5.34:

$$a = 1 + (\gamma - 1)\left(1 - \frac{1}{\alpha^2}\right) \tag{5.28}$$

$$b = \frac{8\beta}{\alpha \mathrm{Pr}} \tag{5.29}$$

$$\lambda_{c_i} = \frac{\pi(i - 1/2)}{D_n} \tag{5.30}$$

$$Z_0 = \frac{4\bar{\rho}\bar{c}}{\pi d^2} \tag{5.31}$$

$$w = b^2 - \frac{8b\beta}{\alpha} + \frac{\lambda_{c_i}^2}{\alpha^2} \tag{5.32}$$

$$y = \gamma b^2 - \frac{8ab\beta}{\alpha} + \frac{a\lambda_{ci}^2}{\alpha^2} \tag{5.33}$$

$$z = \gamma y + (\alpha - \gamma)\frac{a\lambda_{c_i}^2}{\alpha^2} \tag{5.34}$$

Although the equation reduces to that of a second order system, the model resolves either the low-order impedance-capacitance response or where the transducer volume approaches zero, the first tube harmonic. Having substituted numerical values

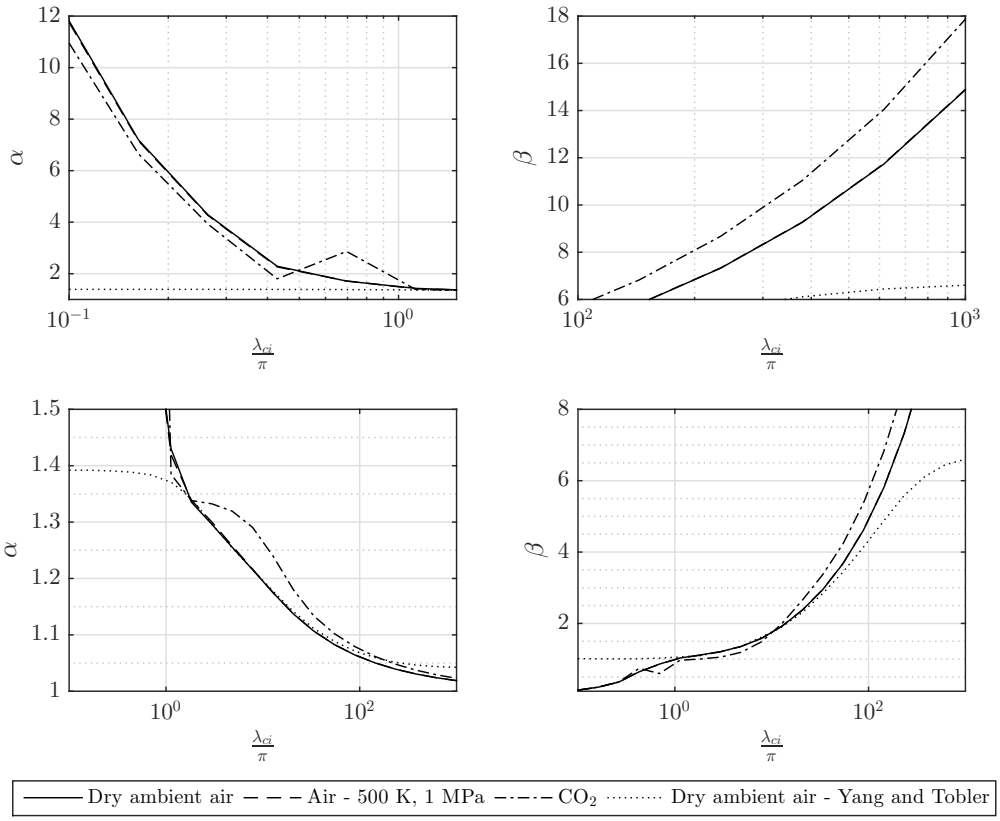


Figure 5.31: The natural frequency and damping ratio modification factors (α and β) as defined by Yang and Tobler (1991) for use in the proposed model.

describing a tube-transducer system in to equation 5.27, the system parameters of interest are yielded by standard second order system relations where the denominator is of the form $ms^2 + cs + k$:

$$\omega_n = \sqrt{\frac{k}{m}} \qquad (5.35) \qquad\qquad \zeta = \sqrt{\frac{k}{m}} \qquad (5.36)$$

The -3 dB frequency (ω_{-3dB}) can then be calculated:

$$\omega_{-3\,\mathrm{dB}} = \omega_n \sqrt{1 - 2\zeta^2 + \sqrt{4\zeta^4 - 4\zeta^2 + 2}} \qquad (5.37)$$

For under-damped systems ($\zeta < 1$) where the resonance magnitude is greater than +3 dB, it would be better to consider the upper limit of the bandwidth to be $\omega_{+3\mathrm{dB}}$ which occurs at a frequency less than ω_n. That is when:

$$\frac{1}{2\zeta} > \sqrt{2} \tag{5.38}$$

$$\omega_{+3\,\mathrm{dB}} \approx 0.55\omega_n \tag{5.39}$$

The model is applied across a range of examples in the following section and compared to experimental results.

5.8.3 Experimental validation of the new probe model

5.8.3.1 Experimental technique

Experimental frequency responses were determined for a number of tube lengths and transducers volumes. The experimental set up consisted of an aluminium cup with stainless steel tubular connections shown in Figure 5.32. By stretching a latex balloon over the cup and inflating until failure, an input pressure step of approximation -0.1 bar was generated. The (output) pressure at the end of each tube was measured with a First Sensor (Sensor Technics) CTE-8000 2 bar absolute pressure transducer (uncalibrated combined uncertainty of 0.1% FSO) connected via a machined fitting. The transducer volume was measured to be approximately 200 mm^3 using a 10 mm^3 pipette. The input pressure was measured with a CTE-8000 2 bar absolute transducer. The volume of the output transducers could also be reduced to approximately zero by filling each with a mixture of water and detergent (to avoid air bubbles). The pressure transducers were sampled at 20 kHz with a National Instruments 9205 16-bit analogue to digital converter. The data was digitally low-pass filtered at 1 kHz, which was well above the frequencies of interest (e.g. the first and second resonant frequencies).

Each tube assembly effectively consisted of a length (l_p) of flexible plastic tube with nominal internal diameter of 1.37 mm connected to hardware at each end which consisted of a length ($l_{ss} = 25.4\,\mathrm{mm}$) of stainless steel tube with a nominal

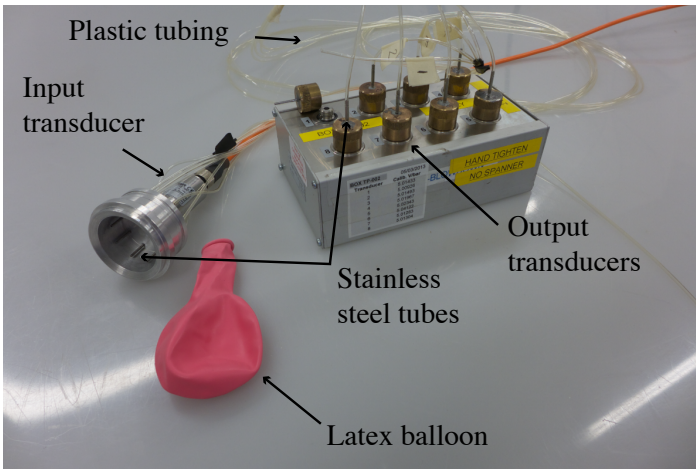


Figure 5.32: Photograph of complete experimental set up.

internal diameter of 1.06 mm. This style of assembly (see Figure 5.33) is ubiquitous in laboratory aerodynamics experiments. Each assembly of total length l was replicated 4 times and tested simultaneously (in parallel).

From the measured input and output signals in the time domain, low-order transfer function models and corresponding Bode plots were estimated using MATLAB. This method focused on estimating the low frequency modes of the system, which was sufficient for validation of the proposed low-order modal model. 4 pole transfer functions were used where the relative order of the transfer function was 1. This captured the first 1 to 2 modes of each system. The results are presented in the following section.

5.8.3.2 Experimental results compared to proposed model

The results for total tube length (l) equal to 0.45 m, 1.05m and 2.55 m are presented in Figures 5.34 to 5.36. For each case, the response predicted by the dissipative friction,

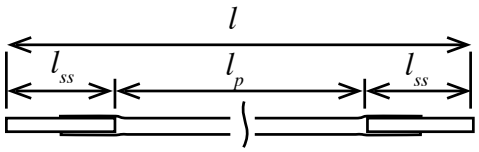


Figure 5.33: Schematic of effective experimental tube set up.

distributed parameters model approach is shown for two cases; the first (solid line) considers the specific length and internal diameter of each of the three distinct tube sections; the second considers only the total length (l) and the internal diameter of the longest (plastic) tube. In the cases examined, approximating the 3-tube system as a single tube produced only a small error.

In each case, four identical tube assemblies were tested simultaneously. As shown in Figures 5.34 to 5.36, the agreement between tubes was good in all but 2 cases. In the cases of $V_T \approx 0$ and $l = 1.05$ m and 2.55 m, an outlier existed. This was most likely due to a water droplet contaminating the tube, which was observed after the tests for the tubes in question.

For the under-damped cases of Figures 5.34 and 5.35 ($l = 0.45$ m and 1.55 m) the first mode of the experimental data agreed well with both models. The phase angle agreement was also good in all cases up to and including the first harmonic. For the over-damped cases of Figure 5.36, particularly where $V_T = 200\,\text{mm}^3$, the agreement in terms of the magnitude was not as good as for the other cases.

5.8.3.3 Discussion

The results presented in the previous section demonstrated good agreement between the proposed model and the distributed parameter, dissipative friction model in terms of the first resonance frequency. Reasonable agreement between these two models was demonstrated for an over-damped case. In this regard, where the goal is to estimate bandwidth in terms of a magnitude cut off value, the proposed model should produce results adequately consistent with the best available approach—the distributed parameter, dissipative friction model—and certainly an improvement over existing, simple models. The experimental data confirmed the usefulness of the proposed model, particularly for under-damped cases (small l/d^2) but highlighted that care should be taken in the case of relatively long (large l/d^2) tubes where experimental

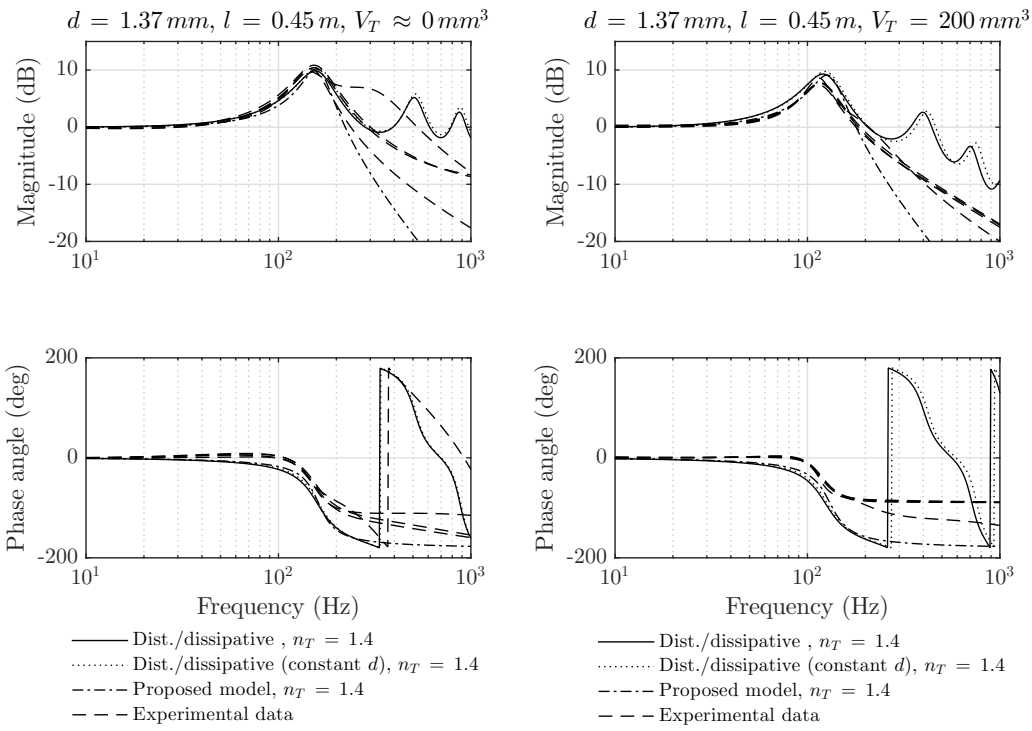


Figure 5.34: Experimental results for $l = 0.45$ m, $V_T = 200\,\text{mm}^3$ and $\sim 0\,\text{mm}^3$.

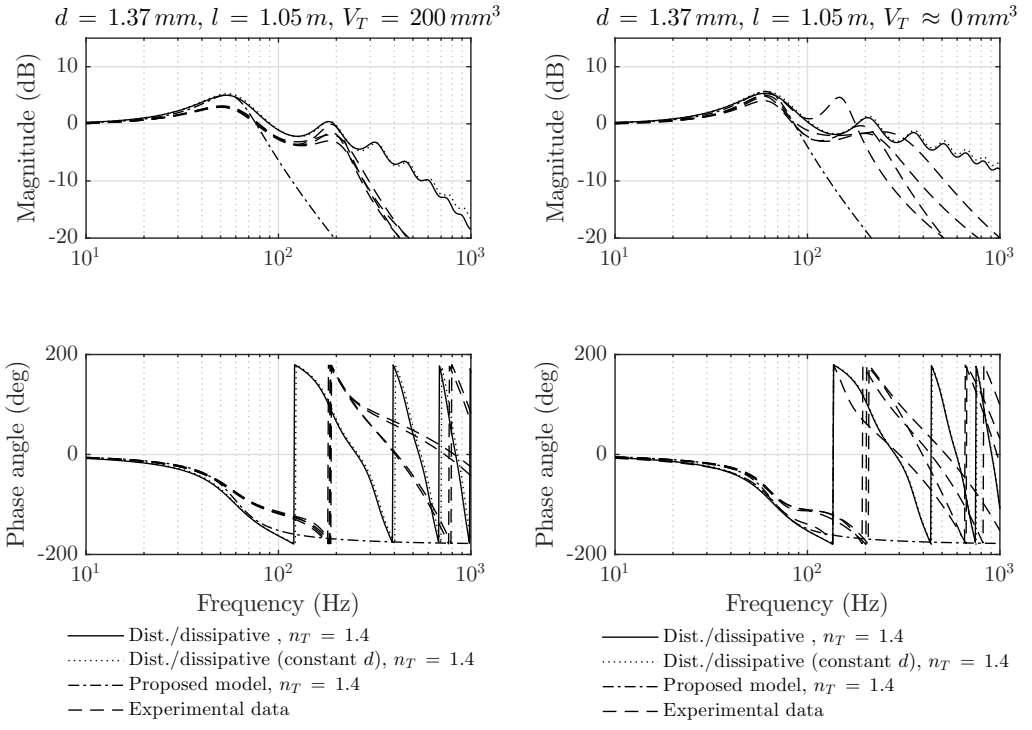


Figure 5.35: Experimental results for $l = 1.05$ m, $V_T = 200\,\text{mm}^3$ and $\sim 0\,\text{mm}^3$.

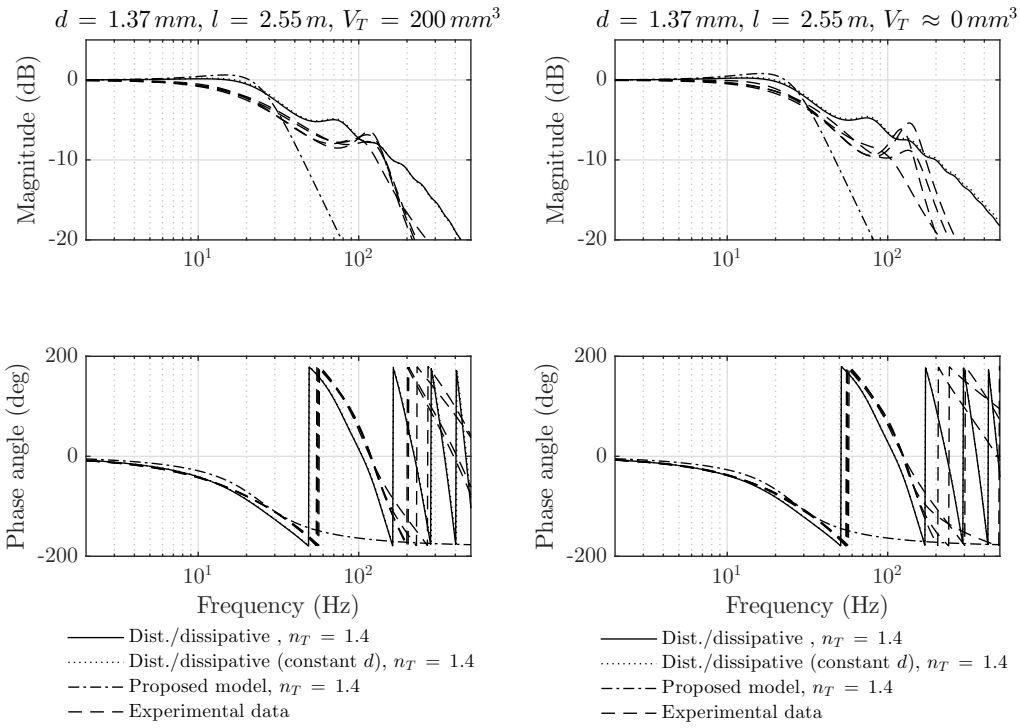


Figure 5.36: Experimental results for $l = 2.55$ m, $V_T = 200\,\text{mm}^3$ and $\sim 0\,\text{mm}^3$.

results differed most from both the proposed model and the distributed parameters, dissipative friction model.

Bergh and Tijdeman (1965) noted that the deviation of the physical system from the nominal dimensions (particularly for d) is a likely source of error. This is a problem common to all modelling approaches. In order to minimise overall error in estimating bandwidth, it is important that the model used is at least capable of accurately describing the low-order response of the idealised geometry. Where accuracy is critical (or where a signal reconstruction is necessary), experimental characterisation of the frequency response should be carried out.

A useful observation was that for a system of mixed tube diameters (specifically where d is smaller at each end - Figure 5.33), the response did not deviate significantly from a simplified case assuming a single diameter (d for the longest tube) and a summed length. For the tube configuration and diameters considered above this appears to be a reasonable assumption where $l_{ss} < 0.1l$.

5.9 Conclusions

Addressing the need to investigate the performance of the OLCS in advance of its use in OTRF turbine tests, an experimental facility was developed. The facility consisted of a high-pressure air supply system which interfaced with the OLCS, providing flow to the test section, and alloying characterisation of the system's performance—in particular the 2D flow profiles at the inlet plane—at atmospheric conditions.

A large bespoke vortex tube was designed and constructed for coolant production, enabling the measurement of inlet temperature profiles. While the system was effective at producing the required quantity of coolant at significantly reduce (-60 K with respect to the mainstream) temperature, heat transfer along the interconnecting system and within the OLCS itself limited the ultimate temperature difference significantly - to 10-15 K.

Extensive steady temperature and pressure instrumentation was employed, with the focus being that related to the inlet traverse system. At the inlet, low speed data was collected with thermocouple probes and a five-hole probe . Similar attempts were made to measure unsteady properties in order to characterise the inlet turbulence, although unsuitable probes limited the usefulness of this data. In general, the facility yielded important experimental characterisation data for the OLCS – this is presented in Chapter 6.

Chapter 6

Experimental results from the OLCS

6.1 Introduction

The OLCS was characterised prior to being installed in the OTRF using a facility described in Chapter 5. Experimental results are collectively presented in this chapter for clarity and ease of comparison.

While CFD simulations are discussed primarily in Chapters 4 and 4.7, a range of 1D and 2D data derived from CFD results accompany the experimental data presented in this chapter. The CFD data presented in this chapter were from the simulations presented in Chapter 4.7 only. These simulations closely matched the experiments in terms of boundary conditions and domain geometry (excluding the vanes in all cases). Finally, the target profiles are included for the sake of comparison.

Definitions of non-dimensional terms used to present data (e.g. $T_{0\,eff}$ and $p_{0\,q}$) are explained in Chapter 2.

6.2 Summary of cases and measurements

6.2.1 Test cases and conditions

The experimental data presented in this chapter examined 4 distinct configurations of the OLCS, covering two fundamentally different conditions. The two sets of

conditions—the atmospheric approximations to SILOET and LEMCOTEC conditions—are described in Table 6.1 (which is repeated from Chapter 4.7 for convenience). The specific cases are summarised in Table 6.2. Experimental run numbers are noted in figure captions.

Table 6.1: Summary of operating conditions.

		SILOET		**LEMCOTEC**	
Property	**Units**	**OTRF**	**ATM**	**OTRF**	**ATM**
p_{rig}	Bar abs	5.54	1.0	8.50	1.0
$\dot{m}_{Tot}$	kg/s	15.0	2.0	23.0	1.8
x		0.12	0.10	0.23	0.18
$T_{0\,h}$	K	500	285	530.6	285
$T_{0\,c}$	K	290	275	290	275
$\mathrm{Re_{Sw}}$	($\times 10^5$)	5.6	1.5	7.3	1.1
$\mathrm{M_{Sw}}$		0.12	0.07	0.11	0.06

Table 6.2: Summary of experimental cases at atmospheric conditions

Case	**Condition**	**Swirler ψ (°)**	**Swirler assembly axial offset (mm)**	**Swirler axial jet**
A	SILOET ATM	20	40	Yes
B	SILOET ATM	20	40	No
C	LEMCOTEC ATM	35	25	No
D	UNIFORM ATM	Tu plate	0	N/A

Case A and B consider the SILOET (atmospheric) conditions with and without the swirler axial jet, which has identified as affecting the flow structure in Chapter 4.7. Case C considers the LEMCOTEC (atmospheric) conditions without the swirler axial jet, since this was shown not to affect the flow similarity between atmospheric and OTRF conditions. Case D considers the uniform configuration (with turbulence generation plate) with mainstream flow only.

6.2.2 Measurements

A range of steady and unsteady measurements were attempted as part of the experimental characterisation of the OLCS. These are summarised in Table 6.3 and

explained in further detail in Sections 6.3 to 6.5. Data was collected on $r-\theta$ planes at the inlet ('P_{IN}') and throat ('P_{TH}') locations, and in case D, on an $z-\theta$ plane at mid-span. P_{IN} (half an axial chord upstream of the vane) and P_{TH} are defined in Figure 5.8 of Chapter 5.

Table 6.3: Summary of experimental measurements; measurement type and location.

Case	**10 pitch** $(r-\theta)$	**3 pitch planar** $(r-\theta)$			3 **pitch planar** $(z-\theta)$
	β, α	β, α, p_0	T_0	Tu	Tu
A B C	P_{IN}, P_{TH}	P_{IN}, P_{TH}	P_{IN}, P_{TH}	P_{IN}, P_{TH}	None
D	None	P_{IN}, P_{TH}	None	P_{IN}, P_{TH}	Mid-span
Section	6.3	6.4	6.4	6.5	6.5

6.3 Steady periodicity traverse data

Circumferential traverses over a range of 10 swirler pitches ($\pm 90°$) at 3 radial heights were carried out for cases A to C at planes P_{IN} and P_{TH}. The purpose of these traverses was to verify the periodicity of the OLCS to a greater (circumferential) extent than implied by the complete 2D area traverses (presented below). The traverses were carried out at 3 arbitrary radial heights (noted on the plots). Periodicity traverses were not carried out for case D (turbulence plate) due to its relative simplicity and otherwise uniform properties (i.e. no periodic non-uniformity was expected).

The traverse measurements were of steady pressure and velocity properties with the five-hole probe described in Chapter 5. The data was low-pass filtered to focus on the pitch-wise periodic trends. Periodicity is considered in terms of swirl (β) and pitch (α) traces in Figure 6.1.

The traverse data over 10 swirler pitches illustrate the clear periodic trend in terms of β and α for cases A-C. The traces are characterised by a wavelength of 1 swirler pitch, as expected. There is some variation in magnitude across the

investigated range, however the periodicity of the system was considered to be good. The figure illustrates that case C was characterised by stronger swirl than cases A and B, as expected (larger ψ). In each case, the swirl strength is reduced at the throat plane as compared to the inlet plane, consistent with the reduction in area and increase in axial velocity. Further discussion of the inlet characteristics is presented below with respect to the planar traverse data.

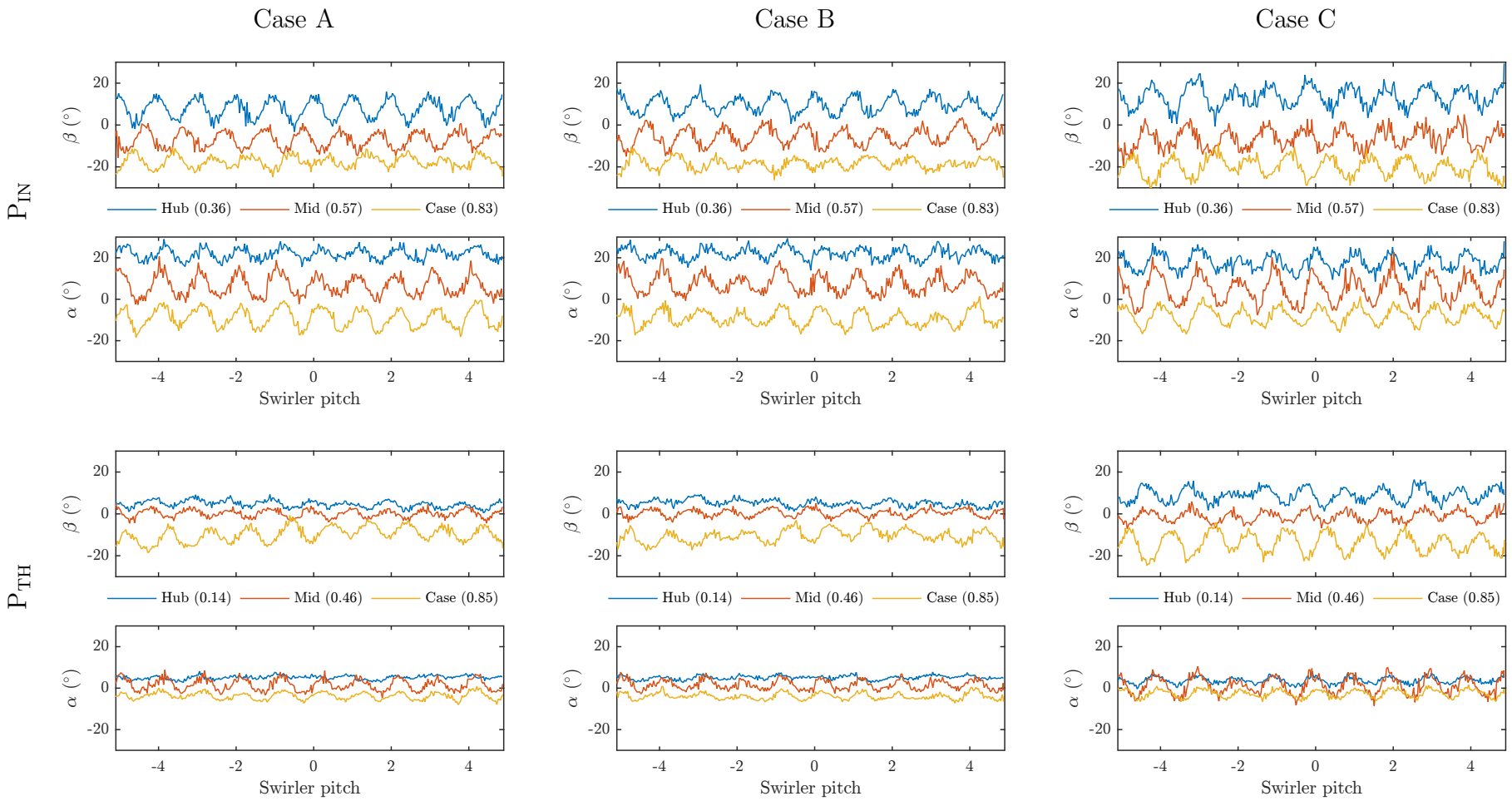


Figure 6.1: Swirl (β) and pitch (α) angle traverses over 10 swirler pitches for cases A (R1614, R1615), B (R1619, R1616), and C (R1685, R1684).

6.4 Steady planar traverse data

Steady traverses were carried out on $r-\theta$ planes for cases A to D. Measurements were taken at planes P_{IN} and P_{TH}, although only the former is presented. It is noted that all experiments (and accompanying CFD) utilised the turbine inlet contraction profile of the SILOET turbine. While the LEMCOTEC inlet contraction profile differed, the 1D area profile was very similar so the effect on results was expected to be small.

The purpose of the traverses was to characterise the steady flow properties in high resolution on the 2D inlet plane. All inlet plane measurements covered a circumferential range of $\pm 27°$ (3.0 swirler pitches) where the origin was at a swirler axis. The measurements derived from the five-hole probe covered a radial range of 19% to 91% at the inlet plane. The temperature measurements covered a radial range of 2% to 99% by utilising a goose-neck thermocouple probe (described in Chapter 5) to gain additional access at the hub; the results were extrapolated to the radial extents. The discrepancy in radial coverage towards the case (between the five-hole probe and TC probe) was due to the difference in probe diameters. The radial height of the traverse sweeps are marked on each plot at the swirler pitch origin. The results are discussed by case below.

6.4.1 SILOET - cases A and B

The results for case A are presented in Figure 6.2. Firstly, the agreement in terms of the 2D profiles between the time-average URANS results (see Chapter 4.7, Figures 4.36 to 4.39) and the target profiles was very good for all properties; the CFD development work had progressed the design as far as possible. It was noted that the target total pressure profile (in terms of $p_{0\,q}$) was approximately scaled to allow comparison (since no upstream information was available). The experimental data agreed very well with the URANS predictions in terms of swirl (β) and pitch (α) angles. The distribution of total pressure ($p_{0\,q}$) is very similar between URANS and

experiment, although the magnitude differs. $p_{0\,q}$ is based on the total pressure loss across the swirler and mainstream vortex which is the likely source of the discrepancy. The total temperature data (in terms of $T_{0\,eff}$) showed the poorest agreement, displaying greater mixing in the experimental data than predicted by the URANS. This is in agreement with expectations of URANS predictions (as in Chapter 3) and the findings of Andreini et al. (2015). The experimental profile could be improved by reducing the coolant momentum flux which would reduce the mixing.

The results for case B are presented in Figure 6.3. As with case A, the agreement in terms of the 2D profiles between the time-average URANS results (see Chapter 4.7) and the target profiles was very good for all properties. The peak swirl magnitude was reduced with respect to case A, with the increased mixing in the mainstream due to PVC formation the likely cause. Reduced mixing of the coolant and mainstreams—apparent in the total pressure and temperature profiles—appears to have been a follow-on effect, resulting from the reduction in mainstream swirl.

The experimental data for case B agreed well with the URANS predictions in terms of swirl (β) and pitch (α) angles. Similar discrepancies existed for the total pressure and total temperature plots, as described by case A.

On the basis of the planar inlet data, there was little distinction between case A (with axial jet) and case B (without). Therefore no conclusions could be made on the basis of this experimental data regarding PVC formation; indeed only subtle differences existing in the equivalent URANS data presented alongside.

Figure 6.4 presents 1D profiles for cases A and B. 1D experimental data was limited to radial locations where five-hole probe measurements were taken - for $T_{0\,eff}$ velocity information was required for mass-averaging. The plots of swirl (β) and pitch angles (α) (area-weighted circumferential average) show good agreement between the experimental and URANS data, as per the 2D profiles discussed above. The plot of $T_{0\,eff\,\bar{\theta}}$ illustrates reasonable agreement between experimental and URANS data (for the limited range of experimental data) but shows that compared to the target, the

coolant was confined more to the endwall regions; this could also be inferred from the 2D plots. The total pressure (as $p_{0\,q\,\bar{\theta}}$) illustrates good agreement in terms of characteristic, although with discrepancy in terms of magnitude which was attributed to prediction of pressure loss through the swirler and VB flow region in URANS; it is recalled that the target was approximately scaled to produce a $p_{0\,q}$ value.

6.4.2 LEMCOTEC - case C

The results for case C are presented in Figure 6.5. The experimental data agreed well with the URANS predictions in terms of swirl (β) and pitch (α) angles. The total pressure profile (in terms of $p_{0\,q}$) showed a similar characteristic between the experimental and URANS data, although with a bias towards greater loss in the latter. Both total pressure profiles were characteristic of well-defined vortices, with the low-pressure core clearly visible for each swirler pitch. The total temperature $T_{0\,eff}$ distribution illustrated a significant under-prediction of mixing by the URANS simulation, as in cases A and B, although with a broad agreement in terms of coolant migration (i.e. the sawtooth pattern).

The LEMCOTEC configuration of the OLCS did not benefit from the same predictive (URANS) design effort as the SILOET configuration of cases A and C. The URANS simulation presented was carried out in parallel to the experiments, and it is noted that the predicted total temperature profile was not optimal, with significant migration of hot gas to the end walls. This was despite pre-swirling (approximately 20°) of the coolant (implemented both in the simulation and experiment) in order to reduce the velocity mismatch with the main stream. The experimental profile, characterised by greater mixing and lower peak endwall temperatures was more suitable as a turbine inlet condition.

Figure 6.6 presents 1D profiles for case C. Experimental data were over a limited range of span values (explained in the previous section). As explained in Chapter 4, the 1D reductions of the LEMCOTEC target profiles were used to guide

the design, due to the inconsistent nature of the provided 2D targets. In terms of the swirl angle (β), the agreement between experiment, URANS and target was good. In terms of pitch angle (α), URANS produced good predictions with respect to the experimental data, although both were in disagreement with the target data. The discrepancy at low values of radial span suggested that the target data was derived from different turbine inlet geometry; the pitch angle in all other data presented (including of cases A and B) was heavily dependent on hub geometry in this span-wise region.

The total temperature profiles (Figure 6.6) indicated that in terms of URANS predictions, the LEMCOTEC configuration produced a result reasonably consistent with the (1D) target. The experimental data—over the available range—was characterised by lower values of $T_{0\,eff\,\bar{\theta}}$ as compared to URANS (and target), resulting from greater mixing of coolant stream to the mainstream. The profile of $p_{0\,q\,\bar{\theta}}$ showed a similar characteristic, although with a bias, as discussed above for the 2D profile.

6.4.3 Uniform - case D

The experimental results for case D are shown in Figure 6.7. In this case there were no explicit target profiles, and URANS results have been omitted since the case was relatively trivial in 2D. Due to the expected uniformity of properties, measurements were taken over a reduced span-wise extent. As expected, the mean swirl angle (β) was zero and the pitch angle (α) was uniform in the pitch-wise direction, varying in the span-wise direction with the contracting annulus. The total pressure drop resulting from the turbulence plate was very small.

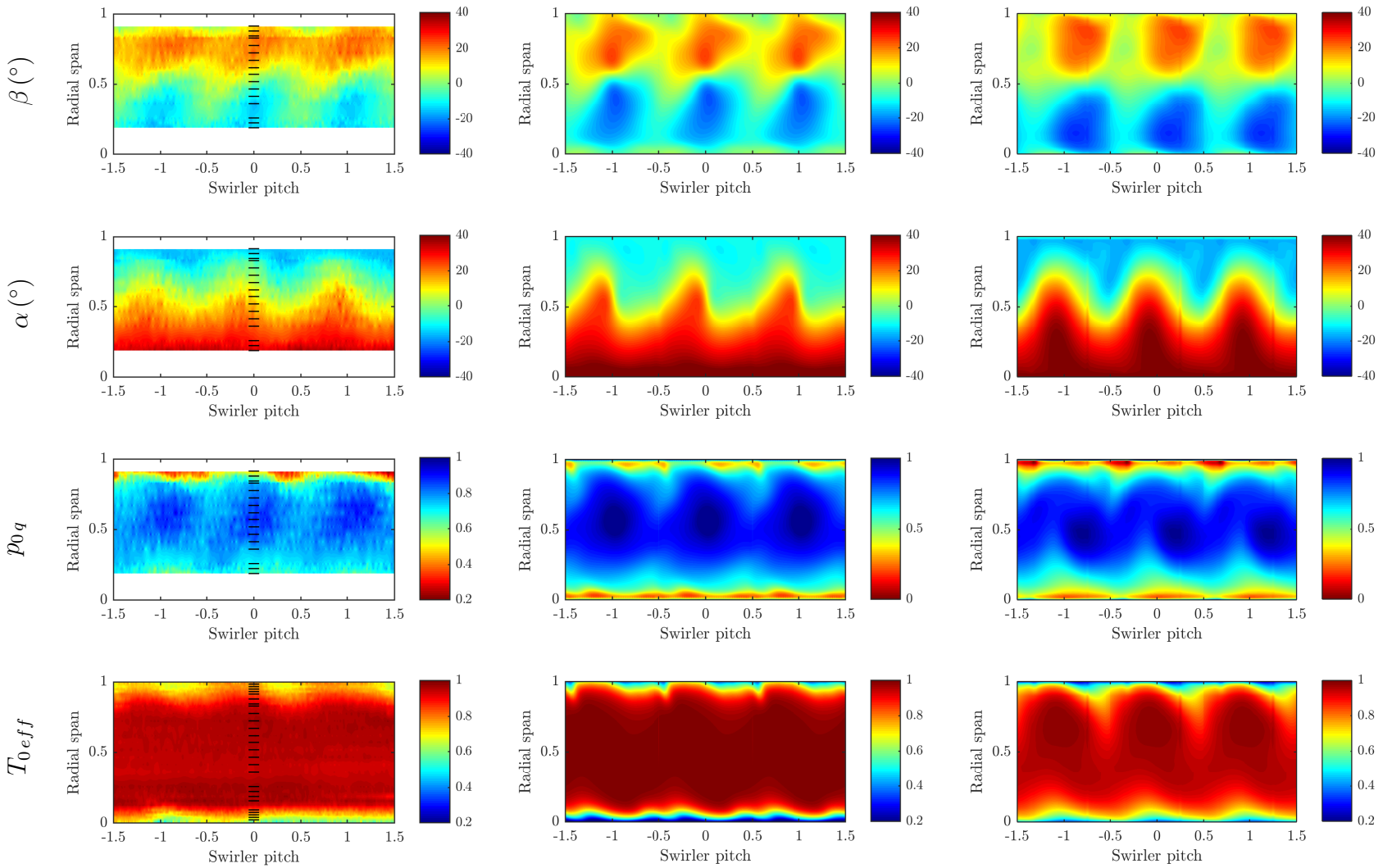


Figure 6.2: Case A inlet (P_{IN}) profiles. L-R: Experimental (R1602-13) and URANS (with axial jet), and target profiles.

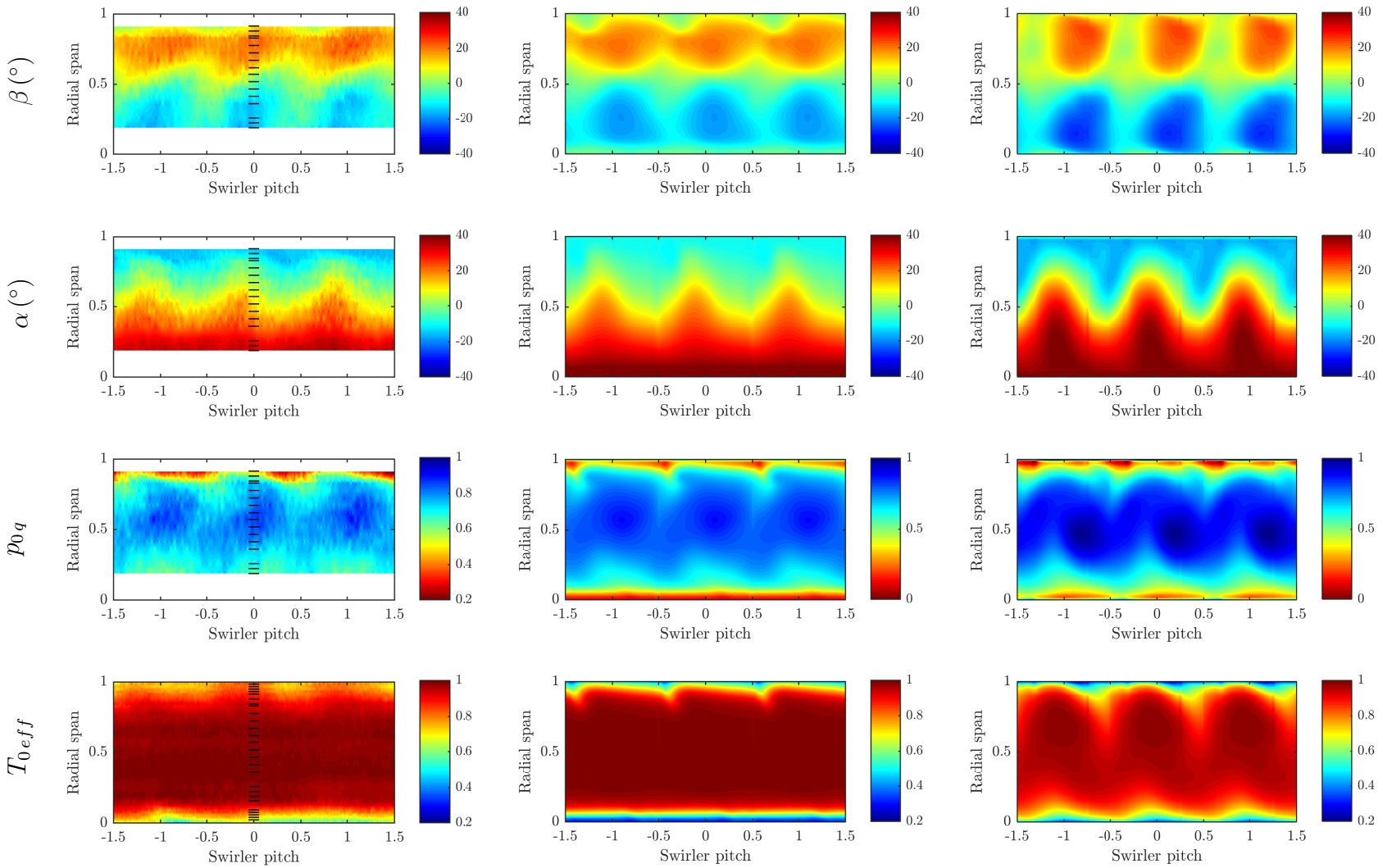


Figure 6.3: Case B inlet (P_{IN}) profiles. L-R: Experimental (R1588-94) and URANS (without axial jet), and target profiles.

6.5 Unsteady traverse data

Traverse measurements were taken with high frequency response probes in an attempt to characterise the inlet turbulence characteristics produced by the OLCS. The measurements were first attempted using a total pressure probe utilising an embedded Kulite transducer, although issues with signal distortion meant data acquired with the probe was not meaningful; the probe and dynamic response is discussed in Chapter 4.

In a further attempt to yield unsteady data, a single wire hot-wire probe (described in Chapter 4) was employed. A single wire hot-wire probe was suitable for characterising the uniform configuration (case D), since the flow direction was relatively one-dimension near the mid-span region. For the highly three-dimension flow of cases A to C, a single wire probe is poorly suited but was the only option available. By necessity, the hot-wire measurements were carried out at isothermal conditions. The probe wire was aligned with the tangential direction.

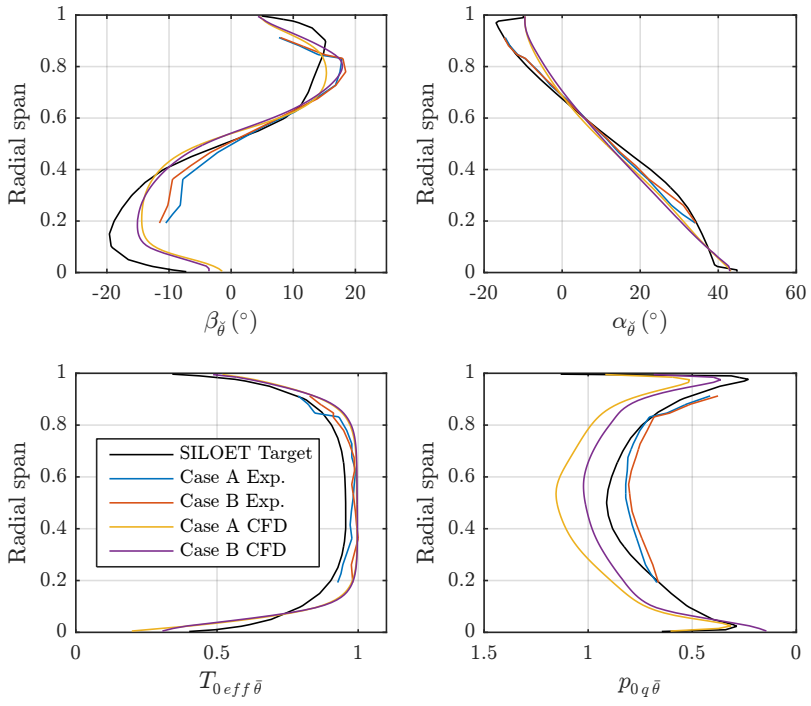


Figure 6.4: Circumferentially-averaged profiles for cases A and B.

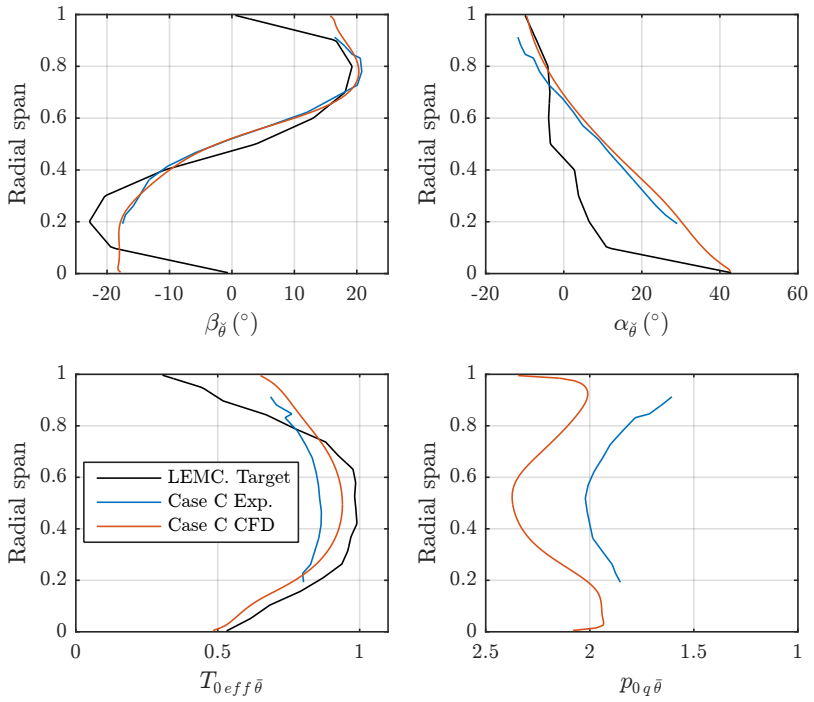


Figure 6.6: Circumferentially-averaged profiles for case C.

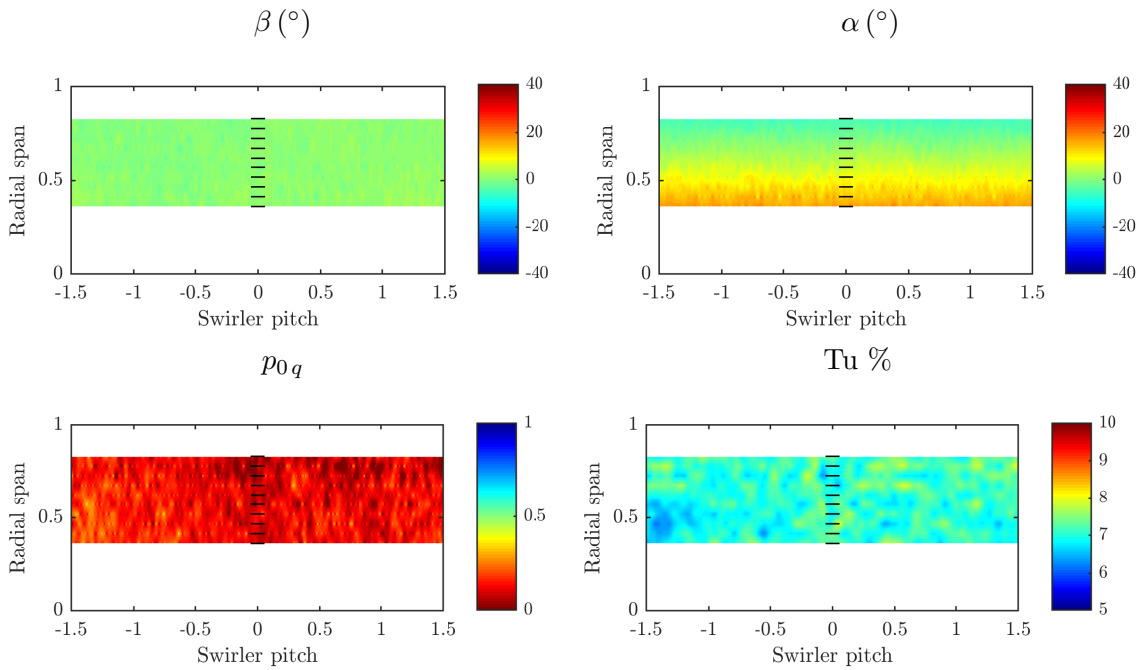


Figure 6.7: Case D inlet (P_{IN}) experimental (R1642-44) profiles.

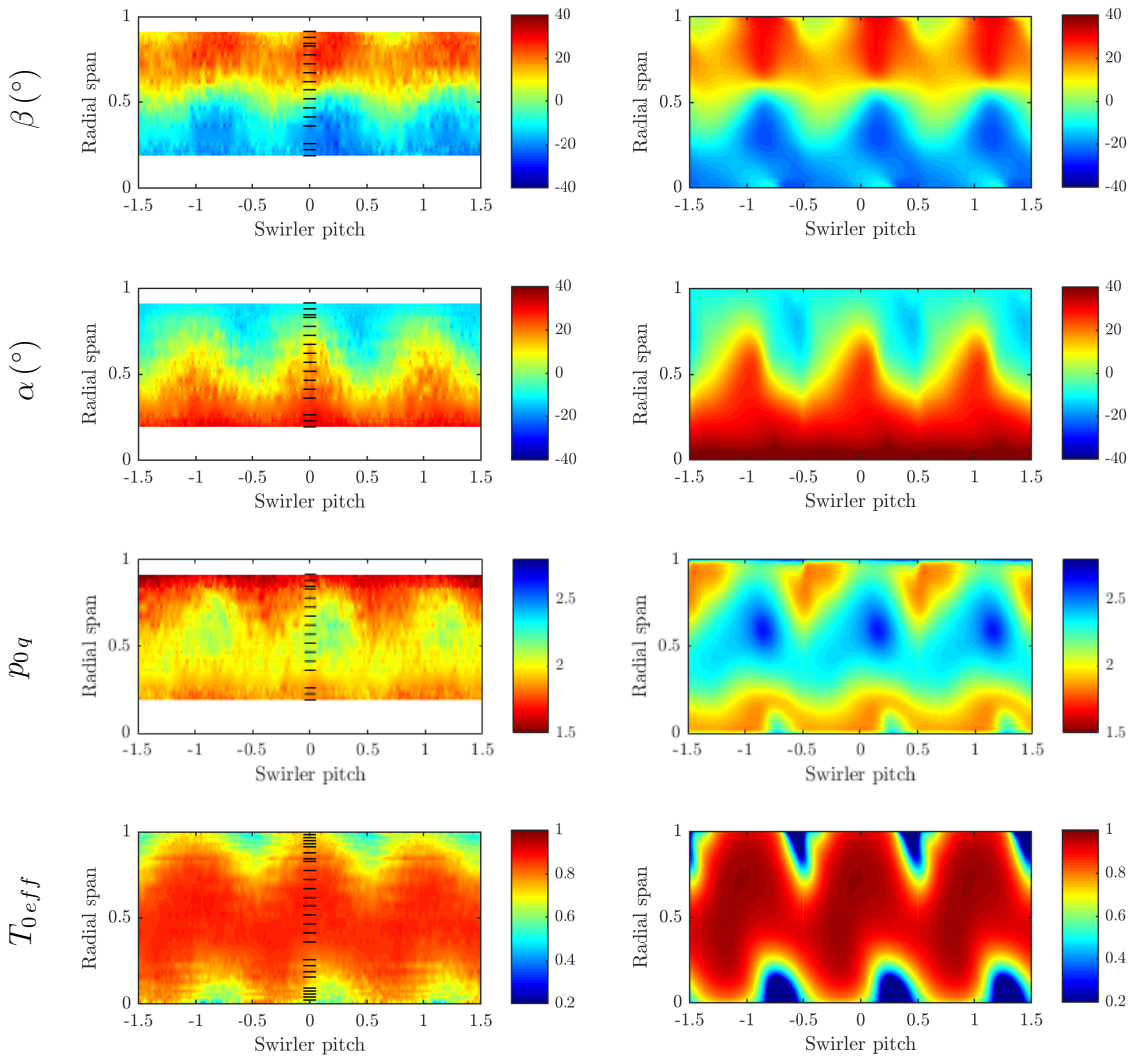


Figure 6.5: Case C inlet (P_{IN}) profiles. L-R: Experimental (R1671-77) and URANS (without axial jet).

6.5.1 SILOET - cases A and B

Turbulence intensity data for cases A and B are shown in Figure 6.8. The data was calculated based on the local mean velocity, rather than the mean across the entire plane. Agreement in terms of magnitude of turbulence intensity was poor (although was of the correct order of magnitude, and comparable to that measured by Bacci et al. (2015b) for a similar system), and was attributed to the single wire probe being unsuitable for the highly three-dimensional flow. The experimental data, in both cases, showed a region of high turbulence at the vortex core, which was expected; for

case B this was very clear. The measured peak turbulence intensity of $16 - 20\%$ was consistent with the expectation that turbulence would be high as a result of turbulence generation in the vortex central recirculation zone. Due to the shortcomings of the derived turbulence data, further reduction (e.g. to yield integral length scale) was not carried out, and data was not collected for case C.

The high-speed hot-wire measurements as well as the low-speed multi-hole probe data were examined in the frequency domain to identify any dominant modes, with the specific goal of identifying the formation and suppression of a PVC between cases B and A. URANS predicted a PVC frequency of approximately 250 Hz for case B. When consider the aforementioned data taken at the inlet plane, no dominant modes which could be attributed to PVC oscillations could be conclusively identified– the spectra for both cases B and A were very similar.

It is likely that the pressure fluctuations caused by the PVC would have been weaker at the inlet plane than in the vicinity (as predicted by simulations) of the PVC as itself. In this case, the PVC fluctuations may have been weaker than the turbulent and acoustic fluctuations. The feed system consisted of noisy sonic nozzles

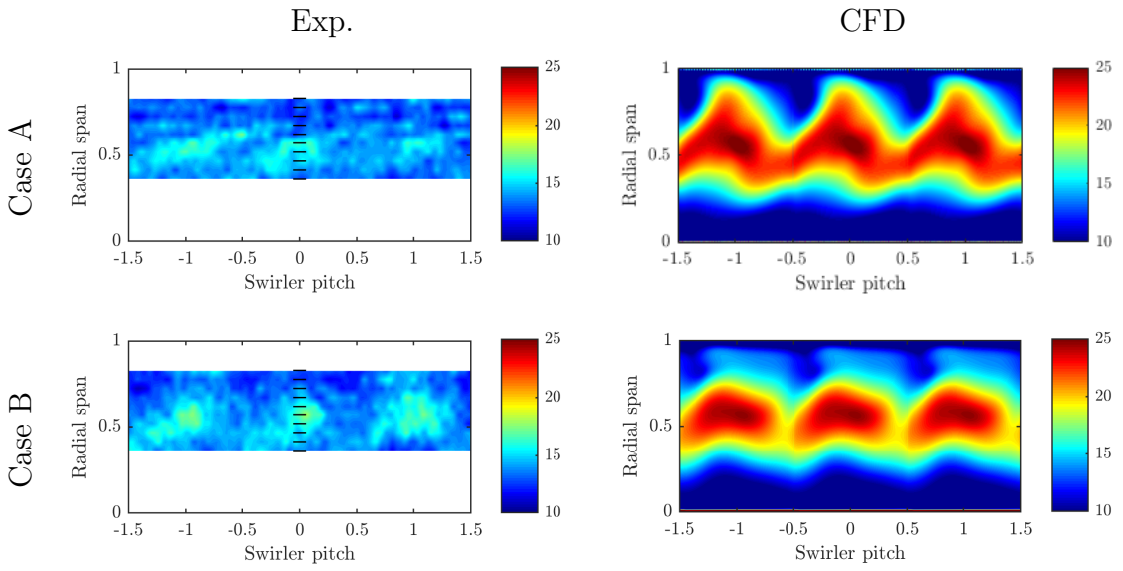


Figure 6.8: Case A (R1562-63) and B (R1577-78) inlet (P_{IN}) turbulence intensity (%) profiles.

and an array of flexible feed hoses of uneven length (approximately 1.5 to 3.0 m) with fundamental frequencies in the range of 50 to 110 Hz and harmonics in the frequency range of interest.

It is important to note that given the measurement locations considered (the inlet plane), the lack of dominant frequency attributable to PVC oscillations in case B does not rule out the formation of one, as predicted by simulations. It does make verifying the suppression of the PVC in case A (compared to case B) impossible. This could be investigated in the OTRF experiments by installing one or more sub-miniature pressure transducer in the swirler diffuser region, where simulations predicted the largest amplitude oscillations.

6.5.2 Uniform - case D

Hot-wire traverse measurements were taken for the uniform case (D). As the velocity field was much more uniform for this configuration, the single wire probe was more appropriate. The wire was aligned with the tangential direction so that it would unambiguously respond to axial and radial velocity components.

The unsteady traverse data for the uniform case with elevated turbulence is shown in Figure 6.7. The data was measured using a hot-wire probe (described in Chapter 4). The turbulence intensity was measured at $7-8\%$ and was uniform across the traverse region. The evolution of the turbulence intensity was measured on a circumferential-axial ($z-\theta$) plane, from far upstream—adjacent the turbulence rods—to the inlet plane. This is shown in Figure 6.9. The wakes were well-resolved at the expected locations (2 per swirler pitch), while the turbulence intensity decayed towards a uniform value of approximately $7-8\%$, in agreement with Figure 6.7.

6.6 Conclusions

An experiment was designed and constructed to characterise the OLCS prior to its installation in the OTRF. While the results were intended to compliment OTRF data,

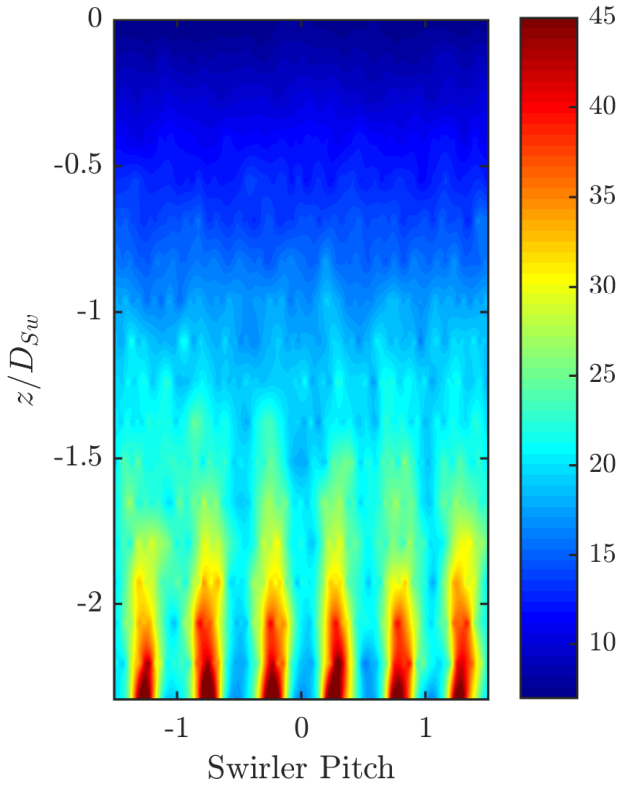


Figure 6.9: Case D (R1642-44) turbulence intensity on a $z-\theta$ plane at mid-span. z origin is the inlet plane location.

OTRF schedule delays meant that they were the only data available for publication within this thesis. Data from the OTRF at design conditions will be of great interest once available.

The results for the SILOET configuration (cases A and B) agreed well with URANS predictions and targets in terms of 2D inlet profiles; the experimental total temperature indicated greater mixing than predicted, however. The level of agreement confirmed the suitability of the system, and the predictive ability of URANS for the prediction of the flow structure (if not the thermal field). The potential for an altered flow structure (as discussed in Chapter 4.7) remains, and experimental data at OTRF conditions remains of interest as final confirmation of the system performance.

Unsteady data for cases A and B confirmed—although with relatively high uncertainty—that the turbulence intensity produced by the simulator would be high

$(15-20\%)$. The results were not in good agreement with URANS in terms of distribution or magnitude, and would not be suitable as non-uniform boundary conditions for CFD. Analysis of the unsteady data with the goal of identifying PVC formation and suppression proved inconclusive.

The results for the LEMCOTEC configuration (case C) demonstrated a set of inlet profiles suitable for the LEMCOTEC lean-burn turbine experiments. In terms of 1D targets, the agreement was satisfactory. The results, when compared to URANS predictions, once again highlighted the capability of URANS in predicting flow structure as well as its weakness in predicting mixing.

The results for the uniform configuration (case D) confirmed that the system would produce uniform flow conditions with elevated $(7-8\%)$ turbulence intensity. Detailed traverse data in the axial direction confirmed the decay of turbulence intensity to a uniform distribution at the inlet plane.

Chapter 7

Conclusions

A combustor simulator capable of reproducing turbine inlet conditions representative of a modern lean-burn engine has been developed, manufactured and experimentally characterised. The system will be used in the near future for experimental studies of modern high pressure gas turbine designs in the OTRF, yielding some of the first data of this kind in a scaled rotating turbine facility.

The OLCS, once commissioned and operating in the OTRF, will be instrumental in the study of combustor-turbine interactions in the context of lean-burn combustor flows and film-cooled high pressure turbine components. The experimental results will be of direct use to engine designers and CFD users and developers. The optimisation of film-cooled turbine components for lean-burn combustor conditions is a critical step in realising simultaneous NO_X emissions reductions and engine efficiency gains. Realising these improvements over the coming decades is of central concern to engine manufactures, airlines and regulators alike.

The study required the development of both methods and physical understanding (of the problems associated with simulating swirling combustor flows) that will be relevant to future combustor simulator development programmes. In particular, this is the first time problems associated with simulating lean-burn flows have been addressed. The problem of flow similarity between reacting flows (characterised by strong thermal gradients and axial acceleration) and non-reacting is central to the design of simulators of this kind. Some fundamental differences in flow similarity (e.g.

PVC formation) can be overcome, however, greater collaboration between engine designers and developers of combustor simulators is required to fully understand the 3D flow structure in the engine case, and therefore the properties which should be matched by the simulator.

As part of the development of the OLCS, two additional experimental methods problems were examined: the development of an open source five-hole probe for aerodynamic measurements, and the development of a pressure probe response model. Both of these problems arose in the development of the experimental facility used to characterise the OLCS. It was demonstrated that additive manufacturing can be readily used to produce accurate five-hole probes which could be used in many experiments without experimental calibration; a result which will widen access to this fundamental experimental tool. The proposed pressure probe response model addresses a clear need for a simple but accurate tool for designing tube-transducer pressure measurement systems, and indeed, five-hole probe systems.

The following sections highlight the main conclusions from the preceding chapters related directly to the OLCS.

7.1 Numerical methodology

A numerical study of past OTRF combustor simulators was carried out as a means to develop a numerical approach, the limitations of which, were well understood. This approach was then applied to the predictive design of the OLCS. The study examined the OTRF EOTDF Generator and swirl simulator, each comprising a key element of the OLCS – temperature non-uniformity and swirling flow, respectively. It was found that:

- URANS demonstrated weakness in predicting the mixing of adjacent streams as manifest by the resultant downstream temperature distribution being less mixed out than in the experiment.

- The temperature distribution was best predicted by the $k-\omega$ SST model due to it resolving vortical structures which drive mixing processes.
- The EOTDF Generator case was made particularly difficult for a RANS-based simulation by the matched stream velocities, which placed emphasis on vorticity generation in the upstream boundary layers.
- Significantly improved results would require a scale-resolving simulation approach. This kind of simulation resolves the vortical structures which govern mixing, rather than modelling them.
- URANS demonstrated capability in terms of capturing the overall flow structure of swirling flows, displaying good agreement with experimental data.

7.2 Development of the OLCS

The development of the OLCS was carried out utilising 3D URANS as a predictive tool. The development study focused on achieving a set of 2D profiles of total temperature, total pressure, and swirl and pitch angle (for the SILOET turbine) at the vane inlet. The system was to be modular such that it could also create conditions for a second experimental programme, LEMCOTEC, as well as future OTRF turbine programmes. The development study revealed that significant challenges exist relating to variable swirling flow structure, the latter being sensitive to Reynolds number, swirl number, geometry and combustion. Having overcome some of these challenges, a modular combustor simulator system was designed and manufactured. The key findings were:

- Swirling flows are complex and subject to instability phenomena—vortex breakdown and precessing vortex cores—which are not completely understood. The lack of understanding means predicting or quantifying flow similarity is challenging.

- The flow structure and prevailing instabilities are sensitive to Reynolds number, swirl number, geometry and heat release due to combustion. Simply matching engine combustor geometry will not result in flow similarity; the key challenge to designers of simulators
- The formation or suppression of a PVC influences mixing processes in the mainstream, altering downstream swirl strength and influencing coolant mixing.
- It was demonstrated that a low-momentum axial jet at the swirler centre could be used to suppress PVC formation in isothermal flows, as it often is by combustion. This provides one mechanism by which flow similarity can be controlled by the designer.
- The ideal simulator design process would draw upon extensive combustor data to understand the mainstream flow structure, rather than 2D downstream profiles which offer only limited insight to upstream flow features.
- Water jet cutting from aluminium was identified as a cost-effective means to produce axial swirlers.

A further CFD study examined the final OLCS hardware with a specific interest in the similarity of flow between nominal OTRF conditions and a set of near-atmospheric conditions. It was found that for cases without a PVC, satisfactory flow similarity existed between the two sets of conditions. The structure of the PVC was affected by the change in Reynolds number between the OTRF condition and atmospheric condition cases. Caution is required when scaling the system to different conditions of geometry.

7.3 Experimental results

Steady and unsteady measurements were taken using the experimental facility discussed above. The overarching conclusions drawn from this data, with respect to URANS predictions and target data were:

- The OLCS was demonstrated experimentally to produce periodic aerodynamic inlet conditions based on extensive traverses over 180° of the annulus.
- Agreement was good (between experiments, URANS and targets) in all cases in terms of steady measurements of aerodynamic properties at the vane inlet. Swirl and pitch angle profiles were in excellent agreement in 2D (and 1D).
- Total temperature profiles showed poorer agreement in all cases, with consistent under-prediction of mixing by URANS being the cause (there was relatively good agreement between URANS and targets).
- Although significant effort was invested in attempts to characterise the unsteady aerodynamic inlet properties, high quality data were not collected for swirling cases. This problem could only be overcome with more suitable probes, i.e. a calibrated 3-wire hot-wire probe.
- For the uniform case, the unsteady data gave a value of inlet turbulence intensity as being $7 - 8\%$, and uniform across the plane. This was in agreement with URANS predictions and the design target.
- It was not possible to conclusively identify the signature of a oscillating PVC structure. This may have been limited by the measurement methods employed.

7.4 Recommendations for future work

The following recommendations for future work are given base on lessons learnt in this study:

- As interest moves increasingly towards combustor simulators which replicate engine profiles across all properties, and particularly where this involves swirl, a greater knowledge of the combustor (to be emulated) would assist the simulator designer greatly. That is, a full understanding of the upstream flow field, rather than simply 2D profiles at the combustor-turbine interface.

- Future combustor simulator development studies should consider pilot experiments that operate at matched non-dimensional conditions to reduce uncertainty around flow similarity. The ECAT facility at Oxford could provide a suitable test bed.
- Laser diagnostics (e.g. particle image velocimetry) would provide much greater understanding of simulator flows, allowing additional fundamental understanding to be drawn from research of this kind.
- Hybrid RANS-LES methods, particular the Scale Adaptive Simulation, should become the preferred method for this kind of work as computational resources allow.

Based on the experience in developing the experimental facility, the following recommendations were made for future work:

- Despite the high performance of the vortex tube, significant heat transfer to the fluid through the distribution hardware and the OLCS itself reduced the ultimate temperature difference significantly. This system should be revised if reused in future.
- Where stepper motors are used to control probe traverse systems, attention should be paid to proper electrical installation to preserve the quality of sensor signals.
- Monolithic graphite burst disks should be used where fluctuating back-pressure exists on the downstream (vent) line.
- The use of embedded Kulite probes for turbulence measurement is not straight forward - dynamic calibration should not be neglected.

References

Alekseenko, S. V., Kuibin, P. A., and Okulov, V. L. (2008). *Theory of Concentrated Vortices*. Berlin: Springer-Verlag. ISBN: 978-3-540-73375-1.

Almondo, A. and Sorli, M. (2006). "Time Domain Fluid Transmission Line Modelling using a Passivity Preserving Rational Approximation of the Frequency Dependent Transfer Matrix". In: *International Journal of Fluid Power* 7.1, pp. 41–50. ISSN: 1439-9776.

Andreini, A., Facchini, B., Insinna, M., Mazzei, L., and Salvadori, S. (2015). "Hybrid RANS-LES Modeling of a Hot Streak Generator Orientated to the Study of Combsutor-Turbine Interaction". In: *Proceedings of ASME Turbo Expo 2015*. Montreal, Quebec, Canada, pp. 1–12.

ANSYS (2013). "Theory Guide". In: *ANSYS Help System 14.5*. Release 14. ANSYS, Inc.

Ayalew, B. and Kulakowski, B. T. (2005). "Modal Approximation of Distributed Dynamics for a Hydraulic Transmission Line With Pressure Input-Flow Rate Output Causality". In: *Journal of Dynamic Systems, Measurement, and Control* 127.3, p. 503. ISSN: 00220434.

Bacci, T., Caciolli, G., Facchini, B., Tarchi, L., Koupper, C., and Champion, J.-l. (2015a). "Flowfield and Temperature Profiles Measurements on a Combustor Simulator dedicated to Hot Streaks Generation". In: *Proceedings of ASME Turbo Expo 2015*. Montreal, Quebec, Canada, pp. 1–14.

Bacci, T., Facchini, B., Picchi, A., Tarchi, L., Koupper, C., and Champion, J.-l. (2015b). "Turbulence Field Measurements At the Exit of a Combustor Simulator Dedicated to Hot Streaks Generation". In: *Proceedings of ASME Turbo Expo 2015*. Montreal, Quebec, Canada, pp. 1–14.

Barringer, M. D., Thole, K. A., and Polanka, M. D. (2004). "Developing a Combustor Simulator for Investigating High Pressure Turbine Aerodynamics and Heat Transfer". In: *Proceedings of ASME Turbo Expo 2004*. ASME, pp. 565–575. ISBN: 0-7918-4168-5.

Barringer, M. D., Thole, K. A., and Polanka, M. D. (2009a). "Effects of Combustor Exit Profiles on Vane Aerodynamic Loading and Heat Transfer in a High Pressure Turbine". In: *Journal of Turbomachinery* 131.2.

Barringer, M. D., Thole, K. a., Polanka, M. D., Clark, J. P., and Koch, P. J. (2009b). "Migration of Combustor Exit Profiles Through High Pressure Turbine Vanes". In: *Journal of Turbomachinery* 131.2. ISSN: 0889504X.

Beard, P. F., Smith, A., and Povey, T (2011). "Impact of Severe Temperature Distortion on Turbine Efficiency". In: *Proceedings of ASME Turbo Expo 2011*. Vancouver, British Columbia, pp. 1–14.

Beard, P. F., Smith, A. D., and Povey, T. (2013). "Effect of Combustor Swirl on Transonic High Pressure Turbine Efficiency". In: *Journal of Turbomachinery* 136.1. ISSN: 0889-504X.

Bergh, H and Tijdeman, H (1965). *Theoretical and experimental results for the dynamic response of pressure measuring systems*. Tech. rep. NLR-TR F.238. Amsterdam: National Aero- and Astronautical Research Institute, p. 21.

Bryer, D. W. and Pankhurst, R. C. (1971). *Pressure-probe methods for determining wind speed and flow direction*. London: H.M.S.O. ISBN: 77859536.

Butler, T. L., Sharma, O. P., Joslyn, H. D., and Dring, R. P. (1989). "Redistribution of an inlet temperature distortion in an axial flow turbine stage". In: *Journal of Propulsion and Power* 5.1, pp. 64–71. ISSN: 0748-4658.

Caldwell, W. I., Coon, G. A., and Zoss, L. (1959). *Frequency response for process control*. Ed. by L. M. Zoss and G. A. Coon. McGraw-Hill series in control systems engineering. New York: McGraw-Hill. ISBN: 125825669X.

Cameron, C. D., Samuelsen, G. S., and Brouwer, J (1989). "A model gas turbine combustor with wall jets and optical access for turbulent mixing, fuel effects, and spray studies". In: *Symposium (International) on Combustion* 22.1, pp. 465–474.

Celik, I. B., Ghia, U., Roache, P. J., Freitas, C. J., Coleman, H., and Raad, P. E. (2008). "Procedure for Estimation and Reporting of Uncertainty Due to Discretization in CFD Applications". In: *Journal of Fluids Engineering* 130.7, p. 78001. ISSN: 0098-2202. URL: http://dx.doi.org/10.1115/1.2960953http://fluidsengineering.asmedigitalcollection.asme.org/article.aspx?articleid=1434171.

Centolanzi J, F. (1957). "Characteristic of a 40 cone for measuring mach number, total pressure, and flow angles at supersonic speeds". Moffett Field, California. URL: https://ntrs.nasa.gov/search.jsp?R=19930084789.

Chana, K., Cardwell, D., and Jones, T. (2013). "A review of the Oxford Turbine Research Facility". In: *Proceedings of ASME Turbo Expo 2013*, pp. 1–17. ISBN: 9780791855164.

Chana, K. S., Hurion, J. R., and Jones, T. V. (2003). "The Design, Development and Testing of a Non-Uniform Inlet Temperature Generator for the QinetiQ Transient Turbine Research Facility". In: *Proceedings of ASME Turbo Expo 2003*, pp. 1–8.

Chigier, N. A. and Beer, J. M. (1964). "Velocity and Static-Pressure Distributions in Swirling Air Jets Issuing From Annular and Divergent Nozzles". In: *Journal of Basic Engineering* 86.4, pp. 788–796. ISSN: 0098-2202. URL: http://dx.doi.org/10.1115/1.3655954.

Clark, N. N. and Atkinson, C. M. (1988). "Amplitude reduction and phase lag in fluidized-bed pressure measurements". In: *Chemical Engineering Science* 43.7, pp. 1547–1557. ISSN: 00092509.

CRDM (2013). *CRDM Tolerance Standards*. Tech. rep. 6. High Wycombe: 3D Systems Europe.

Cumpsty, N. A. and Horlock, J. H. (2006). "Averaging Nonuniform Flow for a Purpose". In: *Journal of Turbomachinery* 128.1, p. 120. ISSN: 0889504X.

DLR (2014). *Neuer Turbinenprüfstand NextGeneration Turbine (NG-Turb)*. Tech. rep. Gottingen, Germany: Deutsches Zentrum für Luft- und Raumfahrt, p. 4.

Dominy, R. G. and Hodson, H. P. (1993). "An Investigation of Factors Influencing the Calibration of Five-Hole Probes for Three-Dimensional Flow Measurements". In: *Journal of Turbomachinery* 115.3, p. 513. ISSN: 0889504X.

Dorney, D. J., Gundy-Burlet, K. L., and Sondak, D. L. (1999). "A Survey Of Hot Streak Experiments And Simulations". In: *International Journal of Turbo and Jet Engines* 16.1, pp. 1–16. ISSN: 2191-0332.

Faler, J. H. and Leibovich, S (1977). "Disrupted states of vortex flow and vortex breakdown". In: *Physics of Fluids* 20.9, p. 1385.

Ford, C. L., Carrotte, J. F., and Walker, A. D. (2012). "The Impact of Compressor Exit Conditions on Fuel Injector Flows". In: *Journal of Engineering for Gas Turbines and Power* 134.11, p. 9. ISSN: 07424795.

Goodisman, M. I., Oldfield, M. L. G., Kingcombe, R. C., Jones, T. V., Ainsworth, R. W., and Brooks, A. J. (1992). "An Axial Turbobrake". In: *Journal of Turbomachinery* 114.2, pp. 419–425. ISSN: 0889-504X.

Goodson, R. E. (1970). "Distributed system simulation using infinite product expansions". In: *SIMULATION*, pp. 255–263. ISSN: 0037-5497.

Goodson, R. E. and Leonard, R. G. (1972). "A Survey of Modeling Techniques for Fluid Line Transients". In: *Journal of Basic Engineering* 94.2, p. 474. ISSN: 00219223.

Gowland, R. (2010). *Design and manufacture of a 4" supersonic probe calibration facility*. Tech. rep. Oxford: Dept. Engineering Science, University of Oxford.

Griffini, D., Insinna, M., Salvadori, S., and Martelli, F. (2015). "Clocking Effects of Inlet Non-Uniformities in a Fully Cooled High-Pressure Vane: A Conjugate Heat Transfer Analysis". In: *Proceedings of ASME Turbo Expo 2015*. Montreal, Quebec, Canada, pp. 1–13.

Grotjans, H, Menter, F. R., Burr, R., and Glueck, M. (1998). *Higher order turbulence modelling for industrial applications*. Tech. rep.

Guo, B., Langrish, T. a. G., and Fletcher, D. F. (2001). "Simulation of turbulent swirl flow in an axisymmetric sudden expansion". In: *AIAA Journal* 39.1, pp. 96–102. ISSN: 0001-1452.

Haldeman, C, Mathison, R, and Dunn, M (2004). "Design, Construction and Operation of a Combustor Emulator for Short-Duration High-Pressure Turbine Experiments". In: *40th AIAA/ASME/SAE/ASEE Joint Propulsion Conference and Exhibit*. Joint Propulsion Conferences. American Institute of Aeronautics and Astronautics.

Haldeman, C. W. (1989). "An Experimental Study of Radial Temperature Profile Effects on Turbine Tip Shroud Heat Transfer". PhD thesis. Massachusetts Institute of Technology, pp. 1–190.

Hall, B. F., Chana, K. S., and Povey, T. (2013). "Design of a Non-Reacting Combustor Simulator With Swirl and Temperature Distortion With Experimental Validation". In: *Proceedings of ASME Turbo Expo 2013*. International Gas Turbine Institute.

Hall, B. F., Chana, K. S., and Povey, T. (2014). "Design of a Nonreacting Combustor Simulator With Swirl and Temperature Distortion With Experimental Validation". In: *Journal of Engineering for Gas Turbines and Power* 136.8. ISSN: 0742-4795.

Harvey, J. K. (1962). "Some observations of the vortex breakdown phenomenon". In: *Journal of Fluid Mechanics* 14.04, pp. 585–592.

Henderson, D. (2009). *A new 4" pressurised transonic wind tunnel*. Tech. rep. Oxford: Dept. Engineering Science, University of Oxford.

Herrada, M. and Shtern, V. (2003). "Vortex breakdown control by adding near-axis swirl and temperature gradients". In: *Physical Review E* 68.4, p. 41202.

Hilditch, M. A., Fowler, A, Jones, T. V., Chana, K. S., Oldfield, M. L. G., Ainsworth, R. W., Hogg, S. I., Anderson, S. J., and Smith, G. C. (1994). "Installation of a turbine stage in the Pyestock Isentropic Light Piston Facility". In: *ASME 1994 International Gas Turbine and Aeroengine Congress and Exposition*. American Society of Mechanical Engineers.

Hirsch, C. (1993). *Advanced Methods for Cascade Testing*. Neuilly sur Seine: NATO Advisory Group for Aerospace Research and Development. ISBN: 9789283507178.

Huang, Y. and Yang, V. (2009). "Dynamics and stability of lean-premixed swirl-stabilized combustion". In: *Progress in Energy and Combustion Science* 35.4, pp. 293–364. ISSN: 03601285.

Hunter, G. W., Neudeck, P. G., Okojie, R. S., Beheim, G. M., Powell, J. A., and Chen, L. (2003). "An overview of high-temperature electronics and sensor development at NASA Glenn Research Center". In: *Journal of Turbomachinery* 125.October 2003, pp. 658–664. ISSN: 0889504X.

Hurrion, J. (2002). "The effect of an inlet temperature profile on the heat transfer to gas turbine blades". PhD thesis. University of Oxford.

Iberall, A. S. (1950). "Attenuation of oscillatory pressures in instrument lines". In: *Journal of Research of the National Bureau of Standards* 45.1, p. 85. ISSN: 0091-0635.

Insinna, M., Griffini, D., Salvadori, S., and Martelli, F. (2014a). "Conjugate heat transfer analysis of a film cooled high-pressure turbine vane under realistic combustor exit flow conditions". In: *Proceedings of the ASME Turbo Expo*. Vol. 5A. Dusseldorf, Germany, pp. 1–14. ISBN: 9780791845714.

Insinna, M., Salvadori, S., and Martelli, F. (2014b). "Simulation of Combustor/NGV Interaction Using Coupled RANS Sovlers: Validation and Application to a Realistic Test Case". In: *Proceedings of ASME Turbo Expo 2014*. Dusseldorf, Germany, pp. 1–12.

International Civil Aviation Organization (2011a). *Aircraft Engine Emissions*. URL: `http://www.icao.int/environmental-protection/pages/aircraft-engine-emissions.aspx` (visited on 12/15/2015).

— (2011b). *Technology Standards*. URL: `http://www.icao.int/environmental-protection/Pages/technology-standards.aspx` (visited on 12/15/2015).

Jawarneh, A. M. and Vatistas, G. H. (2006). "Reynolds Stress Model in the Prediction of Confined Turbulent Swirling Flows". In: *Journal of Fluids Engineering* 128.6, pp. 1377–1382. ISSN: 00982202.

Jochmann, P, Sinigersky, A, Koch, R, and Bauer, H. J. (2005). "URANS Prediction of Flow Instabilities of a Novel Atomizer Combustor Configuration". In: *Proceedings of ASME Turbo Expo 2005*, pp. 1–9.

Johansson, M., Povey, T., Chana, K., Wallin, F., and Abrahamsson, H. (2014). "Aerodynamic and Heat Transfer Measurements on an Intermediate Turbine Duct Vane". In: *Proceedings of ASME Turbo Expo 2014*. Dusseldorf, Germany, pp. 1–10.

Kempf, A, Malalasekera, W, Ranga-Dinesh, K. K. J., and Stein, O (2008). "Recirculation and vortex breakdown in isothermal and reacting swirling flows: insights from two different large eddy simulation programs [Published as: Large eddy simulations of swirling non-premixed flames with flamelet models: a comparison of numerical ". In:

Khanal, B., He, L., Northall, J., and Adami, P. (2013). "Analysis of Radial Migration of Hot-Streak in Swirling Flow Through High-Pressure Turbine Stage". In: *Journal of Turbomachinery* 135.July 2013, p. 041005. ISSN: 0889-504X.

Kilik, E. (1976). "The influence of swirler design parameters on the aerodynamics of downstream recirculation region". PhD thesis. Cranfield University.

Kirshner, J. M. (1975). *Design theory of fluidic components*. Ed. by S. Katz. New York: Academic Press. ISBN: 0124102506.

Klapdor, E. V. (2010). "Simulation of Combustor - Turbine Interaction in a Jet Engine". PhD thesis. Technische Universtat Darmstadt.

Koupper, C., Caciolli, G., Gicquel, L., Duchaine, F., Bonneau, G., Tarchi, L., and Facchini, B. (2014). "Development of an Engine Representative Combustor Simulator Dedicated to Hot Streak Generation". In: *Journal of Turbomachinery* 136.11, p. 111007. ISSN: 0889-504X.

Krause, N and Dudzinsky, J (1969). "Flow -Direction Measurement with Fixed-Position Probes". Cleveland, Ohio. URL: https://ntrs.nasa.gov/search.jsp?R=19690030674.

Krichbaum, A., Werschnik, H., Wilhelm, M., Schiffer, H.-P., and Lehmann, K. (2015). "A Large Scale Turbine Test Rig for the Investigation of High Pressure Turbine Aerodynamics and Heat Transfer with Variable Inflow Conditions". In: *Proceedings of ASME Turbo Expo 2015*. Montreal, Quebec, Canada, pp. 1–13.

Lefebvre, A. H. and Ballal, D. R. (2010). *Gas Turbine Combustion*. Third. Boca Raton, FL: CRC Press, pp. 1–560.

LEMCOTEC (2012). *Lemcotec - Objectives*. URL: http://www.lemcotec.eu/page/about-lemcotec/objectives.php (visited on 12/18/2015).

Lilley, D. G. (1977). "Swirl Flows in Combustion: A Review". In: *AIAA Journal* 15.8, pp. 1063–1078. ISSN: 0001-1452.

Liu, X. and Liu, Z. (2014). "Investigation of the energy separation effect and flow mechanism inside a vortex tube". In: *Applied Thermal Engineering* 67.1-2, pp. 494–506. ISSN: 13594311.

Lo Jacono, D, Sørensen, J. N., Thompson, M. C., and Hourigan, K (2008). "Control of vortex breakdown in a closed cylinder with a small rotating rod". In: *Journal of Fluids and Structures* 24.8, pp. 1278–1283.

Lu, X., Wang, S., Hong-Gye Sung, S, Hsieh, H.-Y., and Yang, V. (2005). "Large-eddy simulations of turbulent swirling flows injected into a dump chamber". In: *Journal of Fluid Mechanics* 527, pp. 171–195. ISSN: 0022-1120.

Main, A., Day, C., Lock, G., and Oldfield, M. (1996). "Calibration of a four-hole pyramid probe and area traverse measurements in a short-duration transonic turbine cascade tunnel". In: *Experiments in Fluids* 21.4. ISSN: 0723-4864. URL: http://link.springer.com/10.1007/BF00190681.

Massini, M., Miller, R. J., and Hodson, H. P. (2011). "A New Intermittent Aspirated Probe for the Measurement of Stagnation Quantities in High Temperature Gases". In: *Journal of Turbomachinery* 133.4, p. 041022. ISSN: 0889504X.

Mathison, R. M., Haldeman, C. W., and Dunn, M. G. (2012). "Aerodynamics and Heat Transfer for a Cooled One and One-Half Stage High-Pressure TurbinePart I: Vane Inlet Temperature Profile Generation and Migration". In: *Journal of Turbomachinery* 134.1, p. 11006.

Menter, F. R. (2012). *Best Practice: Scale-Resolving Simulations in ANSYS CFD*. Tech. rep. April. ANSYS Germany GmbH, pp. 1–70.

Mitchell, A. M. and Délery, J. (2001). "Research into vortex breakdown control". In: *Progress in Aerospace Sciences* 37.4, pp. 385–418. ISSN: 03760421.

Moss, R. W. and Oldfield, M. L. G. (1991). "Measurements of Hot Combustor Turbulence Spectra". In: *International Gas Turbine and Aerospace Congress and Exposition*. Orlando, FL.

Nachtigal, C. L. (1990). *Instrumentation and Control: Fundamentals and Applications*. New York: John Wiley & Sons, Inc., p. 311. ISBN: 0471880450.

Nichols, N. B. (1962). "The linear properties of pneumatic transmission lines". In: *ISA Transactions* 1.1, pp. 5–14.

Nocera, F. (2011). *Design and manufacture of a 4" supersonic probe calibration facility*. Tech. rep. Oxford: Dept. Engineering Science, University of Oxford.

Norris, G. (2013). *Rolls Reach Critical Design Review Milestone For A350-1000*. URL: `http://aviationweek.com/awin/rolls-reaches-critical-design-review-milestone-a350-1000` (visited on 12/13/2015).

Oberleithner, K., Terhaar, S., Rukes, L., and Oliver Paschereit, C. (2013). "Why Nonuniform Density Suppresses the Precessing Vortex Core". In: *Journal of Engineering for Gas Turbines and Power* 135.12, p. 121506. ISSN: 0742-4795.

O'Connor, J. and Lieuwen, T. (2011). "Further Characterization of the Disturbance Field in a Transversely Excited Swirl-Stabilized Flame". In: *Proceedings of ASME Turbo Expo 2011*, pp. 1–12.

Omega (2015). *Comparison of Time Constant vs . Overall Outside Diameter of Bare Thermocouple Wires or Grounded Junction Thermocouples In Air*. Tech. rep. Stamford, CT: Omega Engineering Limited, p. 2.

Paniagua, G., Denos, R., and Oropesa, M. (2002). "Thermocouple Probes for Accurate Temperature Measurements in Short Duration Facilities". In: *Proceedings of ASME Turbo Expo 2002* 2 A, pp. 209–217.

Povey, T, Jones, T. V., and Chana, K. S. (2003). "Heat Transfer and Aerodynamics of an Intermediate Pressure Nozzle Guide Vane With and Without Inlet Temperature Non-Uniformity". In: *Proceedings of ASME Turbo Expo 2003*, pp. 1–9.

Povey, T., Chana, K. S., Jones, T. V., and Hurrion, J. (2007). "The Effect of Hot-Streaks on HP Vane Surface and Endwall Heat Transfer: An Experimental and Numerical Study". In: *Journal of Turbomachinery* 129.1, p. 32. ISSN: 0889504X.

Povey, T, Oldfield, M. L. G., and Haselbach, F (2008). "Transonic turbine vane tests in a new miniature cascade facility". In: *Proceedings of the Institution of Mechanical Engineers, Part A: Journal of Power and Energy* 222.5, pp. 529–539. ISSN: 0957-6509. URL: http://pia.sagepub.com/lookup/doi/10.1243/09576509JPE534.

Povey, T. and Qureshi, I (2008). "A hot-streak (combustor) simulator suited to aerodynamic performance measurements". In: *Proceedings of the Institution of Mechanical Engineers, Part G: Journal of Aerospace Engineering* 222.6, pp. 705–720.

— (2009). "Developments in Hot-Streak Simulators for Turbine Testing". In: *Journal of Turbomachinery* 131.3, p. 31009.

Qureshi, I, Smith, A. D., Chana, K. S., and Povey, T. (2012). "Effect of Temperature Nonuniformity on Heat Transfer in an Unshrouded Transonic HP Turbine: An Experimental and Computational Investigation". In: *Journal of Turbomachinery* 134.1.

Qureshi, I. and Povey, T. (2011). "A combustor-representative swirl simulator for a transonic turbine research facility". In: *Proceedings of the Institution of Mechanical Engineers, Part G: Journal of Aerospace Engineering* 225.7, pp. 737–748. ISSN: 0954-4100. URL: http://pig.sagepub.com/content/225/7/737.

Qureshi, I., Beretta, A., Chana, K., and Povey, T. (2011a). "Effect of Aggressive Inlet Swirl on Heat Transfer and Aerodynamics in an Unshrouded Transonic HP Turbine". In: *Proceedings of ASME Turbo Expo 2011*. Vancouver, British Columbia, pp. 1–13.

Qureshi, I., Beretta, A., and Povey, T. (2011b). "Effect of Simulated Combustor Temperature Nonuniformity on HP Vane and End Wall Heat Transfer: An Experimental and Computational Investigation". In: *Journal of Engineering for Gas Turbines and Power* 133.3.

Qureshi, M. I. (2010). "Effect of Engine-Realistic Temperature Profile and Swirl on HP Turbine Aerodynamics and Heat Transfer". PhD thesis. University of Oxford.

Rahim, A. and He, L. (2014). "Rotor Blade Heat Transfer of High Pressure Turbine Stage Under Inlet Hot Streak and Swirl". In: *Journal of Engineering for Gas Turbines and Power* 137.c, pp. 1–19. ISSN: 0742-4795.

Ramakrishnan, V. (2004). "Non-Conventional Multi-Hole Pressure Probes Non-Conventional Multi-Hole Pressure Probes". MSc Thesis. Texas A&M University. URL: http://oaktrust.library.tamu.edu/handle/1969.1/52.

Ranque, G. J. (1934). *Method and apparatus for obtaining from alpha fluid under pressure two currents of fluids at different temperatures.*

Rediniotis, O. K. and Kinser, R. E. (1998). "Development of a Nearly Omnidirectional Velocity Measurement Pressure Probe". In: *AIAA Journal* 36.10, pp. 1854–1860. ISSN: 0001-1452. URL: http://dx.doi.org/10.2514/2.278.

Reichert, B. a. and Wendt, B. J. (1994). "A new algorithm for five-hole probe calibration, data reduction, and uncertainty analysis". Cleveland, Ohio. URL: https://ntrs.nasa.gov/archive/nasa/casi.ntrs.nasa.gov/19950005965.pdf.

Richards, W. B. (1986). *Propagation of sound waves in tubes of noncircular cross section*. Tech. rep. Cleveland, Ohio: Lewis Research Center, NASA, p. 33.

Roach, P. E. (1987). "The generation of nearly isotropic turbulence by means of grids". In: *International Journal of Heat and Fluid Flow* 8.2, pp. 82–92. ISSN: 0142727X.

Rolls Royce (2015). *The Jet Engine*. Fifth. New York: John Wiley & Sons, p. 288. ISBN: 978-1-119-06599-9.

Roux, S., Lartigue, G., Poinsot, T., Meier, U., and Bérat, C. (2005). "Studies of mean and unsteady flow in a swirled combustor using experiments, acoustic analysis, and large eddy simulations". In: *Combustion and Flame* 141.1-2, pp. 40–54.

Schmid, G., Krichbaum, A., Werschnik, H., and Schiffer, H.-P. (2014). "The impact of realistic inlet swirl in a 1 and 1/2 stage axial turbine". In: *Proceedings of ASME Turbo Expo 2014*, pp. 1–11.

Schwab, J., Stabe, R., and Whitney, W. (1983). "Analytical and experimental study of flow through an axial turbine stage with a nonuniform inlet radial temperature profile". In: *19th Joint Propulsion Conference*. Joint Propulsion Conferences. NASA, Lewis Research Center. American Institute of Aeronautics and Astronautics.

Selle, L., Lartigue, G., Pointsot, T., Koch, R., Schildmacher, K.-U., Krebs, W., Kaufmann, P., and Veynante, D. (2003). "Compressible Large Eddy Simulation of turbulent combustion in complex geometry on unstructured meshes". In: *Combustion and Flame* 137.4, pp. 1–31.

Shang, T. and Epstein, a. H. (1997). "Analysis of Hot Streak Effects on Turbine Rotor Heat Load". In: *Journal of Turbomachinery* 119.3, p. 544. ISSN: 0889504X.

Simone, S., Montomoli, F., Martelli, F., Qureshi, I, Povey, T., and Chana, K. S. (2012). "Analysis on the Effect of a Nonuniform Inlet Profile on Heat Transfer and Fluid Flow in Turbine Stages". In: *Journal of Turbomachinery* 134.1, p. 11012.

Sperrin, D. (2012). *Experimental characterisation of a variable Mach variable Reynolds number calibration tunnel*. Tech. rep. Oxford: Dept. Engineerin Science, University of Oxford.

Terhaar, S., Oberleithner, K., and Paschereit, C. O. (2015). "Key parameters governing the precessing vortex core in reacting flows: An experimental and analytical

study". In: *Proceedings of the Combustion Institute* 35.3, pp. 3347–3354. ISSN: 15407489. URL: http://dx.doi.org/10.1016/j.proci.2014.07.035.

Terhaar, S., Reichel, T., and Schrödinger, C. (2013). "Vortex Breakdown and Global Modes in Swirling Combustor Flows with Axial Air Injection". In: *43rd Fluid Dynamics Conference* 31.1, pp. 1–16. ISSN: 0748-4658.

Thirumaleshwar, M. (2009). *Fundamentals of Heat and Mass Transfer*. Delhi: Pearson Education. ISBN: 9788177585193.

Treaster, A. L. and Yocum, A. M. (1978). "The calibration and application of five-hole probes". URL: http://www.dtic.mil/dtic/tr/fulltext/u2/a055870.pdf.

Turrell, M. D., Stopford, P. J., Syed, K. J., and Buchanan, E. (2004). "CFD Simulation of the Flow Within and Downstream of a High-Swirl Lean Premixed Gas Turbine Combustor". In: *Proceedings of ASME Turbo Expo 2004*, pp. 31–38. ISBN: 0-7918-4166-9.

University of Southampton (2015). *Rolls-Royce SILOET Project*. URL: http://www.southampton.ac.uk/engineering/research/projects/rolls-royce-siloet-project.page (visited on 12/18/2015).

Van Ommen, J. R., Schouten, J. C., Vander Stappen, M. L. M., and Van Den Bleek, C. M. (1999). "Response characteristics of probe-transducer systems for pressure measurements in gas-solid fluidized beds: How to prevent pitfalls in dynamic pressure measurements". In: *Powder Technology* 106.3, pp. 199–218. ISSN: 00325910.

Wang, P., Bai, X. S., Wessman, M., and Klingmann, J. (2004). "Large eddy simulation and experimental studies of a confined turbulent swirling flow". In: *Physics of Fluids* 16.9, pp. 3306–3324.

Wang, S., Yang, V., Hsiao, G., Hsieh, S.-Y., and Mongia, H. C. (2007). "Large-eddy simulations of gas-turbine swirl injector flow dynamics". In: *Journal of Fluid Mechanics* 583, pp. 99–122.

Wankhede, M. J., Bressloff, N. W., Keane, A. J., Caracciolo, L., and Zedda, M. (2010). "An Analysis of Unstable Flow Dynamics and Flashback Mechanism Inside a Swirl-Stabilised Lean Burn Combustor". In: *Proceedings of ASME Turbo Expo 2010*, pp. 1–11.

Wegner, B., Maltsev, A., Schneider, C., Sadiki, A., Dreizler, A., and Janicka, J. (2004). "Assessment of unsteady RANS in predicting swirl flow instability based on LES and experiments". In: *International Journal of Heat and Fluid Flow* 25.3, pp. 528–536.

Westley, R. (1957). *Vortex Tube Performance Data Sheets*. Tech. rep. Cranfield, UK: The College of Aeronautics, Cranfield, pp. 1–38.

Woodward, J. (2013). *Experimental characterisation of a variable Mach variable Reynolds number calibration tunnel*. Tech. rep. Oxford: Dept. Engineering Science, University of Oxford.

Xie, H.-Y and Geldart, D (1997). "The response time of pressure probes". In: *Powder Technology* 90.2, pp. 149–151. ISSN: 00325910.

Yang, S. L., Siow, Y. K., Peschke, B. D., and Tacina, R. R. (2003). "Numerical Study of Nonreacting Gas Turbine Combustor Swirl Flow Using Reynolds Stress Model". In: *Journal of Engineering for Gas Turbines and Power* 125.3, pp. 804–811.

Yang, W. C. and Tobler, W. E. (1991). "Dissipative Modal Approximation of Fluid Transmission Lines Using Linear Friction Model". In: *Journal of Dynamic Systems, Measurement, and Control* 113.1, pp. 152–162. ISSN: 0022-0434.

Yasa, T. and Paniagua, G. (2012). "Robust procedure for multi-hole probe data processing". In: *Flow Measurement and Instrumentation* 26, pp. 46–54. ISSN: 09555986. URL: `http://proceedings.asmedigitalcollection.asme.org/proceeding.aspx?articleid=1632336`.

Yilmaz, M., Kaya, M., Karagoz, S., and Erdogan, S. (2009). "A review on design criteria for vortex tubes". In: *International Journal of Heat and Mass Transfer*, pp. 1–20.